Fabrication and Thermoelectric Characterization of Nanostructured Silicon

Dissertation

zur Erlangung des akademischen Grades
doctor rerum naturalium (Dr. rer. nat.)

vorgelegt der
Mathematisch-Naturwissenschaftlich-Technischen Fakultät
(mathematisch-naturwissenschaftlicher Bereich)
der Martin-Luther-Universität Halle-Wittenberg

von
Johannes de Boor
geboren am 25. Juni 1981 in Waren an der Müritz

Gutachter/in:

1. PD Dr. Hartmut Leipner
2. Prof. Dr. Kornelius Nielsch
3. Prof. Dr. Friedemann Völklein

Halle (Saale), den 21.01.2011

verteidigt am 08.06.2011

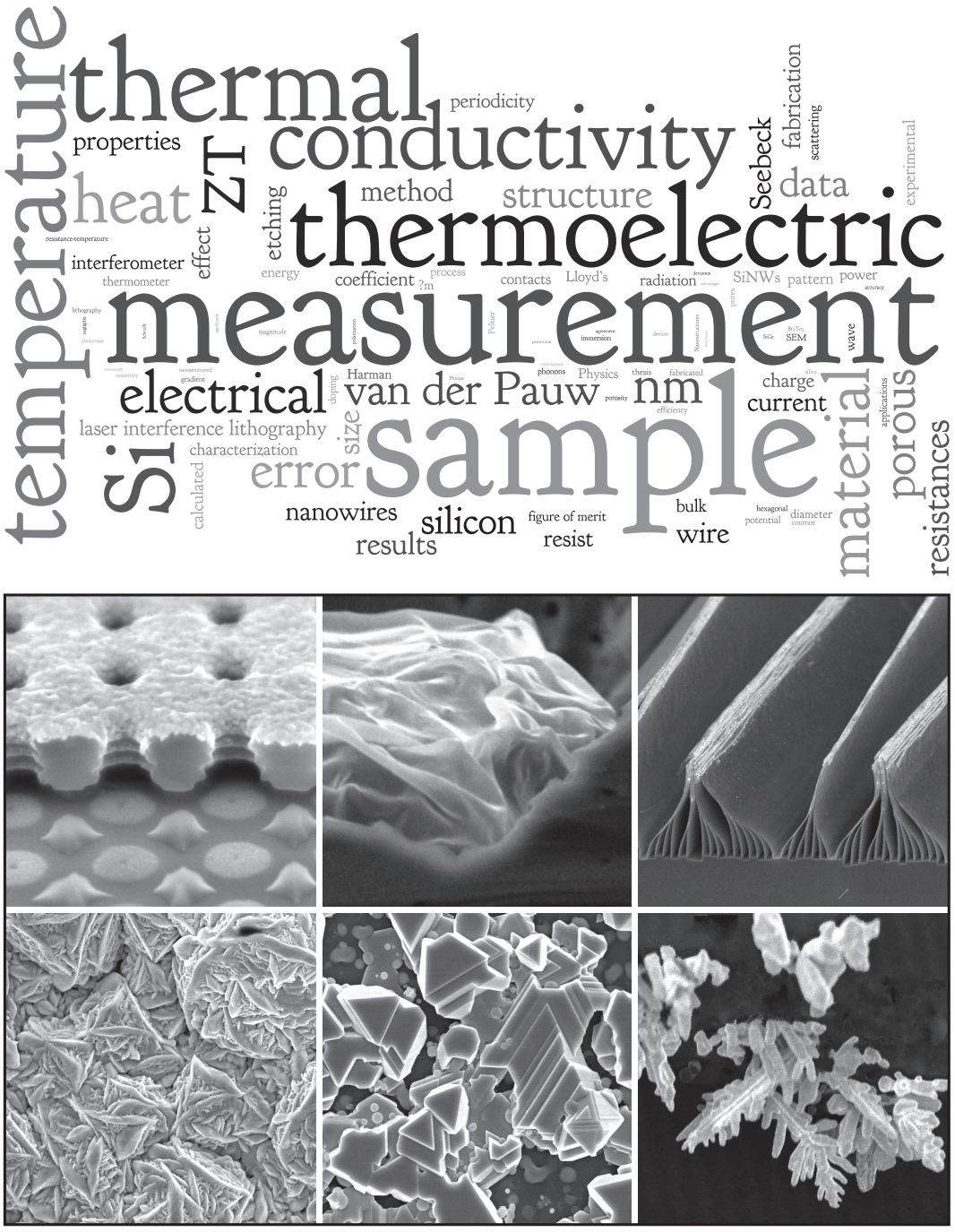

Figure 1: Top: thesis subject index. Catch-words of the thesis are displayed with their size according to their number of appearances using `http://www.wordle.net/` Bottom: Science is not always ugly...

Preface

Thermoelectric materials convert (waste) heat directly into usable electricity and thereby help to increase power efficiency. It has been shown in 2008 that silicon nanowires can be processed such that they have thermoelectric properties comparable to Bi_2Te_3, the state-of-the-art material. Since silicon has great advantages in terms of abundance and processability compared to Bi_2Te_3, nanostructured Si is a high potential candidate for future thermoelectric applications. This thesis deals with the fabrication of macroscopic amounts of well-ordered, single crystalline silicon nanowires with a defined geometry, a novel measurement method for the complete characterization of thermoelectric materials, and the thermoelectric properties of porous Si, which is an alternative approach to fabricate thermoelectric nanostructured silicon.

The opening survey in Chapter 1 starts with an introduction to the basic thermoelectric phenomena and established thermoelectric materials. For efficient thermoelectric materials high electrical but low thermal conductivity is necessary. As discussed in Chapter 1, electrical and thermal transport are coupled in bulk materials. This interdependency limits the achievable efficiency and led to a relative standstill in the field of thermoelectrics after 1960. In the 1990s several concepts have been proposed to create superior thermoelectric materials. Of those concepts the most successful is to decouple heat and charge transport by nanostructuring the material. This allows diminishing thermal conduction without affecting the electrical properties of the material and thereby enhances the overall thermoelectric efficiency. It has been shown previously that this concept can be successfully applied to silicon

nanowires. Single nanowires can be utilized for proof-of-principle studies. However, for a silicon-nanowire-based thermoelectric device a large number of nanowires is necessary, preferable with a uniform geometry of each individual wire.

One approach to fabricate macroscopic amounts of silicon nanowires with defined position and geometry is presented in Chapter 2. Metal-assisted etching, a simple wet chemical etching process, has been combined with laser interference lithography to create arrays of silicon nanowires with uniform diameters strictly periodic over areas of several cm^2. The working principle of laser interference lithography using a standard Lloyd's mirror interferometer is discussed first, then two improvements of the interferometer are presented. One combines the standard interferometer with immersion lithography and extends the working area of the interferometer to smaller periodicities and structure sizes. The second improvement allows the patterning of genuinely hexagonal structures at a single exposure. For nanowire fabrication laser interference lithography has been used to create a noble metal mesh on a silicon substrate. If the patterned substrate is immersed in an etching solution, the silicon beneath the metal film is selectively etched away while the uncovered parts remain; this leads to the emergence of silicon nanowires. Adjusting the parameters of the lithography the geometry, position, and ordering of the wires can be tailored. The obtained arrays of silicon nanowires with tailored geometry present a crucial step towards the realization of a silicon nanowire-based thermoelectric device.

Chapter 3 is dedicated to the field of thermoelectric measurement techniques. In order to extract the thermoelectric properties of materials its Seebeck coefficient, electrical conductivity, and thermal conductivity have to be obtained. Here we present a measurement concept that enables the determination of those three properties concurrently on the same sample. This measurement approach can be naturally combined with a direct figure of merit measurement which can be used to cross-check of the experimental results. After demonstrating the feasibility of the method on two materials an overview over the different measurement errors of

the technique is given. The most relevant ones are analyzed in detail in the main text while a detailed discussion on the minor errors can be found in Appendix B. The chapter is concluded with a discussion and demonstration on how to minimize experimental errors for thermoelectric van der Pauw measurements.

Chapter 4 is based on the preceding parts of the thesis. We have fabricated porous Si, which can be thought of as the inverse structure to an array of Si nanowires. Porous Si is fabricated by electrochemical etching and initially exhibits a very low electrical conductivity so that it is inappropriate as thermoelectric material. We show that the electrical conductivity can be increased dramatically by doping and surface passivation. It is furthermore shown that properly prepared porous Si exhibits thermoelectric properties superior to its bulk counterpart. However, further improvement is necessary and therefore a systematic investigation of the thermal conductivity of porous Si as a function of structure size, i.e. average wall thickness is presented. It is indicated that porous Si with a structure size below 10 nm is necessary to obtain a material with thermoelectric properties comparable to state-of-the-art materials.

The appendices contain further, more detailed technical information for the interested reader: Appendix A shows that convection and conduction through air are negligible if working in high vacuum while Appendix B presents a thorough analysis of further experimental errors of the thermoelectric van der Pauw method. The fabrication of the porous samples that are discussed in Chapter 4 is outlined in more detail in Appendix C while deeper insight on the measurement procedure and the data analysis for the thermal conductivity measurement with the 3ω -method is provided in Appendix D.

Contents

Preface **I**

1 Introduction **1**
1.1 Thermoelectric phenomena 1
1.2 Thermoelectric materials and applications 5
1.3 Strategies for improved thermoelectrics 8
1.4 Conclusion 12

2 Fabrication of Si Nanostructures by Interference Lithography **14**
2.1 Laser interference lithography 14
2.1.1 General principle 15
2.1.2 Immersion laser interference lithography 23
2.1.3 Three-beam interference lithography 28
2.2 LIL structures for thermoelectric applications 32
2.2.1 Arrays of silicon nanowires 32
2.2.2 Silicon nanofins 36
2.3 Summary of Chapter 2 40

3 Thermoelectric van der Pauw Measurements **41**
3.1 Measurement system 41
3.1.1 Setup 41
3.1.2 Instrumentation and programming interface 43
3.2 Realization of thermoelectric van der Pauw measurements 46
3.2.1 Summary 57
3.3 Two-heater thermoelectric van der Pauw measurements 58
3.4 Error analysis 61
3.4.1 Effect of heat losses 62
3.4.2 Calculation of the sample temperature profile 64
3.4.3 Errors due to heat loss through the electrical connections . . 67
3.4.4 Errors due to radiative heat loss 67
3.4.5 Errors of the Seebeck measurement 69
3.4.6 Error of the combined ZT 70
3.4.7 Errors of the Harman ZT_H measurement. 70

3.4.8 Comparison of combined and Harman ZT 71
3.5 Error minimizing strategies 71
3.6 Summary of Chapter 3 73

4 Thermoelectric Characterization of Porous Silicon 75
4.1 Fabrication of porous silicon 77
4.2 Electrical conductivity and figure of merit of porous silicon 78
4.2.1 Doping and passivation 79
4.2.2 Thermoelectric characterization 80
4.3 Thermal conductivity of porous silicon 83
4.3.1 Thermal conductivity of bulk silicon 84
4.3.2 Thermal conductivity measurements with the 3ω method . . 87
4.3.3 Measurement results for porous silicon 89
4.4 Summary of Chapter 4 98

5 Summary, Open Questions, and Outlook 99

A Convection and Thermal Conductivity of Air at Low Pressures i

B Further Errors of Thermoelectric van der Pauw Measurements iii
B.1 Error propagation for the van der Pauw equation iii
B.2 Systematic errors due to sample and contact geometry v
B.3 Self heating of the wires vii
B.4 The influence of thermal contact resistances vii
B.5 Further errors of the HarmanZT_H measurement xi
B.6 Errors of the temperature measurement xii
B.7 Error due to incorrect resistance-temperature calibration xiii
B.8 Errors of the two-heater thermoelectric van der Pauw measurement . xiv

C Fabrication of Porous Silicon xvi

D Details and Error Analysis of the 3ω Method xx
D.1 Details of the 3ω measurement xx
D.2 Error analysis of the 3ω method xxv

Bibliography xxix

Publikationsliste xlvii

Lebenslauf xlix

Errata

Between submission for evaluation (21.01.2011) and submission for publication (13.06.2011) of this thesis two inaccuracies have been noted, these shall be corrected here.

1.) Page 56, taking the effect of the Seebeck coefficient of the wires into account: Eqn. (3.12) must be rewritten as

$$ZT_{\mathrm{H,sample}} = ZT_{\mathrm{H,meas}} \left(\frac{U^S_{\mathrm{sample}}}{U^S_{\mathrm{sample}} - U^S_{\mathrm{wire}}} \right)^2 = ZT_{\mathrm{H,meas}} \left(\frac{S_{\mathrm{sample}}}{S_{\mathrm{sample}} - S_{\mathrm{wire}}} \right)^2 , \quad (1)$$

since the relative Seebeck coefficient effects both the measured voltage and the arising temperature gradient; the correction term therefore enters quadratically. The correction is relatively small so that all conclusion drawn in this section still remain valid.

The same holds true on p59, where the two-heater method is discussed. The correct equations for the calculation of $ZT_{\mathrm{H,sample}}$, S_{sample}, and κ as well as a correct measurement data set are given in

J. de Boor and V. Schmidt. Efficient thermoelectric van der Pauw measurements. *accepted in Applied Physics Letters*, 2011.

2.) Page 96, discussion on the thermal conductivity of porous Si:

Although stated differently in the thesis it is possible to understand the experimental results quantitatively in terms of a simple kinetic model for the heat transport. The model is based on a reduction of the phonon mean free path due to the nanostructuring and explains both the temperature and structure size dependence of the experimental data. The model and the interpretation is discussed in

J. de Boor, D. S. Kim, X. Ao, D. Hagen, A. Cojocaru, H. Fö ll and V. Schmidt. Temperature and structure size dependence of the thermal conductivity of porous silicon. *submitted to Europhysics Letters*, 2011.

List of Symbols

Abbreviations

AAO	anodized aluminum oxide
AC	alternating current
BC	boundary condition
DC	direct current
DMM	digital multimeter
FWHM	full width at half maximum
ILIL	immersion laser interference lithography
LIL	laser interference lithography
NW	nanowire
PID	proportional/integral/differential (coefficients)
pSi	porous Si
pSiGe	porous SiGe
RPM	rounds per minute
SEM	scanning electron microscope
SiNW	silicon nanowire
TEM	transmission electron microscope
VLS	vapour-liquid-solid
ZIF	zero injection force (socket)

Frequently used symbols

Symbol	Description
a	sample side length [m]
a	factor related to fitting interval in 3ω measurement; dimensionless
A	sample cross sectional area [m^2]
b	half of the heater width used for 3ω measurement [m]
c	specific heat capacity [$J/(Km^3)$]
d	sample thickness [m]
D	thermal diffusivity [m^2/s]
e	elementary charge $\approx 1.6 \cdot 10^{-19}$ C

$\hat{e}$	polarization unit vector
E	energy [J]
E_F	Fermi energy [eV]
$\vec{E}$	electrical field [V/m]
f	(excitation) frequency [1/s]
h	Planck constant $\approx 6.6 \cdot 10^{-34}$ Js
I	electrical current [A]
$I(r)$	intensity [W/m^2]
j	electrical current density [A/m^2]
$\vec{k}$	wave vector [1/m]
$\vec{k_f}$	fringe vector [1/m]
k_B	Boltzmann constant $\approx 1.38 \cdot 10^{-23}$ J/K
l	sample length [m]
l	heater length [m]
$l^{\gamma}_{\mathrm{mfp}}$	phonon mean free path [m]
l^{e}_{mfp}	electron mean free path [m]
L	Lorenz factor $\approx 2.4 \cdot 10^{-8}$ WΩ/K^{-2}
m	sample mass [kg]
m^*	effective mass [kg]
n	charge carrier concentration [cm^{-3}]
n_i	refractive index of medium i; dimensionless
p	periodicity [m]
p	porosity; dimensionless
P	power [W]
P_{J}	Joule heating [W]
P_{Pel}	Peltier heating/cooling [W]
q	heat flux [W/m^2]
q	phonon wave vector [1/m]
R	reflectivity; dimensionless
R	Resistance [Ω]
R^{th}	thermal resistance [K/W]
S	Seebeck coefficient [V/K]
$\Re(\Delta T)$	real part of the temperature amplitude [K]
t	time [s]
t	thickness [m]
T	temperature [K]
T_M	average temperature [K]
U	voltage, potential difference [V]
U_S	Seebeck voltage [V]
U_Ω	Ohmic voltage [V]
v	speed (of sound) [m/s]
v	electronic Brownian motion velocity [m/s]

v_D	electronic drift velocity [m/s]
V	volume [m^3]
ZT	thermoelectric figure of merit; dimensionless
ZT_H	thermoelectric figure of merit by Harman method; dimensionless
α	linear resistance-temperature coefficient [Ω/K]
δ	contact radius/side length
δ	structure size, average wall thickness [m]
Δ	contact displacement [m]
Δ	difference (of e.g. temperature)
$\triangle$	Laplace operator
ϵ	emissivity; dimensionless
ϕ	electrostatic potential [V]
η	efficiency [%]
κ	thermal conductivity [W/(mK)]
κ_e	electronic thermal conductivity [W/(mK)]
κ_l	lattice thermal conductivity [W/(mK)]
μ	charge carrier mobility [Vs/cm^2]
ν	(phonon) frequency [1/s]
π	Peltier coefficient [V]
θ	angle between incoming light and substrate normal [°]
ρ	density [$1/m^3$]
ρ	resistivity [Ωcm]
σ	electrical conductivity [S/m]
σ_B	Stefan-Boltzmann constant $\approx 5.68 \cdot 10^{-8}\,W/m^2K^{-4}$
τ^{th}	thermal relaxation or scattering time constant [s]
ω	circular frequency [1/s]

Chapter 1

Thermoelectrics - Introduction and Survey

Most of the consumed electrical power is produced by burning fossil fuels in combustion engines with efficiencies below 50%, therefore power of the order of $\approx 10\,\mathrm{TW}$ is dissipated uselessly as waste heat each year [BP09]. This figure is expected to rise in the coming years while the amount of fossil energy sources decreases. Further problems arise, since the burning of fossil fuels produces greenhouse gases and mankind becomes increasingly aware of the current and future consequences of climate change [wik10a]. In order to tackle both problems, enormous efforts are undertaken to replace fossil fuels by renewable energy sources and/or use the produced electrical energy more efficiently. Thermoelectricity has the potential to be part of the solution because thermoelectric materials can convert waste heat directly into electrical energy and thereby increase energy efficiency.

The thesis begins with an introductory survey to thermoelectrics. In Section 1.1 basic phenomena like the Seebeck and the Peltier effect will be introduced and it will be shown, how these effects can be used for waste heat to energy conversion and cooling. The key parameter for a high efficiency of these processes is the so-called figure of merit ZT, whose physical interpretation and background will be established. Section 1.2 gives a short overview over thermoelectric materials and their current applications. The following Section 1.3 first illustrates why the field of thermoelectrics reached a relative standstill after 1960 and then discusses several approaches to superior thermoelectric materials that have been proposed and realized.

1.1 Thermoelectric phenomena

The two basic thermoelectric phenomena are the Seebeck and the Peltier effect. These can best be explained considering a thermocouple as shown in Figure 1.1.

Here two different electrically conducting materials x and y are joined at two

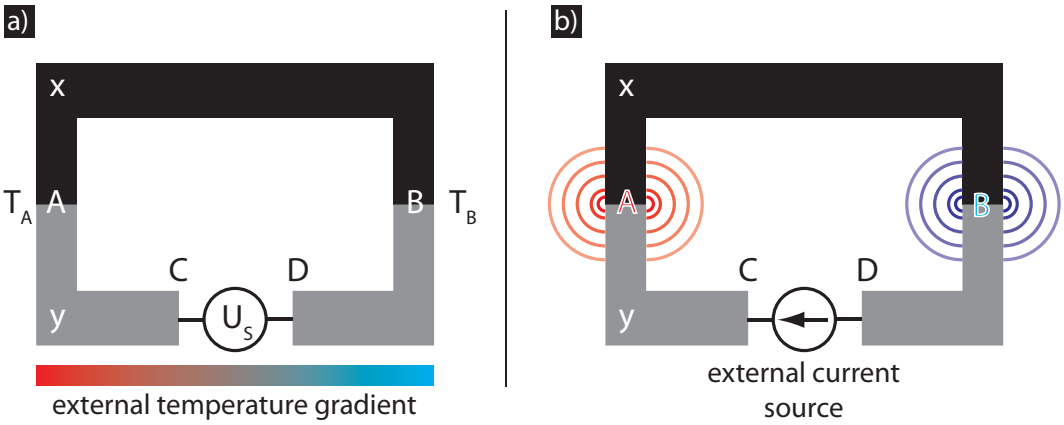

Figure 1.1: Basic thermoelectric phenomena. a) Seebeck effect: an external temperature gradient in a material couple xy joined at A and B causes a potential difference between C and D. b) Peltier effect: If a current is driven through two thermoelectric materials heat is absorbed at one junction and released at the other. Note that there is no external electrical current in a) and no external temperature gradient in b).

junctions A and B. If these two junctions are at different temperatures, a voltage U_S arises between C and D. This voltage is proportional to the temperature difference, i.e. $U_S \propto (T_A - T_B)$, as found by T. J. Seebeck [See23]. The constant of proportionality is called the differential Seebeck coefficient S_{xy} of the material couple and defined by

$$S_{xy} = -\frac{U_{CD}}{\Delta T_{AB}} \,. \tag{1.1}$$

The definition is here such that for $S_{xy} > 0$ and $T_A > T_B$ the electrical potential is lower at C than at D, i.e. if the circuit was shorted the electrical current[1] would flow clockwise [Row06].

The somewhat opposite situation is shown in Figure 1.1b). Here an electrical current I is driven externally in a clockwise direction through the circuit. Now heating with a rate P_{Pel} occurs at one of the junctions and cooling with $-P_{\mathrm{Pel}}$ at the other. The differential Peltier coefficient π_{ab} is the constant of proportionality between I and P_{Pel} and given by

$$\pi_{ab} = \frac{P_{\mathrm{Pel}}}{I} \,; \tag{1.2}$$

it is positive if junction A is heated and B cooled.

Superconducting materials below the critical temperature have a Seebeck coefficient of $S = 0$ [Row06, Nol01] and from measurements on couples of superconductors and other materials absolute values for S and π can be determined, not only differential values as in Figure 1.1. The Seebeck and Peltier coefficient are coupled by

[1] It is referred to the physical, not the technical current direction throughout this thesis.

the Kelvin relation [Nol01]

$$\pi = ST\,, \tag{1.3}$$

where T is the absolute temperature. The heat produced by the Peltier effect can hence be written also as

$$P_{\mathrm{Pel}} = IST\,. \tag{1.4}$$

A simplified microscopic explanation of both effects is as follows: the charge carriers in a material occupy states according to the Fermi function $f(E) = [\exp((E - E_F)/k_BT) - 1]^{-1}$, where E_F is the Fermi energy and k_B the Boltzmann constant. If a piece of the material is at higher temperature than another, charge carriers in the hotter part will have a higher energy and a larger momentum on average and will therefore travel to the colder part of the material. Thus a potential difference arises which is observed as Seebeck voltage. This voltage is negative if electrons are the majority charge carriers and positive for holes; the migration of the majority charge carriers is balanced in steady state by electrostatic repulsion. The Peltier coefficient on the other hand, corresponds to the difference of the average charge carrier energy and the Fermi energy, divided by the elementary charge e. This energy difference is material specific and therefore charge carriers either release or absorb energy when traveling from one material to the other. This energy manifests macroscopically as Peltier heating or cooling.

Based on these two phenomena, thermoelectric devices can work in two different ways. If an external temperature gradient is applied, a Seebeck voltage arises and the resulting current can be used to drive a resistive load, i.e. (waste) heat can be converted into electrical energy. In the other operation mode an external electrical current is driven through a thermoelectric couple and one junction is used for cooling of external parts utilizing the Peltier effect. Since the Seebeck voltage and the Peltier cooling are proportional to the differential Seebeck coefficient of the two materials, usually materials with Seebeck coefficients of opposite signs are combined. In practice several thermoelectric couples are arranged electrically in series but thermally in parallel to increase the power output or the cooling rate, respectively [Sny08, Nol01]. It can be shown, that the maximum efficiency $\phi_{\max}$, i.e. the highest ratio of electrical power output and heat energy absorbed at the hot side, is approximately given by[2][Row06]

$$\phi_{\max} = \frac{T_H - T_C}{T_H} \frac{\sqrt{1 + Z\bar{T}} - 1}{\sqrt{1 + Z\bar{T}} + T_C/T_H}\,, \tag{1.5}$$

with $\bar{T} = 0.5(T_H + T_C)$. The first factor is the Carnot efficiency which is the maximum efficiency for any thermodynamical process converting heat into mechanical or electrical energy. In the second factor the so-called thermoelectric figure of merit

[2] Assumptions: constant material properties within each material, negligible electrical and thermal contact resistances

ZT appears, which is determined by the material properties and is given by[3]

$$ZT = \frac{\sigma S^2 T}{\kappa}\,, \tag{1.6}$$

where σ and κ are the electrical and thermal conductivity, respectively, and S the already introduced Seebeck coefficient. The main conclusions from Eqs. (1.5) and (1.6) are: first, the efficiency for heat to electrical power conversion with a thermoelectric generator depends (like any other thermodynamical energy conversion process) on the absolute process temperatures and the temperature differences. Furthermore, it also depends on a material parameter, the figure of merit ZT, and increases approximately linear with it, at least for small ZT. It can be shown that the efficiency of thermoelectric cooling depends on ZT in a similar way, see e.g. [Row06]. A good thermoelectric material must have a high electrical conductivity, a large Seebeck coefficient and a low thermal conductivity. This is often summarized under the catch-phrase that thermoelectric materials should be a 'phonon-glass electron-crystal'. This can be understood intuitively: the material must have a high electrical conductivity (like crystalline semiconductors) to keep the re-conversion of electrical power into resistive heat as low as possible. The thermal conductivity must be as small as in glasses to minimize the heat flow through the material that tries to level the external temperature gradient. S must be as high as possible because the used current is driven by the voltage developing due to the Seebeck effect.

The electrical conductivity relates the current density $\vec{j}$ and the electrical field $\vec{E}$ and is defined for an isotropic material by

$$\vec{j} = \vec{E}\sigma = \frac{\partial \phi}{\partial \vec{r}}\sigma\,, \tag{1.7}$$

where the current density and the gradient of the electrical potential ϕ are parallel and no thermal gradient exists. The electrical conductivity is in general a second-order tensor, however, for isotropic materials or the electric field along one of the symmetry axes, it simplifies to a scalar and is the reciprocal of the resistivity, i.e. $\sigma = \rho^{-1}$. This will be assumed throughout this thesis.

The thermal conductivity κ is likewise defined

$$q = \frac{\partial T}{\partial r}\kappa\,, \tag{1.8}$$

where $q = P/A$ is the heat flow density (analogue to j) and the temperature gradient ∇T the thermal equivalent of the electric field $E = \nabla\phi$. The analogy between electrical and thermal quantities will be exploited in Chapter 3 to establish the thermoelectric van der Pauw measurement method.

[3]The ZT in Eq. (1.5) is actually the figure of merit of the couple, which is roughly the average of the figures of merit of the two materials forming the couple. However, the material and the couple ZT are identical if the conductivities of the materials are equal and the Seebeck coefficients are opposite equal.

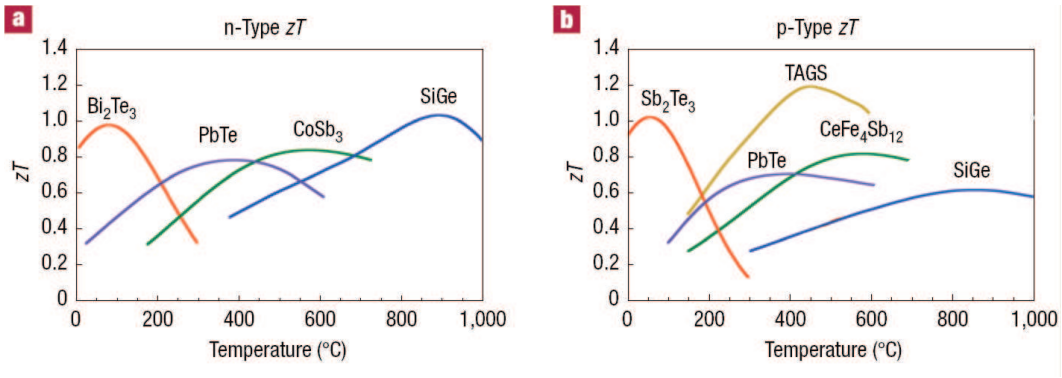

Figure 1.2: Thermoelectric figure of merit for n-type materials in a) and p-type materials in b). The shown materials are either commercially available or at least used in industrial research. Adapted by permission from Macmillan Publishers Ltd: Nature Materials [Sny08], Copyright 2009.

A further, less important thermoelectric effect is the Thompson effect. The Thompson effect is the reversible generation/absorption of heat P_{Th} accompanying a current flow through a thermoelectric material with a temperature gradient and arises because S is temperature-dependent. The Thomson coefficient τ is defined as [Nol01]

$$P_{\mathrm{Th}} = \tau I \frac{\partial T}{\partial x}\,, \tag{1.9}$$

where x is the spatial coordinate.

1.2 Thermoelectric materials and applications

In this section state-of-the-art materials and their applications are discussed. It also serves to illustrate similarities between different thermoelectric materials and to give a feeling for the magnitudes of thermoelectric quantities.

Figure 1.2 shows ZT for several thermoelectric materials as function of temperature, both for n and p materials, i.e. materials with $S < 0$ and $S > 0$, respectively. The most widely used materials are alloys from Bi_2Te_3 and Sb_2Te_3. Bi_2Te_3 was recognized as high potential thermoelectric material in the 1950s and triggered a decade of intense research on thermoelectrics [Gol54, Ros61]. It was realized soon that alloying of Bi_2Te_3 with Sb_2Te_3 and Bi_2Se_3 can further reduce the thermal conductivity and fine-tune the electrical properties. These alloys from Bi_2Te_3 have peak ZTs around unity at room temperature and are therefore commercially used in Peltier elements. Peltier elements are used for cooling or temperature regulation e.g. in laser cavities, in scientific laboratories, in life science applications, and in car seats [Wit89, Sny08, Row06, Tri08]. Bi_2Te_3 is also used for thermoelectric power generation e.g. if attached to the exhaust pipe of cars [Bas94, Mat02]. For

energy harvesting in the temperature range from $500 - 900\,\mathrm{K}$ materials containing group-IV elements are commonly used; prominent examples are PbTe, GeTe, or alloys like LAST (lead-antimony-silver-telluride) or TAGS (tellurium-antimony-germanium-silver) [Yan08, EG05]. For high temperature applications SiGe alloys are employed. These are used for waste-heat recovery in vehicles [Iko98] and, very prominently, for the powering of space-flight missions, where waste heat generated by a slow radioactive decay is used to power a thermoelectric generator, see e.g. [Row06].

The figure of merit and its constituents are shown in Figure 1.3a) using fitted empirical data for Bi_2Te_3 at room temperature as example [Row95, Sny08]. The axes scalings relate to ZT on the left hand side and to σ, S, and κ on the right hand side of the diagram.

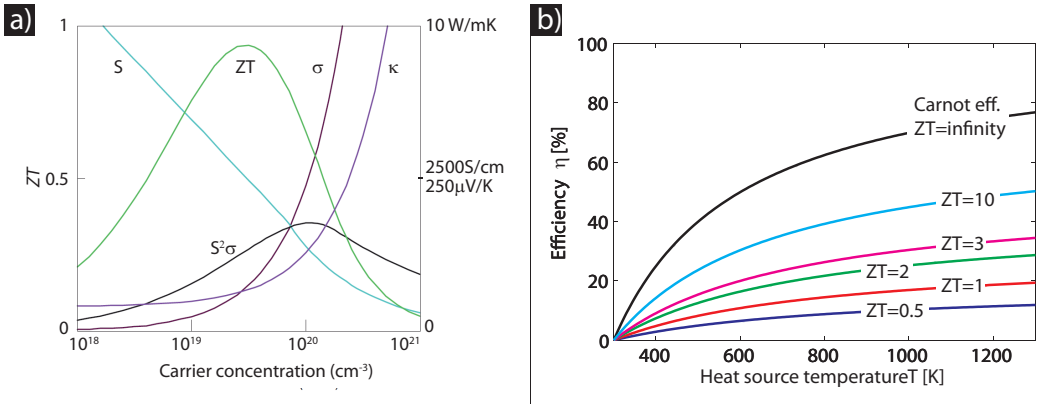

Figure 1.3: a) Thermoelectric properties of Bi_2Te_3 as function of charge carrier concentration. While a low carrier concentration causes high S and low κ, only a high carrier concentration results in a high electrical conductivity. Optimization of ZT therefore requires to find a compromise; the highest ZT is obtained for a carrier concentration around $10^{19} - 10^{20}\,\mathrm{cm}^{-3}$. This regime corresponds to heavily doped semiconductors and is typical for thermoelectric materials. Taken from [Sny08] and modified. b) Efficiency for thermoelectric power generation after Eq. (1.5) for different ZTs. The heat source temperature is given as abscissa while the heat sink temperature is fixed at 300 K. Energy conversion efficiency increases with heat source temperature and with increasing ZT, it remains well below the Carnot limit ($ZT \to \infty$) though, for all available ZTs.

While the exact numbers are of course Bi_2Te_3-specific, the orders of magnitude are typical for common thermoelectric materials. In particular the charge carrier density regime is typical for thermoelectrics. Bi_2Te_3 has its maximum ZT at $10^{19} - 10^{20}\,\mathrm{cm}^{-3}$ and is thus a heavily doped semiconductor. The optimal electrical conductivity is around $1000\,\mathrm{Scm}^{-1}$, the Seebeck coefficient around $200\,\mu\mathrm{VK}^{-1}$ and the thermal conductivity around $1\,\mathrm{Wm}^{-1}\mathrm{K}^{-1}$. It can clearly be seen, that the maximum ZT can not be found by an optimization of the *individual* constituents

with respect to the charge carrier concentration. In fact, optimizing ZT requires a compromise between high S, σ and low κ. The interplay between these three material properties will be analyzed in more detail in Section 1.3.

Thermoelectric generators have many advantages compared to mechanical heat engines: they have no moving parts, need no lubrication or other maintenance to operate, and work very reliably even under harsh conditions as proven e.g. during space flight missions. Furthermore, thermoelectric cooling provides a way of temperature regulation that, in terms of controllability and precision, can hardly be matched otherwise. The efficiency of both processes is largely independent of device size, in contrast to traditional heat engines that are less efficient for smaller devices [Vin09].

Given the facts that there is a great need for increased energy efficiency together with the tremendous amounts of waste heat energy, the question arises why thermoelectric materials have still found only niche applications and why the world market for thermoelectric generators and refrigerators is only around 3×10^8 US$ per year [Vin09]. This is a small number compared to other energy technologies like solar energy and wind power, which have market volumes of 10×10^9 € and 6×10^9 €, respectively, in Germany only [Fra10].

The answer to this is basically given in Figure 1.3b), where the efficiencies of thermoelectric energy conversion are plotted for different ZTs. The figure of merit for commercially available materials falls between 0.5 and 1.0 in the temperature range of question[4]. At such ZT values the energy conversion efficiency for available materials is still low, way below the theoretical Carnot limit. This low efficiency is one of the mayor reasons why thermoelectrics only plays a minor role in energy harvesting or cooling. Besides efficiency other important criteria for the applicability of thermoelectric materials are cost, availability, and processability. This regarding many of the state-of-the art materials have clear disadvantages: Ge is expensive [Bux09], Pb is poisonous and there are tendencies to restrict its application [Pbw11], and Te is one of the rarest stable accessible elements with a yearly production of ≈ 100 t. Te is already relatively expensive, while prices are expected to go up furthe, due to the increased demand of the solar cell industry [Zwe10]. It is therefore not only important to identify high efficiency materials, but also inexpensive and easily processable thermoelectric materials. It can be seen from Figure 1.3b) that the efficiency does increase sub-linearly with ZT, i.e. the impact of doubling ZT is higher for smaller ZTs. For many applications it might be better to find/design an inexpensive material with a ZT around unity than finding an expensive material with $ZT = 2$. The next section will introduce several ways to design materials with improved thermoelecric properties.

[4]Note that it is usually necessary to operate thermoelectric generators over a not too small temperature range. So, even if materials have a peak ZT of $ZT \geq 1$ at a certain temperature, the average ZT for the operational temperature range will be somewhat lower. A possibility to decrease this effect are segmented or graded thermoelectric materials, see e.g. [Mül03, Sny08].

1.3 Strategies for improved thermoelectrics

After a first boom in the 1950s the field of thermoelectrics reached a relative standstill that lasted till the 1990s. The reason was that after the "discovery" of Bi_2Te_3 and related alloys, few materials with comparable or better properties could be identified. In this section the interplay between σ, κ, and S will be illuminated and it will be shown how it limits the achievable ZT for common bulk materials. In the 1990s and the following years several ideas have been proposed and experimentally verified to overcome those limits, a development that lead to a renewed interest in thermoelectrics, novel materials with superior properties and increased research activities in the field of thermoelectrics. These ideas will be discussed as they were partly pursuit during the course of this thesis.

But let us start with the optimization of thermoelectric properties and its limitations. As already displayed in Figure 1.3 the charge carrier concentration n does affect σ, S, and κ and is therefore of paramount importance in the optimization process. Since the electrical conductivity is given by

$$\sigma = en\mu\,, \tag{1.10}$$

where e is the elementary charge and μ the mobility of the charge carriers, it is clear that a high charge carrier concentration favors a high electrical conductivity. The thermal conductivity, on the other hand, should be as low as possible. However, the electrical and the thermal conductivity are coupled since the total thermal conductivity is the sum of the lattice thermal conductivity (heat conduction by phonons) κ_l and the thermal conductivity due to the charge carriers κ_e. The electronic thermal conductivity is related to the electrical conductivity by the Wiedemann-Franz law [Fra53][5]:

$$\kappa_e = L\sigma T = en\mu LT\,, \tag{1.11}$$

where L is the Lorenz factor, $2.4 \cdot 10^{-8}\,\mathrm{W\Omega K^{-2}}$ for free electrons. Using the numbers from Figure 1.3 at optimal ZT the electronic thermal conductivity amounts to $\kappa_l \approx 2.4 \cdot 10^{-8}\,\mathrm{W\Omega K^{-2}} \cdot 10^5\,\Omega^{-1}\mathrm{m}^{-1} \cdot 300\,\mathrm{K} \approx 0.7\,\mathrm{Wm^{-1}K^{-1}}$ and is not negligible. The contribution of the charge carriers to thermal transport limits the benefit of increasing the charge carrier density eventually.

Probably even more important is the trade-off between electrical conductivity and Seebeck coefficient with respect to n. As discussed previously the Peltier coefficient and hence the Seebeck coefficient are proportional to the energy difference between the Fermi energy and the average energy of the charge carriers, which in turn depends on various parameters like temperature, density of states, and mobility, but also on the energy difference between Fermi energy and band edge. Since the Fermi level approaches the band edge for higher n, it is qualitatively clear that S

[5] Note that the Wiedemann-Franz law does not account for bipolar thermal transport, which is, however, important for most materials only at high temperatures [Sny08].

usually decreases as n increases. A simple quantitative relation can be given for the limit of a degenerate semiconductor (single, parabolic band and energy-independent scattering approximation), where S is given in terms of n by [Sny08]

$$S = \frac{8\pi^2 k_B^2}{3eh^2} m^* T \left(\frac{\pi}{3n}\right)^{2/3} \tag{1.12}$$

(k_B: Boltzmann's constant, h: Planck's constant, m^* density-of-states effective mass) and thus decreases with increasing n. For most thermoelectric materials n is not high enough for the degenerate semiconductor approximation to be a very good approximation. A more exact description is given e.g. in [Nol01], the general statement, however, that S decreases with increasing n, remains valid; see also Figure 1.3. In summary, optimization of ZT with respect to n requires a compromise between S, σ, and κ while the resulting optimum charge carrier concentration is material specific.

A second material parameter that might be used for optimization, but that is also subject to an inherent trade-off, is the effective mass of the charge carriers. It can be seen from Eq. (1.12) that a large effective mass would favor a high S. The mobility μ in Eq. 1.10 on the other hand, decreases with large effective mass and leads to smaller σ [Sze81]. A general optimal value for the effective carrier mass can not be given and there are good thermoelectric materials with low and high effective masses [Sny08].

The mentioned trade-offs illustrate why material optimization is challenging and the field of thermoeletrics came to relative standstill between 1960 and 1990. This is furthermore visualized in Figure 1.4, where reported maximal values for ZT are given with respect to their publication date. After 1995 several reports for materials with thermoelectric properties superior to the already mentioned traditional materials appeared. The improvements are mainly based on two basic ideas: Firstly, disentangling of S and σ can lead to an enhancement of the power factor σS^2 and secondly a reduction of the lattice thermal conductivity by nanostructuring without deteriorating the charge transport significantly.

Let us first discuss the three main concepts to reduce the lattice thermal conductivity: the first is to scatter phonons within the unit cell of the crystal by providing scattering centers like vacancies, loosely bound heavy atoms ('rattlers'), and atomic mass differences from alloying. Famous examples are the alloys of Bi_2Te_3, the clathrates, and the skutterudites [Pou06, Ber03, Fel00]. The second approach relies on complex unit cells where some regions work as electronic crystal and others as phonon glass [Gas05]. The third way is to create scattering interfaces at a length scale between typical electron and phonon mean free paths, thus disrupting heat but not charge transport. The latter approach is so far the most successful one and will be exploited in Chapter 4 using Si. It will therefore be examined in a bit more detail.

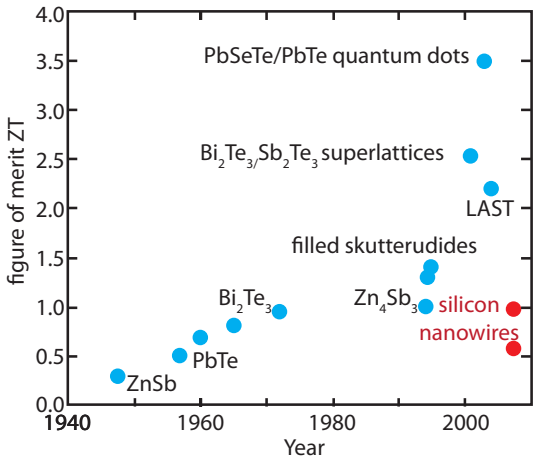

Figure 1.4: Improvement of thermoelectric materials. The figure shows reported figures of merit and their publication date. The renewed interest of thermoelectrics in the 1990s led to significantly improved thermoelectric materials. The reports on SiNWs show a ZT that is comparable to the state-of-the-art material Bi_2Te_3 [Hoc08, Bou08]. Higher ZTs have been reported e.g. for superlatice structures but Si has significant advantages with respect to processability, abundance and costs as discussed in the main text. Reproduced from [Zhe08].

In a simple approximation the lattice thermal conductivity is given by

$$\kappa_l = \frac{1}{3} c v l^{\gamma}_{\mathrm{mfp}} \,, \tag{1.13}$$

where $c = c_p \rho$ is the specific heat capacity, v the speed of sound and $l^{\gamma}_{\mathrm{mfp}}$ the mean free path of the phonons, i.e. their average traveling distance between scattering events. The charge carrier mobility, which is proportional to the electrical conductivity Eq. (1.10), can likewise be expressed in terms of a charge carrier mean free path l^{e}_{mfp} [Sze81, mob10]

$$\sigma = en\mu = en\frac{v_d}{E} = \frac{e l^{e}_{\mathrm{mfp}}}{m^* v} \,, \tag{1.14}$$

where E is the magnitude of the electric field, v_d the drift velocity of the charge carriers, e the elementary charge and v their Brownian motion velocity. Internal or external interfaces in nanostructures can decrease the mean free path. If these interfaces can be designed such that the phonon mean free path is decreased but the charge carrier mean free path remains unaffected then ZT would increase. This is possible since $l^{\gamma}_{\mathrm{mfp}} \gg l^{e}_{\mathrm{mfp}}$ in many materials, e.g. $l^{\gamma}_{\mathrm{mfp}} \approx 43\,\mathrm{nm}$ and $l^{e}_{\mathrm{mfp}} < 12\,\mathrm{nm}$

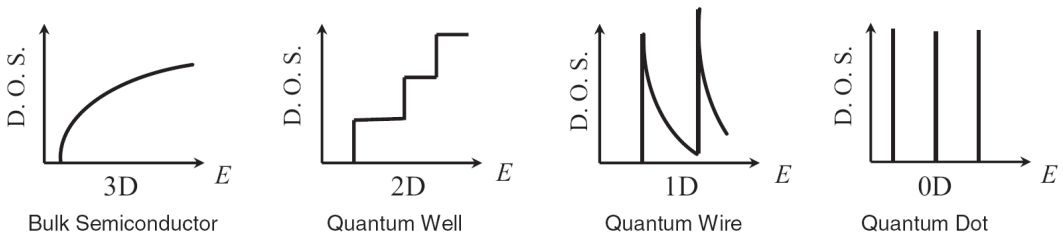

Figure 1.5: Electronic density of states (D.O.S) for a) a bulk semiconductor, b) a two-dimensional thin film, c) a one-dimensional nanowire and d) a quantum dot. Systems with lower dimensionality have a higher DOS that can improve the thermoelectric properties of materials. Taken from [Dre07].

for highly doped bulk Si[6,7]. Furthermore, phonons of different wavelengths are differently important for heat conduction and it is possible to scatter predominantly those phonons that carry most of the heat.

The proof-of-principle of this concept was provided using Bi_2Te_3/Sb_2Te_3 superlattice structures by Venkatasubramanian *et al.* [Ven01] in 2001. They measured a $ZT > 2$ which was mainly caused by a reduction of the thermal conductivity while the electrical conductivity was not altered significantly. Thereafter, the concept was confirmed for several other material systems, notably also for Si in 2008. While bulk Si is a poor thermoelectric material ($ZT_{T=300\,\mathrm{K}} \approx 0.01$) due to its high thermal conductivity of $\kappa_{\mathrm{Si}} \approx 150\,\mathrm{Wm^{-1}K^{-1}}$, two groups showed $ZT > 0.5$ at room temperature for Si nanowires [Bou08, Hoc08]. Again, the main reason for an enhanced ZT was a drastic reduction of the thermal conductivity by more than one order of magnitude.

The key point for an enhancement of the power factor is that quantum phenomena provide means to partly disentangle σ and S which are coupled in bulk materials as discussed previously. When the system size approaches the angstrom scale in one or several dimensions, the density of states changes dramatically as depicted schematically in Figure 1.5. In two seminal papers Hicks and Dresselhaus showed that the change in density of states can lead to drastic enhancements of ZT, provided that the structures are restricted in one or two dimensions to less than 10 Å [Hic93b, Hic93a]. The experimental proof for this concept was given in 1996 for PbTe quantum wells [Hic96]. A related concept is the so-called electron filtering [Zid06]: In superlattice or quantum dot supelattice structures one can create energy barriers that filter the electrons which have low energies ("cold electrons") and

[6] As discussed in Section 4.3.1 the phonon mean free path is an average quantity whose precise value depends on how the averaging is performed. Another value stated often for Si is a mean free path of 300 nm which increases the difference between electron and phonon mean free path even further [Ju99].

[7] The mean free path can be estimated from the mobility and the thermal velocity. Using $l^e_{\mathrm{mfp}} = v\tau$ with $\tau = \mu m^*/e$ and inserting $\mu = 100\,\mathrm{cm^2V^{-1}s^{-1}}$ for highly doped Si, $v = 10^5\,\mathrm{ms^{-1}}$ [Iof11] and the free electron mass yields $l^e_{\mathrm{mfp}} \approx 12\,\mathrm{nm}$.

contribute only little to the Seebeck coefficient while letting hot electrons pass. It has been shown that this can enhance S more than it decreases σ and thus leads to higher power factors.

Enhancement of power factor and lattice thermal conductivity reduction can be combined for further ZT enhancement. Harman *et al.* reported $ZT = 3.5$ at 570 K for a $PbTe/PbSe_{0.98}Te_{0.02}$ quantum dot superlattice structure. They found both an increase of the power factor $S^2\sigma$ and a decrease of the thermal conductivity compared to bulk PbTe and PbSe [Har05]. There are also increasing number of reports on so-called nanocomposites with superior thermoelectric properties. Nanocomposites are nanostructured bulk materials with more than one constituent that are fabricated by e.g. ball milling and hot pressing [Bux09]. For these type of materials, also power factor enhancement and thermal conductivity reduction at the same time have been reported [Dre07].

1.4 Conclusion of Chapter 1

In summary it has been shown that nanostructuring can be used to fabricate materials with superior thermoelectric properties. On the other hand it is clear that macroscopic amounts of nanostructured materials are necessary for most real-life devices. We show in Chapter 2 how laser interference lithography and metal-assisted etching can be used to fabricate arrays of ordered Si nanowires that have a well-defined geometry and homogeneous over macroscopic areas. These wires have diameters down to 65 nm so that size effects and superior thermoelectric properties can be expected. In Chapter 4 the fabrication and the thermoelectric properties of porous Si, a related kind of nanostructured Si are discussed. Nanocomposites, or more general, nanostructured bulk thermoelectric materials like porous Si appear to be very promising from a practical point of view. For such samples bulk measurement techniques can be applied, whilst for nanowires or thin films more sophisticated techniques have to be employed [Hoc08, Bou08, Völ10, Hic96]. As optimizing a thermoelectric material usually requires repeated characterization, fast and easy measurements are essential. The other big advantage of the nanostructured bulk materials is that their production is often less involved than e.g. the fabrication of quantum dot superlattices. Their fabrication moreover appears to be easily scalable.

Thermoelectric measurements are an important part of this thesis, therefore the introduction is concluded with a remark on thermoelectric measurements: As can be seen from Figure 1.4 and the various references there have been many reports on materials with superior ZT; however, few measurements could be confirmed by others and no device with efficiencies as high as expected from the ZT values has been realized [Sny08][8]. Direct efficiency measurements are complex and most

[8] Harman *et al.* [Har02] used an n-type quantum dot superlattice to build a Peltier cooler. Indeed they show, that the cooling power of this "device" is superior to n-type Bi_2Te_3, however, since they used a metal wire as p-leg the cooling power of the whole device is lower than for the commercially

reported ZTs have been obtained from measurements of σ, S, and κ and use of Eq. (1.6). The relative error of Z is given by

$$\frac{\Delta Z}{Z} = \frac{\Delta\sigma}{\sigma} + 2\frac{\Delta S}{S} + \frac{\Delta\kappa}{\kappa}\,, \tag{1.15}$$

and while σ can usually be determined with an accuracy better than 5%, relative errors of 10-20% are not unusual for S and κ measurements. The relative error for ZT can thus amount easily to 50%[9][Sny08]. Another source for uncertainties is that often different quantities are measured on different sample pieces and since small inhomogeneities can cause significant variations of thermoelectric properties within a sample [Che05], combining measurement results from different samples can lead to erroneous results. Further work in thermoelectrics must therefore aim for reproducibility and careful cross-checking of the measurement data. The thermoelectric van der Pauw method which will be presented in Chapter 3 can measure all properties on a single sample and allows several cross-checks.

available combination of p and n Bi_2Te_3. Progress in thermoelectric devices has also been presented in [Ven01, Har06].

[9] Note also, that if κ is determined indirectly from thermal diffusivity and heat capacitance measurements, as is done in many transient measurement methods, the error might increase further.

Chapter 2

Fabrication of Si Nanostructures by Laser Interference Lithography

2.1 Laser interference lithography

Laser interference lithography (LIL) is frequently applied to the fabrication of ordered arrays of nanostructures [Bru05]. It enables fabrication of two- or even three-dimensional templates [Lai05, Moo06, Ram08] with perfect ordering over complete wafers[Che02] and gives the user precise control over pattern ordering and geometry of the individual elements. The perfect long range order is a distinct difference to structuring methods based on self-assembly and gives LIL an advantage over techniques such as nanosphere-lithography [Hua07], anodic alumina pore etching [Kaw89, Nie01], or block-copolymer lithography [Cha09]. Since LIL provides defined microscopic structures on a macroscopic scale, it can be a powerful tool to fabricate materials that have potential for thermoelectric applications. We have employed LIL to fabricate arrays of Si nanowires (SiNWs) and Si fins with defined geometry and ordering. The first section of this chapter will deal with LIL itself, the fabrication of thermoelectric nanostructures will be treated in Section 2.2.

In the first section of this chapter the basic working principle of LIL will be explained and our system, a Lloyd's mirror interferometer, will be described. A Lloyd's mirror interferometer is a relatively simple optical setup and flexible in terms of the periodicity of the created pattern, in contrast to other setups like Mach-Zehnder interferometers [Zeh91, Mac92]. In Section 2.1.2 and 2.1.3 two improvements/modifications of a standard Lloyd's mirror interferometer will be shortly presented: an immersion Lloyd's interferometer and a two-mirror Lloyd's interferometer [dB09, dB10b]. The two-mirror setup allows production of hexagonal patterns with a single exposure, whilst the immersion interferometer extends the range of achievable structure sizes to below 50 nm. These two extensions of a Lloyd's inter-

ferometer have been developed during the course of this thesis.

2.1.1 General principle

Photoresist patterns were fabricated in a Lloyd's mirror interferometer setup. We will start with the setup and the basic physics of interfering electromagnetic waves. A more detailed and comprehensive description can be found in classic electrodynamics textbooks, e.g. [Jac99]. Then the fabrication of resist patterns is explained in detail and the various parameters that affect the obtained patterns are discussed.

Lloyd's mirror interferometer

The setup used for LIL is shown in Figure 2.1a). The laser used for illumination is a frequency-doubled Ar-ion laser (Lexel SHG) with a wavelength λ of 244 nm and a typical output power of 3 mW. Following the beam propagation the setup consists of: a shutter (Thorlabs) to control exposure times, a spatial filter, and a Lloyd's mirror interferometer. The spatial filter (Newport) consists of an objective lens (focal length of 3.4 mm) that expands the laser beam, and an aperture with a diameter of 10 μm to remove optical noise and enhance the quality of the beam. The Lloyd's mirror interferometer itself consists of a rotational stage, a mirror (5 cm $\times$ 5 cm), and the sample holder. A metallic mirror (Al-coating) rather than a dielectric mirror is used because the reflectivity of metallic mirrors shows only minor dependence on the incidence angle. All components are fixed on an actively damped optical table to minimize the effect of vibrations on the interference pattern.

Intensity homogeneity across the macroscopic sample is a prerequisite for the fabrication of homogeneous patterns. The radial intensity profile of the laser is approximately Gaussian

$$I(r) = I_0 \exp(-r^2/(2s^2)) \,, \tag{2.1}$$

with a full width at half maximum (FWHM) of 0.15 mm in front of the objective lens. The beam radius s and the FWHM are related by FWHM $= 2\sqrt{\ln 2}s \approx 2.35s$. The distance between lens and interferometer is ≈ 1.4 m and so the radial intensity profile of the expanded laser beam at the interferometer I' is given by

$$I'(r) = I'_0 \exp(-r^2/(2s'^2)) \tag{2.2}$$

$$\text{with } s' = \frac{0.15\,\text{mm} \times 1400\,\text{mm}}{3.4\,\text{mm} \times 2.35} \approx 26.3\,\text{mm} \,, \tag{2.3}$$

where s' is the beam radius at the interferometer stage. The relative intensity at $r = 10$ mm is ≈ 0.93, which is sufficient. Better homogeneity can be achieved by simply increasing the distance between objective lens and interferometer; this, however, comes at the cost of increased exposure time.

Due to its large curvature radius, the electromagnetic field of the laser light $\vec{E}(\vec{r})$

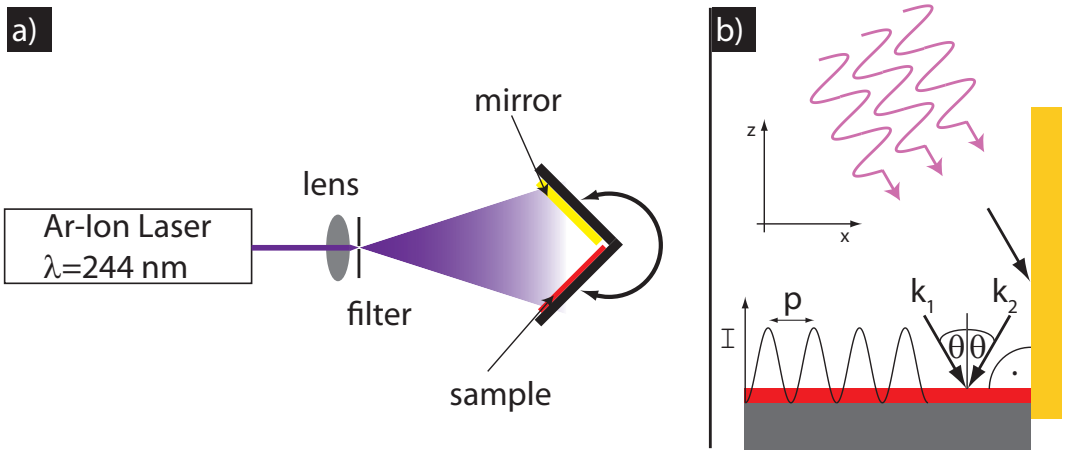

Figure 2.1: a) Laser interference lithography setup: The laser beam is expanded by an objective lens and filtered by a 10 μm pinhole. b) Interference in a Lloyd's mirror interferometer: A fraction of the laser light is directly incident on the sample at an angle θ. Another fraction is reflected at the mirror (yellow) which is perpendicular to the substrate. Thus this fraction of the light is incident at an angle $-\theta$. Interference of the two waves creates a static sinusoidal intensity distribution with a periodicity p in the photosensitive material (red).

can be described in terms of plane waves:

$$\vec{E}(r) = E_0 \hat{e} \exp(i\vec{k}\vec{r}) \,, \tag{2.4}$$

where E_0 is the amplitude, $\hat{e}$ the unit vector in the direction of $\vec{E}(r)$, or the polarization of the electromagnetic wave, and $\vec{k}$ the wave vector of the electromagnetic wave; i is the imaginary unit. The magnitude of the wave vector is related to the wavelength of the laser by $k = |\vec{k}| = 2\pi/\lambda$ and the time-dependence of the field is given by $E(r,t) = \Re(\vec{E}(r)\exp(i\omega t))$, where $\Re$ denotes the real part and ω the circular frequency. Note that not the electric field itself , but the intensity I is "recorded" in the photosensitive material and therefore responsible for pattern formation. It is related to $\vec{E}$ by

$$I = \frac{c}{4\pi}\sqrt{\frac{\varepsilon}{\mu}}\left\langle \vec{E}(\vec{r},t)^2 \right\rangle \,, \tag{2.5}$$

where c is the speed of light, ε the permittivity and μ the permeability. If the averaging $\langle\rangle$ is performed over a time interval much larger than the temporal periodicity of the wave, the time dependence vanishes and the intensity is

$$I \propto \vec{E}(\vec{r}) \cdot \vec{E}^*(\vec{r}) \,, \tag{2.6}$$

where the constants of proportionality are dropped for simplicity and $\vec{E}^*$ is the complex-conjugated of the electrical field. Obviously, the intensity of a single plane

wave is spatially uniform and thus of little interest for patterning. The intensity of two superpositioned plane-waves

$$\vec{E_1}(\vec{r}) = E_{1,0}\hat{e_1}\exp(i\vec{k_1}\vec{r}) \tag{2.7}$$
$$\vec{E_2}(\vec{r}) = E_{2,0}\hat{e_2}\exp(i\vec{k_2}\vec{r} + i\Delta\phi)\,, \tag{2.8}$$

($\Delta\phi$ accounts for an arbitrary phase shift between both waves), is

$$I_{12} = \left|\vec{E_1}(\vec{r}) + \vec{E_2}(\vec{r})\right|^2 \tag{2.9}$$
$$= I_1 + I_2 + 2\sqrt{I_1 I_2}(\hat{e_1}\cdot\hat{e_2})\cos[(\vec{k_1} - \vec{k_2})\vec{r} + \Delta\phi]\,, \tag{2.10}$$

where the amplitudes have been replaced by the (measurable) intensities $I_1 = |E_{1,0}|^2$. It can be seen that the intensity depends on the polarization of the two waves $\hat{e_1}\cdot\hat{e_2}$ and is not spatially uniform, as for a single plane wave. In fact, the intensity shows a sinusoidal modulation with a periodicity

$$p = \frac{2\pi}{|\vec{k_1} - \vec{k_2}|} = \frac{2\pi}{|\vec{k_f}|}\,, \tag{2.11}$$

in the direction of $\vec{k_f}$, where $\vec{k_f} := \vec{k_1} - \vec{k_2}$ is denominated as fringe vector.

In the specific case of a LIL setup as shown in Figure 2.1b) one has to consider the wave vector of the direct incident light and the wave vector of the light reflected from the mirror. Since the mirror is perpendicular to the substrate normal, the waves are incident at the angles θ and $-\theta$, measured from the substrate normal. The wave vectors follow from geometrical considerations:

$$\vec{k_1} = k(\sin\theta, 0, -\cos\theta) \tag{2.12}$$
$$\vec{k_2} = k(-\sin\theta, 0, -\cos\theta)\,, \tag{2.13}$$

and thus the fringe vector is given by

$$\vec{k_f} = k_{1x}\hat{x} + k_{1y}\hat{y} + k_{1z}\hat{z} - (k_{2x}\hat{x} + k_{2y}\hat{y} + k_{2z}\hat{z}) = 2k_{1x}\hat{x} = 2k_1\sin\theta\hat{x}\,. \tag{2.14}$$

Using $k = |\vec{k}| = 2\pi/\lambda$, p can be expressed as function of wavelength and θ only:

$$p = \frac{\lambda}{2\sin\theta}\,. \tag{2.15}$$

So far, electromagnetic waves and interference in vacuum have been discussed. However, the interference pattern is transferred into a photosensitive medium, called photoresist as described in Subsection 2.1.1. It is therefore necessary to consider interference in a medium with refractive index n_i. In the medium, the wave vectors of the plane waves have to be replaced by $k \to n_i \cdot k$ and Eq. (2.15) has to be rewritten

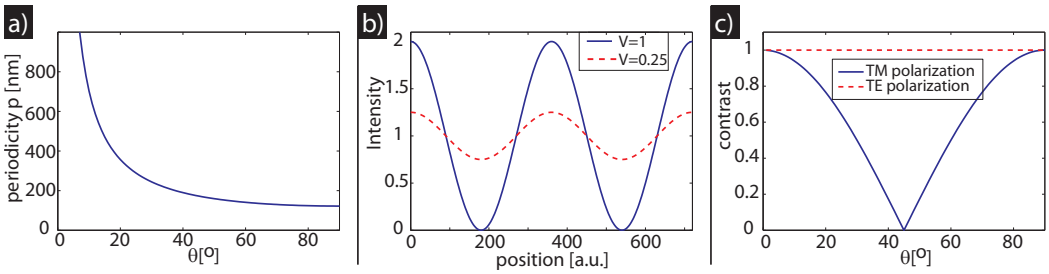

Figure 2.2: a) Periodicity vs. θ. b) Interference pattern at low and high contrast as defined in Eq. (2.18). c) maximal contrast for transverse electric and transverse magnetic polarization vs. θ.

as

$$p = \frac{\lambda}{2n_i \sin\theta_i}\,, \tag{2.16}$$

where θ_i is the angle to the substrate normal in the corresponding medium. It should be noted though that the tangential component of the wave vector is conserved upon refraction [Jac99]. Thus for the situation shown in Figure 2.1b) the fringe vector $\vec{k_f}$ and the periodicity p are the same in air and in photoresist. Conservation of the tangential component of the wave vector can also be expressed in form of the well-known Snell's law

$$\frac{\sin\theta_1}{\sin\theta_2} = \frac{n_2}{n_1} \tag{2.17}$$

and Eq. (2.16) is most conveniently computed by using θ_{air} and $n_{\text{air}} \approx 1$, because θ_{air} is experimentally easily accessible. Eq. (2.16) is plotted in Figure 2.2a). It can be seen that interference patterns with periodicities larger than $\lambda/2 = 122\,\text{nm}$ can be created with the employed setup. Changing p requires only a rotation of the interferometer, which can be done easily since its mounted on a rotational stage. The rotational axis is in the center of the beam so that no realignment is necessary after adjusting p. This is in distinct contrast to other types of interferometers, where changing p often requires dis- and reassembling as well as realignment of optical components [Zeh91, Mac92, Moo06].

Another important parameter besides the periodicity is the contrast or visibility V of the interference pattern. It is defined by

$$\begin{aligned} V &= \frac{I_{\min} - I_{\max}}{I_{\min} + I_{\max}} = \frac{\hat{e_1}\cdot\hat{e_2}\cdot 2\sqrt{I_1 I_2}}{I_1 + I_2} \text{ with} \\ I_{\max} &= I_1 + I_2 + 2\sqrt{I_1 I_2}(\hat{e_1}\cdot\hat{e_2}) \\ I_{\min} &= I_1 + I_2 - 2\sqrt{I_1 I_2}(\hat{e_1}\cdot\hat{e_2})\,. \end{aligned} \tag{2.18}$$

The intensity pattern for high and low contrast is shown in Figure 2.2b) and it is clear that for a good transfer of the interference pattern into a photosensitive material

high contrast is crucial. Contrast depends on the amplitude of the interfering waves and on their polarization. The interfering plane waves are linear polarized with the polarization orientation $\hat{e}$ depending on the setup. Any arbitrary polarization can be expressed by superposition of transverse electric polarization (polarization perpendicular to the plane defined by $\vec{k_1}$ and $\vec{k_2}$) and transverse magnetic polarization (polarization in the plane defined by $\vec{k_1}$ and $\vec{k_2}$). If both plane waves have transverse electric polarization, $\hat{e_1} \cdot \hat{e_2}$ is always unity and contrast is maximized. If both waves show transverse magnetic polarization $\hat{e_1} \cdot \hat{e_2} = -\cos(2\theta)$ and the contrast depends on θ, as shown in Figure 2.2c).

In the employed setup, we used transverse electric polarization to ensure optimal contrast. Even for transverse electrical polarization the contrast is not unity if the two interfering parts of the beam have different amplitudes, be it due to a reflectivity $R < 1$ of the mirror shown in Figure 2.1 or because of the intensity distribution of the beam not being uniform. Nevertheless, even for a relatively large amplitude mismatch $I_2 = 0.8I_1$ the contrast is still $V = 0.994 \approx 1$, which is sufficient for most practical applications.

Another prerequisite for high contrast intensity patterns is temporal and spatial coherence. The temporal coherence length has to be larger than optical path length differences between different fractions of the laser light. For the employed laser, the temporal coherence length is specified as 10 m by the manufacturer, which is orders of magnitude larger than any possible optical path difference. A lower-limit theoretical estimation of the spatial coherence can be obtained from the van Cittert-Zernike theorem, see e.g. [Sol99]. This gives the spatial coherence for a small, incoherent light source. Considering the pinhole diameter of 10 μm as the diameter of the light source and inserting the parameters of our setup one can estimate that resist patterns with a width of 5 mm should not suffer from spatial coherence loss. One should keep in mind though that this estimation is a lower limit and since the laser light is not completely incoherent one can expect that the effect of spatial coherence loss is much smaller. Insufficient spatial coherence would lead to differences in pattern quality between the fraction of the resist that has been close to the mirror compared to the resist that was further away from the mirror. Such effect has not been observed for samples with a width of > 3 cm.

Issues of minor importance for this thesis, but potentially interesting for the reader, include systematic errors of p due to misalignment of the interferometer with respect to the beam, a non-perpendicular mirror, the effect of substrate bending, and a more detailed description of the influence of spatial and temporal coherence on the obtained interference pattern. This and more is thoroughly described in the PhD thesis of Mr. Walsh [Wal04].

Photoresist patterns

With the Lloyd's mirror interferometer an interference pattern is created that has a sinusoidal modulation in one spatial direction. This pattern can be transferred

into a photosensitive material, termed photoresist. In short, upon illumination, the cross-linking between polymer chains in the resist increases/decreases for a negative/positive resist. Furthermore, the solubility of the resist can be modified by light-induced chemical reactions within the resist [Moo07]. Thus the exposed and unexposed parts behave chemically different, and when brought into contact with an appropriate solution, the developer, are selectively removed. A simple model for the behavior of the resist is the ideal binary response model [Ji08]: considering a negative resist, the parts of the resist that experience a dose $D = I \cdot t$ above a certain threshold exposure dose D_{tr} will remain after developing, while resist parts with $D < D_{\mathrm{tr}}$ are developed away. The threshold dose is a parameter of the resist, but can be influenced by the post-baking temperature. Usually D_{tr} decreases with increasing post-baking temperature [Moo07, Ji08]. The intensity the sample is exposed to, depends on the nominal intensity I_0 given by the laser, on the angle θ, and on the reflectivity of the air-resist interface $R_{\mathrm{air,PR}}$ as well as the resist-substrate reflectivity $R_{\mathrm{air,sub}}$. The intensity of a sample at angle θ is given by

$$I = I_0((1 - R_{\mathrm{air,PR}})(1 + R_{\mathrm{air,sub}}) \cos\theta)\,. \tag{2.19}$$

For large θ the intensity decreases and thus the time to achieve D_{tr} increases. Depending on the desired pattern and on the setup conditions, samples were exposed between 1 and 30 min during this study, without discernible differences in pattern quality.

For a given sample and fixed θ the fraction of the resist that receives a dose $> D_{\mathrm{tr}}$ increases with increasing exposure time. For a fixed p one can thus control the width of the resist stripe to a certain degree.

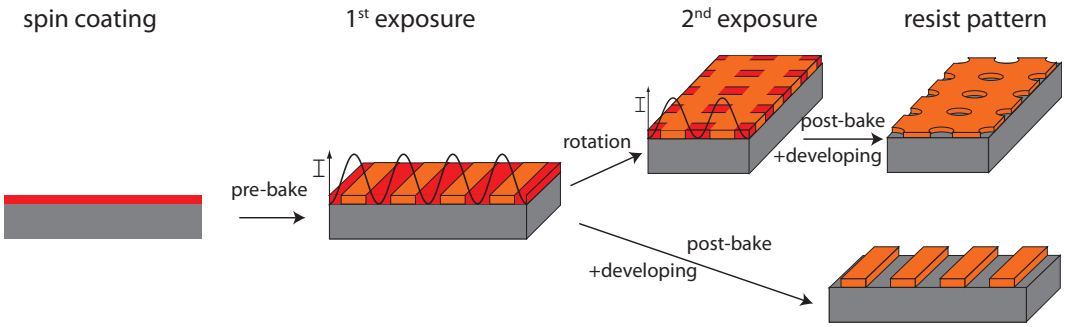

Figure 2.3: Fabrication scheme of photoresist patterns: Spin-coating is followed by a pre-bake and exposure. The resist pattern is obtained after post-bake and development. Two-dimensional patterns can be fabricated by two exposures with a rotation of the sample in between.

The full fabrication scheme is shown in Figure 2.3. Using the negative resist AR-N 4240 the individual steps were

1. Rinsing with acetone, isopropanol and de-ionized water to clean the wafers.

2. 10 min drying on a hot plate at 200 °C to remove any residual water.

3. Spin-coating of primer AR 300-80: 3 s at 500 rounds per minute (RPM), then 30 s 2000 RPM. A primer improves adhesion between substrate and resist, which becomes critical for small resist structures.

4. Bake-out of the primer at 200 °C for 30 s. Cooling of the sample.

5. Spin-coating of resist: 3 s 500 RPM, 30 s 4000 RPM. We used only the negative resist AR-N 4240, diluted with AR 300-12 in the ratio 1:2 or 1:4. Diluting 1:2 yielded resist thicknesses around 150-200 nm while with a dilution of 1:4 films with a thickness of around 100 nm were fabricated.

6. Pre-bake at 85 °C for 2 min. The pre-bake enhances the sensitivity of the resist against illumination.

7. Exposure in the Lloyd's mirror LIL setup.

8. Post-bake at 85 °C for 30 min. The post-bake increases the degree of cross-linking in the resist and enhances its selectivity tremendously. Moreover it reduces the effect of the vertical standing wave, that arises due to back-reflection from the substrate as explained in the text below.

9. Developing for 30 s in AR 300-47 or AR 300-475.

10. Removing (optional): developed resist can be removed with acetone or remover AR 300-70. All chemicals were obtained from Allresist GmbH, Germany.

A single exposure yields a resist line-grating. If two-dimensional structures are desired, the sample has to be rotated after the exposure and then exposed a second time, as shown in Figure 2.3. In Figure 2.4 exemplary SEM images of resist patterns are displayed. SEM images were recorded with a JSM-6701F (JEOL), usually with an acceleration voltage of 3 kV.

A striking feature of the fabricated patterns is their regularity. The patterns are strictly periodic over cm^2 and virtually defect free. In b) and c) patterns with different types of two-dimensional structuring are shown. Long exposures lead to a continuous resist film with an array of holes (see b)), while short exposure times result in an array of resist posts as shown in c). In Figure 2.3d) and e) cross section images of a) and c) are presented. Arrays of resist posts are used to fabricate arrays of SiNWs as discussed in Subsection 2.2.1. The height of the resist stripes/posts is around 150 nm and both show some undercut. The reason for the non-perpendicular side walls is the reflection of the laser light from the Si substrate. The reflected light interferes with the incoming light and creates a vertical standing wave. Its period

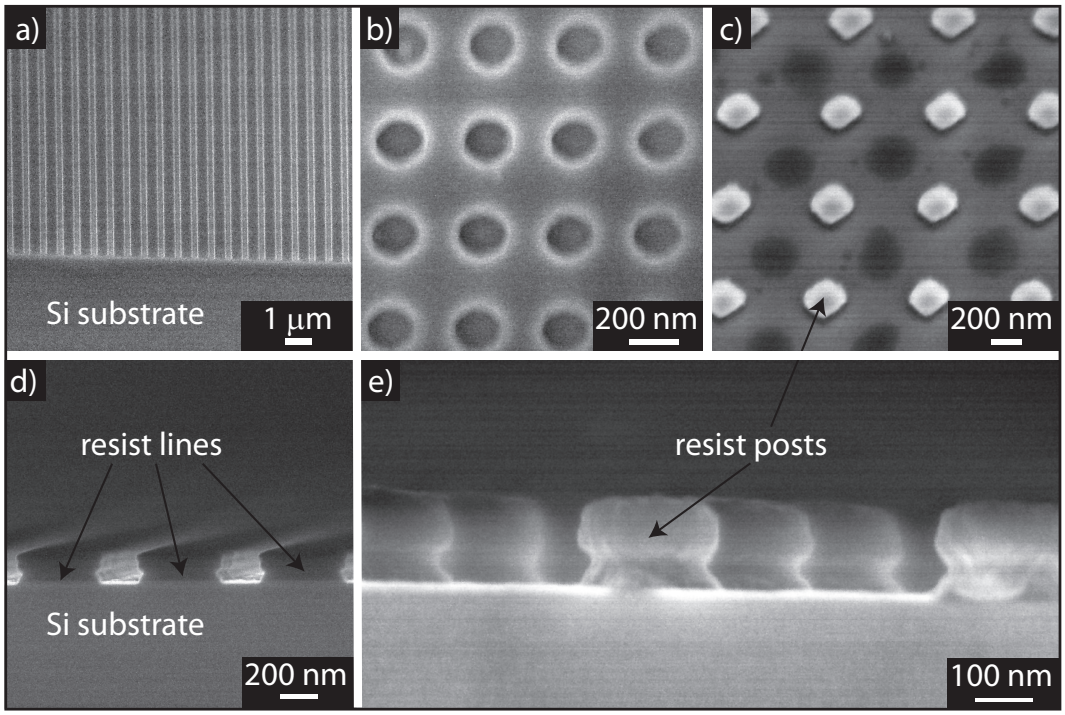

Figure 2.4: SEM images of photoresist patterns on Si substrates: A line pattern is shown in bird's eye view in a) and in cross section in d). A continuous resist film with an array of holes is presented in b), while the inverse structure, an array of resist posts is displayed in top view and cross section in c) and e), respectively.

p_{vsw} can be deduced from geometrical considerations similar to what was presented in section 2.1.1 and is

$$p_{\mathrm{vsw}} = \frac{\lambda}{2n_{\mathrm{PR}} \cos\theta} \tag{2.20}$$

in the direction normal to the surface. The undercut becomes more severe for smaller resist structures and eventually limits the obtainable structure size. This problem can be overcome by an anti-reflection coating that minimizes the back reflection from the substrate [Wal04, Ji08, Che01]. Generally, an anti-reflection coating improves the resist profile but requires additional fabrication steps and equipment, wherefore this approach was not pursued during this work.

For most applications, the resist pattern is only an intermediate step for further structuring. This can be done by etching the substrate material (wet chemical etching or reactive ion etching) [Lan96, Köh99, Win92] or by selective deposition of another material. Examples for both approaches are presented in Figure 2.5 and are combined in Subsection 2.2.1 for the fabrication of SiNWs. Figure 2.5a) shows a resist pattern after thermal evaporation of $\approx 20\,\mathrm{nm}$ Ag. A continuous Ag film is observable, as well as isolated metal islands in the holes of the resist. In b) the same sample after dissolution of the resist is displayed and now an array of uniform silver

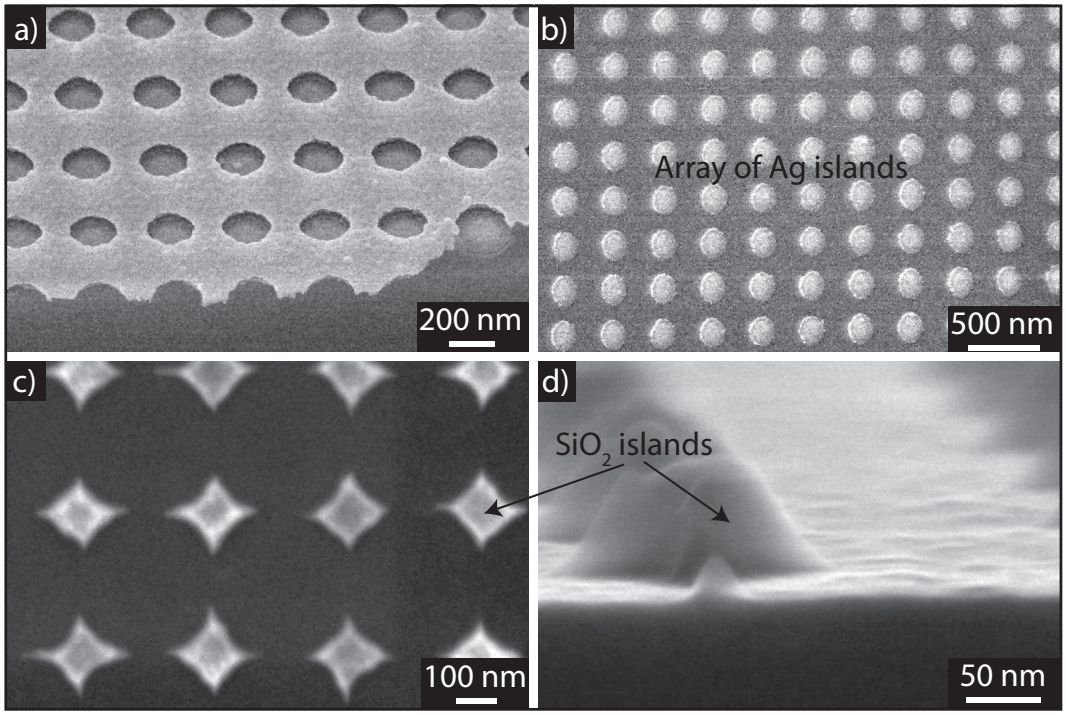

Figure 2.5: Applications of LIL: Resist after evaporation of 20 nm Ag before a) and after lift-off b). In b) an array of regular Ag islands is visible. c) and d) show arrays of SiO_2 islands that have been produced by wet chemical etching.

islands can be seen. Arrays of metal islands can be used for nanowire growth [Kim07], for magnetic data storage[Mar03], or for optical applications [Sch10b, Siv10]. In c) and d) an array of SiO_2 islands on a Si substrate is displayed. A resist post pattern was fabricated on a Si wafer with a 70 nm top SiO_2 layer. After development the sample was immersed in 5% hydrofluric acid (HF) for 3 min and the SiO_2 was etched away except for the areas beneath the resist posts. Due to its mechanical stability such a SiO_2 pattern might e.g. be used as stamp in nanoimprint lithography [Cho95, Cho96, Aus04].

2.1.2 Immersion laser interference lithography

Immersion lithography is a concept to extend the working range of lithographic techniques to smaller structure sizes and higher densities [Kaw89, Bra06, Bru05]. People are interested in smaller structures for several reasons. Firstly, smaller structures can correspond to a higher structure density, i.e. to faster devices. Secondly, the physics of nano-scale objects often differs substantially from the physics of their bulk counterparts. Considering Si for example, the electronic quantum confinement in nanoporous Si leads to visible photoluminescence [Leh91]. In terms of thermoelectrics, the increasing impact of electron/phonon surface scattering as well as the

more pronounced charge carrier depletion due to localized surface states with decreasing structure size are important [Sch10a, Hoc08, Bou08, Hic93b].

Regarding LIL, it can be seen from Eq. (2.16) that the minimal periodicity is $\lambda/2$. And while it is possible to vary the structure size by adjusting the exposure time it is difficult to reduce the structure size below $p/4$ [Ji08]. One way to reduce periodicity *and* structure size is to employ lasers with smaller wavelength. Another option for smaller periodicities is to place a medium with high refractive index in the optical path. Doing so, the wavelength in the medium with refractive index n is smaller than the wavelength in vacuum by a factor that corresponds to n [Jac99]. In standard lithography often a liquid is used for that purpose, therefore this type of lithography is known as immersion lithography [Kaw89, Bru05].

Immersion interference lithography has been employed previously in a multi-beam setup [Blo06] and a Talbot prism [Bou04] to produce patterns with periodicities below 50 nm. However, these setups are designed to produce patterns with fixed periodicities. If periodicities are to be changed, optical components have to be replaced or exchanged and time-consuming realignment is required. Therefore we aimed for combining the more flexible Lloyd's mirror interferometer with immersion lithography. As described in Subsection 2.1.1 a Lloyd's interferometer basically consists of a sample holder and a mirror perpendicular to it. In order to decrease the obtainable structure sizes the mirror is replaced by a prism with $n_{\mathrm{prism}} \approx 1.5$. One side of the prism has a metal-coating and acts as a mirror. A standard and an immersion Lloyd's mirror interferometer are directly compared in Figure 2.6 and it can be seen that the working principles are the same: part of the light is reflected from the mirror and interferes with the directly incident light, creating a sinusoidal interference pattern in the resist.

There are, however, differences as well. The wave vectors of the electromagnetic waves are $\vec{k}_0 n_{\mathrm{air}}$ in air and $\vec{k}_0 n_{\mathrm{prism}}$ in the prism ($\vec{k}_0$: wave vector in vacuum), thus, following the line of argument of Section 2.1.1, the periodicity for the immersion interference lithography (ILIL) setup is

$$p = \frac{\lambda}{2 n_{\mathrm{prism}} \sin\theta_{\mathrm{prism}}}\,, \tag{2.21}$$

and thus a factor of $n_{\mathrm{prism}}/n_{\mathrm{air}}$ smaller than in the standard setup. A second difference is that the angles to the substrate normal inside and outside of the prism, θ and θ', respectively, are not identical; due to the refraction at the air/prism interface. While θ enters Eq. (2.21), θ' is experimentally easily accessible. From simple geometrical considerations, it can be seen that θ and θ' are related by

$$\frac{\sin(60^\circ - \theta')}{\sin(60^\circ - \theta)} = \frac{n_{\mathrm{Prism}}}{n_{\mathrm{air}}}\,. \tag{2.22}$$

The third difference is a layer of an immersion liquid between the prism and the resist. If there was an air gap between prism and resist, total internal reflection would

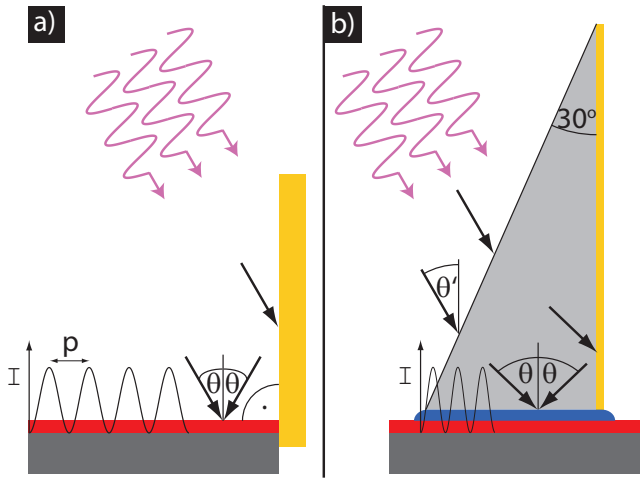

Figure 2.6: a) Standard Lloyd's mirror interferometer: A fraction of the light from an expanded laser beam reaches the sample directly while another fraction after reflection from a mirror (yellow); this results in a sinusoidal intensity pattern across the sample. The substrate (dark gray) is coated with photoresist (red) as described in Section 2.1.1. b) Scheme of the immersion Lloyd's mirror interferometer that was developed during this thesis. Here the laser light is directed onto a triangular prism at an angle θ' to the sample normal. Instead of by a separate mirror, the light is reflected by the metal-coating (yellow) of the prism. The working principle is as in in a) but the periodicity in b) is smaller due to the refractive index of the prism. Total reflection at the bottom side of the prism is avoided by using an immersion liquid (blue). Taken from [dB10b] and modified.

occur for $\sin\theta \geq n_{\text{air}}/n_{\text{prism}}$ i.e. $\theta \geq 41.5°$. Since one is usually interested in small periodicities, i.e. large θ, this is undesirable, but can potentially be circumvented if a substance with a higher refractive index is situated between photoresist and prism.

We have used 30°-60°-90° prisms, so-called Littrow prisms, for the ILIL setup. Prisms with dimensions 22 mm × 37.9 mm × 22 mm made from fused silica were purchased from Altechna Co. Ltd., Lithuania. The long leg of the prism acted as mirror and had an Al coating ($\lambda/10$ quality). Littrow prisms are standard components in laser optics (used e.g. for wavelength selection in laser cavities), and are therefore relatively inexpensive (≈ 100 $). Regarding the choice of prism angles, one should consider that depending on the angle between prism normal and incident light, a part of the incident light is reflected at the prism/air interface, increasing exposure time. To reduce reflection, laser light should enter the prism nearly perpendicularly for the range of periodicities that is desired. So, one is not restricted to 30°-60°-90° prisms, they just have to be rectangular. For the employed prism, reflection at the air/prism interface is minimal for $\theta = 60°$, corresponding to θ'=60°, i.e. small periodicities.

The refractive index of the silica prism can be calculated from the Sellmeier

equation and is $n_{\text{prism}} = 1.51$ at 244 nm [Mal65]. The refractive index of water is $n_{H_2O} \approx 1.38$ [Hal73, Kap06], and therefore the critical angle for total internal reflection is $\theta_{\text{crit}} \approx 66°$. It is of course possible to use liquids with higher refractive indexes [Kap06] to increase the critical angle even further. However, since $\sin(65°) = 0.91 \approx 1$ the reduction in periodicity is only very moderate for angles θ larger than 65°.

To test the setup, we used standard silicon wafers as substrate for the photoresist. The fabrication process was described in Subsection 2.1.1, here usually a resist diluted at a ratio of 1:4 was used. While the samples were rinsed with deionized water, they were carefully pressed against the short side of the prism. Doing so, a thin water film separated prism and sample. Sometimes air bubbles can be observed between prism and sample. Since air bubbles tend to go up in water due to buoyancy, they can be removed by soft pushes on the sample. We also experimented with glass slides (thickness 0.2 mm) as spacers between sample and prism to have a well-defined distance. However, better results were achieved without the spacers.

Figure 2.7a) shows a low magnification SEM image of the obtained resist pattern after a single exposure and development. One can see a regular and uniform line pattern. From the higher magnification image presented in Figure 2.7b) a periodicity of $90 \pm 2\,\text{nm} \approx 0.37\lambda$ can be deduced from image analysis. This is well below the limit of a standard Lloyd's mirror and fits to the result expected from Eq. (2.21): $p_{\text{ILIL}} = 93\,\text{nm}$ at $\theta' = \theta = 60°$. The width of the resist stripes is $43 \pm 4\,\text{nm}$ and exhibits some roughness. One reason for the roughness is that the employed resist is a standard, non-chemically amplified resist with a spatial resolution of $\approx 50\,\text{nm}$. Moreover, since the fabrication process was not done in a cleanroom, the presence of dust particles can not be excluded. Possible stray light would effect the contrast and thus the resist profile more severely than in the standard LIL setup. An anti-reflection coating would at least suppress the back-reflection from the resist-substrate interface and thereby reduce stray light and improve the resist profile.

As indicated in Subsection 2.1.1 resist patterns are usually only an intermediate step in the fabrication scheme. Figure 2.7c) shows a silver line pattern that was obtained after evaporation of 15 nm Ag and subsequent lift-off with acetone. The metal stripe pattern is again regular and has a stripe width of $47 \pm 6\,\text{nm}$.

One of the big advantages of a Lloyd's mirror interferometer is the ease with which patterns with different periodicities can be fabricated. This still holds for the ILIL setup and a couple of experiments at different θ' have been conducted. The resulting periodicities were deduced from SEM images and are shown in Figure 2.8 as red diamonds. The black line represents the theoretical curve for the ILIL setup according to Eq. (2.21), while the periodicity of a standard Lloyd's mirror interferometer (Eq. (2.16)) is plotted as dotted line.

It can be seen that structures with $86 \pm 4\,\text{nm} \leq p \leq 132 \pm 5\,\text{nm}$ have successfully been fabricated. Larger θ' and smaller p are not accessible due to total internal reflection, while structures with larger periodicities are not of interest, since they

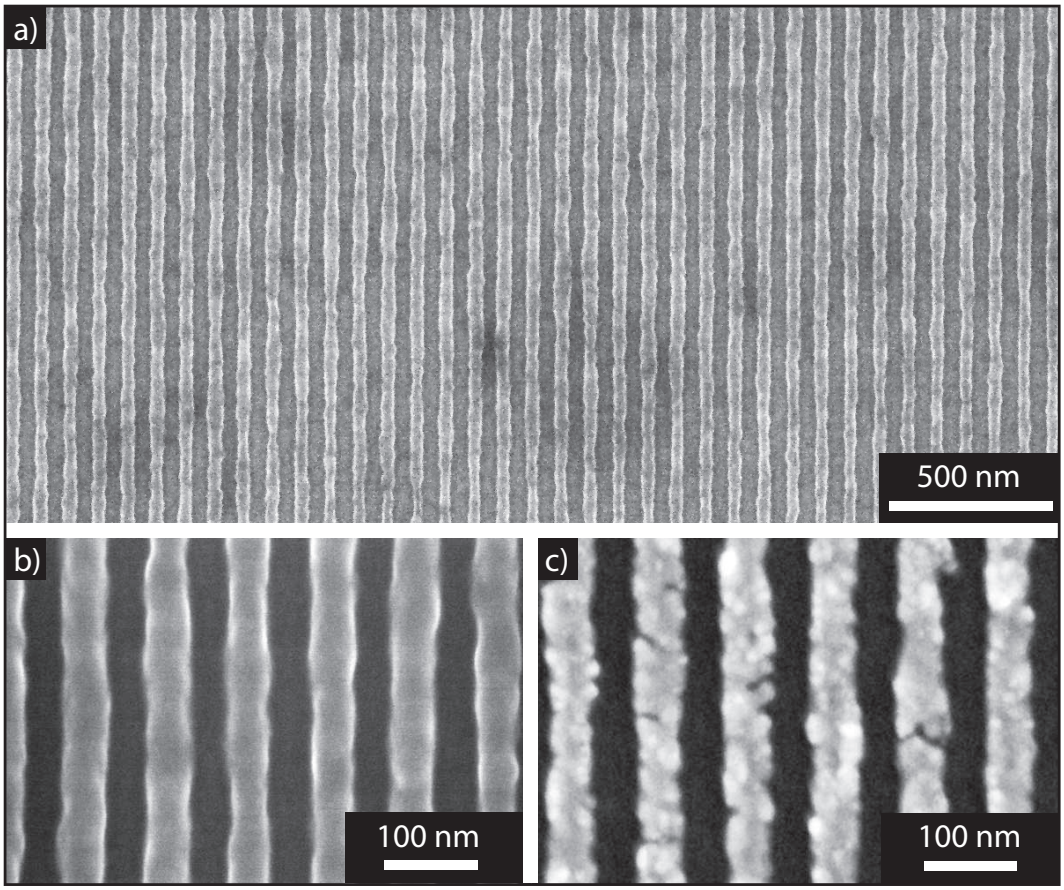

Figure 2.7: SEM images of photoresist patterns after exposure in ILIL setup and development. a) Low magnification image of a sample after exposure at $\theta = \theta' = 60°$, showing the periodicity and regularity of the pattern. b) The same sample at higher magnification; the width of the resist lines is 43 ± 4 nm. c) Patterned silver lines after evaporation of 15 nm Ag onto the sample shown in a) and b) and subsequent lift-off. Taken from [dB10b] and modified.

can be fabricated in the standard setup. The measured periodicities follow the theoretical curve albeit being systematically about 5% too small. The most probable error source is an incorrect measurement of θ', mainly because $\theta' = 0$ could not be determined experimentally with an accuracy better than 3°. Other error sources are inaccuracies in the analysis of the SEM images and a refractive index of the prism that was different from the assumed value of $n_{\text{prism}} = 1.51$.

The results shown in this section have been obtained with a laser with $\lambda = 244$ nm. The concept, however, is general and can be applied to lasers with different, in particular smaller wavelengths, provided that the laser source fulfills the coherence requirements for the desired sample sizes. This is especially appealing for immersion lithography, since the refractive index of SiO_2 and other typical prism materials

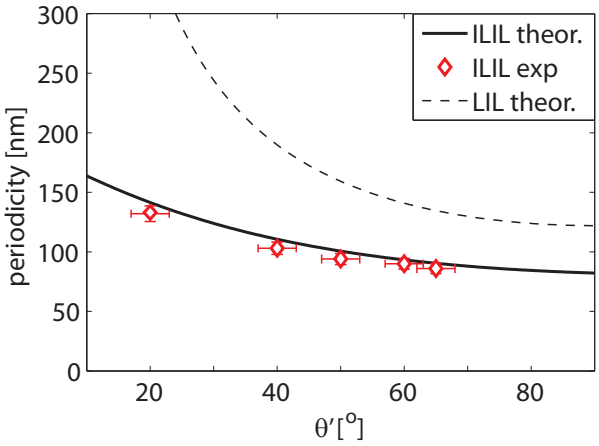

Figure 2.8: Periodicity of the ILIL interferometer as a function of the angle between substrate normal and laser beam in air for a laser wavelength of 244 nm. The values calculated from Eq. (2.21) are given by the solid line while the measurement data is shown as diamonds. For comparison the periodicity of a standard Lloyd's mirror interferometer (Eq. 2.16) is plotted as dashed line. The smallest obtainable periodicity for a standard Lloyd's interferometer is $\lambda/2 = 122$ nm, while with prism and immersion liquid the working range is expanded well below 100 nm. Taken from [dB10b] and modified.

increases with decreasing wavelength [Smi04], and thus the "gain" will be twofold if smaller wavelengths are applied.

A novel, simple, and inexpensive modification of a Lloyd's mirror interferometer has been developed during the course of this thesis. Using a metalized fused silica prism, photoresist line patterns with sub-100 nm periodicity and 45 nm width were fabricated. This is beyond the smallest periodicities achievable with a standard Lloyd's mirror interferometer and shows that the setup extends the working range of LIL to smaller dimensions. Since the working principle is essentially unchanged the immersion Lloyd's mirror interferometer retains the advantages of the standard setup, in particular the flexibility in periodicity.

2.1.3 Three-beam interference lithography: hexagonal patterns at a single exposure.

In this section we will present a three-beam alternative of a Lloyd's mirror interferometer that allows for the fabrication of hexagonal photoresist patterns at a single exposure. Single exposure in a standard Lloyd's interferometer or the immersion interferometer yields a resist line grating, see Section 2.1 and Section 2.1.2, respectively. However, for applications like ordered nanowire growth/etching [Kim07, Cho08] or magnetic/ferroelectric media for data storage [Mar03, Han09], two-dimensional pat-

terns like dot arrays are required. As discussed before, this can be achieved with a Lloyd's interferometer by a double exposure of the sample, see e.g. Figure 2.3 and 2.4. A rotation of the sample is required in between the two exposures and makes the fabrication process more demanding. Rotating the sample by 90°yields a pattern with square symmetry and round resist posts/holes. Other symmetries may be required as well, in particular patterns with hexagonal symmetry, since these have the highest areal density and are therefore ubiquitous in self-organized processes like nanosphere lithography [Hua07] or the anodization of aluminum [Lee06]. Using a standard Lloyd's interferometer, a rotation of the sample by 60°between the two exposures yields a pattern with hexagonal symmetry, the individual resist posts/holes are, however, elliptically deformed [Lee06].

Thus, a standard two-beam Lloyd's interferometer is not an ideal setup with respect to the fabrication of patterns with hexagonal symmetry. Optical setups with three beams that can be aligned independently of each other are a possibility to produce hexagonal patterns with round structures, but these setups are designed for patterning at fixed periodicities [Moo06, Lu07]. Furthermore, they are more complex than a Lloyd's interferometer and less convenient to handle. We have therefore designed a three-beam version of a Lloyd's interferometer, which is presented in Figure 2.9, and can be compared directly to a standard two-beam Lloyd's interferometer.

In contrast to a standard Lloyd's interferometer, which consists of a sample holder and a single mirror, the three-beam interferometer consists of a sample holder and two mirrors. These mirrors are perpendicular to the sample plane and at an angle of 120°with respect to each other. Due to the reflection of the light at the now two mirrors there are three incident plane waves, whose wave vectors have a threefold symmetry as shown in Figure 2.9e). This results in a hexagonal intensity pattern, as depicted in Figure 2.9f). The wave vectors for the two-beam setup are stated in Eq. (2.13), for the three-beam setup they follow from geometry:

$$\begin{aligned} \vec{k}_{1,3-\mathrm{beam}} &= k(-\sin\theta, 0, -\cos\theta)\,, \\ \vec{k}_{2,3-\mathrm{beam}} &= k(0.5\sin\theta, \sqrt{3/4}\sin\theta, -\cos\theta)\,, \\ \vec{k}_{3,3-\mathrm{beam}} &= k(0.5\sin\theta, -\sqrt{3/4}\sin\theta, -\cos\theta)\,. \end{aligned} \tag{2.23}$$

As for the two-beam setup, a key quantity is the periodicity of the intensity pattern of the three-beam setup. Since the wave vectors have a threefold symmetry, the intensity pattern will have one, too. Generalizing the argument from Section 2.1 the periodicity of the pattern in a certain direction $\vec{d}$ is given by

$$p_d = \frac{2\pi}{\vec{k}_f \cdot \vec{d}}. \tag{2.24}$$

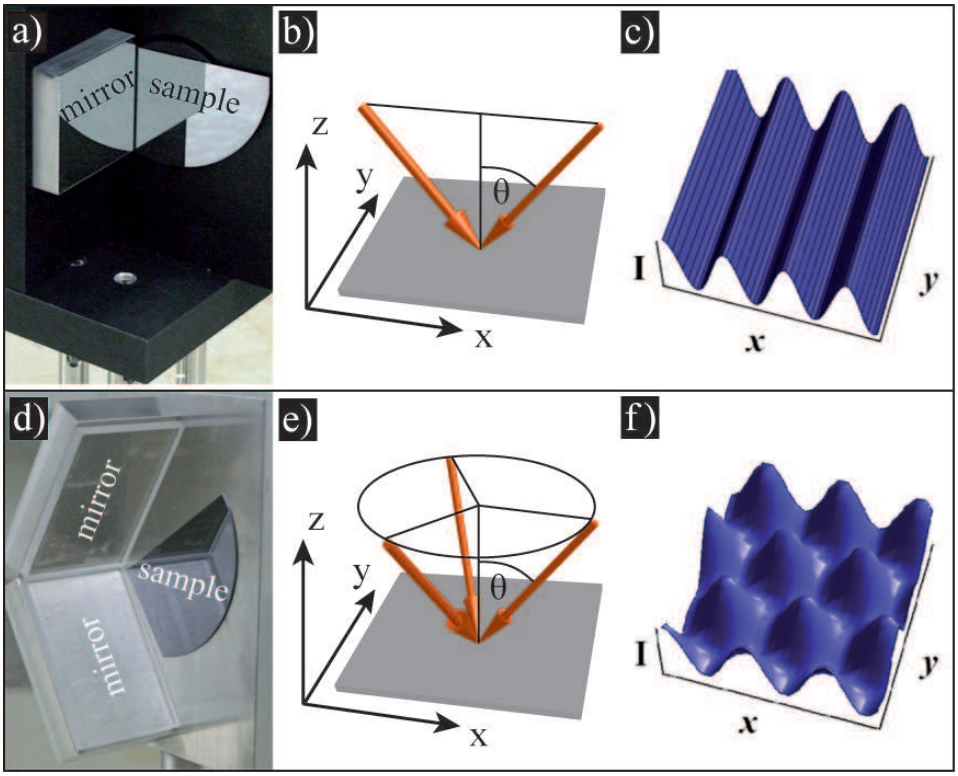

Figure 2.9: Comparison of two-beam and three-beam interferometer. a) Photograph of a standard Lloyd's interferometer, b) resulting wave vectors and intensity pattern with a one-dimensional periodicity in c). d) Three-beam Lloyd's interferometer, e) resulting wave vectors and hexagonal intensity pattern f). Taken from [dB09].

The fringe vectors $\vec{k_f}$ can be calculated for each combination of the wave vectors:

$$\begin{aligned} \vec{k}_{f,12} &= k(-1.5\sin\theta, -\sqrt{3/4}\sin\theta, 0)\,, \\ \vec{k}_{f,13} &= k(-1.5\sin\theta, \sqrt{3/4}\sin\theta, 0)\,, \\ \vec{k}_{f,23} &= k(0, \sqrt{3}\sin\theta, 0)\,. \end{aligned} \tag{2.25}$$

Considering the periodicity along the x-y projection of $\vec{k}_{1,3-\mathrm{beam}}$ it follows for the three fringe vectors

$$\begin{aligned} p_{12} &= \frac{2\pi}{\vec{k}_{f,12}\cdot(1,0,0)} = \frac{2\pi}{1.5\sin\theta k} = \frac{\lambda}{1.5\sin\theta}\,, \\ p_{13} &= = \frac{\lambda}{1.5\sin\theta}\,, \\ p_{23} &= = 0\,, \end{aligned} \tag{2.26}$$

thus, the periodicity along the x-axis is $\lambda/(1.5\sin\theta)$. From symmetry follows that

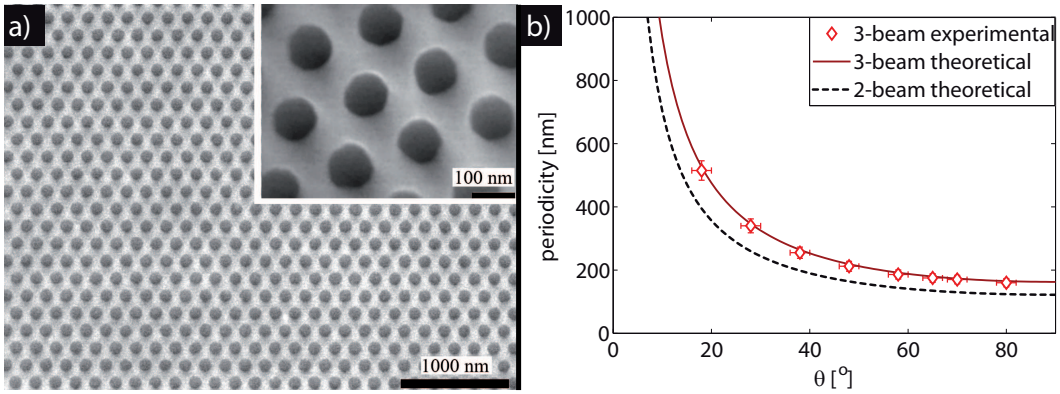

Figure 2.10: (a) SEM image of a photoresist pattern after exposure in the three-beam setup and development. The periodicity of the pattern is $p = 186$ nm while the holes in the photoresist have a diameter of around 100 nm. (b) Periodicity vs. angle to the normal of the sample θ for a three-beam Lloyd's interferometer and $\lambda = 244$ nm. As in a standard Lloyd's interferometer setup θ is adjusted by rotating the sample holder in the plane of the optical table. The solid red line corresponds to Eq. (2.27) while the red marker represent experimental results, which match the theoretical curve very well. With the three-beam setup periodicities above 165 nm are continuously achievable. The periodicity of a standard two-beam setup (Eq. (2.16)) is illustrated as a dashed-dotted line for comparison.

the periodicity is the same along the x-y projections of the other wave vectors. The overall periodicity of the hexagonal intensity pattern p_{Hex} can then be defined as

$$p_{\mathrm{Hex}} = \frac{\lambda}{1.5 n_{\mathrm{air}} \sin\theta_{\mathrm{air}}} \,. \tag{2.27}$$

For correctness and consistency the effect of the medium (here air) has to be included in Eq. (2.27).

For experimental realization, Si wafers were used as substrates and prepared as described in Section 2.1.1. The distance between spatial filter and sample holder was around 1 m and typical illumination times were 1 to 5 minutes. Both dielectric mirrors (75x50x5 mm with a HfO_2/SiO_2 multilayer coating, Laseroptik GmbH, Garbsen, Germany), and metallic mirrors have been employed in the setup.

An SEM image of the resist pattern obtained after an exposure time of $t = 150$ s at $\theta = 58°$ is shown in Figure 2.10a). On the low magnification image the large-scale regularity of the hexagonal resist pattern is clearly visible while the close-up inset shows the smooth feature of the photoresist. A distinct advantage of the three-beam interferometer is that the obtained pattern show true hexagonal symmetry, i.e. the resist holes/post are round and not elliptical as for the two-beam setup; for a detailed discussion see [dB09]. As for the two-beam setup, the periodicity of the three-beam setup can be varied by a rotation of the whole interferometer, thus

by adjusting θ. Experimental results for different θ are presented in Figure 2.10b). The experimental data fits very well to Eq. (2.27) and it can be concluded, that periodicities above 165 nm are continuously accessible.

The introduced three-beam interferometer is no full replacement of the standard two-beam setup, mainly because it can produce only hexagonal patterns. The periodicity is also larger by a factor of 4/3 and the contrast is not unity, since the three beams are not completely transverse electrically polarized to each other. It is advantageous, however, if patterns with hexagonal symmetry are required or if just any two-dimensional structure is required, since these can be fabricated with the three-beam setup faster and more conveniently.

As structuring technique, and in particular regarding hexagonal patterning, LIL competes with techniques based on self-organizing processes, like pre-patterning with nano-sphere lithography [Hua07], or anodization of aluminum [Li98]. These techniques usually offer only short-range order and a domain-like structure on a larger scale. The LIL fabricated resist patterns show strict long range order over cm^2 and can even be used to enforce long-range order on self-assembling processes, see e.g. [Lee06].

2.2 LIL structures for thermoelectric applications

After presenting the working principle of LIL in Section 2.1, this Section will deal with the fabrication of Si nanostructures using LIL. We have combined LIL patterning with a simple, electroless, wet-chemical method – the so-called metal-assisted etching – to fabricate arrays of SiNWs with diameters between 350 nm and 65 nm, see Section 2.2.1. Another interesting structure for thermoelectric investigations are Si fins which were fabricated by anisotropic KOH etching. LIL was used to define and vary the fin thickness (Section 2.2.2).

2.2.1 Arrays of silicon nanowires

In 2008, two groups investigated the thermoelectric properties of SiNWs and showed that those can have $ZT > 0.5$ at room temperature [Bou08, Hoc08]. Since Si is relatively cheap and a huge technological processing background is already available, SiNWs appear to be promising candidates for thermoelectric applications. Hochbaum *et al.* [Hoc08] compared the properties of differently prepared SiNWs and showed that nanowires fabricated by so-called metal-assisted etching had lower κ and thus larger ZT than SiNWs grown by the vapour-liquid-solid-mechanism [Sch10a]. Metal-assisted etching of Si is a relatively new process, but received an enormous amount of attention, due to its simplicity and practicability. There have been several hundred publications on this topic within the last years, see e.g. [Li00, Pen06, Hua07, Hua08, Hua09, Gey09]. Metal-assisted etching usually consists of the following steps: firstly a somehow patterned metal film (usually gold or sil-

ver) is brought onto a Si substrate. Secondly the sample is immersed in a solution containing HF and an oxidative agent, usually H_2O_2. Due to the redox potential of the agent Si is oxidized and subsequently removed by HF. The key point is, that the metal film acts as catalyst for this reaction, i.e. the etching speed far away and in the vicinity of the metal film differ by several orders of magnitude. If a closed metal-film containing holes is employed, SiNWs can be obtained from the etching, since, to a very good approximation, only the Si below the metal film is etched away, so that the metal film sinks into the Si substrate. The picture presented here is only a rough approximation. Process details are discussed in literature, and partly still under investigation. An overview about process parameters like choice of metal, Si doping and orientation, etching solution composition, and etching temperature can be found in a recent review by Huang and Geyer *et al.* [Hua11].

In their mentioned work on SiNWs for thermoelectrics, Hochbaum *et al.* measured single nanowires [Hoc08] while Boukai *et al.* measured several hundred [Bou08]; for a real device, however, one has to find a way to produce macroscopic amounts. Macroscopic amounts of SiNWs can be fabricated by metal-assisted etching fast and simply, as shown by Peng *et al.* [Pen06], who deposited an irregular metal film by precipitation of elemental Ag from a salt solution. The wires obtained in this fashion are of irregular shape and have varying "diameters". The thermoelectric properties of SiNWs depend sensitively on their diameter and therefore control over wire geometry is necessary for thermoelectric applications. Control over wire position is furthermore desirable, since it simplifies contacting and assessing the wire areal density. For these reasons, several prepatterning techniques have been combined with metal-assisted etching. To mention are: nanosphere lithography, AAO masks, and LIL [Hua07, Gey09, Cho08]. The former two techniques give Si nanowires in a hexagonal pattern with some control of nanowire diameter. However, the obtained wires show only a short-range order and a domain structure on larger scales. Such a domain structure complicates contacting of the individual wires and often leads to wires with different geometries (thus properties) at the domain walls. LIL, on the other hand, yields pattern with strict long-range order and very well defined geometries. Choi *et al.* have combined LIL and metal-assisted etching to fabricate arrays of SiNWs with round or elliptical shapes of various length and sizes. However, the smallest wires they presented had a diameter of 150 nm, which is way too large for thermoelectric applications. Hochbaum *et al.* showed their best ZT for nanowires with a diameter of ≈ 50 nm. Thus for an earnest attempt to fabricate SiNWs for thermoelectrics one should aim for huge amounts of geometrically well defined wires with diameters approaching 50 nm.

We have matched LIL with metal-assisted etching to produce arrays of regular SiNWs with various densities and diameters down to 65 nm. The fabrication scheme together with the corresponding SEM images is shown in Figure 2.11. At first, arrays of resist post are fabricated by double exposure as described in Subsection 2.1.1 on (100) Si wafers ($0.3 - 0.7\Omega$cm). Subsequent exposure to an O_2 plasma (100 W, 15-

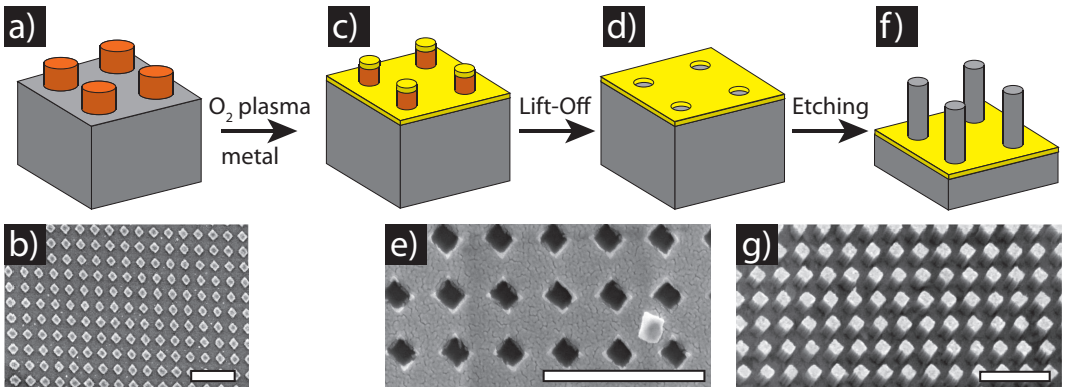

Figure 2.11: Fabrication scheme for ordered arrays of SiNWs and corresponding SEM images: Arrays of resist posts are created by LIL (a, b); resist post size can be decreased by O_2 plasma treatment, the posts are then covered with a thin but continuous metal film (c); the metal caps are lifted-off by dissolution of the resist (d, e); immersion of the sample in the HF/H_2O_2 solution yields arrays of uniform SiNWs. The scale bar corresponds to 1 μm in each of the SEM images.

90s) reduces the size of the resist posts by several tens of nanometers and is used to fabricate arrays of small posts. Secondly, the sample is coated with a Au film by thermal evaporation (Auto 306, Edwards). This is followed by a lift-off of the photoresist. At this fabrication step, the Si sample is covered with a Au film with a regular array of holes (see Figure 2.11e)), whose sizes corresponds to the size of the resist posts. The final step, metal-assisted etching, is done at room temperature in a solution containing 5.0 M HF and 0.42 M H_2O_2. For the chosen parameters the etching proceeds along the <100> direction, i.e. perpendicular to the surface. As example, nanowires with $p \approx 357$ nm are shown in Figure 2.11g); the wires are arranged in a square pattern and very regular. For a successful fabrication one has to choose the "correct" film thickness: a Au film thickness above 15 nm was found to be necessary to obtain a closed film. For thinner films additional holes in the metal film led to the etching of "parasitic" wires at undesired positions. On the other hand, lift-off becomes unsuccessful for too thick metal films, this became important especially for resist posts, whose size (and height) had been decreased by O_2 plasma treatment.

By adjusting exposure angle and times, the periodicity and the size of the resist posts can be chosen. Since the diameter of the wires matches the diameter of the resist posts, arrays of wires with various diameters and densities can be fabricated. The etching speed depends on the etching solution composition [Hua11], but is approximately constant, thus wires length can be controlled by etching time. Examples are shown in Figure 2.12.

For application of the wires in thermoelectrics or electronics, good electrical

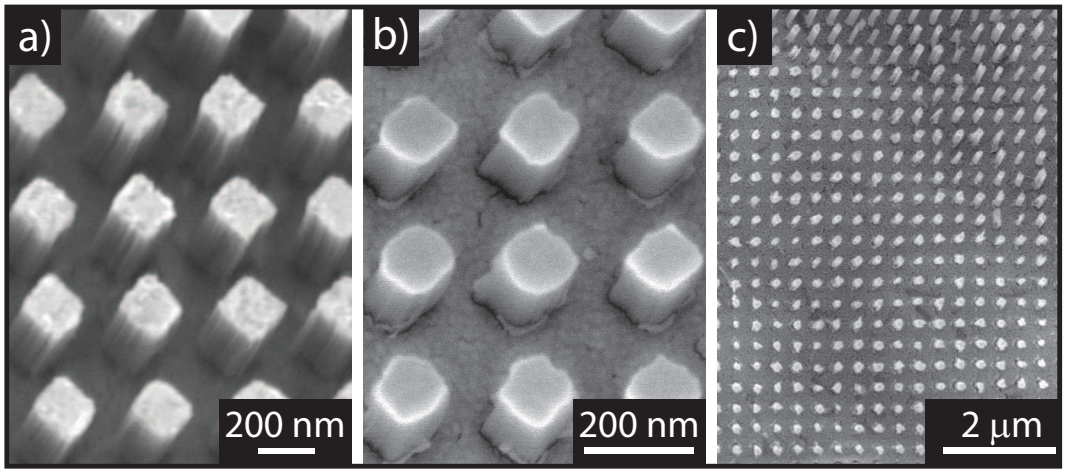

Figure 2.12: Arrays of SiNWs: a) is a close-up of Figure 2.11g); it can be seen that the wires have an almost rectangular shape with a diagonal of $\approx$ 230 nm length. In b) nanowires with a periodicity of 244 nm and a diameter of approx 150 nm are shown. Wires with diameters around 60 nm and a periodicity of 190 nm are presented in c). Note that a periodicity of 190 nm corresponds to an areal density of $2.8 \times 10^7\,\mathrm{mm}^{-2}$. Taken from [dB10a] and modified.

conductivity of the wires is paramount. This can only be guaranteed for single-crystalline wires. As can be seen from the transmission electron microscope images in Figure 2.13d) and e) the wires itself are indeed single-crystalline and moreover form a single crystal with the Si substrate. Since the wires were etched from a single crystal this comes not unexpected and shows a principal advantage of metal-assisted etching compared to nanowire growth techniques.

Nanowires with diameters below 100 nm are finally shown in Figure 2.14. Measuring the diameters d of the wires shown in 2.14a) yields $d = 66 \pm 8\,\mathrm{nm}$.

A high nanowire density is desirable for most applications. The density D is given by $D = p^{-2} = 1.7 \cdot 10^7\,\mathrm{mm}^2$ for the wires shown in Figure 2.14. This is larger than density values reported previously, obtained by LIL or nanosphere lithography [Cho08, Hua07] and comparable to results obtained with AAO templates [Gey09]. Advantageous compared to grown wires is that the etched wires all have the same height. This simplifies contacting which is nessary for thermo(-electric) measurements and device implementation. Moreover, the wires are etched along the Si <100> direction, while VLS grown wires usually grow along the <110>, <111>, or <112> direction [Sch10a]. For electronic applications, the <100> direction is often preferred [Zha09].

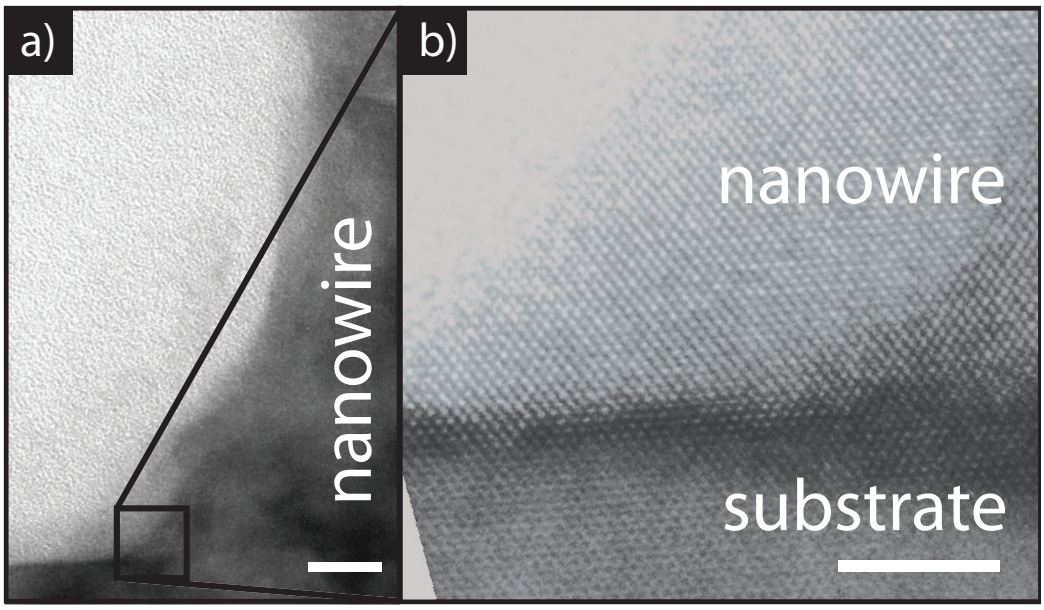

Figure 2.13: TEM images of a single SiNW. a): nanowire foot and Si substrate; b): high resolution TEM. It can be concluded that the wire and substrate form a single crystal (scale bars are 10 nm and 5 nm in a) and b), respectively). Taken from [dB10a] and modified.

2.2.2 Silicon nanofins

As prospective new materials for thermoelectrics, not only one-dimensional structures like SiNWs shown in Subsection 2.2.1 but also two-dimensional structures like thin films or quantum wells have received a great deal of attention. In fact, it has been a thin film measurement reported 2001 by Venkatasubramanian *et al.* [Ven01] that renewed interest in thermoelectrics significantly. In this paper Venkatasubramanian *et al.* studied a thin film sample composed of Bi_2Te_3/Sb_2Te_3 and found a figure of merit $ZT = 2.4$ at room temperature. Although a higher thermoelectric efficiency is predicted for nanowires compared to thin films [Hic93b, Hic93a], thin films have considerable advantages over NWs. They are more easily and in larger quantities produced and they are furthermore much easier characterized [Ber09], a consequential advantage, since singling out a good thermoelectric material usually requires a lot of optimization, thus characterization.

Since the effect of confinement in one or more dimensions is a fundamental physical question thin films are furthermore test-cases for the modeling of lower-dimensional objects.

Si thin films are often prepared by wafer-bonding [Mas88, Bru95] or by growth techniques [Tab81]. Here we present a simple alternative way to produce two-dimensional Si structures of well-defined and adjustable thickness. By combining LIL and anisotropic KOH etching arrays of vertical standing Si fins have been pro-

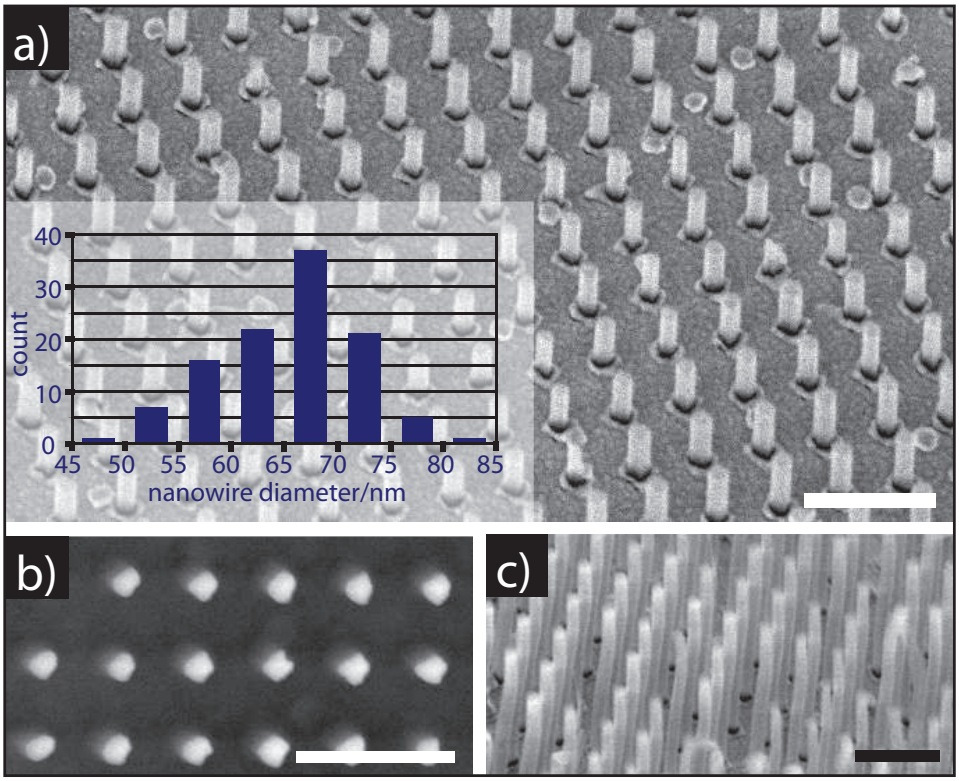

Figure 2.14: Arrays of sub-100 nm SiNWs. a): Low magnification tilted view showing regularity and good homogeneity of the nanowires. The size distribution of the wires shown is given in the inset, the wires have an average diameter of 66 nm with a standard deviation of 8 nm, the periodicity is 244 nm. A top view of the same sample is shown in b). The sample was re-etched and the resulting, much longer wires are shown in subfigure c). The scale bar corresponds to 500 nm in each image. Taken from [dB10a] and modified.

duced; fin widths and height can be adjusted by choosing different optical or etching parameters. The obtained structures show good homogeneity and might be used to investigate size effects of the thermal conductivity.

The fabrication is shown as scheme in Figure 2.15, with the corresponding SEM images below the scheme. Si wafers with a SiO_2 layer of 25 nm-100 nm thickness are used as substrates, SiO_2 covering is achieved by thermal growth in dry oxygen [Nic82]. Resist stripes are prepared with LIL as described in Subsection 2.1.1, a sample SEM image is shown in Figure 2.15b). The pattern is transferred into the silica layer by etching in 5% HF. For this concentration the etching rate is ≈ 30 nm/min and allows convenient handling [Mai66]. The resist itself shows some resistance against dissolution or detaching from the silica layer. For clarity it has therefore been removed in the SEM image shown in Figure 2.15 d), and so silica stripes on a Si substrate are visible. This pattern of silica stripes is then used as

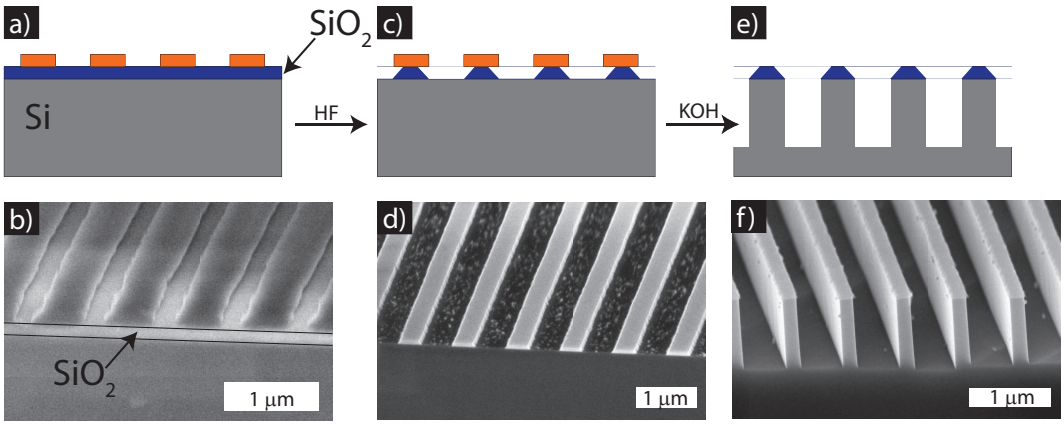

Figure 2.15: Fabrication scheme for Si nanofins with the corresponding SEM images. a) and b): Resist stripes are prepared on a Si substrate, covered with a SiO_2 layer. c) and d): The structure is transferred into the SiO_2 layer by etching in a HF solution. The resist remains during this step on top of the SiO_2 stripes but was removed before taking the SEM shown in d. e) and f): Si fins are created by anisotropic KOH etching. Due to the high selectivity between different crystallographic directions in Si the Si fins show virtually no tapering.

template for KOH etching. KOH etching is a standard process in Si micro-machining [Cam95, Bau97, Köh99]. In an alkaline solution Si is etched (without applied bias) according to the following reaction [Leh02]

$$\mathrm{Si} + 2\mathrm{OH}^- + 4\mathrm{H_2O} \rightarrow \mathrm{Si(OH)_6^{-2}} + 2\mathrm{H_2}\,. \tag{2.28}$$

KOH etching is highly anisotropic due to the different bondings of Si atoms at the Si/electrolyte interface. In <100> and <110> Si an interface Si atom has two Si-Si bondings and two Si-H bondings which can be attacked by the OH^- groups of the electrolyte. If the H end groups are replaced by OH the two Si-Si bonds get weakened due to polarization and the Si interface atom can be dissolved from the bulk completely. In <111> Si however, an interface atom has three Si-Si bonds and only one Si-H bond. Now only one H can be replaced by OH and the remaining three Si-Si bonds are not sufficiently weakened to allow a fast dissolution of the Si interface atom [Leh02]. Consequently, at room temperature the etching rate along the Si <111> direction is two to three orders magnitude smaller than along the <100> or <110> direction [Sei90]. Thus, a [111] plane in a Si crystal acts like an etch-stop. If the SiO_2 lines are parallel to the <111> axis in Si, grooves are etched into the Si wafer. SiO_2 has also a very low etching rate [Sei90] and so the silica patterns hinders a dissolution of the fins from the top.

The resist is removed very fast in the basic KOH solution. A silicon wafer is cleaved most easily along the <111> directions, thus in the LIL setup the sample has to be arranged such that the stripes are parallel to the cleaving edge, which can

be done manually with fair precision.

Since resist stripe width can be tuned by adjusting exposure time and angle and the fin depth is roughly proportional to etching time [Sei90], this method allows for the fabrication of Si fins with different width and depth. Examples for fins with widths between 60 nm and 500 nm are shown in Figure 2.16.

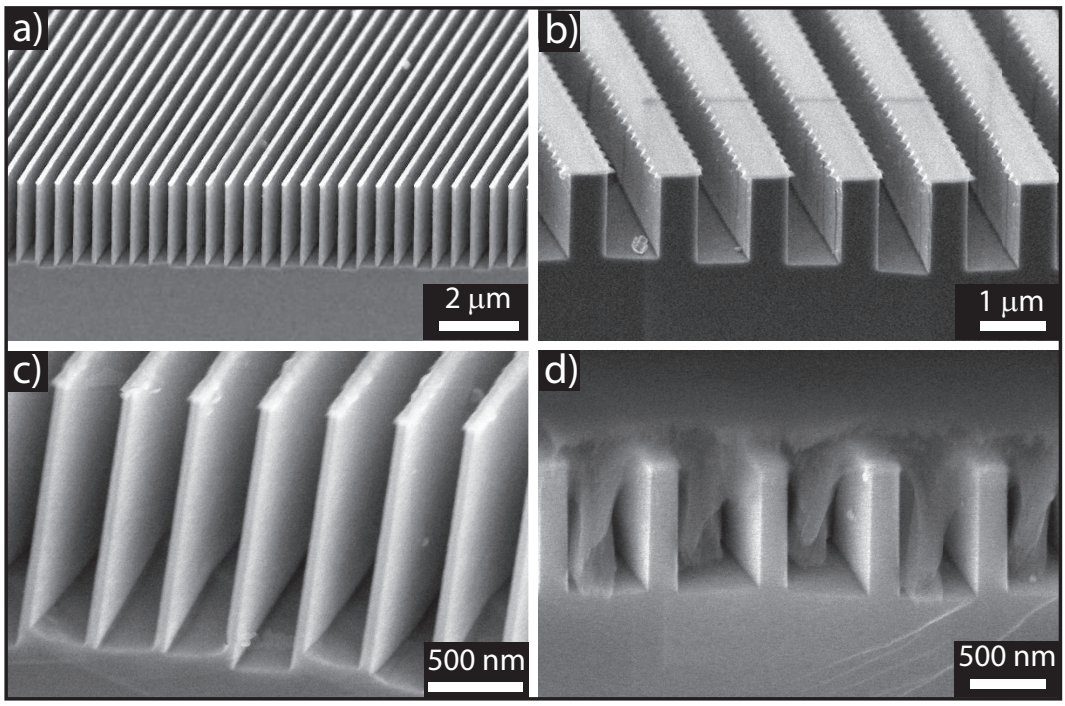

Figure 2.16: Examples for Si fins. The fins shown in a) have a width of 60 nm and a length of more than 2 μm, i.e. an aspect ratio > 30. Moreover, a striking regularity and large-scale uniformity is clearly visible. Thicker fins with a width of 500 nm are shown in b). Subfigure c) presents a close-up of fins with a width of 60 nm, while in d) Si fins embedded in polymer are shown.

It has been noted that for very large aspect ratios the fins collapse and attach to each other, as shown in Figure 1, top image on the right hand side. The reason are presumably adhesive forces during the drying process. These can be minimized if the samples are dried supercritically, e.g. in a CO_2 atmosphere [Cha09]. Thermal conductivity of the fins can be measured on the Si substrate with techniques like the 3-omega technique [Cah87, Cah89] or time-domain thermal reflectance [Cah04, Per09]. If the thermal properties are to be measured with the 3-omega technique, the fins have to be covered with a thin insulating layer. An SEM image of an embedded sample is shown in Figure 2.16d), where a layer of photoresist polymer was brought onto the sample by spin-coating. In total, a powerful approach for the fabrication of Si nanofins has been presented. The obtained structures allow systematic investigations of size effects on the thermal conductivity or other physical

quantities in Si.

2.3 Summary of Chapter 2

The working principle of LIL using a Lloyd's mirror interferometer has been presented. Interference of two or more beams leads to a temporally constant, but spatially varying intensity profile that can be transferred into a physical pattern of a photosensitive material by simple wet chemistry. The fabricated patterns show a striking regularity and their properties, i.e. the feature size and their periodicity can be chosen by adjusting the optical parameters. Furthermore, an immersion Lloyd's interferometer has been designed and presented which extends the working range to significantly smaller periodicities. Finally, a three-beam Lloyd's interferometer has been introduced, which has the power to produce truly hexagonal patterns after a single exposure.

LIL has been combined with two wet-chemical etching methods to produce Si nanostructures. On the one hand Si fins with width between 50 nm and 500 nm have been produced by KOH etching using silica stripes as mask. On the other hand metal-assisted etching has been employed to fabricate SiNWs with diameters down to 60 nm and areal densities up to $2 \times 10^7\,\mathrm{mm}^{-2}$. Using LIL produces arrays of nanostructures that are strictly periodic over cm^2 and have a homogeneous geometry (width, diameter, length) that can be tailored by setting the LIL/etching parameters. While Si fins represent a test case for size effects on two-dimensional objects, arrays of SiNWs represent one step towards the realization of a Si-based thermoelectric device.

Chapter 3

Thermoelectric van der Pauw Measurements

During the course of this thesis, the thermoelectric van der Pauw measurement method has been developed. This is a novel technique that comprises electrical and thermal conductivity measurements as well as Seebeck coefficient and direct figure of merit gaging. With this method a complete thermoelectric characterization of materials is possible. In the first section of this chapter, Section 3.1, the employed setup will be introduced. The thermoelectric van der Pauw method itself will be presented in Section 3.2. Error analyses are important to validate physical results, so much the more for a novel measurement technique. For this reason a table with an overview of experimental errors and a detailed discussion of the most significant problems is presented in Section 3.4. Section 3.5 concludes this chapter with a discussion on the minimization of experimental errors and gives experimental proofs how this can be achieved.

3.1 Measurement system

The groundwork of this thesis, i.e. the setup for thermoelectric measurements will be introduced in this section. The employed setup, its possibilities and limitations will be discussed. Furthermore, the instrumentation and the user interface will be introduced. The possibility to run various types of temperature-dependent thermoelectric measurements in a fully automated fashion was paramount for the progress of the work.

3.1.1 Setup

As discussed in Chapter 1 the efficiency of a thermoelectric generator is linked to the thermoelectric figure of merit ZT, which itself can be expressed in terms of basic

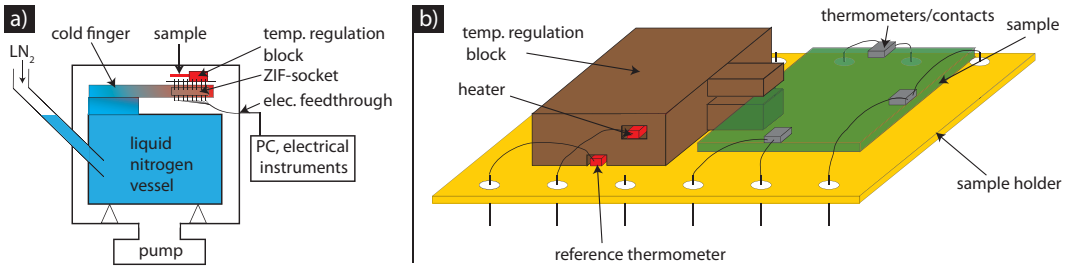

Figure 3.1: a) Thermoelectric measurement system and b) detailed view of the sample holder. The sample holder with suspended sample was used for thermoelectric van der Pauw measurements. For 3ω measurements (see Section 4.3) a similar holder with the sample on top of the temperature regulation block was used. A detailed description of measurement system and sample holder is given in the text.

material parameters

$$ZT = \frac{\sigma S^2 T}{\kappa}. \tag{3.1}$$

Here σ and κ are the electrical and the thermal conductivity, respectively, S is the Seebeck coefficient and T the absolute temperature. For a complete thermoelectric characterization a measurement system has to be designed that provides measurement options for these three quantities. Furthermore, these quantities are interdependent (see Section 1.3), which requires repeated measurements for material optimization, thus measurements have to be fast, convenient, and reliable. Moreover, a measurement system should be designed such that temperature-dependent measurements are possible. This is important for two reasons: firstly, many microscopic parameters like charge carrier mobility or phonon mean free paths are strongly temperature-dependent and information about those can be retrieved from temperature dependent measurements of σ, S, κ. From a device point of view it is vital since thermoelectric devices are always operated over a temperature range, often up to several hundred Kelvin, therefore temperature-dependent knowledge about material properties is indispensable.

Many measurement systems operate either exclusively below or above room temperature by sample cooling or heating [Hoc08, Bou08, Bof05, Zho05]. Our system was designed such that measurements could be performed over a broad temperature range. Using a combination of liquid nitrogen cooling and resistive heating the sample temperature could be varied between 120 K and 500 K in our setup.

The employed thermoelectric measurement system is shown in Figure 3.1a) while Figure 3.1b) shows the sample holder in more detail. For thermal conductivity measurements heat exchange with the environment by conduction through the ambient gas and by convection is highly detrimental. It is therefore necessary to measure thermal properties in high vacuum with pressures $< 10^{-5}$ mbar [Sal09, Row06, Nol01], see also Appendix A. The measurement chamber (Trinos Vakuum Systeme, Ger-

many) consists of an outer chamber, an inner chamber and the sample stage. The inner chamber has a volume of roughly 15 l and can be filled with liquid nitrogen. The outer chamber can be evacuated and is connected to a membrane pump (Vacuubrand, Germany) and a turbo pump (Pfeiffer Vacuum, Germany). The sample is thermally connected to the liquid nitrogen filled inner chamber by a copper cold finger. A ZIF (zero injection force) socket (Aeries Electronics, Inc., USA) is integrated in the cold finger, in the socket the sample holder with the sample can be inserted. From the ZIF socket electrical leads are connected to feedthroughs of the outer vacuum chamber, which in turn are connected to the electrical measurement instruments and a PC. In Figure 3.1b) the sample holder plus sample are shown in more detail. On the sample holder (Schott Electronics, Germany) a metal block (copper or aluminum) is mounted, in which a resistive heater (Pt100) and a resistance thermometer (Pt1000, both from Jumo GmbH, Germany) are embedded. For the thermoelectric van der Pauw measurement the sample is mechanically attached to the heat sink by a clamp. Again, good thermal contact is ensured by the use of graphite between sample and clamp. Electrical connections are made from the sample, the heater, and the thermometer to the pins of the sample holder.

In order to control the sample temperature the heating power is adjusted by a Lakeshore 332 temperature controller such that the reference thermometer matches the desired temperature with an accuracy of 0.01 K. Good thermal contact between metal block, thermometer and sample is important because the measured reference temperature should be as close as possible to the actual sample temperature. This is achieved by applying thermally conductive paste (RS Components GmbH, Germany) between these parts. The sample holder is covered by a lid which can minimize radiative heat loss of the sample if it has a temperature close to the sample temperature. Therefore good thermal contact between metal block and sample holder is ensured by screwing the metal block on the sample holder. Between sample holder and metal block as well as sample holder and lid thin graphite or silver foil is placed. This reduces thermal contact resistances further[Asa93, Kho97, Lam97].

The sample holder can be inserted into the ZIF socket and electrically connected by a clamp mechanism inside the socket. The electrical connections between sample and sample holder (soldering and/or high temperature conductive silver paste, Polytec Pt, Germany) can be made outside of the measurement chamber which makes preparation convenient. The sample holders have 16 or 24 pins (electrically insulated from the main part of the sample holder) for multiple electrical connections to the sample. In particular, this allows for the concurrent measurement of three resistance heaters for the 3ω thermal conductivity measurements (see Section 4.3) or the thermoelectric van der Pauw measurement.

3.1.2 Instrumentation and programming interface

The instrumentation for the thermoelectric measurements comprises of a Lakeshore 332 temperature controller, a Keithley 2182 nanovoltmeter, a Keithley 6221 AC/DC

current source, and a Keithley 3706 digital multimeter (DMM), which was combined with a Keithley 3721 dual multiplexer card. For temperature measurements standard platinum resistors like Pt1000 with known resistance-temperature behavior (see Eq. (3.4)) are employed. These are connected to one of the two input channels of the Lakeshore temperature controller, which converts the measured resistances internally into temperatures. The temperature controller furthermore provides a primary and a secondary PID control loop which can supply up to 50/10 W heating power. For heating mostly Pt100 are employed. In practice a setpoint is defined for one of the thermometers and the temperature controller automatically provides electrical power such that the recorded temperature reaches the setpoint at the reference thermometer. For this to work efficiently the proportional/integral/derivative (PID) coefficients of the control-loop have to be set according to the system design and the thermal connection between heater and reference thermometer has to be sufficiently good. If there are large thermal resistances or capacitances between thermometer and heater, temperature regulation will be very slow or fail completely.

The DMM is mainly used for voltage and resistance recordings during a thermoelectric van der Pauw measurement. In combination with the multiplexer card concurrent four-point measurements of up to 10 resistances are feasible. This is a prerequisite for the realization of the thermoelectric van der Pauw measurement which will be described in the following section.

Unintended static or slowly varying thermoelectric voltages arising inside the measurement system can lead to incorrect electrical measurements. For electrical conductivity measurements this can be overcome with the employed nanovoltmeter and current source, which can be operated combined in a lock-in mode: the current source provides a square wave current output and the voltmeter takes a triggered reading at each high and low output level. This lock-in AC measurement cancels the mentioned static or slow thermoelectric voltages from within the system and significantly increases measurement accuracy. This type of measurement can be performed at frequencies of up to 12 Hz.

The electrical instruments are controlled by MATLAB programs [MAT11] that have been developed together with the system and have been adopted according to measurement requirements. Once the electrical connections are made, the temperature-dependent thermoelectric measurements run fully automatically, which enabls overnight measurements and an efficient use of the system. A screenshot of the graphical user interface is shown in Figure 3.2.

In total the setup and the software allow for a highly automated, efficient and convenient measurement of thermoelectric samples.

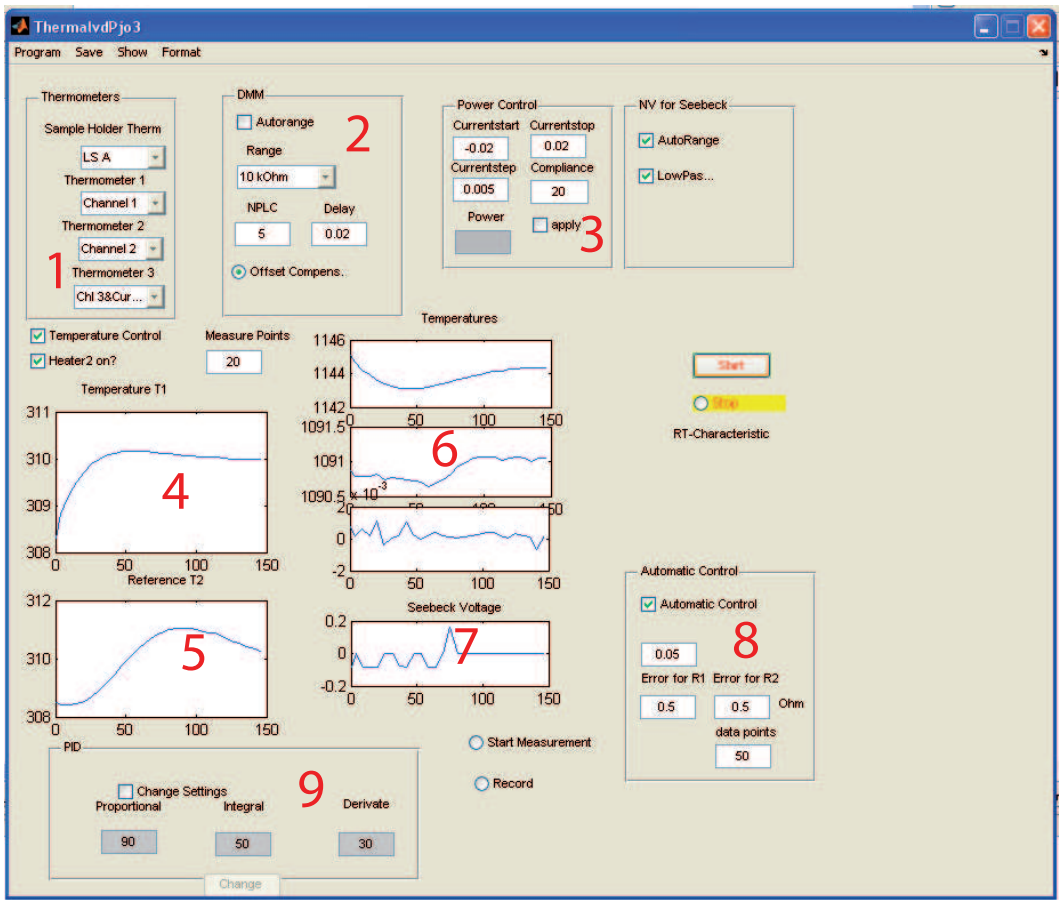

Figure 3.2: Graphical user interface of the software for thermoelectric measurement. Using the software one can assign different measurement quantities (reference temperature, resistances) to different channels of the system (1). One can also set instrument parameters like measurement range or the integration time for DMM or nanovoltmeter (2). For the thermal van der Pauw measurement (Section 3.2) it is necessary to create a temperature gradient across the sample. The power supplied to the resistive heater can be set in 3. 4 and 5 display in real-time the two temperatures measured with the temperature controller, while 6 and 7 display measured resistances and Seebeck voltages. The PID coefficients can be changed in 9. When changing sample temperature, resistances and Seebeck voltages where measured permanently, but recorded for later analysis only once the sample reaches a steady state. For an automatic measurement thus stability criteria have to be defined (8). These are e.g that the measured temperature differs from the setpoint by less than 0.05 K and that the measured resistance R1 did not change by more than 0.5 Ω within the last 200 s. The recorded data is saved once the measurement is completed and is analyzed with different MATLAB scripts.

3.2 Principle and realization of a thermoelectric van der Pauw measurement

As discussed in Chapter 1 optimizing the thermoelectric properties of materials requires delicate adjustment of parameters like the charge-carrier concentration; for most materials, there will be additional degrees of freedom. In case of porous silicon, whose properties will by discussed in Chapter 4, experimental parameters include porosity, average structure size as well as doping and annealing temperatures and times. The exact parameters of course depend on the investigated material system, but optimization of a zoo of parameters is typical for the engineering process of good thermoelectric materials [Sny08, Nol01]. In consequence repeated measurements of all thermoelectric quantities are indispensable for the material optimization process. Ideally one would have a measurement system which allows a fast, convenient and precise measurement of all thermoelectric quantities on one sample. This would allow a fast assessment of the quality of the material under test and thus a rapidly converging optimization process.

However, studying the literature, the situation is rather opposite. There exist various measurement methods for each of the three components that usually require different sample preparation and measurement setups [Cah87, Cah04, Par61, vdP58a, Völ90]. There are also several reports of combinations of σ and S measurements [Sin09, Bof05, Bur01, Zho05], or S and κ measurements [Yan02, Zha10]. Furthermore, a direct ZT measurement [Har58, Har59] can also be combined with a σ or S measurement [Iwa05, Kob08].

Nevertheless, a convenient all-in-one solution that does not require a special geometry is still missing. In this chapter we will present a concept for a complete thermoelectric characterization as well as a successful experimental realization. This novel method permits the measurement of σ, S, κ, and ZT concurrently on the same sample using the same setup. It is therefore a powerful tool in the pursuit of superior thermoelectric materials. The method is based on a standard method for electrical characterization which was invented in 1958 by L. J. van der Pauw [vdP58a], which therefore will be explained first. Afterwards it will be discussed how this concept can be transferred to a thermal conductivity measurement. Combining electrical and thermal measurements the Seebeck coefficient S can be obtained so that ZT can be calculated. The method will be introduced using the data of measurements on Ni as example. Then, measurements on InSb, a better thermoelectric material, will be presented. Here furthermore a direct determination measurement of ZT by means of a four-point Harman measurement will be introduced. This complements the measurements of σ, κ, and S and can be used to cross-check the experimental data.

L. J. van der Pauw showed that the electrical conductivity of a sample can be determined by two simple four-point resistance measurements. These two measurement configurations are shown in Figure 3.3.

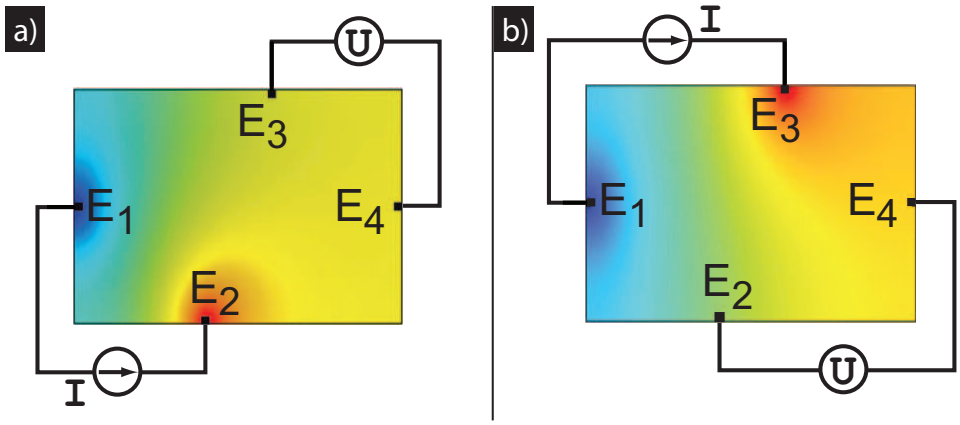

Figure 3.3: Electrical van der Pauw measurement. The sample is equipped with four electrical contacts E_1-E_4. The color coding represents the electrical potential: the potential decreases from red to blue. a): Current is driven from $E_2 \rightarrow E_1$, the voltage is measured between E_4 and E_3, and $R_{21,43} = U_{43}/I_{21}$ can be calculated. b): Current from $E_3 \rightarrow E_1$ and measurement of $R_{31,42} = U_{42}/I_{31}$.

In the first configuration a current I_{21} is driven from contact E_2 to E_1. Between the other two contacts the voltage U_{43} is measured. This gives the first resistance $R^{AC}_{21,43} = U_{43}/I_{21}$. In order to avoid the build up of a thermoelectric voltage alternating current has to be used for conductivity measurements of thermoelectric samples [Har59, Nol01]. Then, the function of the leads is changed such that a second resistance, $R^{AC}_{31,42} = U_{42}/I_{31}$, is obtained by driving a current from E_3 to E_1 and measuring the voltage between E_4 and E_2. Provided that the thickness d of the sample is known, σ can then be obtained by solving the van der Pauw equation:

$$\exp(-\pi\sigma\, d\, R_{21,43}) + \exp(-\pi\sigma\, d\, R_{31,42}) = 1\ . \tag{3.2}$$

For this equation to be valid, several conditions have to be met: the sample has to be thin, homogeneous, without holes, and the current flow from source to sink has to be two-dimensional; finally infinitesimal small contacts have to be located at the edge of the sample [vdP58a]. These conditions can be met experimentally only approximatively. However, the van der Pauw method is robust with respect to these requirements. A quantitative analysis shows that the effect of contact size and sample thickness can be kept below 2% easily, see the error analysis in Section 3.4. The van der Pauw method is a four point measurement and therefore insensitive to electrical contact resistances. In contrast to the linear four point method [Sch06] the van der Pauw method has neither requirements on sample shape (except uniform thickness) nor on contact positioning.

After introducing the electrical van der Pauw measurement technique we will now turn to the similarity between electrical and thermal physics to extend the

concept of van der Pauw to thermal measurement techniques. As explained in the following, there is a fundamental analogy between the principles of electrical and thermal physics. The electrostatic potential ϕ obeys the Laplace equation $\triangle\phi = 0$ in a material without free charges; $\triangle$ is the Laplace operator. The electrostatic potential gives rise to an electrical current density j_{el} that is related to the electrostatic potential by $j_{\mathrm{el}} = -\sigma\nabla\phi$ where the factor of proportionality σ is the electrical conductivity. The governing equations are analogous in a static thermal physics situation in the absence of heat sinks or sources: the temperature T obeys a Laplace equation $\triangle T = 0$. A temperature gradient gives rise to a heat flux $j_{\mathrm{therm}} = q$ and the constant of proportionality between temperature gradient and heat flux is the thermal conductivity κ: $q = -\kappa\nabla T$. The measurement quantities in an electrical van der Pauw measurement are voltage or potential difference U, current $I = jA$ and resistance $R = U/I$. These macroscopic quantities also have their thermal equivalents: temperature difference ΔT, heat flow $P = qA$ and thermal resistance $R^{\mathrm{therm}} = \Delta T/P$. Table 3.2 summarizes analogue electrical and thermal quantities.

variable	electrical	thermal
potential	ϕ	T
potential difference	U	ΔT
current density	j_{el}	q
current	I	P
resistance	$R = U/I$	$R^{\mathrm{th}} = \Delta T/P$
conductivity	σ	κ

Table 3.1: Comparison of basic quantities in electrical and thermal physics

Due to the analogy the electrical van der Pauw measurement concept can be transferred to thermal conductivity measurements. To do so the sample has to be equipped with a heater and a heat sink as well as two thermometers. Then a heat flow P can be created and a temperature difference ΔT measured. If this is done in two configurations (analogues to Figure 3.3) two thermal resistances $R^{\mathrm{th}}_{21,43} = \Delta T_{43}/P_{21}$ and $R^{\mathrm{th}}_{31,42} = \Delta T_{42}/P_{31}$ are determined and κ can be calculated from

$$\exp(-\pi\kappa\, d\, R^{th}_{21,43}) + \exp(-\pi\kappa\, d\, R^{th}_{31,42}) = 1\,, \tag{3.3}$$

which is the thermal equivalent to the electrical van der Pauw equation [Pau99]. In comparison to the electrical measurement two additional things have to be considered for a practical realization. Firstly, the van der Pauw method requires perfect insulation of the sample except for the sink. While electrical insulation is easily accomplished, the sample can lose heat e.g. by conduction to the environment, by convection and by radiation. These heat loss mechanisms can not be prevented completely but extenuated to an acceptable level, as will be shown in Section 3.4. Convection and conduction to the environment can be easily minimized by suspending the sample (leaving one thermal contact as heat sink) and performing the

measurements at high vacuum $p < 10^{-5}$ mbar. The second point is that one of the thermometers in the first configuration has to act as heat source in the second measurement configuration, i.e. its function has to be exchangeable. We equipped the sample with three resistive heaters that can be used as thermometers as well as heat source. A drawing and a photograph of the sample, the connections and the heat sink is shown in in Figure 3.4.

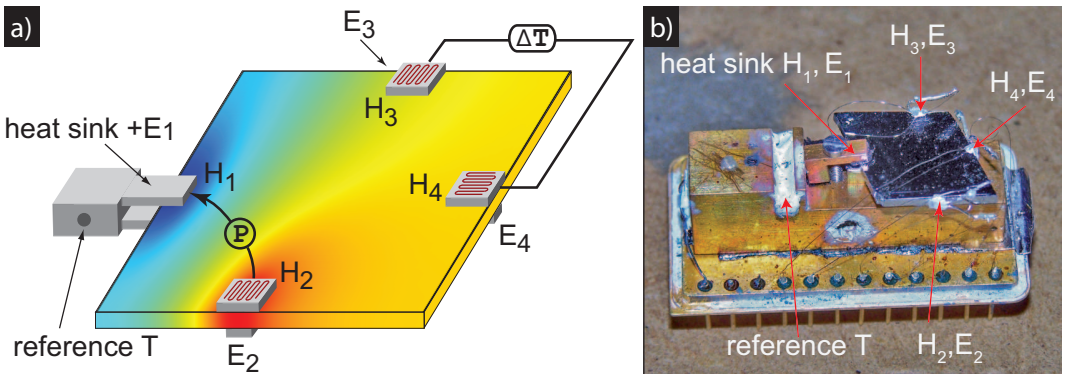

Figure 3.4: Drawing and photograph of a sample prepared for a thermoelectric van der Pauw measurement. The sample is equipped with four electrical contacts E_1-E_4 and three resistive heaters H_2-H_4; it is thermally connected to the heat sink H_1. The heat sink itself contains a heater and a reference thermometer and is used to control the sample temperature. The heater H_2 creates a heat flow P_{21} from $H_2 \rightarrow H_1$ and thus a temperature gradient within the sample as indicated by the color coding (red $\rightarrow$ hot, blue $\rightarrow$ cold). The heaters H_3 and H_4 are used as thermometers and measure the temperature difference ΔT_{43}. From these values $R^{\text{th}}_{21,43} = \Delta T_{43}/P_{21}$ can be calculated. Performing a second measurement with H_3 used as heater $R^{\text{th}}_{31,42} = \Delta T_{42}/P_{31}$ can be deduced and κ can be calculated from Eq. (3.3). The four electrical contacts are used to determine σ by an electrical van der Pauw measurement. They can furthermore be used to measure S, and thus ZT can be calculated from Eq. (3.1). Additionally, the figure of merit ZT can also be measured directly by means of a four-point Harman method. Image taken from [dB10c] and modified.

The heat sink is equipped with a separate heater and reference thermometer that are connected to the Lakeshore temperature controller which allows adjusting the temperature of the heat sink and thus the sample. Three resistive heaters (Pt1000) are glued onto the sample with a thermally conductive glue (Cerambond). They are electrically insulated from the sample but electrically connected to the pins of the sample holder, similar to Figure 3.1b). In order to perform precise resistance or electrical power measurements all heaters/thermometers are connected in a four point manner, two to the digital multimeter, which measured resistances and the third to current source and nanovoltmeter, measuring electrical power $P = U \cdot I$. To evaluate Eq. (3.3) the measured resistances have to be converted into temperatures,

which is done by means of a resistance-temperature calibration.

The heater creates a heat flow $P = UI$, where I is here the current supplied to the heater and U the voltage drop. From the measured resistances of the two thermometers ΔT can be deduced and R^{th} be calculated. Usually, R^{th} measurements were performed for several heating current values, i.e. different heater powers. By doing so, one can to check for errors and an average of the obtained R^{th} values can be used. The resistance-temperature calibration is performed with respect to the reference thermometer within the heat sink (see Figure 3.1b) for zero heating current and was included into the measurement routine. Figure 3.5a) shows a resistance-temperature calibration and b) the measured R^{th} for different heating current values. It can be seen that the two calibration curves are very similar and approximately

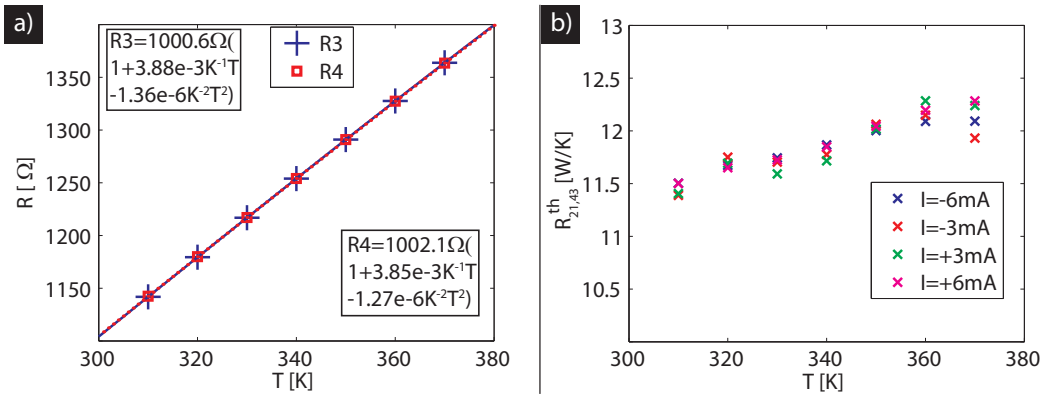

Figure 3.5: a): Resistance-temperature calibration of two Pt1000 on a Ni sample. $R3$ and $R4$ are the resistances of H_3 and H_4, respectively. The coefficients of the resistance-temperature fit are shown as insets and compare well with the expected values for a Pt1000. b): Thermal resistance $R^{\mathrm{th}}_{21,43} = \Delta T_{43}/P_{21}$ for different temperatures and heater current values. The values show only little scattering and no unexpected systematic current dependence. For latter analysis the mean values are taken.

linear. The expected resistance-temperature relation for a Pt1000 is [wik10b]

$$R(T) = 1000\,\Omega(1 + 3.91 \cdot 10^{-3}/KT - 5.775 \cdot 10^{-7}/K^{-2}T^2)\,, \tag{3.4}$$

$$R(T) = 1000\,\Omega(1 + 3.85 \cdot 10^{-3}/KT) \quad \text{for} \quad 0\,^{\circ}\mathrm{C} < T < 100\,^{\circ}\mathrm{C} \tag{3.5}$$

where the temperature T is given in °C and the second relation is the linear approximation for the temperature regime around room temperature. The agreement between the measured and the expected fit coefficients is excellent for the linear resistance coefficients and moderate for the less important quadratic coefficients. With the obtained fit the measured electrical resistances can be converted into temperatures and the thermal resistances can be calculated. These are shown in Figure 3.5b) for four different currents as a function of heat sink temperature. The values

of $R^{\mathrm{th}}_{21,43}$ show no systematic dependence on the heating current level (which would indicate a flawed measurement) and the deviation of the individual values from their mean value is $< 2\%$.

The data shown was obtained from a Ni sample (purity 99.98%, sample size $20 \times 10 \times 0.25\,\mathrm{mm}$). Ni is no applicable thermoelectric material but is often used as reference material for electrical characterization, since it can be obtained at a high purity and has well-defined and reproducible properties [Bof05]. Furthermore, it has a relatively large Seebeck coefficient for a metal and a non-vanishing ZT.

After the first temperature dependent R^{th} measurement a second measurement was taken were H_3 was used as heater and H_2 and H_4 as thermometers. With the two obtained R^{th} data sets the thermal conductivity can be calculated using Eq. (3.3). The results are presented in Figure 3.6a) together with reference data from several sources [Bae69, Bin86, Pow65].

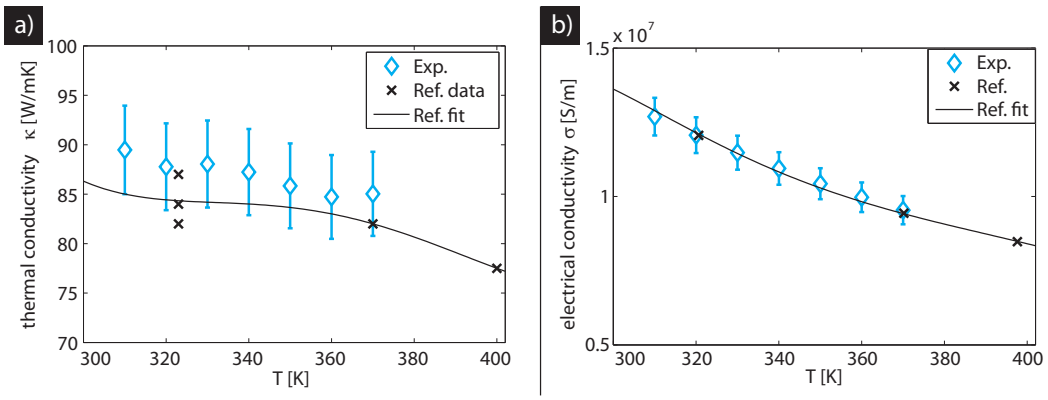

Figure 3.6: a) Measured thermal conductivity of Ni in comparison with reference data from several sources [Bae69, Bin86, Pow65]. The error bars are $\approx 6\%$ and within those errorbars the measured values agree to a polynomial fit through the reference data. b) Temperature dependent electrical conductivity of Ni. The agreement between measured and reference data [Bur01] is excellent, error bars are 4%; their calculation is discussed in Section 3.4.

In addition to the three heaters, the sample is also equipped with four electrical contacts. These can be used to determine the electrical conductivity σ, see Figure 3.3 and Eq. (3.2). The result is shown in Figure 3.6b) and shows excellent agreement with reference data [Bur01].

For the σ and κ measurement the electrical contacts and the resistive heaters can be placed at any position of the sample edge. However, if the electrical contacts are placed at the same lateral position as the heaters, the Seebeck coefficient $S = -U/\Delta T$ can be measured in combination with κ: in the configuration were H_2 is used as heater ΔT_{43} is recorded for the κ measurement. Using the electrical contacts,

U_{43} is recorded simultaneously and S can be calculated from

$$S = -\frac{U_{43}}{\Delta T_{43}}\,. \tag{3.6}$$

The voltage U_{43} is a pure Seebeck voltage, since no electrical current is driven through the sample. For the measurement to be accurate, the temperatures where voltages and temperatures are recorded have to be identical. This can practically be realized if the electrical contact is placed between heater and sample or exactly opposite to it, as shown in Figure 3.4. The latter requires two-dimensional current flow, but this is anyway a prerequisite for the validity of the van der Pauw method. In the second measurement configuration S can be determined from $S = -U_{42}/\Delta T_{42}$, thus two independent measurement can be taken. During the measurements it was observed, that small voltages could be measured even for no applied heat current. These stem from temperature gradients within the sample or within the wiring from the sample to the instruments. It is therefore common practice to determine S rather from $-\partial U/\partial \Delta T$ than from a single value [Bof05, Row06]. A linear fit of U vs. ΔT yields a more accurate value of S and is shown in Figure 3.7a). One has to be aware that the measured S_{meas} is not the Seebeck coefficient of Ni, but the differential Seebeck coefficient of sample and wire material :$S_{\mathrm{meas}} = S_{\mathrm{Ni}} - S_{\mathrm{wi}}$, see Chapter 1 and [Nol01, Row06]. We used Cu wiring for the measurement of the Ni sample, which has a small positive Seebeck coefficient around $2\,\mu\mathrm{VK}^{-1}$ at room temperature. Using a polynomial fit through Cu reference data [Cus58], the measured values were corrected for the wire contribution and S_{Ni} was obtained. The results of the two independent measurements, their mean, and reference data is presented in Figure 3.7b).

From the measured σ, κ, and S the figure of merit can be calculated from Eq. (3.1). The result is shown in Figure 3.8. The "reference ZT" was obtained from the polynomial fits to the reference data shown in Figures 3.6a) and b), and 3.7. The error bars shown correspond to the sum of the relative errors of the individual measurements, which were 4% for σ, 6% for κ, and 10% for the measurement of S. Since ZT depends quadratically on S, the relative error of the Seebeck coefficient measurements adds twice to the relative error. A thorough error analysis is presented in Section 3.4.

Thermoelectric characterization of InSb We now want to prove the applicability of the measurement method to a better thermoelectric material. Bulk InSb has decent thermoelectric properties with $ZT \approx 0.4$ at $T = 700\,\mathrm{K}$ [Bow59], while $ZT > 5$ has been calculated for InSb nanowires [Min04]. We used a basically intrinsic InSb sample with very low Te doping and a size of $10 \times 10 \times 0.5\,\mathrm{mm}$. The charge carrier concentration of the InSb wafer was specified as $1 - 1.5 \times 10^{15}\mathrm{cm}^{-3}$ (at 77 K) by the supplier (Firebird Inc. Canada). This corresponds to about $\approx 3 \times 10^{17}\mathrm{cm}^{-3}$ at room temperature [Osz88]. The results for the complete thermoelectric characterization

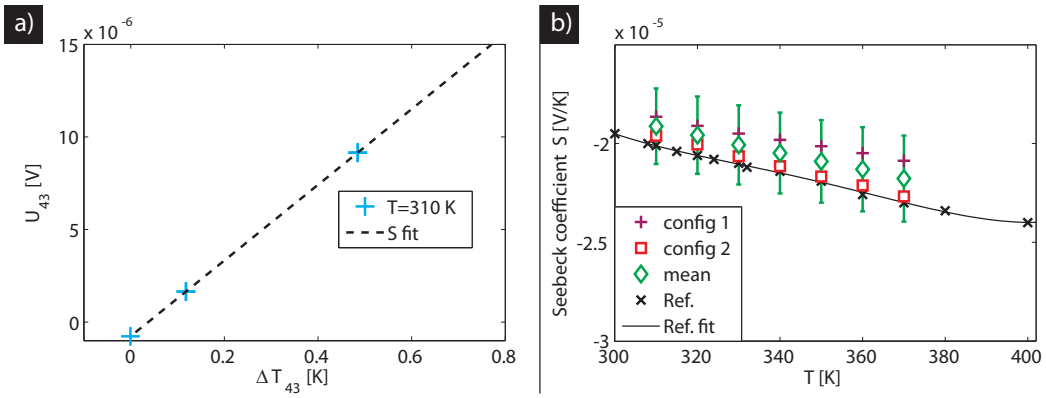

Figure 3.7: a): Measured Seebeck voltage vs. temperature difference for a measurement at $T = 310\,\mathrm{K}$. The Seebeck coefficient is obtained from the fitted slope. b):Temperature dependent Seebeck coefficient of Ni. Shown are the results of the two van der Pauw measurement configurations, their mean values as well as reference data [Bur01]. The agreement between the two independent measurements and the reference data is better than 10%; the error bars correspond to a relative error of 10% and are discussed in Section 3.4.

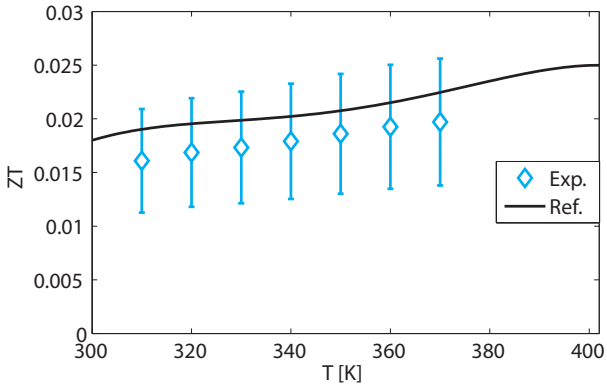

Figure 3.8: Thermoelectric figure of merit of Ni. ZT was calculated from the experimental data and the fits to reference data shown in Figures 3.6a) and b), and 3.7. The error bars correspond to 30% and the agreement between the reference ZT and the ZT calculated from the measured values is good.

are shown in Figure 3.9 together with reference data [Bus61].

In Figure 3.9a) the measured electrical conductivity is plotted together with literature data for intrinsic InSb [Bus61]. The electrical conductivity of a semiconductor strongly depends on the specific impurity concentration, this is particularly true for a high mobility material such as InSb. For the reference data an impurity concentration of $10^{15} - 10^{16}\,\mathrm{cm}^{-3}$ at 90 K is stated, which is comparable, but not identical

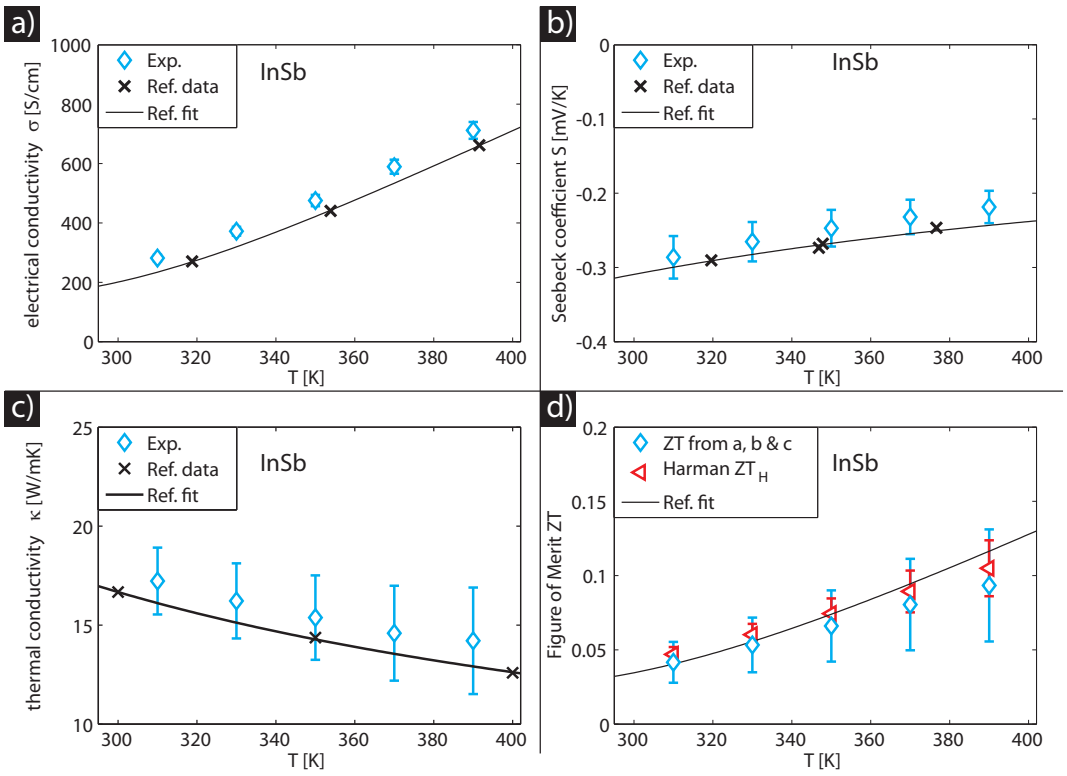

Figure 3.9: Complete thermoelectric characterization of an intrinsic InSb sample. a): Electrical conductivity, error bars 4%. b): Mean Seebeck coefficient, error bars 10%. c) Thermal conductivity, error bars increase with temperature from 13% to 20%. Subfigure d) shows the ZT calculated from the measurement data (blue), the ZT calculated from the reference data (black) and the directly measured ZT_H. ZT_H was measured by means of a four-point Harman method, as explained in the text. The error bars for the combined ZT increase with temperature from 33% to 40% and from 11% to 18% for the directly measured ZT_H. All three ZT values show good agreement. Figure taken from [dB10c] and modified, reference data from [Bus61].

to our sample. For this reason some variations can be expected between different "intrinsic" samples. Here, the conductivity of our sample is somewhat larger than the literature data, but both measured and reference conductivity increase with temperature, as is expected for a small band gap material. The Seebeck coefficient displayed in 3.9b) is the mean of the two independent measurements in the two van der Pauw configurations and has been corrected for the contribution of the Ni wires. The Seebeck coefficient is negative as expected from the n-doping and its absolute value decreases with increasing temperature; the agreement between reference and measured S is within 10%. The thermal conductivity deviates from the reference data by less than 10% as well. In Figure 3.9d) finally, the results for the figure of merit calculated from the reference data and from the measured data presented in

a)- c) are shown in black and blue, respectively. The relative error of the combined ZT is the sum of the relative errors of σ, κ, and S (twofold). For the InSb sample the relative error increases with T from 33% to 40%. This may appear to be a large error, however, it is the sum of three individual measurements and therefore typical for thermoelectric measurements [Sny08]. Nevertheless, the reference and the measured ZT show good agreement, especially for lower T.

Direct measurement of ZT One way to obtain ZT with better accuracy is to directly measure it. In 1959 Harman showed that ZT can be measured directly by simple AC/DC measurements [Har58, Har59, Iwa05]

$$ZT_H = \frac{U_S}{U_\Omega} = \frac{U_{DC} - U_{AC}}{U_{AC}} \,. \tag{3.7}$$

The result of the Harman characterization is labeled ZT_H in the following to distinguish it from the combined ZT. In Eq. (3.7) U_S is the voltage that is caused by the Seebeck effect and U_Ω the ohmic voltage. The equation can be understood as follows: if a current flows from one end of a sample to the other, a potential difference develops between the two ends due to the ohmic resistance of the material, i.e. $U_\Omega = IR = I\rho l/A$, if we assume a linear sample with cross section A and length l here. In a thermoelectric material Peltier heat $P_{\mathrm{Pel}} = IST$ is created at one end of the sample and consumed at the other upon current flow. The Peltier effect creates a heat gradient within the sample and is balanced in steady state by normal heat flow through the sample from hot to cold side. The temperature difference between hot and cold side is given by $\Delta T = P_{\mathrm{Pel}} l/(\kappa A)$. The developed temperature difference causes a potential difference due to the Seebeck effect in addition to the ohmic potential drop. The magnitude of the developed Seebeck voltage is $U_S = \Delta T S$. Combining the last equations yields

$$\frac{U_S}{U_\Omega} = \frac{\Delta T S}{I\rho l/A} = \frac{P_{\mathrm{Pel}} S}{\kappa} \frac{\sigma}{I} = \frac{IST S}{\kappa} \frac{\sigma}{I} = \frac{\sigma S^2 T}{\kappa} \,, \tag{3.8}$$

which is the definition of ZT, see Eq. (3.1). The initial assumption of a sample with linear geometry is not necessary since the geometrical factors cancel. Eq. (3.7) thus holds for samples of arbitrary shape. The second part of Eq. (3.7) uses the fact that the build up time of ohmic and Seebeck voltage differs by orders of magnitude. While the ohmic voltages arises quasi instantaneously (the dielectric relaxation time is $\approx RC$ [Ven01]), the Seebeck voltage has a time constant in the order of seconds, at least for macroscopic samples[1]. If one applies a direct current, one therefore detects $U_\Omega + U_S$, while an AC measurement detects only U_Ω, provided the frequency is high enough.

This measurement technique is known as Harman measurement and was per-

[1] See Subsection 3.4.7 and Eq. (3.45) for a derivation.

formed for the InSb sample in a four-point fashion using the electrical contacts E_1 to E_4, see Figure 3.4. For the measurement of σ, $R^{AC}_{21,43} = U_{43}/I_{21}$ and $R^{AC}_{31,42} = U_{42}/I_{31}$ are determined. By simply measuring these resistances with a direct current as well, ZT_H can be determined directly from

$$ZT_H = \frac{U_{DC} - U_{AC}}{U_{AC}} = \frac{R^{DC}_{21,43} - R^{AC}_{21,43}}{R^{AC}_{21,43}} = \frac{R^{DC}_{31,42} - R^{AC}_{31,42}}{R^{AC}_{31,42}} \,. \tag{3.9}$$

Again, two independent measurements are possible. In Figure 3.9d) the average of both measurements is shown as red diamonds. Similar to the Seebeck measurement the ZT_H measurement has to be corrected for the effect of the wires. The as-measured figure of merit $ZT_{\mathrm{H,meas}}$ is obtained experimentally from

$$ZT_{\mathrm{H,meas}} = \frac{U^S_{\mathrm{sample,wire}}}{U^\Omega_{\mathrm{sample}}} = \frac{U^S_{\mathrm{sample}} - U^S_{\mathrm{wire}}}{U^\Omega_{\mathrm{sample}}} \,, \tag{3.10}$$

while the true figure of merit of the sample $ZT_{\mathrm{H,sample}}$ is given by

$$ZT_{\mathrm{H,sample}} = \frac{U^S_{\mathrm{sample}}}{U^\Omega_{\mathrm{sample}}} \,. \tag{3.11}$$

Combining both equations one obtains

$$ZT_{\mathrm{H,sample}} = ZT_{\mathrm{H,meas}} \frac{U^S_{\mathrm{sample}}}{U^S_{\mathrm{sample}} - U^S_{\mathrm{wire}}} = ZT_{\mathrm{H,meas}} \frac{S_{\mathrm{sample}}}{S_{\mathrm{sample}} - S_{\mathrm{wire}}} \,. \tag{3.12}$$

Consequently the shown ZT_H measurements of InSb (Figure 3.9d)) have been multiplied by $S_{\mathrm{InSb}}/(S_{\mathrm{InSb}} - S_{\mathrm{Ni}})$ to correct for the effect of the Ni wires. In order to calculate the correction factor, the Seebeck coefficient of Ni [Bur01] and the measured Seebeck coefficient of InSb were used. The correction factor depends on temperature and varies between 1.08 (310K) and 1.12 (390K). It can be seen that the ZT obtained from measurement of the individual quantities (blue) agrees well with the Harman ZT_H and that both show good compliance with the reference data.

Combined ZT vs. Harman ZT_H The measurement of ZT_H requires only four electrical contacts and is faster than the determination of the combined ZT. Furthermore, the relative error of ZT_H is smaller than the relative error of the combined ZT, as discussed in Section 3.4 and shown in Figure 3.9. Since the efficiency of a thermoelectric generator/cooler directly depends on ZT the question arises, why one should bother with the more time-consuming thermoelectric van der Pauw measurement. If one is really only interested in a single ZT value, the Harman measurement is indeed the more attractive alternative. However, the more typical situation is that a thermoelectric material is characterized for further optimization. Knowing only ZT does give no hint which of the three basic physical quantities needs further

attention. Furthermore σ, S, and κ are coupled to other material parameters like charge carrier concentration and effective mass as well as phonon mean free paths, see Chapter 1. For a deeper understanding and hence an efficient optimization process, knowledge of σ, S, and κ is indispensable and a single Harman ZT_H measurement insufficient. For most cases it is therefore a quick and useful complement to the thermoelectric van der Pauw measurement, not a replacement.

3.2.1 Summary

In summary, the presented thermoelectric van der Pauw measurement allows (i) a four-point measurement of electrical and thermal conductivity, (ii) two independent measurements of the Seebeck coefficient in a four-point geometry, and (iii) two direct measurement of the thermoelectric figure of merit ZT_H by means of a four-point Harman measurement.

It has several advantages compared to other measurement techniques. The most important one is that by the newly presented method σ, S, and κ can be determined concurrently on a single sample; thereby permitting a complete thermoelectric characterization. Compared to the situation where individual quantities have to be measured in different setups this saves preparation and measurement time and can also decrease experimental errors.

The second gain is a consequent realization of four-point measurements. This renders the method insensitive to thermal and electrical contact resistances which are often troublesome in thermoelectric measurements, see e.g. [Ven01].

Very advantageous is furthermore that it offers several possibilities to cross-check the obtained experimental data. Firstly one can compare the ZT calculated from the measurement of the individual quantities with the directly measured Harman ZT_H, which of course should be identical within the measurement accuracy. Secondly, one can perform two independent measurements of S and ZT_H, observed discrepancies indicate experimental errors as well. One can thirdly check whether $R^{AC}_{21,43}/R^{AC}_{31,42}$ equates $R^{th}_{21,43}/R^{th}_{31,42}$ throughout the measurements. Since the ratio of the resistances stems only from sample geometry and contact arrangement, it should be identical for thermal and electrical conductivity measurements. Consistency in all these points does not prevent inaccurate measurements, but inconsistencies indicate experimental errors undeniably and quickly.

A nice plus of the method is that it works for arbitrary sample geometries and contact arrangements; the only restriction is a uniform thickness. Since not all thermoelectric materials are easily sliceable/breakable this is an advantage.

Very important from a practical point of view is furthermore that the method requires very little sample preparation. In fact, merely three electrical contacts and three resistive heaters have to be attached to the sample, this can be done with silver paste and thermally conductive paste. Compare this e.g. to the 3ω method, where preparation requires lithographic pre-patterning, see Chapter 4.3. Moreover, the employed system does not require any sophisticated electronics and is easy to

realize. Merely a current source, several voltmeters and a vacuum chamber are needed.

The measurement method has many distinct advantages compared to state-of-the-art techniques. Nevertheless, there are some restrictions which shall not be concealed. The method is a steady-state method. If heat sink temperature or heating power are changed, the system needs to equilibrate before measurements are performed. This usually takes several minutes and is thus slower than e.g. the flash method for thermal conductivity measurements [Par61]. Since it is a steady-state method and the samples furthermore have a relatively large surface/volume ratio, measurement of κ and ZT is more severely affected by radiation losses than e.g. the thermal conductivity measurement with the 3ω -method [Cah87]. Strategies to minimize this effect are presented in Section 3.5. A further restriction is that the method is an in-plane characterization technique. For anisotropic samples two measurements on differently cut samples are necessary.

Before focusing on the errors of the thermoelectric van der Pauw method we want to present a modified measurement approach, that allows for an even faster complete thermoelectric characterization.

3.3 Two-heater thermoelectric van der Pauw measurements

In this section a modification of the thermoelectric van der Pauw measurement presented in Section 3.2 will be introduced. Consider a sample as shown in Figure 3.4, but equipped only with the heaters/thermometers H_2 and H_3. The measurement described in the following will be referred to as two-heater thermoelectric van der Pauw measurement, in contrast to the three-heater van der Pauw measurement that was introduced earlier. The σ and ZT measurement are performed using the four electrical contacts E_1-E_4 as described before. For the third measurement first a heat flow from H_2 to H_1 is created and the Seebeck voltage $U_{S,43}$ is measured. Secondly a heat flow from H_3 to H_1 is created and $U_{S,42}$ is recorded. Using $R^{th} = \Delta T/P = -U_S/(SP)$ the thermal van der Pauw equation (3.3) can be rewritten as

$$\exp\left(+\pi d\,\frac{\kappa}{S}\frac{U_{S,43}}{P_{21}}\right) + \exp\left(+\pi d\,\frac{\kappa}{S}\frac{U_{S,42}}{P_{31}}\right) = 1\,, \tag{3.13}$$

whose solution yields the ratio κ/S. Since σ and ZT can be measured separately, κ and S can be determined from the definition of ZT (3.1) and so all thermoelectric quantities are again measured on a single sample. In order to avoid the effect of Seebeck voltage offsets $\partial U_S/\partial P$ rather than U_S/P should be used. This can be obtained by varying P, in analogy to what was presented in Figure 3.7.

For correctness, the effect of the Seebeck coefficient of the wires S_w has to be taken into account. Using the same notation as in the section about the three-

heater thermoelectric van der Pauw measurement (see Eq. (3.10) and Eq. (3.12)) the actually measured quantities are

$$ZT_{\mathrm{H,meas}} = ZT_{\mathrm{H,sample}} \frac{S_{\mathrm{sample}} - S_{\mathrm{wire}}}{S_{\mathrm{sample}}} = \frac{\sigma S_{\mathrm{sample}} T}{\frac{\kappa}{S_{\mathrm{sample}}}} \frac{S_{\mathrm{sample}} - S_{\mathrm{wire}}}{S_{\mathrm{sample}}}\,, \tag{3.14}$$

and

$$\left(\frac{\kappa}{S}\right)_{\mathrm{meas}} = \frac{\kappa}{S_{\mathrm{sample}}} \frac{S_{\mathrm{sample}}}{S_{\mathrm{sample}} - S_{\mathrm{wire}}}\,. \tag{3.15}$$

Combining both equations yields

$$ZT_{\mathrm{H,meas}} = \frac{\sigma S_{\mathrm{sample}} T}{\left(\frac{\kappa}{S}\right)_{\mathrm{meas}} \frac{S_{\mathrm{sample}} - S_{\mathrm{wire}}}{S_{\mathrm{sample}}}} \frac{S_{\mathrm{sample}} - S_{\mathrm{wire}}}{S_{\mathrm{sample}}} = \frac{\sigma S_{\mathrm{sample}} T}{\left(\frac{\kappa}{S}\right)_{\mathrm{meas}}}\,. \tag{3.16}$$

Now, S_{sample} can be calculated from the measured quantities $\left(\frac{\kappa}{S}\right)_{\mathrm{meas}}$ and $ZT_{\mathrm{H,meas}}$:

$$S_{\mathrm{sample}} = ZT_{\mathrm{H,meas}} \left(\frac{\kappa}{S}\right)_{\mathrm{meas}} \frac{1}{\sigma T}\,. \tag{3.17}$$

With S_{sample} known, the sample figure of merit is given by

$$ZT_{\mathrm{sample}} = ZT_{\mathrm{meas}} \frac{S_{\mathrm{sample}}}{S_{\mathrm{sample}} - S_{\mathrm{wire}}}\,, \tag{3.18}$$

and κ by

$$\kappa = \left(\frac{\kappa}{S}\right)_{\mathrm{meas}} \left(S_{\mathrm{sample}} - S_{\mathrm{wire}}\right). \tag{3.19}$$

In order to prove the feasibility of the two-heater thermoelectric van der Pauw method the measurement data of InSb (see Figure 3.9 for the three-heater measurement results) is reanalyzed. From the measured heating powers and Seebeck voltages $\partial U_S/\partial P$ is determined. $(\kappa/S)_{\mathrm{meas}}$ is obtained from Eq. (3.13) and from the result all thermoelectric quantities can be calculated as described. The results are shown in Figure 3.10. Subfigure a) shows $(\kappa/S)_{\mathrm{meas}}$ while b) shows the Seebeck coefficient obtained from Eq. (3.17) together with the result of the three-heater measurement and reference data [Bus61]. Both measurement results differ by $\approx 10\%$, but the two-heater result agrees better with the reference data, especially for higher temperatures. This is not true for the thermal conductivity results: the two-heater results is $\approx 15\%$ larger than the three-heater results and more than 20% larger than the reference data, the discrepancy furthermore increases with temperature.

Figure 3.10d) shows the two-heater Harman ZT_H calculated from Eq. (3.18), the three heater ZT calculated from measurement of the individual quantities, the Harman ZT_H from the three-heater measurement and the reference ZT. The raw data is the same for the two-heater and the three heater Harman ZT_H, however both are multipied with a correction factor that depends on the measured Seebeck sample coefficient, see Eq. (3.18) and Eq. (3.12). Since those values are slightly different for

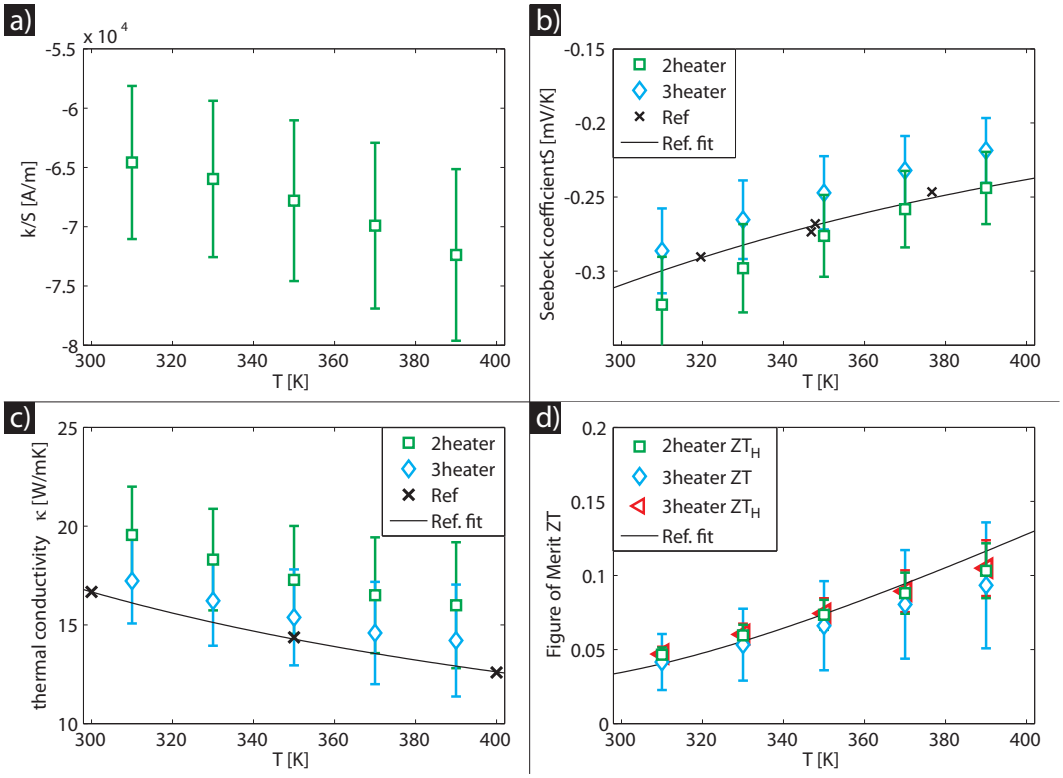

Figure 3.10: Complete thermoelectric characterization with the two-heater van der Pauw measurement. The same sample and measurement data as shown in Figure 3.9 were used. a): κ/S_{meas} as determined from Eq. (3.13). b) Seebeck coefficient calculated with Eq. (3.17) in comparison with the result from the three-heater measurement and reference data. The electrical conductivity data that was used for the calculation of S is shown in Figure 3.9a). The results agree within the error bars, which correspond to 10% relative error. c) Two-heater, three-heater, and reference thermal conductivity. The two-heater results are $\approx 20\%$ larger than the reference data, which is worse than the three-heater results. d) Calculated and measured figures of merit. Although obtained from the same measurement the two-heater ZT_H and the Harman ZT_H from the three heater measurement are not completely identical since the correction factors accounting for the effect of the Ni wires differ slightly. The agreement between the directly measured ZT_H, the three-heater ZT calculated from the measurement of σ, S, and κ and the reference ZT is fair and is better at lower temperatures. Reference data from [Bus61].

the two-heater and three-heater measurement, the ZT_Hs are close but not identical.

The details of the error calculation are presented in Appendix B.8. It is shown there that the S and κ determined by the two-heater method have basically the same errors as the results obtained with the three-heater method.

Compared to the three-heater thermoelectric van der Pauw measurement the two-heater measurement exhibits some disadvantages. One is that it is less robust

since only three independent measurements are taken (σ, ZT, and κ/S) while the three-heater variant allows four independent measurements (σ, ZT, S, and κ). It is furthermore only suitable for thermoelectric materials. If the material under investigation has a ZT too small to be determined accurately, its Seebeck coefficient and thermal conductivity can not be determined either.

On the other hand, it has several advantages: since only two heaters are required, the sample preparation is even faster than for the three-heater variant. One heater less also means four wires less through which heat can be lost. The second benefit is that the measurement does not require a resistance-temperature calibration. This is especially advantageous if quick measurements at only a single temperature are desired. With the two-heater measurement really only measurements at a single temperature are necessary, while with the three-heater method the calibration would require resistance measurements at several temperatures and would thus take longer. The necessity of a resistance temperature calibration furthermore requires to use heaters with a relative pronounced temperature dependence. For the two-heater measurement there is no such requirement.

In summary two-heater thermoelectric van der Pauw measurements also permit a complete characterization of thermoelectric materials. Compared to the three-heater measurement presented in Section 3.2 it offers faster measurement results and less sample preparation at the expense of the ability to cross-check the experimental results.

3.4 Error analysis for the thermoelectric van der Pauw measurements

So far we have presented the concept for a measurement technique and its successful realization, proven by the shown experimental data. Since physical data is only as good as the error related to it, it is now important to analyze the errors of the thermoelectric van der Pauw measurement method which was described in Section 3.2. The section starts with the main result: Table 3.4 lists the different errors and their significance. From this table the most important errors can be identified; these are discussed subsequently.

Most errors can be estimated by considering a square sample with symmetrically placed contacts/heaters/thermometers[2]. These results are supported or complemented by experimental findings or finite element simulations. For each of the quantities σ, κ, S, and ZT the effect of uncertainties in several experimental parameters is analyzed. In the third column the reference to the section that is dedicated to this error is given. In the forth and fifth column the relative errors for the Ni and InSb sample are given; for these samples the results were presented in Section 3.2.

[2]Comparing different sample geometries/contact arrangements it is found that a square sample with symmetric contact arrangement gives an upper limit for measurement errors. This is shown in Appendix B.1.

The errors are calculated for $T = 310\,\mathrm{K}$ and are usually not strongly temperature dependent. This does not hold for the effect of radiative heat losses which scale with T^3. Therefore here the relative errors are calculated for $T = 310\,\mathrm{K}$ and $T = 390\,\mathrm{K}$. The relative errors of σ, κ and S (twofold) are added up, except for the errors in σ and κ due to incorrect and finite thickness, which cancel. The sum then gives the relative error of the combined ZT from Eq. (1.6). Afterwards, the errors for the ZT_H obtained by means of the four-point Harman measurement are listed. Since this measurement was performed for InSb, but not for Ni, the errors are listed for InSb only. The direction of the error is indicated by the algebraic sign in the sixth column: "-" indicates that the quantity is measured too small due to the error while "+" indicates that it is measured too large. In the final column an evaluation of the importance of each of the errors is given. Naturally, this a subjective assessment. People interested in samples with a negligible emissivity will not consider radiation important, but the evaluation should hold for typical thermoelectric materials.

It can be seen that the systematic error due to radiative heat loss is the most severe one, this error affects the κ and the ZT_H measurement equally. Furthermore important is the error that arises due to imperfect placing of the electrical contacts with respect to the thermometers which influences the S measurement. Of some relevance are furthermore the effect of heat loss through the electrical wires between sample and sample holder and the result of a too low measurement frequency for the Harman ZT_H measurement.

For a quantification of the errors it is necessary to calculate the temperature profile of the sample under measurement conditions, i.e. with a temperature gradient that is caused by a heat flow from the heater to the heat sink. The mentioned errors will be discussed in the following, other points to consider like the effect of finite sample thickness, finite contact size, contact resistances or an incorrect calibration are dealt with in Appendix B.

3.4.1 Effect of heat losses

One requirement of the van der Pauw method is the insulation of the sample. While this does not constitute a problem for electrical measurements, good thermal insulation is hard to ensure. The effect of imperfect insulation can be seen qualitatively from the thermal van der Pauw equation (3.3) with symmetric contact arrangement:

$$\kappa = \frac{\ln 2}{\pi d R^{\mathrm{th}}} = \frac{\ln 2}{\pi d}\,\frac{P}{\Delta T}\,. \tag{3.20}$$

If a fraction of the heat is lost then the assumed heat flow P is larger than the actual one and the measured ΔT is smaller than it would be without heat loss; thus κ is determined too large.

There are three heat loss mechanisms: convection and conduction through the surrounding medium, conduction through the leads to the electrical contacts and resistance thermometers, and radiation. To avoid heat loss through the surrounding

quantity	error source	Section	Ni	InSb	sign	relevance
σ	fin. thickn. d	B.2	<-1%	<1%	–	low
σ	cont. size δ	B.2				low
σ	cont. displ. Δ	B.2	1.5%	1.5%	±	low
σ	thickn. err.	B.2	<1%	<1%	±	low
σ	$\sum \sigma$		<3.5%	<3.5%		
κ	fin. thickn. d	B.2	<1%	<1%	–	low
κ	cont. size δ	B.2				low
κ	cont. displ.	B.2	1.5%	1.5%	±	low
κ	thickn. err.	B.2	<1%	<1%	±	low
κ	heat loss wires	3.4.3	1.2%	1.3%	+	average
κ@310 K	radiation	3.4.4	0.5%	7.5%	+	high
κ@390 K	radiation	3.4.4	1.0%	15.0%	+	high
κ	wire self heat	B.3	<0.1%	<0.1%	+	low
κ	calibration	B.7	<0.1%	<0.1%	+	low
κ	$\sum \kappa$@310 K		<5.4%	<12.5%		
κ	$\sum \kappa$@390 K		<5.9%	<20.0%		
S	fin. thickn. d	B.2	<0.1%	<0.1%	–	low
S	cont. displ.	3.4.5	10%	10%	±	high
S	calibration	B.7	<0.1%	<0.1%	–	low
S	$\sum S$		10.2%	10.2%		
***ZT* comb.**	$\sum ZT$@310 K	3.4.6	**26%**	**33%**		
***ZT* comb.**	$\sum ZT$@390 K	3.4.6	**26%**	**40%**		
ZT_H	heat loss wires	3.4.3		1.3%	–	average
ZT_H@310 K	radiation	3.4.4		7.5%	–	high
ZT_H@390 K	radiation	3.4.4		15.0%	–	high
ZT_H	wire self heat	B.5		<0.1%	±	low
ZT_H	AC frequency	3.4.7		1.5%	–	average
$\boldsymbol{ZT_H}$	$\sum ZT_H$@310 K			**11%**	-	
$\boldsymbol{ZT_H}$	$\sum ZT_H$@390 K			**18%**	-	
T	heat flow P	B.6	1.3 K	1.5 K	+	low

Table 3.2: Error overview: This table lists the relative errors of the σ, S, κ, and ZT_H for the thermoelectric van der Pauw measurements.

medium the samples are suspended, with thermal/mechanical contact to the environment only at one position, which acts as heat sink. Convection and conduction through the surrounding gas can be decreased to a negligible level by performing the measurements in high vacuum [Sal09]. This is shown in Appendix A. In order to quantify the effects of radiation and conduction through the electrical connections the temperature profile of the sample has to be obtained.

3.4.2 Calculation of the sample temperature profile

In order to estimate heat loss by radiation and through the leads knowledge about the temperature profile of the sample is necessary. In general, the temperature profile is obtained by solving the stationary heat equation

$$\kappa \triangle T = P_{\text{loss}} \,, \tag{3.21}$$

where P_{loss} accounts for the various heat loss mechanisms. For the thermal conductivity, the Seebeck, and the ZT_H measurement it is necessary to have a temperature gradient across the sample. Since the amount of heat loss itself depends on the temperature and therefore varies spatially over the sample, the heat loss equation becomes a coupled integral-differential equation which can not easily be solved analytically in the general case. It could be solved numerically in analogy to approach presented by Weiss *et al.* [Weiss2008], however, the important points can be demonstrated clearer by finding an analytical solution to a simplified problem. Therefore the temperature profile will be calculated for $P_{\text{loss}} = 0$ and simplified boundary conditions (BCs). From the obtained idealized temperature profile heat loss through wires and by radiation as well as the effect of displaced contacts on the S will be quantified. It will also be shown that the chosen simple BCs are sufficiently correct.

Let us consider again a square sample with side length a, thickness d, and a semicircular heater with radius $\delta/2$ that is placed at $x = a/2,\ y = 0$ in the sample plain. Setting $P_{\text{loss}} = 0$ in Eq. (3.21) and disregarding the effect of the sample boundaries for the moment this is a problem with cylindrical symmetry and the steady state heat equation (3.21) becomes

$$\kappa \triangle T_H(r) = \partial_r (r \partial_r T_H) = 0 \,. \tag{3.22}$$

The BCs are as follows: Firstly, the amount of heat P produced in the heater flows uniformly from heater to sample, i.e. over a semi-cylinder with area $0.5\pi\delta d$:

$$\frac{-P}{\pi \delta d} = \kappa \partial T_H(r)|_{r=0.5\delta} \tag{3.23}$$

The heater itself shall have uniform temperature $T_{H,0}$ and the temperature profile should be steady, i.e. $T_H(0.5\delta) = T_{H,0}$; in this case the heat equation can be solved by simple integration. Inserting the BCs yields a logarithmic temperature profile

$$T_H(r) = T_{H,0} - \frac{P}{\pi \kappa d} \ln\left(\frac{r}{0.5\delta}\right) \,, \tag{3.24}$$

the slope of which increases with decreasing heater size and decreasing sample thickness at constant P. The above reasoning also holds for the case of a semi-cylindrical heat sink at $x = 0\ y = a/2$ with a heat "production" of $-P$. The temperature

profile of such a sample is

$$T_S(r') = T_{\mathrm{S},0} + \frac{P}{\pi\kappa d}\ln\left(\frac{r'}{0.5\delta}\right), \tag{3.25}$$

where $T_{\mathrm{S},0}$ is the heat sink temperature. The temperature profile of sample with heater and heat sink is given by a linear combination of source and sink profile

$$T = T_M + \frac{P}{\pi\kappa d}\left(\ln\left(\frac{r'}{0.5\delta}\right) - \ln\left(\frac{r}{0.5\delta}\right)\right) = T_M + \frac{P}{\pi\kappa d}\left(\ln\left(\frac{r'}{r}\right)\right), \tag{3.26}$$

where $T_M = (T_{\mathrm{H},0} + T_{\mathrm{S},0})/2$ is the average temperature of the sample. The experimental situation is such that $T_{\mathrm{S},0}$ (the heat sink temperature) is set, while T_M and $T_{\mathrm{H},0}$ depend on P. Setting

$$T(x = \delta/2, y = a/2) \stackrel{!}{=} T_{\mathrm{S},0} \tag{3.27}$$

and converting $r = \sqrt{(x-a/2)^2 + y^2}$ and $r' = \sqrt{x^2 + (y-a/2)^2}$ into Cartesian coordinates this yields

$$T_{\mathrm{S},0} = T_M + \frac{P}{\pi\kappa d}\ln\left(\frac{\sqrt{(\delta/2)^2 + (a/2-a/2)^2}}{\sqrt{(\delta/2-a/2)^2 + (a/2)^2}}\right) \tag{3.28}$$

$$= T_M + \frac{P}{\pi\kappa d}\ln\left(\frac{\delta}{\sqrt{2}a}\right) = T_M - \frac{P}{\pi\kappa d}\ln\left(\frac{\sqrt{2}a}{\delta}\right), \tag{3.29}$$

for $\delta \ll a$. Inserting this in Eq. (3.26) yields the temperature profile of the sample:

$$T(x,y) = T_{\mathrm{S},0} + \frac{P}{\pi\kappa d}\left[\ln\left(\frac{\sqrt{2}a}{\delta}\right) + \ln\left(\frac{\sqrt{x^2 + (y-a/2)^2}}{\sqrt{(x-a/2)^2 + y^2}}\right)\right]. \tag{3.30}$$

The temperature difference between heat sink and heat source is

$$T_{\mathrm{H},0} - T_{\mathrm{S},0} = 2(T_M - T_{\mathrm{S},0}) = \frac{2P}{\pi\kappa d}\ln\left(\frac{\sqrt{2}a}{\delta}\right), \tag{3.31}$$

and proportional to P and inversely proportional to κ as for a linear geometry. It is interesting to compare the temperature difference between heater and sink to the (measured) temperature difference between the two thermometers. If those are placed at T_3: $x = a/2$, $y = a$ and T_4: $x = a$, $y = a/2$ as shown in Figure 3.4, their difference is $T_4 - T_3 = P\ln 2/(\pi\kappa d)$ and the ratio of the two temperature differences is approximately

$$\frac{T_{\mathrm{H},0} - T_{\mathrm{S},0}}{T_4 - T_3} = \frac{\ln 2}{2\ln\left(\frac{\sqrt{2}a}{\delta}\right)} \approx 8, \tag{3.32}$$

for $\delta = 0.1a$. Thus, the measured temperature difference is roughly one order of magnitude smaller than the one between heater and sink.

For the derivation of Eq. (3.30) the effect of the sample edges has been neglected. If the sample is thermally insulated no heat flows across the sample edges and the isothermal lines are perpendicular to the sample edge. This can be included in the solution of the heat equation by choosing appropriate boundary conditions, however, this complicates solving of the heat equation and subsequent analysis. In Figure 3.11 exact and approximate solution of the problem are compared and it can be seen that the introduced deviations are small. a) and b) show the exact solution, while c) shows the temperature profile and isothermal lines according to Eq. (3.30). The numerical result was obtained with the finite-element-method program COMSOL[3], which computes temperature profiles by solving the heat equation numerically for the designed geometry. For the shown result, a fixed temperature was set for the sink contact, a heat flow for the heating contact and insulation at the sample edges. The isotherms are similar in both calculations.

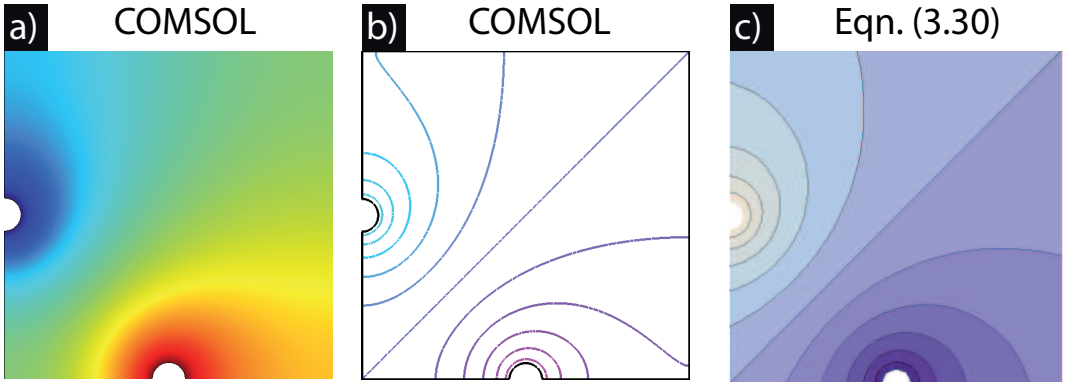

Figure 3.11: Temperature profile of a square sample with a semi-circular heat source and heat sink. a) Exact numerical solution obtained by the FEM program COMSOL. For the heat source a heat flow was set, for the heat sink a fixed temperature and for the rest of the sample insulating boundary conditions. b) Isotherm lines of the profile shown in a). c) Approximate solution from Eq. (3.30) with 11 isotherms as in b). The exact and the approximate temperature profile appear very similar as can be seen from the distribution and the shape of the isotherms. Small differences can be seen at the sample edges where the isothermal curves are not exactly perpendicular in c) as they are in b). However, the differences are minor and the temperature profile from Eq. (3.30) is found to be a good approximation.

[3]The basic operation mode of COMSOL is as follows: One defines the basic physics and underlying differential equations (here steady state heat transfer), implements the sample geometry and the relevant parameters (e.g. sample thermal conductivity) and sets the boundary conditions for the sample (e.g. heat flux in and out of the sample, insulated areas). The program splits the sample into a large number of cells and then calculates the resulting temperature profile by solving the heat equation simultaneously for a each cell. Although not a universal remedy it can help to visualize physical phenomena and give numerical solutions to a specific problem. Further information can be found under [COM11] and in the handbooks of the software.

3.4.3 Errors due to heat loss through the electrical connections

We can now estimate the heat that flows from the electrical contacts $E_2 - E_4$ and the heaters/thermometers $H_2 - H_4$ via the electrical wiring to the sample holder $P_{\mathrm{loss,w}}$. The heat loss through a single wire is given by

$$P_{\mathrm{loss,w}} = \Delta T \left(\frac{l_w}{\kappa_w n_w A_w} \right)^{-1} , \tag{3.33}$$

and depends on the temperature difference between the two ends; n_w, κ_w, l_w and A_w are number, thermal conductivity, length and cross sectional area of the wire. The sample holder ends of the wires are at heat sink temperature due to good thermal contact between heat sink and sample holder. The temperature of the wire ends at the sample depends on their position. Five wire ends are at heat source temperature T_2, five at the temperature of the thermometer T_4 and another five at the temperature of T_3. Assuming again a square sample with symmetrical contacts and using Eqs. (3.31) and (3.32) the ratio of heating power and loss through the wires becomes

$$\begin{aligned} \frac{P_{\mathrm{loss,w}}}{P} &= \frac{2\ln(\sqrt{2}a/\delta)\kappa_w n_{w2} A_w}{\pi\kappa d l_w} + \frac{(2\ln(\sqrt{2}a/\delta) + \ln 2)\kappa_w n_{w4} A_w}{2\pi\kappa d l_w} \\ &+ \frac{(2\ln(\sqrt{2}a/\delta) - \ln 2)\kappa_w n_{w3} A_w}{2\pi\kappa d l_w} \qquad (3.34) \\ &= \frac{2\ln(\sqrt{2}a/\delta)\kappa_w n_{w2} A_w}{\pi\kappa d l_w} + \frac{(\ln\sqrt{2}a/\delta)\kappa_w (n_{w4} + n_{w3}) A_w}{\pi\kappa d l_w} \qquad (3.35) \end{aligned}$$

For measurement of the Ni sample ($a \geq 1$cm, $\delta = 1.2$mm, $\kappa = 85$W/mK, $d = 0.25$mm) Cu wires ($l_w = 0.05\,\mathrm{m}$, $\kappa_w = 400\,\mathrm{Wm^{-1}K^{-1}}$, $A = \pi(25 \times 10^{-6}\,\mathrm{m})^2$) were used and thus $P_{\mathrm{loss,w}}/P = 1.2\% \ll 1$. For the InSb sample ($a = 1\,\mathrm{cm}$, $\delta = 1.2\,\mathrm{mm}$, $\kappa = 17\,\mathrm{Wm^{-1}K^{-1}}$, $d = 0.5\,\mathrm{mm}$) Ni wires ($l_w = 0.05\,\mathrm{m}$, $\kappa_w = 90\,\mathrm{Wm^{-1}K^{-1}}$, $A = \pi(35 \times 10^{-6}\,\mathrm{m})^2$) were used and the relative heat loss amounts to $\approx 1.3\%$. For the samples measured the heat lossed through the wiring is thus small compared to the created heat and will not affect the measurement severely. It can also be seen from Eq. (3.35), that heat loss can be diminished by using long and thin wires made from a material with low thermal conductivity.

3.4.4 Errors due to radiative heat loss

The last mechanism for heat loss is radiation. A body at temperature T, which is in thermal exchange with its environment at T_0, has a net power emission of [IV08]

$$P_{\mathrm{loss,rad}} = \epsilon\sigma_B A(T^4 - T_0^4) \approx 4\epsilon\sigma_B A T_0^3 (T - T_0)\,, \tag{3.36}$$

where ϵ is the sample emissivity, $\sigma_B = 5.67 \cdot 10^{-8}\,\mathrm{WK^{-4}}$ the Stefan-Boltzmann constant, and A the total surface area of the sample. The approximation ($T^4 -$

$T_0^4) \approx 4T_0^3(T - T_0)$ holds for $(T - T_0) \ll T_0$, which was fulfilled for the performed experiments. If the body has a spatially varying temperature Eq. (3.36) can easily be generalized to

$$P_{\text{loss,rad}} = 4\epsilon\sigma_B T^3 \int \mathrm{d}A(T(x,y) - T_0)\,. \tag{3.37}$$

However, the temperature profile of the considered samples is symmetrical (see Figure 3.11) and the integral can be further simplified to

$$P_{\text{loss,rad}} = 4\epsilon\sigma_B T_M^3 (T_M - T_0) \int \mathrm{d}A\,, \tag{3.38}$$

where T_M is the mean sample temperature from Eq. (3.31). Taking $A = 2a(a+d) \approx 2a^2$ as the surface area, the ratio of heating power and radiation loss is

$$P_{\text{loss,rad}}^{\text{rel}} = \frac{P_{\text{loss,rad}}}{P} = \frac{8a^2\epsilon\sigma_B T_0^3 \ln(\sqrt{2}a/\delta)}{\pi\kappa d}\,. \tag{3.39}$$

Using an emissivity of $\epsilon = 0.6$ [Lev98] for InSb, Eq. (3.39) yields $\approx 7.5\%$ at 310 K and $\approx 15\%$ at 390 K for the employed sample.

For polished Ni the radiative heat loss is less pronounced due to the higher material thermal conductivity and the lower emissivity, which is $\epsilon_{Ni} \leq 0.1$ [Emi10]. The relative power loss is thus $\approx 0.5\%$ at 310 K and $\approx 1\%$ at 390 K.

Eq. (3.39) yields the relative power loss for given sample properties and temperature. However, the measurement quantity used to determine κ is the measured temperature difference and it is not clear upfront how $P_{\text{loss,rad}}^{\text{rel}}$ relates to the change in temperature difference and hence the measurement error. Furthermore, Eq. (3.39) has been obtained for simplified BCs and so the accuracy has to be checked. We have therefore performed a simulation of the thermal conductivity measurement in COMSOL using the parameters of the InSb sample. The simulation has been performed with and without radiation losses and from the differences the validity of (3.39) can be tested.

For the simulation we defined a square sample with heater, sink and thermometers arranged as in Figure 3.4. Due to the symmetrical arrangement the apparent thermal conductivity of the sample can be obtained from the simplified version of the thermal van der Pauw equation (3.20). Using the InSb sample geometry, $T_{\text{S},0} = 310\,\text{K}$, and $P = 0.01\,\text{W}$ the following temperature difference is obtained between the thermometers $\Delta T = T(H_4) - T(H_3) = 311.827\,\text{K} - 311.569\,\text{K} = 0.258\,\text{K}$ without radiation losses. Inserting this temperature difference in Eq. (3.20) yields $\kappa = 17.1\,\text{Wm}^{-1}\text{K}^{-1}$, which is very close to $\kappa = 17.0\,\text{Wm}^{-1}\text{K}^{-1}$, which was used as input parameter the for simulation[4]. Now that we have shown that this 'virtual' measurement yields correct results the same analysis can be done taking into account radiation losses. Performing the same simulation but allowing radiation loss over the sample surface ($\epsilon = 0.6$) the "measured" temperature difference is

[4]Small differences can arise from finite size contacts and rounding errors.

$\Delta T = 311.577\,\mathrm{K} - 311.340\,\mathrm{K} = 0.234\,\mathrm{K}$. Now, the apparent thermal conductivity is $\kappa = 18.6\,\mathrm{Wm^{-1}K^{-1}}$, i.e. 9% larger than without radiation losses.

The effect of radiation losses can be calculated precisely with a finite-element simulation program like COMSOL. Thus, one could in principle quantify systematic errors by inserting the sample parameters in the simulation. On the other hand, the result for the measurement error of the numerical simulation is comparable to the more convenient analytical estimation given by Eq. (3.39), which will therefore be used to quantify radiation loss errors for κ and ZT_{H}.

3.4.5 Errors of the Seebeck measurement

The most severe error of the S measurement arises from imperfect placement of the electrical contacts with respect to the heaters/thermometers. Let us assume that the heater, heat sink, and the two thermometers are placed symmetrically at the center of the edges, as shown in Figure 3.4. Using Eq. (3.30) the temperature difference between the two thermometers (H_4, H_3)is given by ($x_4 = a$, $y_4 = 0.5a$, $x_3 = 0.5a$, $y_3 = a$)

$$\Delta T_{43} = \frac{P}{\pi\kappa d}\left[\ln\left(\frac{\sqrt{x_4^2 + (y_4 - a/2)^2}}{\sqrt{(x_4 - a/2)^2 + y_4^2}}\right) - \ln\left(\frac{\sqrt{x_3^2 + (y_3 - a/2)^2}}{\sqrt{(x_3 - a/2)^2 + y_3^2}}\right)\right]. \qquad (3.40)$$

If the electrical contacts are placed at the same positions as the thermometers they will sense the Seebeck voltage that corresponds to this temperature difference and S will be measured correctly. However, if one or both electrical contacts are misplaced, the measured Seebeck voltage does not correspond to the measured temperature difference. Using $a = 1\,\mathrm{cm}$ the correct $\Delta T_{43}^{\mathrm{id}}$ is

$$\Delta T_{43}^{\mathrm{id}} = \frac{P}{\pi\kappa d}(\ln 2) \approx \frac{P}{\pi\kappa d}(0.69)\,. \qquad (3.41)$$

If e.g. the electrical contact E_3 is misplaced by 1 mm in x and y with respect to H_3, i.e. $x_3 = 0.004$, $y_3 = 0.009$ the temperature difference is

$$\Delta T_{43}^{\mathrm{real}} \approx \frac{P}{\pi\kappa d}(0.817) \approx 1.18\Delta T_{43}^{\mathrm{id}}\,. \qquad (3.42)$$

It can be concluded, that careful positioning of the contacts is indispensable. One would notice displaced contacts from differences between the Seebeck measurements in the two measurement configurations. After characterizing $\approx$ 100 samples we found that the results of the two measurements differed typically by less than 10%, see e.g. Figure 3.7.

3.4.6 Error of the combined ZT

If ZT is calculated from Eq. (1.6), the relative error is the sum of the relative errors of σ, S, and κ, where the error of S counts twice.

$$\frac{\Delta ZT}{ZT} = \frac{\Delta\sigma}{\sigma} + 2\frac{\Delta S}{S} + \frac{\Delta\kappa}{\kappa}\,, \tag{3.43}$$

Note though, that the errors in σ and κ that are caused by the finite sample thickness and an incorrect thickness measurement do not add up but cancel, since they are the same for σ and κ. Adding up all discussed errors (except the mentioned two) this amounts to $\Delta ZT/ZT = 26\%$ for the Ni sample and $\Delta ZT/ZT = 33\%$ for the measured InSb sample at 310 K. This may appear large, but is actually very typical for thermoelectric measurements [Sny08].

3.4.7 Errors of the Harman ZT_H measurement.

Heat losses With the Harman-method, ZT_H is determined from the Seebeck voltage a sample develops if an electrical current is driven through it, see Eqs. (3.7) or (3.9). Since $ZT \propto U_S \propto \Delta T$, the ZT_H measurement is affected by heat losses through the wires and by radiation. Due to these losses the temperature difference will be reduced and ZT_H will be measured too small. The magnitude of the error is the same as for the κ measurement, see Subsections 3.4.3 and 3.4.4. In addition to the errors due to heat losses the Harman ZT_H is also measured incorrectly if the AC resistance measurement frequency is too small or if the DC measurement is taken before equilibrium is reached.

Measurement frequencies The (temporal) period of the AC resistance measurement has to be smaller than the build up time of the Seebeck voltage in order to distinguish ohmic and thermoelectric response. The build up of the Seebeck voltage is given by

$$U_S(t) = U_{S,\infty}(1 - \exp[-t/\tau^{\mathrm{th}}])\,, \tag{3.44}$$

where $U_{S,\infty}$ is the Seebeck voltage in steady-state and the time constant τ^{th} the thermal equivalent to the dielectric relaxation (RC) time constant: $\tau^{\mathrm{th}} = R^{\mathrm{th}}C^{\mathrm{th}}$. Using $R^{\mathrm{th}} = l/(\kappa A)$ and rewriting the thermal capacitance of the sample as $C^{\mathrm{th}} = c\rho V$, where c is the specific heat, ρ the density and V the volume of the sample, the thermal time constant is given by

$$\tau^{\mathrm{th}} = \frac{l^2 c\rho}{\kappa} = \frac{l^2}{D}\,, \tag{3.45}$$

where D is the thermal diffusivity. Inserting the numbers for the InSb sample gives

$$\tau^{\mathrm{th}}_{\mathrm{InSb}} \approx \frac{10^{-4}\,\mathrm{m}^2 200\,\mathrm{Jkg}^{-1}\mathrm{K}^{-1} 5800\,\mathrm{kgm}^{-3}}{17\,\mathrm{Wm}^{-1}\mathrm{K}^{-1}} \approx 6.8\,\mathrm{s}\,. \tag{3.46}$$

The measurement frequency was $\approx 10\,\mathrm{Hz}$ which means that $U_S^{\mathrm{InSb}}(0.1\,\mathrm{s}) \approx 0.015 \cdot U_{S,\infty}$. The AC resistance is measured too large, since it contains a fraction of the Seebeck voltage ΔU_S. The (incorrect) measured ZT_H is

$$ZT_H = \frac{U_{DC} - U_{AC}}{U_{AC}^{\mathrm{meas}}} = \frac{U_{DC} - (U_{AC}^{\mathrm{id}} + \Delta U_S)}{(U_{AC} + \Delta U_S)} = \frac{U_S - \Delta U_S}{(U_{AC} + \Delta U_S)} \approx \frac{U_S - \Delta U_S}{U_{AC}}\,; \tag{3.47}$$

i.e. for the InSb sample ZT was measured $\approx 1.5\%$ too small. This systematic error is acceptable, but could be further reduced using a higher measurement frequency.

A second type of error affects the DC measurement: if the measurement is taken before the Seebeck voltages reaches its steady-state value, U_{DC} is measured too small. In our experiments the DC measurement was taken after $35 - 45\,\mathrm{s}$. After $35\,\mathrm{s}$ the Seebeck voltage reaches $\approx 0.994 U_{S,\infty}$; the error for the DC measurement is therefore negligible.

Electrical contact resistances and wire heating For the Harman ZT measurement a current is driven through the sample and the electrical connections. If the Joule heat created due to wire or contact resistance is comparable to the Peltier heat, the temperature gradient across the sample and thus the measured ZT_H will be changed. Since the Joule heat scales with I^2 but the Peltier heat only with I, one can often observe an apparent dependence of ZT_H on the current. However, since the Peltier heat changes its sign upon current change while the Joule heat remains unaffected the correct ZT_H can be obtained by measurement of ZT_H in both current direction and averaging the corresponding values. A more detailed analysis and visualizing experimental data is presented in Appendix B.5.

3.4.8 Comparison of combined and Harman ZT

As discussed, the combined ZT from Eq. (3.1) includes the errors of the σ, S, and κ measurement. Of the systematic errors heat losses were clearly the most important factor. The relative errors due to heat losses are the same for the Harman ZT_H and κ and thus for the combined ZT. However, the Harman ZT_H does not suffer from geometrical systematic errors (contact size, positioning) nor from the considerable error due to imperfect placing of the electrical contacts with respect to the thermometers of the Seebeck measurement. The relative error of the Harman ZT_H is therefore significantly smaller than the relative error of the combined ZT, see Table 3.4.

3.5 Error minimizing strategies

In this subsection strategies for thermoelectric van der Pauw measurements with low systematic errors are presented. Of all types of errors considered, heat loss by radiation is clearly the most severe and affects the ZT_H and the κ measurement

equally. The systematic errors are most easily analyzed from Eq. (3.39), which relates the amount of power lost by radiation to the total power created in the heater[5]

$$P^{\mathrm{rel}}_{\mathrm{loss,rad}} = \frac{P_{\mathrm{loss,rad}}}{P} = \frac{8a(a+d)\epsilon\sigma_B T_0^3 \ln(\sqrt{2}a/\delta)}{\pi\kappa d}\,. \tag{3.48}$$

The relative power loss and thus the measurement error increases with decreasing κ, which is unfortunate since good thermoelectric materials have a low thermal conductivity. However, there are other parameters that can be adjusted such that measurements can be performed with good accuracy for low κ materials. First of all one can design the samples to have a larger thickness-to-length ratio, since this reduces the geometrical term $a(a+d)/d$. The requirement for two-dimensional heat flow of the van der Pauw equation sets an upper limit to this, but as stated earlier the systematic error is <2% up to $d/a = 0.5$. This ratio can be increased further if the contacts are placed at the sample side faces and not on top or bottom. Doing so, Kasl and Hoch showed accurate (electrical) van der Pauw measurements up to $d/a = 2$ [Kas05].

Surprising on the first glance is the second option to reduce systematic errors: if the whole sample is scaled linearly the measurement error also decreases linearly, since $P^{\mathrm{rel}}_{\mathrm{loss,rad}} \propto a(a+d)/d$. Exploiting this, Hafizovic *et al.* measured thin layers of silica with a related method [Haf02], although the samples had an unfavorable thickness-to-length ratio. Their approach required lithographic prepatterning of the heaters though, which would complicate measurement preparations severely.

The third factor affecting accuracy is the temperature. The error scales with T^3 which means that low temperature measurements are significantly more accurate. The accuracy furthermore scales with the sample emissivity ϵ, which can be reduced e.g. by metalization of the surface. In order to back the above error discussion a thermal conductivity measurement on a SiO_2 slide was performed. The dimensions were ($a = 1$cm, $\delta = 1.2$mm, $d = 0.5$mm) and since $d/a = 0.05$ the geometry is clearly not optimal for thermal van der Pauw measurements. On the other hand, radiation losses will be clearly recognizable from the results and therefore anything reducing radiation loss can be identified the easier. If one assumes $\kappa = 1.4\,\mathrm{Wm^{-1}K^{-1}}$ and $\epsilon = 1$ it follows from Eq. (3.39) $P_{\mathrm{loss,rad}}/P \approx 1.4$ and therefore a highly inaccurate measurement can be expected[6]. The measurement results are shown in Figure 3.12a) and are $\approx 100\%$ too large compared to the reference data, which was obtained by means of a 3ω measurement (see Section 4.3). To improve the measurement the sample surface was coated with $\approx 50\,\mathrm{nm}$ Ag by thermal evaporation. Since metals have a low emissivity [Emi10] this decreases the emissivity of the sample, while the contribution of the silver layer to heat conduction is negligible. The results of the coated sample are shown in Figure 3.12a) as well and it can be seen that the deviation

[5] Eq. (3.39) was written for the case $d \ll a$, here the general case $A = 2a(a+d)$ is stated.

[6] $P_{\mathrm{loss,rad}} > P$ is unphysical and stems from the fact that the radiation losses in Eq. (3.39) are calculated from the ideal temperature profile. This is only a good approximation if the radiation losses are not too large, which is not the case here.

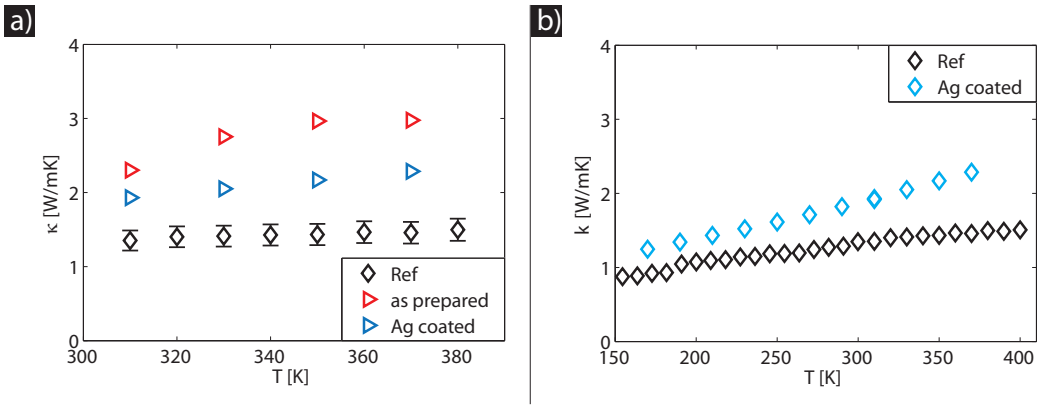

Figure 3.12: Reducing radiation losses in a thermal conductivity measurement on a glass slide. a) Measured thermal conductivity of a glass slide before (red) and after coating with $\approx 50\,\mathrm{nm}$ Ag. The Ag coating reduces the sample emissivity and hence the discrepancy to the reference data (black) is strongly diminished. b) Thermal conductivity of the Ag coated sample for a larger temperature regime. Since radiation losses scale with T^3 the deviation from reference data decreases for lower temperatures.

from reference data is roughly halved. The effect of temperature on measurement accuracy can clearly be seen in Figure 3.12b) where measurement results between 170 K and 370 K are presented. As expected from Eq. (3.39) the discrepancy between reference and measured data decreases with decreasing temperature.

Finally, even a low thermal conductivity material can be measured with the presented thermoelectric van der Pauw method, provided that the sample geometry is chosen appropriately. Bi_2Te_3 is the state-of-the-art thermoelectric material and has $\kappa \approx 1\,\mathrm{Wm^{-1}K^{-1}}$ and an emissivity that strongly depends on the exact composition [Seh62]. For the estimation of the radiation error we will use an average value of $\epsilon = 0.6$, also reported in [Bow61]. If we choose the sample with small but still manageable dimensions ($a = 5\,\mathrm{mm}$, $d = 2.5\,\mathrm{mm}$, $\delta = 1\,\mathrm{mm}$) the relative heat loss from Eq. (3.48) amounts to $P^{\mathrm{rel}}_{\mathrm{loss,rad}} = 0.3\%$ at 100 K, $P^{\mathrm{rel}}_{\mathrm{loss,rad}} = 2.0\%$ at 200 K and $P^{\mathrm{rel}}_{\mathrm{loss,rad}} = 6.9\%$ at 300 K; i.e. up to room temperature the κ and Harman-ZT measurement would be reasonably accurate and a complete thermoelectric characterization feasible.

3.6 Summary of Chapter 3

In this chapter a novel method for the concurrent measurement of σ, S, κ, and ZT has been presented. The method is based on the electrical van der Pauw measurement and the fundamental analogy between electrical and thermal physics has been exploited to transfer the concept of van der Pauw to a thermal conductivity measurement technique. An incorporated Seebeck and a four-point ZT measurement by

means of the Harman method complement the measurement approach to a complete thermoelectric characterization technique. Experimental data has been presented for two different materials and showed good agreement with reference data.

A thorough error discussion is desirable for all presented physical data but indispensable for a novel measurement technique. Therefore in Section 3.4 first an overview over the experimental errors was given and then a detailed discussion of the most important ones; the less significant errors are presented in Appendix B. It has been shown that the most severe systematic error is due to radiative heat loss, which affects the κ and the ZT_H measurement. For this reason strategies to minimize radiative heat loss have been discussed in Section 3.5 and experiments have been presented which show decreased experimental errors.

Chapter 4

Thermoelectric Characterization of Porous Silicon

The thermoelectric properties of porous silicon are the focus of this chapter. Porous Si is a material similar to silicon nanowires (SiNWs) for which very good thermoelectric properties have been reported in 2008 [Hoc08, Bou08]. Both publications showed ZT values close to unity at room temperature and argued that the increase in ZT is mainly due to a reduction in the thermal conductivity while the power factor is largely unaffected compared to its bulk value. The structure size of the nanowires, i.e. their diameter, was chosen such that phonon transport is diminished significantly, but charge carrier transport not. With a ZT of unity Si would be competitive to state-of-the-art materials, in particular with the advantage that silicon is abundant and relatively inexpensive. A further, very important advantage is the enormous technological background for silicon. Si is probably world's best investigated material and various practical problems that might occur on the way from concept to device (charge carrier tuning, good electrical and thermal contacts, packing materials with suitable properties to name but a few) have already been solved for Si, but not necessarily for other, new thermoelectric materials. Especially for low power applications like remote sensors Si is very attractive. For such devices efficiency is not crucial but the compatibility with standard microelectronic fabrication is highly advantageous.

On the other hand, SiNWs as presented in the mentioned publications are not easily applicable in real devices. First, for most applications enormous amounts of nanowires would be necessary with at least some degree of control in order to get reliable characteristics of the device. The wires furthermore have to be aligned and contacted individually, which is not trivial from a technical point of view. Porous Si, however, has the potential to combine the silicon-specific advantages with a simple, scalable process that readily produces macroscopic amounts. The material is single-crystalline yet nanostructured with Si wall thicknesses that are at least partially controllable. In analogy to SiNWs this offer the possibility to adjust the structure

size of the material such that the thermal conductivity decreases but electronic properties might be preserved. Since the samples are macroscopic, bulk characterization techniques can be applied, which accelerates the material optimization process compared to nanowires.

The potential of porous Si (pSi) as thermoelectric material has also been recognized by theoretical physicists. Using molecular dynamics Lee *et al.* calculated an optimum ZT of ≈ 0.4 for porous Si with a square arrangement of circular pores [Lee08a]. While the typical dimensions (pore diameter and spacing $\approx 1\,\mathrm{nm}$) were very small the authors also showed that the shape of the pore has negligible influence on the results and furthermore that a strict periodicity of the pores is not required. The same has been argued by Dresselhaus [Dre07] and is important in view of the somewhat non-ordered structures of the mesoporous Si samples that are discussed later.

There is also one experimental report on the thermoelectric properties of macroscopic porous Si samples[1] but the reported results seem questionable and will therefore not be used as reference[2].

At first the fabrication of porous Si will shortly be outlined in Section 4.1, while a more fundamental description can be found in Appendix C. Afterwards results on the electrical conductivity and the figure of merit for doped pSi will be presented in Section 4.2. It will be shown that the efficiency of pSi can be enhanced compared to bulk Si. On the other hand, the efficiency remains low compared to state-of-the-art materials. The mayor reason for this is the unexpected high thermal conductivity of the characterized porous Si samples. Therefore systematic thermal conductivity measurements of porous Si for different porosities and structure sizes have been performed and the results will be presented in Section 4.3. Finally, initial results for

[1] In a recent paper Tang *et al.* [Tan10] presented results for holey Si which was prepared by lithographic prestructuring and reactive ion etching of an SOI wafer. Thus this holey Si is essentially a structured thin film and therefore not comparable to the macroscopic porous Si investigated in this thesis.

[2] Yamamoto *et al.* [Yam99] etched a Si wafer ($19\,\mathrm{m\Omega cm}$) from both sides and obtained two $125\,\mu\mathrm{m}$ pSi films connected by a $30\,\mu\mathrm{m}$ bulk Si core. They state an approximate wall thickness of 10 nm and a porosity of $p \approx 0.47$, i.e. the sample is roughly comparable to the samples discussed in Section 4.3. Measuring the in-plane properties of this sandwich structure they obtain $\sigma_{\mathrm{pSi}} \approx 2000\,\mathrm{Sm}^{-1}$, $S_{\mathrm{pSi}} \approx 4000\,\mu\mathrm{VK}^{-1}$, and $\kappa_{\mathrm{pSi}} \approx 22\,\mathrm{Wm}^{-1}\mathrm{K}^{-1}$, which corresponds to a ZT of around 0.45 at room temperature. Although few measurement details are presented, the values for electrical and thermal conductivity appear to be plausible, while the reported value for the Seebeck coefficient raises questions and concerns. First, no details are given how the stated S_{pSi} is deduced from the measured values of bulk Si and the sandwich structure. Second, the reported value is 10 times higher than the Seebeck coefficient of the bulk Si substrate with the same doping concentration and still 3-4 times higher than the Seebeck coefficient of low doped Si. In fact, a value comparable to $S = 4000\,\mu\mathrm{VK}^{-1}$ has not been reported for any kind of Si to the best of my knowledge. While it is in principle possible to increase the Seebeck coefficient beyond its bulk value by nanostructuring (energy filtering or band structure engineering), experimental results and theoretical calculations usually show an increase of up to 50%, which is much smaller than the reported increase by a factor of 10. Furthermore, a Seebeck coefficent of $S = 4000\,\mu\mathrm{VK}^{-1}$ corresponds to a Peltier coefficent of 1.2 V, i.e. the average energy of the charge carriers with respect to the Fermi level would be larger than the Si bandgap.

porous SiGe are presented, which shows lower thermal conductivity than porous Si and might have thermoelectric properties superior to pSi.

4.1 Fabrication of porous silicon

The details of the porous Si fabrication process were not the main area of research during this thesis; most of the samples have been produced by others, mainly Dr. Dong Sik Kim. Thermoelectric characterization of pSi samples, however, was one of the main topics of this thesis and is discussed in the following. Since there is an interplay between thermoelectric properties, sample geometry, and the fabrication parameters, the fundamentals of the fabrication process will be explained and it will be discussed how sample properties can be tuned.

Porous Si is formed under applied bias in an electrochemical cell as shown in Figure 4.1a). This top-down approach to create nanostructured Si is known since the 1950s [Uhl56, Tur58] and has similarities to the metal-assisted etching process introduced in Section 2.2.1. Under anodic bias, i.e. with a negative electrical potential at the silicon sample compared to the other electrode, Si is dissolved directly

$$\mathrm{Si} + 4\mathrm{HF}_2^- + \mathrm{h}^+ \rightarrow \mathrm{SiF}_6^{2-} + 2\mathrm{HF} + \mathrm{H}_2 + \mathrm{e}^- \,, \tag{4.1}$$

upon hole (h^+) injection. The electrical field is largest at the tips of the randomly created pores, therefore further etching proceeds preferentially in the direction of the pores. The Si regions between the pores are partially depleted due to the applied bias. Since current flow is essential for the dissolution process the etching of the Si regions between the pores is stopped when their size approaches the dimension of the space charge region. This prevents the complete Si dissolution, the process is self-limiting, and a Si skeleton with a typical structure size of two times the space charge region width remains. Pore distance and structure size can be adjusted by changing the wafer resistivity and the applied voltage or current density. Exemplary samples are shown in Figure 4.1 and Figure 4.9. Figure 4.1c) and d) are magnified images of the top and the bottom regions of a single sample; it can be seen that the sample is homogeneous on a microscopic scale and that the structure is similar in different regions.

When determining electrical or thermal conductivity the result corresponds to an effective medium consisting of the Si skeleton and vacuum. For a better comparability with data e.g. from nanowires it is necessary to normalize the obtained effective medium result by the porosity p, i.e. $\sigma_{\mathrm{pSi}} = \sigma_{\mathrm{eff}}/(1-p)$. Porosity is the volume fraction of the pores, i.e. $p = V_{\mathrm{pores}}/V_{\mathrm{Si}}$, where V_{Si} is the volume of bulk Si before etching. Porosity has been determined by gravimetric analysis and it holds

$$p = \frac{V_{\mathrm{pores}}}{V_{\mathrm{Si}}} = \frac{m_0 - m_1}{m_{\mathrm{Si}}} = \frac{m_0 - m_1}{\rho_{\mathrm{Si}} A t} \,, \tag{4.2}$$

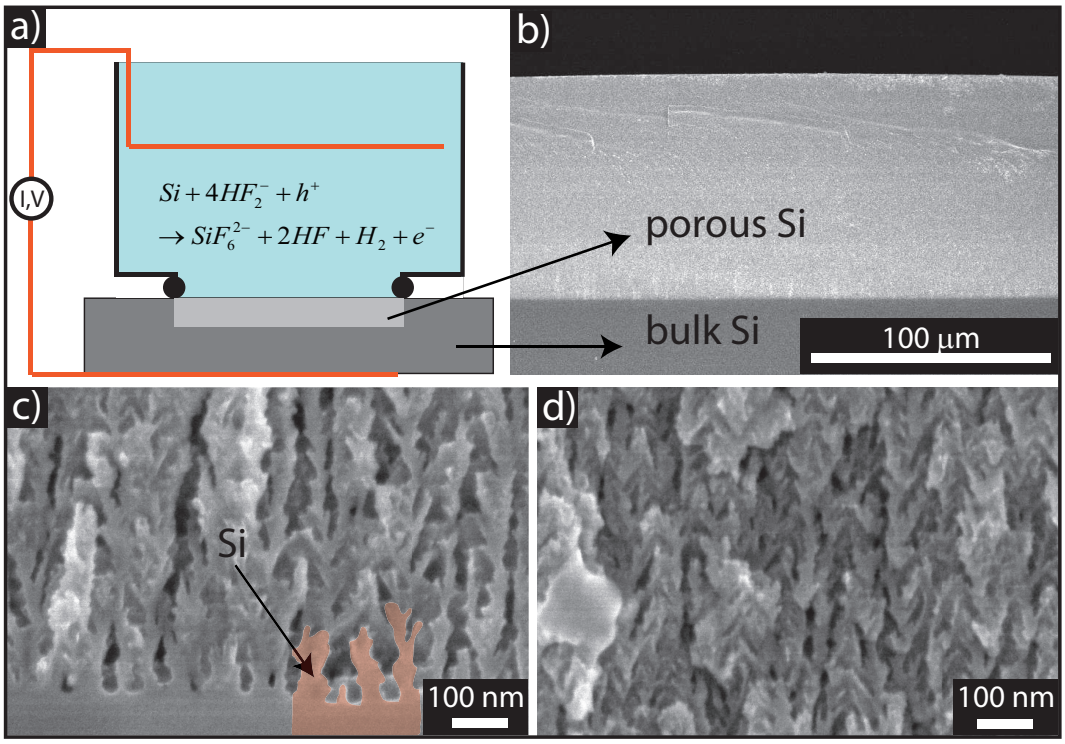

Figure 4.1: a) Scheme of an electrochemical cell used for the fabrication of (mesoporous) Si. b) Large scale SEM image of pSi film on Si substrate. The film has a thickness of 100 μm and appears uniform on a large scale. c) and d) show magnified images of the bottom and the top part of the pSi sample depicted in b). Both appear similar and show that the sample has a homogeneous geometry over the film thickness of 100 μm; the porosity was $p = 0.40$. For better distinction between Si and pores, a part of the Si skeleton is indicated in c).

where m_0 and m_1 are the masses of the sample before and after etching, m_{Si} is the mass of Si (before etching) in the volume that has been etched, $\rho_{Si} = 2.329\,\mathrm{gcm}^{-3}$ the Si density, A the area of the etched film and t its thickness. This measurement relies on a homogeneous pSi film thickness, which was well fulfilled for the later characterized samples. More details on the fabrication as well as the underlying electrochemistry can be found in appendix C.

4.2 Electrical conductivity and figure of merit of porous silicon

In this section the results for the electrical properties of porous Si will be presented. While the etching process was discussed already in Section 4.1 further doping and passivation steps are necessary to enhance the electrical properties. Those will be introduced shortly in Subsection 4.2.1 while the results are presented in Subsection

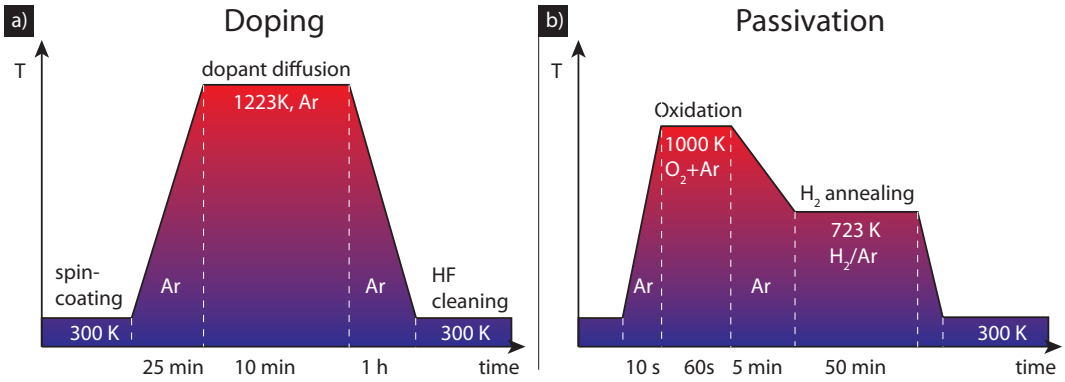

Figure 4.2: Porous Si doping (left) and annealing (right). Typical processing temperatures and times are indicated in the figure, although those were varied between samples in order to optimize thermoelectric properties. Also indicated are the atmospheres under which the process step was performed.

4.2.2. The section is concluded with a discussion of further optimization strategies. For most samples, doping and passivation was performed by Dr. Dong Sik Kim. Preparation parameters were chosen jointly by Dr. Kim and the author after analyzing the results of preceding measurements.

4.2.1 Doping and passivation

The wafers from which the pSi samples are etched have charge carrier concentrations of $10^{17}\,\mathrm{cm}^{-3} - 10^{18}\,\mathrm{cm}^{-3}$. From fundamental considerations (see Section 1.2) and experimental results from SiNW [Hoc08, Bou08] one can expect optimal thermoelectric properties for $10^{19}\,\mathrm{cm}^{-3} < n < 10^{20}\,\mathrm{cm}^{-3}$ which makes re-doping of the pSi samples necessary. It has furthermore been observed that the freshly etched samples show a high resistivity of around $10^5\,\mathrm{m\Omega cm}$. After etching, a low-quality native oxide forms at the pSi surface and the interface Si atoms exhibit many dangling bonds. These can trap charge carriers resulting in an extended, highly resistive depletion layer. Since the structure size is typically less than 100 nm this explains the observed increase in resistivity compared to bulk. Apart from increasing the number of free charge carriers, re-doping also decreases the thickness of the depletion layer and therefore enhances electrical charge transport [Sch10a].

The processing steps after etching of the samples are indicated in Figure 4.2. First the pSi membranes are soaked in spin-on-dopant (Filmtronics Inc., USA) which contains either boron or phosphorous. In order to diffusive the dopant into the pSi the samples are baked at a high temperature ($\approx 1100\,\mathrm{K} - 1300\,\mathrm{K}$) for several tens of minutes in an argon atmosphere. After the dopant diffusion the samples are covered with a thick oxide due to the SiO_2 content of the spin on dopant. This oxide is removed by a dip in HF. Doping homogeneity was checked by Raman spectroscopy.

Due to the interaction of phonons with charge carriers (Fano-effect) the Si Raman peak at $\approx 520\,\mathrm{cm}^{-1}$ becomes asymetric and from the degree of asymmetry one can deduce the charge carrier density. By scanning across sample cross sections doping homogeneity could be confirmed. Further details are given in [Aga10].

The mentioned interface trap states can severely degrade the electrical conductivity. Application of a high quality oxide is a standard measure in silicon processing to decrease the density of interface traps [Sze81]. We produced high quality oxide by rapid oxidation at elevated temperatures. The samples are loaded into a rapid thermal annealer (RTP-1200-100, UniTemp GmbH Germany) that is able to ramp the temperature very fast (up to $100\,\mathrm{Ks}^{-1}$). The number of active surface states can be further reduced by annealing in a H_2 containing atmosphere as diffusing hydrogen atoms have the ability to saturates the dangling bonds [Nic82]. After doping and annealing the samples are contacted and ready for thermoelectric characterization.

4.2.2 Thermoelectric characterization

Typical pSi membranes have a size of $0.25\,\mathrm{cm}^2$ and a thickness of $70\,\mu\mathrm{m} - 100\,\mu\mathrm{m}$. Due to the fragility of the samples a complete characterization by the thermoelectric van der Pauw method is challenging, in particular gluing the heaters onto the sample and soldering all the electrical connections without breaking the sample. On the other hand, for a test whether the concept of porous Si as thermoelectric material is plausible a direct ZT_H measurement by means of the four-point Harman method (see Section 3.2) is sufficient. We therefore adjusted the etching parameters such that the structure size was $\approx 44\,\mathrm{nm}$ and thus comparable to the SiNWs for which $ZT = 1$ had been reported [Hoc08]. The structure size measurement is discussed in Section 4.3.3 and an SEM image of the sample is shown in Figure C.1b). The thermal conductivity of a sample obtained under the same etching conditions was measured separately with the 3ω method (see Section 4.3) and was $\kappa_{\mathrm{eff}} = 7.0\,\mathrm{Wm}^{-1}\mathrm{K}^{-1}$. Taking into account the gravimetrically determined porosity of $p = 0.6$, the thermal conductivity of the silicon matrix itself is $\kappa_{\mathrm{pSi}} = 17.6\,\mathrm{Wm}^{-1}\mathrm{K}^{-1}$. Several samples have been doped under varying conditions in order to obtain optimal properties.

The measurement results for σ and ZT are shown in Figure 4.3, both for boron and phosphorous doping. The doping parameters are given in the figure caption, while the parameters of the passivation and annealing step were kept constant (as indicated in Figure 4.2). From Figure 4.3a) and c) it can be seen that the electrical conductivity increases drastically after doping and passivation and that it can be tuned over several orders of magnitude by adjusting the doping parameters. Since the dopant solubility is known to increase with doping processing temperature and the diffusion length with doping time [Sze81], it can be concluded that the observed increase in σ is in agreement with an increase of charge carrier concentration, as would be expected. The conductivity of the as-etched sample shows a temperature dependence that is typical for Si of that dopant concentration [Bul68], while for the doped samples the electrical conductivity decreases with increasing T. This can be

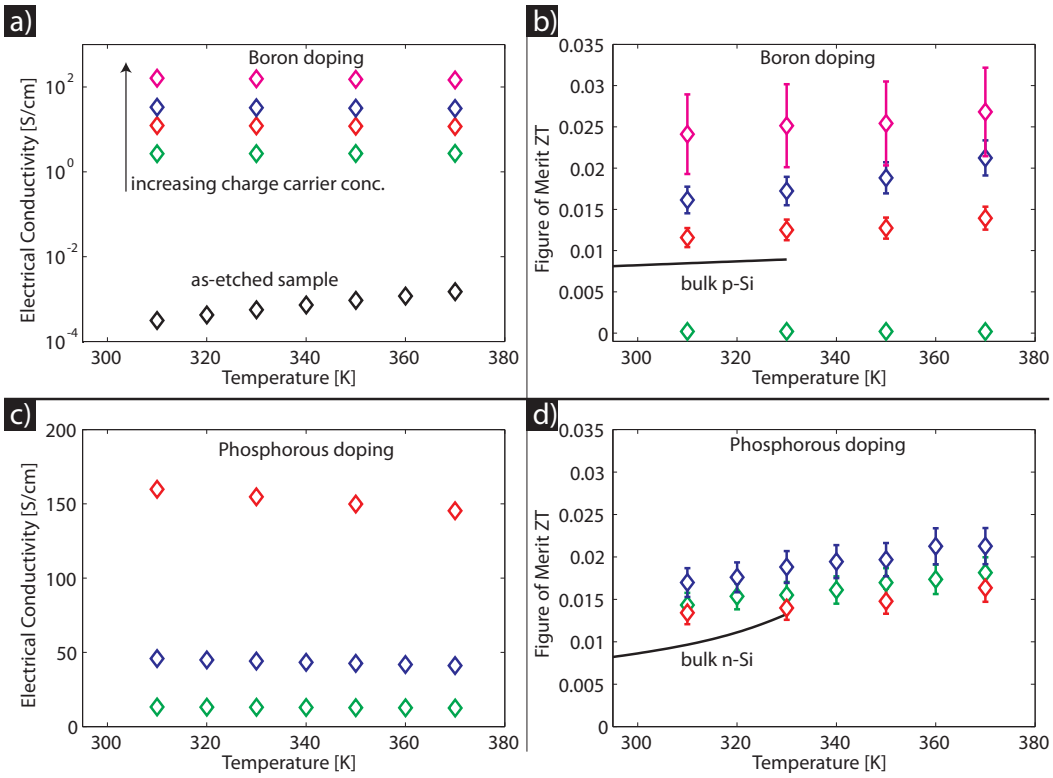

Figure 4.3: Electrical conductivity and figure of merit for a), b) boron and c), d) phosphorous doped porous Si. The doping times and temperatures for the samples shown in a) are $T_{\mathrm{dop}} = 1173\,\mathrm{K}$ for $t_{\mathrm{dop}} = 40\,\mathrm{min}$ (red); $T_{\mathrm{dop}} = 1173\,\mathrm{K}$ for $t_{\mathrm{dop}} = 10\,\mathrm{min}$ (green); $T_{\mathrm{dop}} = 1223\,\mathrm{K}$ for $t_{\mathrm{dop}} = 10\,\mathrm{min}$ (blue) and $T_{\mathrm{dop}} = 1373\,\mathrm{K}$ for $t_{\mathrm{dop}} = 50\,\mathrm{min}$ (magenta); for comparison also the electrical conductivity of an as-etched sample is shown in black. It can be seen that the electrical conductivity increases with doping temperature. In b) the figure of merit of those samples is shown. For sufficient doping ZT_H of the pSi samples exceeds the ZT of optimal doped bulk Si, which is plotted in black for comparison. In c) the electrical conductivity of phosphorous doped samples is shown ($T_{\mathrm{dop}} = 1223\,\mathrm{K}$ for $t_{\mathrm{dop}} = 4\,\mathrm{min}$ (green); $T_{\mathrm{dop}} = 1223\,\mathrm{K}$ for $t_{\mathrm{dop}} = 10\,\mathrm{min}$ (blue); and $T_{\mathrm{dop}} = 1373\,\mathrm{K}$ for $t_{\mathrm{dop}} = 50\,\mathrm{min}$ (red)). The conductivity decreases with increasing temperature as is typical for highly doped semiconductors or metals. The data in c) is shown in a linear plot while a) is plotted on a log scale. The figure of merit for n-pSi in d) exceeds that of bulk Si for properly doped samples and increases with T.

seen in Figure 4.3c) where the data is plotted on a linear scale and is expected for highly doped semiconductors, see e.g. [Web91]. The data shown in a) and c) has been corrected by the porosity, i.e. $\sigma_{\mathrm{pSi}} = \sigma_{\mathrm{meas}}/(1-p)$ and the relative measurement error is 4% as discussed in Section 3.4.

Figure 4.3b) and d) show the ZT_H measured by the Harman method both for n and p-type pSi. In b) it can be seen that the sample with the lowest charge

carrier concentration (green) has a $ZT \approx 0$, while for the others it increases from ≈ 0.01 to 0.025 with increasing charge carrier concentration. With increasing T the figure of merit of all samples increases and the results for p and n-type pSi are comparable. It is important to note that in Figure 4.3d) the sample with the highest charge carrier concentration (red) does not show the largest ZT. As discussed in Section 1.2 there exists an optimum charge carrier concentration and this sample is presumably already too highly doped. The optimum ZT of bulk Si[3] is plotted in b) and d) for comparison and it can be seen that the ZT of pSi is superior to bulk Si for adequate doping conditions, i.e. appropriate charge carrier concentrations. The shown error bars correspond to a relative error of 10% and account for observed deviations between the two performed Harman measurements as well as for the small error due to the AC measurement frequency (see Eq. (3.47)).

Summarizing these initial results on the thermoelectric properties of porous silicon, two main conclusions can be drawn. First it has been shown that pSi can be designed such that it has properties superior to bulk Si, i.e. the validity of the fundamental concept of nanostructuring to improve thermoelectric properties has been successfully proven thereby. The results are comparable to recent data for nanostructured bulk Si obtained by ball-milling and pressing from Bux *et al.* who reported $ZT = 0.023$ at room temperature [Bux09]. The other conclusion is that with a ZT of ≈ 0.02, pSi is as yet not interesting for real applications and the results are furthermore a factor of 50 worse than the two reported results for SiNWs [Bou08, Hoc08]. Reasons for this discrepancy are analyzed in the following and strategies for further improvements of pSi are discussed.

As discussed in Section 3.4 the Harman ZT_H measurement is affected by radiation loss such that ZT_H is measured systematically too small. Using Eq. (3.39) the relative measurement error can be estimated. With $a = 0.005\,\mathrm{m}$, $d = 100\,\mu\mathrm{m}$, $\delta = 0.001\,\mathrm{m}$ and $\kappa_{\mathrm{eff}} = 7.0\,\mathrm{Wm^{-1}K^{-1}}$ and an assumed emissivity of $\epsilon = 1$ the figure of merit ZT is measured $\approx 30\%$ too small at 310 K and 50% at 370 K. A more exact FEM calculation yields similar values: $\approx 23\%$ at 310 K and 39% at 370 K. The emissivity of pSi can be expected to be comparable to unity and it is therefore clear that the measured values are systematically too small. However, since the precise value of ϵ is unknown, a mathematical correction of the measured values assuming $\epsilon = 1$ would be incorrect. Furthermore, the samples all have similar geometries which means that they are intercomparable and the drawn conclusions remain valid. Most important is however, that the measurement error due to radiation losses does not even rudimentally explain the differences between pSi and the reported results for

[3]The electrical conductivity at room temperature as function of charge carrier concentration was obtained for boron and phosphorous doped Si from [Bul93] and the temperature dependence was estimated from the data shown in [Web91]. For the thermal conductivity a fit equation from [Ful68] was employed. Geballe *et al.* [Geb55] measured the Seebeck coefficient for n and p-type Si for charge carrier concentrations up to $2 \cdot 10^{19}\,\mathrm{cm^{-3}}$ and from 20 K to 330 K. This data was combined with an analytical expression for the Seebeck coefficient in the degenerate limit [Nol01] and an polynomial fit in the intermediate region. From the combination of these data sets the maximum bulk Si ZT could be estimated.

the SiNW.

The second point are the electrical properties. Reference experiments have been performed on SOI wafers with a Si thickness of 150 nm. Figure 4.4 shows the electrical conductivity of a pSi sample in direct comparison with a thin Si film.

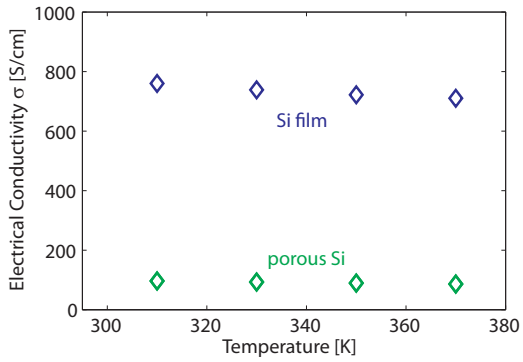

Figure 4.4: Electrical conductivity of pSi sample and Si film for similar doping conditions. It can be seen, that the electrical conductivity of pSi is approximately a factor of eight below that of the Si film.

Both were doped at 1223 K but the displayed conductivities differ by a factor of eight. One possible reason[4] for this is a decreased mobility of the charge carriers in porous Si due to scattering at the pSi/ambient interfaces as has been observed previously [Sim95]. More likely is though that the passivation and annealing step is not optimized and charge carriers are therefore trapped at the surface. Determining the mobility by a Hall measurement would lead to further insight.

The main point is, however, that the thermal conductivity of the electrically measured samples is relatively large ($\kappa_{\mathrm{pSi}} = 17.6\,\mathrm{Wm^{-1}K^{-1}}$) and only a factor of eight below bulk Si. Comparing this with the results from Hochbaum *et al.* ($2\,\mathrm{Wm^{-1}K^{-1}}$ at a similar structure size [Hoc08]) this is somewhat surprising and demands further investigations[5]. For this reason, systematic thermal conductivity measurements as function of structure size were performed. This is the focus of the following section.

4.3 Thermal conductivity of porous silicon

In this section results on the thermal conductivity of porous Si and porous SiGe will be presented. The measurements were performed with the 3ω method, whose work-

[4]The doping times were 50 min for the Si film and 10 min for the pSi sample. Since the dopant diffusion length is already $\approx 2.4\,\mu$m after 10 min [Sze81] this can not explain the observed conductivity difference.

[5]The sample used for the thermal conductivity measurement was undoped. The electronic part of the thermal conductivity is $\leq 1\,\mathrm{Wm^{-1}K^{-1}}$ even at high doping concentrations, and the contribution will furthermore be reduced since electronic charge transport is not as effective as in bulk Si, see Figure 4.4. The electronic contribution is therefore negligible compared to the lattice part.

ing principle will be discussed first. Temperature-dependent results were obtained for several sample porosities and average structure sizes; from this data the thermal conductivity of porous Si as a function of structure size can be inferred. For all samples measured the thermal conductivity exhibits a drastic reduction (one to three orders of magnitude) due to the effects of the nanostructuring. For porous SiGe an even lower thermal conductivity is obtained, presumably due increased scattering of phonons with short mean free paths on the Ge atoms.

The motivation for systematic thermal conductivity measurements is twofold: first this sheds light onto phonon transport on a microscopic level. It will furthermore help to explain the apparent differences between porous Si and SiNWs. In this regard it is interesting to note that while the results for ZT are comparable in both SiNW papers, the measured thermal conductivities differ significantly [Hoc08, Bou08]. At room temperature Boukai *et al.* report $k = 5\,\mathrm{Wm^{-1}K^{-1}}$ and $k = 1\,\mathrm{Wm^{-1}K^{-1}}$ for quadratic nanowires with a side length of 10 nm and 20 nm, respectively, while Hochbaum *et al.* measured $k = 5\,\mathrm{Wm^{-1}K^{-1}}$ and $k = 2\,\mathrm{Wm^{-1}K^{-1}}$ for a wire diameter of 100 nm and 50 nm, respectively. Thus the wires investigated by Hochbaum *et al.* show a much more drastic size effect than the wires in the other study. The authors argue that the reason for this is the high surface roughness of the wires (fabricated by metal-assisted etching, see Section 2.2), however, a thermal conductivity for a single-crystalline 50 nm wire that is comparable to amorphous silica demands further investigations, as also concluded by Hochbaum *et al.* [Hoc08]. The second point is that only with structure-size-dependent thermal conductivity measurements one can estimate the potential of pSi as thermoelectric material and find the structure size that yields acceptable thermoelectric properties.

4.3.1 Thermal conductivity of bulk silicon

In this subsection the thermal conductivity of Si is reviewed. First this establishes the reference, which the later shown results for pSi can be compared to. Second, some basic quantities and concepts can be introduced. These help to understand and illuminate the physics behind the measurement data.

The thermal conductivity of bulk Si over a large temperature range is shown in Figure 4.5 [Gla64]. One can see that the thermal conductivity increases from 8 K to 20 K and decreases approximately linearly on the log-log plot for higher temperatures. The vast majority of the heat in Si is transported by phonons. Treating phonons as ideal gas particles within the solid the thermal conductivity of the lattice can be written as

$$\kappa_l = \frac{1}{3} c(T) v(T) l^{\gamma}_{\mathrm{mfp}}(T)\,, \tag{4.3}$$

where c is the specific heat capacity and v the speed of sound or phonon group velocity. The thermal conductivity is limited by the scattering of phonons with other phonons, boundaries, or impurities. The average distance phonons travel between the scattering events is termed $l^{\gamma}_{\mathrm{mfp}}$, the mean free path of the phonons. Using

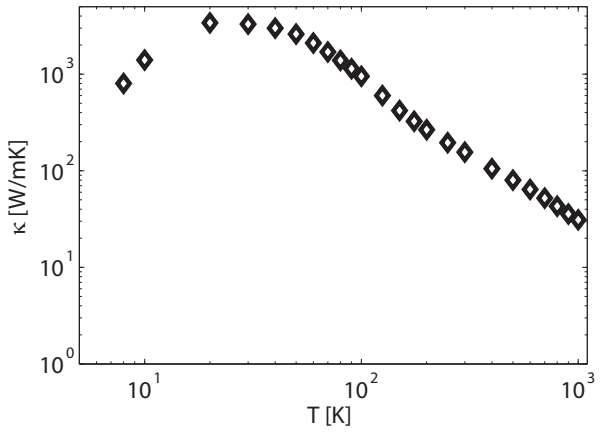

Figure 4.5: Thermal conductivity of bulk Si from [Gla64]. With increasing temperature an increase of the thermal conductivity up to 20 K is observed. Beyond this so-called Umklapp-peak the thermal conductivity is governed by phonon-phonon scattering and shows approximately a T^{-1} dependence. At very high temperatures heat conduction by charge carriers becomes more important and causes deviations from the T^{-1} dependence.

bulk Si values $\kappa_l \approx 150\,\mathrm{Wm^{-1}K^{-1}}$, $c = c_p\rho \approx 1.6 \cdot 10^6\,\mathrm{Jm^{-3}K^{-1}}$, and $v \approx 6500\,\mathrm{ms^{-1}}$ [McC05], the phonon mean free path can be calculated to 43 nm at 300 K. The value for the speed of sound used here is an weighted average over the different phonon branches and in general given by the slope of the phonon dispersion, i.e. the relation between phonon wave vector/momentum and frequency/energy. The phonon dispersion curves for Si are shown in Figure 4.6a), the details are discussed further below.

For high temperatures phonon-phonon scattering determines the thermal conductivity [Nol01]. There are two types of relevant phonon scattering events: in the N-(normal) process two phonons combine and energy and momentum are conserved, while for the U- (Umklapp) processes momentum is not conserved but transferred to the lattice. Two-dimensional representations of the two scattering processes are shown in Figure 4.6b): q_i labels the wave vectors of the phonons, G is the reciprocal lattice vector and the square indicates the two-dimensional Brillouin zone. The N-processes redistribute the phonons but constitute no thermal resistance to first order[6], therefore U-processes govern the thermal conductivity at high temperatures. R. Peierls explained theoretically that the scattering rate of U-processes increases linearly with T for high temperatures, i.e. the phonon mean free path and thus κ show a $1/T$ dependence [Pei29]. This behavior is not restricted to silicon and has been observed first by Eucken [Euc11].

[6]Nevertheless, due to redistributing the phonons N-processes enhance the chance for U-processes and thereby indirectly create a thermal resistance [McC05].

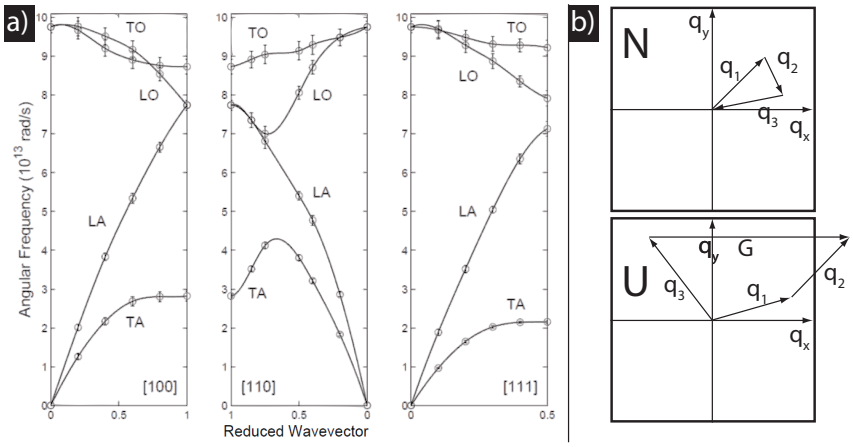

Figure 4.6: a): Phonon dispersions of Si for the [100], [110], and [111] direction. The x-axis is the reduced wave vector $q/q_{\max}$, the y-axis the angular frequency $\omega = 2\pi\nu$ of the phonons and TO, LO, LA, and TA label the different phonon branches, i.e. transverse optical, longitudinal optical, transverse acoustical, and longitudinal acoustical. The two transverse optical and acoustical branches are degenerated in the directions shown here. The velocity of phonons is proportional to the slope of the dispersion curves. Therefore acoustic phonons are responsible for most of the heat transport. b): Phonon N-process (top) and U-process (bottom). While in the N-process energy and momentum are conserved, momentum is transferred to the lattice in the U-process. a) Taken from [McC05].

Phonons are Bosons and their occupation-probability is thus given by $b(\nu) = [\exp(h\nu/k_BT)]^{-1}$. At low temperatures the occupation of states with high energy $h\nu$ and large wave vector becomes less likely and the chances for U-processes diminish. Therefore, at very low temperatures, the phonon mean free path is not determined by phonon-phonon scattering but by phonon-interface scattering. In this regime the phonon mean free path is given by the crystal dimensions and independent of temperature; therefore κ follows the behavior of the specific heat, which shows a T^3 dependence [Deb12]. For somewhat higher temperatures impurity scattering may determine the thermal conductivity before U-processes take over and the thermal conductivity decreases.

With these basic concepts the temperature dependence of the bulk Si thermal conductivity, displayed in Figure 4.5, can be understood qualitatively. However, for a detailed description the simple ideal phonon gas picture used for Eq. (4.3) is not sufficient. It has several shortcomings: first, the speed of sound is not constant as can be seen from the dispersion shown in Figure 4.6; second, there exist transverse and longitudinal as well as acoustic and optical phonons since Si has two atoms per unit cell. These all have different dispersions. It can be seen from Figure 4.6a) that acoustic phonons tend to have larger group velocities than optical phonons. Acoustic phonons are therefore mainly responsible for heat transport. Third, the phonon

mean free path is also energy dependent, since the various scattering mechanisms have different energy dependences. These issues can be accounted for using the following equation, see e.g. [Liu04, Hao09]:

$$\kappa_l = \frac{1}{3}\sum_i \int_0^{\nu_{\max}} c_i(\nu) v_i^2(\nu) \tau_{T,i}(\nu) \mathrm{d}\nu \,. \tag{4.4}$$

The sum is over the different phonon branches and c_i is here the specific heat per frequency. Comparing Eq. (4.4) with Eq. (4.3) one can see that the phonon mean free path has been replaced by the relaxation time τ and the group velocity: $l^{\gamma}_{\mathrm{mfp}}(\nu) = \tau_T(\nu)v(\nu)$. The relaxation time is the inverse scattering rate and relaxation times from different scattering processes are inversely additive[7]:

$$\tau_T^{-1} = \sum_j \tau_j^{-1} \,, \tag{4.5}$$

this is known as Matthiessen's rule [McC05].

When investigating nanostructured Si one would expect thermal conductivity reduction due to boundary scattering when the sample dimensions are of the order of the phonon mean free path. However, since the mean free paths of phonons of different energies are very different, size effects on the thermal conductivity have been observed for films with thicknesses of the order of 1 μm, which is much larger than the average mean free path of 43 nm from Eq. (4.3) [McC05]. Size effects have even been observed for Si films with 10 μm pores and a spacing of 20 μm [Son04]. This emphasizes that for a quantitative modeling of phonon transport Eq. (4.3) is too simple.

With this short discussion the basic quantities to understand the thermal conductivity measurements have been defined. It is also clear, that size effects of the thermal conductivity can be expected for mesoporous Si.

4.3.2 Thermal conductivity measurements with the 3ω method

The 3ω method is a non-steady-state thermal conductivity measurement method that was invented at the beginning of the 20th century by Corbino [Cor10, Cor11], but thoroughly investigated and made popular by Cahill *et al.* in the late 1980s [Cah87, Cah89, Cah90]. First, the basic idea will be introduced, afterwards the measurement system and the equipment and finally the data analysis will be presented.

A schematic picture of a sample prepared for a 3ω measurement is shown in Figure 4.7. The key feature is the metal line which is situated on top of the sample. The metal line has four contacts. Two are used to drive a current and the other two to measure the voltage that drops over a fraction of the metal line with length l. If a current is driven through the metal line, Joule heat P_{J} is produced and the

[7] if the scattering rates due to the different mechanisms are independent of each other.

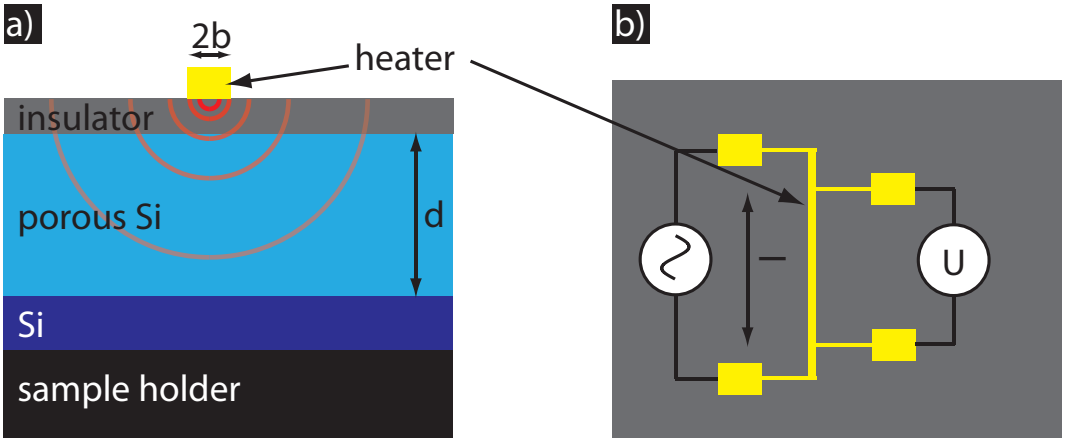

Figure 4.7: Sample prepared for 3ω measurement using pSi as example. On top of the sample is an electrically insulating layer and a metal stripe (heater) with width $2b$. Four electrical contacts are made to the heater, two to drive an alternating current and two to measure the dropping voltage over a fraction of the heater with length l. If an alternating current is driven through the heater, a thermal wave is excited in the heater and spreads into the sample. The measured voltage depends on the amplitude of the thermal wave which in turn depends on the thermal properties of the sample. Appropriate choice of the excitation frequency confines the thermal wave into the porous Si layer and allows to extract the thermal conductivity of it.

metal line temperature increases. It is intuitively clear that the temperature change depends on the sample properties: if the sample is a very good thermal insulator, the temperature increase will be large, while it will be small for a good thermal conductor; this is one of the fundamental ideas of the 3ω method. The second point is that an alternating current with circular frequency ω creates a measurable voltage signal that is proportional to the temperature change in the heater: A current $I(\omega) = I_0 \sin(\omega t)$ creates a potential difference $U(\omega) = RI$. The resistance of the metal line itself is temperature-dependent $R = R_0(1 + \alpha T + ...)$ and since $\Delta T \propto P_\mathrm{J} = RI^2 \propto \sin(2\omega t)$ the measured voltage

$$U = RI = ... + \alpha \sin(2\omega t) \sin(\omega t) ... = ... \alpha \sin(3\omega t) ... \,, \tag{4.6}$$

contains a signal that goes with the third harmonic of the excitation frequency ω (therefrom the name 3ω method) and is furthermore proportional to the amplitude of the temperature change ΔT in the heater. If the linear resistance-temperature coefficient α of the heater is known or obtained from a calibration, ΔT can be extracted from the voltage signal. Using an alternating current has another advantage: While a direct current would create a steady temperature gradient (after some initial phase) across the complete sample, an AC signal creates a thermal wave that decays

rapidly within the sample. In fact it can be shown that

$$|q^{-1}| = \left|\sqrt{\frac{\kappa}{i2\omega\rho c}}\right| \tag{4.7}$$

is a measure of the decay length of the excited thermal wave and $|q^{-1}|$ is consequently known as thermal penetration depth. ρ is here the density and c the specific heat of the sample and it can be seen that the thermal wave decays more rapidly in dense, thermally insulating samples. Since furthermore $|q^{-1}| \propto \sqrt{1/\omega}$ the region of the sample that is affected by the thermal wave can be chosen by adjusting the excitation frequency ω. This can be used to measure films on a substrate as shown in Figure 4.7, without having the substrate affect the measurement.

The exact relation between sample thermal conductivity and measured temperature amplitude/voltage signal is complex [Wan09, Moo96]. However, if ω is chosen such that the thermal penetration depth is much larger than half the width of the heater line b, but smaller than the sample/film thickness d, i.e. if $b \ll |q^{-1}| \ll d$, it an be shown[8] that the amplitude of the thermal wave is given by [Cah87, Moo96]

$$\Delta T = \frac{P}{\pi l \kappa}\left(0.5 \ln \frac{\kappa}{\rho c b^2} + \ln 2 - 0.5772 - 0.5 \ln \omega - 0.25 i\pi\right), \tag{4.8}$$

i.e. the real part of the temperature amplitude $\Re(\Delta T)$ is proportional to $\frac{P}{\pi l \kappa} \ln \omega$. That means if ΔT is extracted from the measured voltage signal κ can be obtained from the slope of ΔT vs. $\ln \omega$. A resistance-temperature calibration is shown in Figure 4.8a) while b) shows the real part of the temperature amplitude vs. excitation frequency. The linear region that is used to determine the thermal conductivity is indicated. This frequency regime can be used to fit the data and κ is obtained from

$$\kappa = \frac{P}{2\pi l} \frac{\partial \ln f}{\partial \Re(\Delta T)}, \tag{4.9}$$

where P – the power supplied to the heater – is predefined in the measurement program. More details on the measurement routine and the sample preparation are described in Appendix D.1.

4.3.3 Measurement results for porous silicon

Apart from thermoelectrics porous Si can be employed in optoelectronics, as sensor, and as thermal insulator [Bis00, Leh91, Woo08, Yer99]. There have been previous experimental and theoretical studies [Ran09], e.g. thermal conductivity measurements on microporous Si [Ges97] and sintered pSi [Wol06]. Benedetto *et al.* report thermal conductivity values for mesoporous Si, however, no structure size is given

[8] The thermal penetration depth must also be much smaller than the length of the heater, otherwise the assumed symmetry in heater direction breaks down. However, this is usually not a problem.

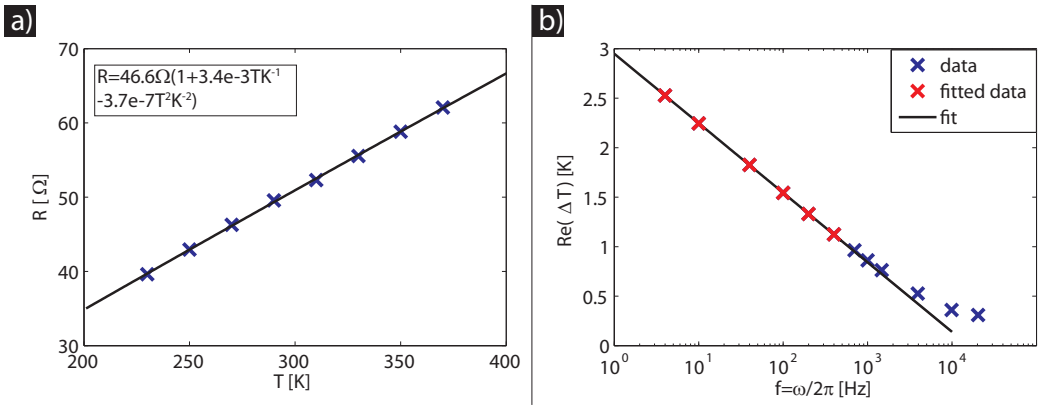

Figure 4.8: a:) Resistance-temperature calibration for an evaporated Pt heater with width $2b = 10\,\mu$m and thickness ≈ 100 nm. The calibration is basically linear with a small quadratic component. A good resistance-temperature fit is crucial for the measurement. b): Real part of the temperature amplitude as a function of frequency (logarithmic); sample is fused silica. In the region where the thermal penetration depth is larger than half the heater width but smaller than the sample thickness $\Re(\Delta T) \propto \ln f$ and the thermal conductivity can be obtained from the slope. The frequency region that was used for fitting is indicated as well as the linear fit, which coincides with the measured data points. At higher frequencies a deviation from the linear fit can be observed, here the penetration depth becomes smaller/comparable to b and Eq. (4.8) becomes invalid.

and it is furthermore unclear, whether the results have been normalized by porosity [Ben97]. We therefore aimed for systematic thermal conductivity measurements in a structure size regime that is relevant for thermoelectrics, i.e. mesoporous Si.

The samples used for 3ω measurements are shown in Figure 4.1a) and c), in Figure 4.9, and in Figure C.1. Their porosity was determined gravimetrically and varied between 0.17 and 0.66, see Eq. (4.2); the sample details are stated in the corresponding figure captions. For further comparison a macroporous Si samples was measured as well. Macroporous Si[9] has a larger wall thickness than mesoporous Si and is therefore interesting for systematic investigations of size effects. A SEM image of a macroporous Si sample is shown in Figure 4.9e). Around the crystalline core a layer of microporous Si is clearly visible. This microporous layer does not contribute significantly to thermal transport but prevents accurate wall thickness measurements. It was therefore removed by a mild oxidation (925 °C for 4 min) and subsequent HF dip. The etched sample is shown in Figure 4.9f).

As described in Subsection 4.3.2 the thermal conductivity is determined from the slope of the real part of the temperature amplitude over the logarithm of the measurement frequency with Eq. (4.9). The slope has to be determined from the frequency interval where the thermal penetration depth $|q^{-1}|$, given by Eq. (4.7), is

[9] For fabrication details see e.g. [Leh02].

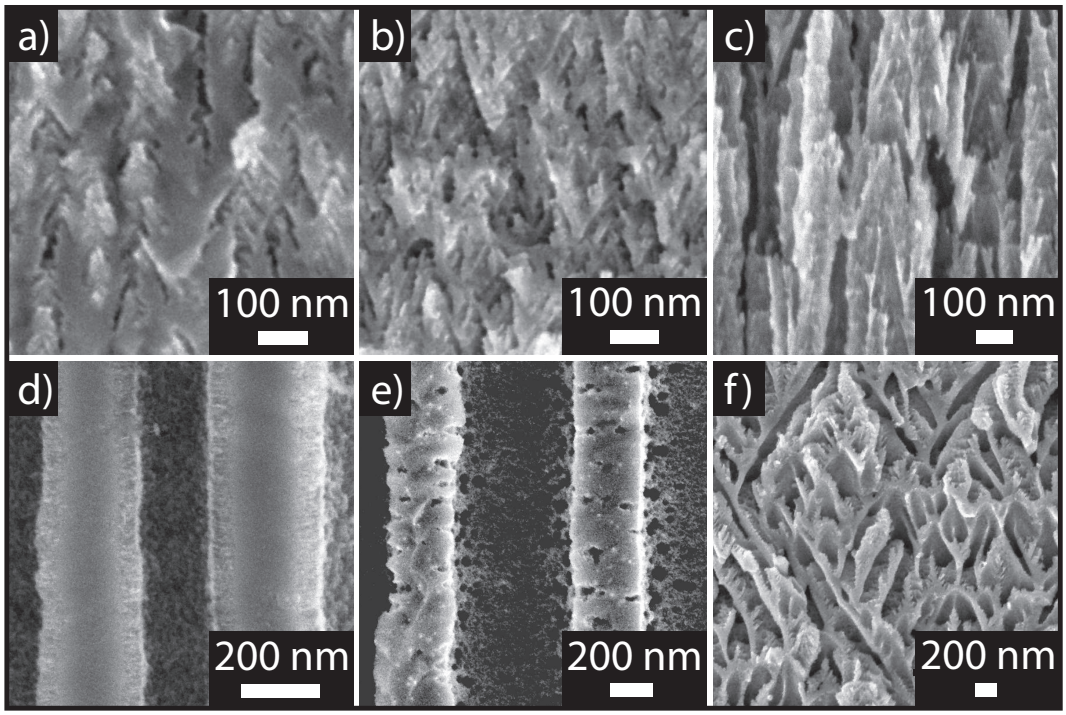

Figure 4.9: SEM images of measured samples. a): $p = 0.17$, $d = 97\,\mu$m, b): $p = 0.33$, $d = 100\,\mu$m, c):$p = 0.66$, $d = 118\,\mu$m, d):$p = 0.5x$, $d = 90\,\mu$m, e) like d), but after mild oxidation and HF dip to remove microporous layer, f): porous SiGe (2.8% Ge) $p = 0.66$, $d = 100\,\mu$m.

much smaller than the film thickness and larger than half the heater width. Plotting $\Re(\Delta T)$ vs. $\ln f$ this region can be recognized since it shows a linear behavior, see e.g. Figure 4.8b). So, after obtaining the raw measurement data, the linear region was identified and an initial value for the thermal conductivity κ_{in} was calculated from Eq. (4.9). Then it had to be checked, whether the obtained κ_{in} and the frequency fitting regime match. To do so, $|q^{-1}|$ was calculated using κ_{in}. The thermal penetration depth furthermore depends on the sample parameters specific heat c and density ρ, which in turn depend on temperature and porosity. Since pSi is basically nanostructured Si, its specific heat is identical to the Si bulk value as also shown in [Wol06]. To account for the temperature dependence a polynomial fit using literature data [Okh72, Iof10] was employed. The density can be obtained from the bulk Si value and the porosity $\rho_{\text{pSi}} = \rho_{\text{Si}}(1-p)$; the temperature dependence of the density is negligible. The fitting region was calculated such that $a \times b \leq |q^{-1}(f)| \leq d/a$, where a is a factor that was chosen between 1.7 and 3. Using the calculated fitting interval κ was recalculated and compared to κ_{in}. Usually both values agreed within 10%. If not, κ was calculated again, using the now obtained value to calculate $|q^{-1}|$ and the fitting region.

The such obtained thermal conductivity is determined systematically too large,

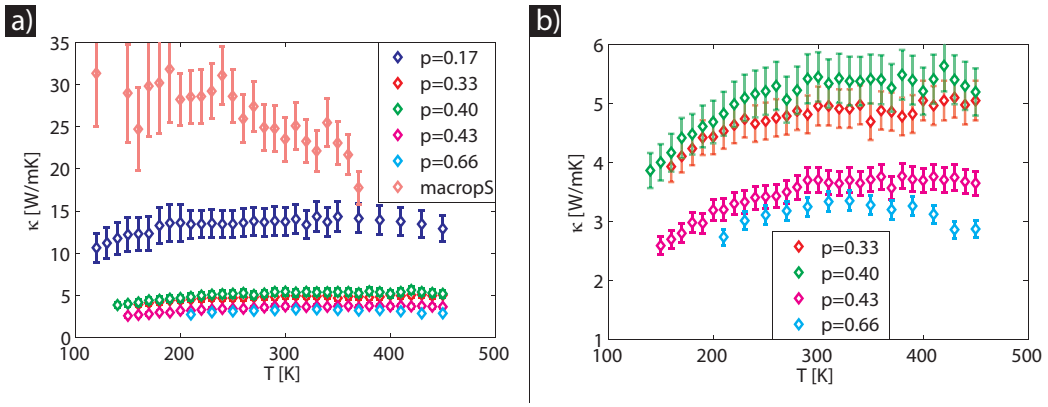

Figure 4.10: Thermal conductivity of porous Si vs. temperature. The porosity of the samples is indicated in the legend, the corresponding SEM images are shown in Figure 4.9 and 4.1. The samples show a decrease of κ for low T, but otherwise only a weak temperature dependence. The curves for the samples with lower thermal conductivity have been plotted for clarity magnified in b). All results have been normalized by the porosity of the samples.

because Eq. (4.8) is exactly valid only for semi-infinite samples with vanishing heater width. For real samples correction factors can be calculated as explained in Appendix D. The presented thermal conductivity data has therefore been divided by the correction factor. The correction factors varied between 1.05 and 1.12 for the samples with $\kappa < 10\,\mathrm{Wm^{-1}K^{-1}}$. For the samples with higher κ the linear fitting range lies partially outside the instrumentally accessible range, therefore the fitting region had to be increased and the correction factors were larger, up to 1.3 at 120 K, where the thermal penetration depth is largest.

Finally, in order to obtain the thermal conductivity of the porous Si matrix, the measured thermal conductivity has to be corrected for the porosity of the sample: $k_{\mathrm{pSi}} = k_{\mathrm{eff}}/(1-p)$, where k_{eff} is the measured thermal conductivity of the effective medium. The results for the samples shown in Figure 4.9 and 4.1 are presented in Figure 4.10.

All samples show a decrease in thermal conductivity that can not be explained by a pure porosity effect[10]. Instead, the observed thermal conductivity reduction is due to a decrease of the phonon mean free path due to increased interface scattering, also called size-effect.

In order to analyze this more quantitatively it is necessary to define a structure size δ of porous Si. The thermal conductivity is governed by the smallest typical

[10] One classical formula for the thermal conductivity of porous media has been derived by Eucken: $\kappa_{\mathrm{porous}}/\kappa_{\mathrm{solid}} = 1 - p/(1+0.5p)$, see [Tic05]. Using this equation one would expect $\kappa_{\mathrm{porous}} = 0.76\kappa_{\mathrm{solid}} \approx 115\,\mathrm{Wm^{-1}K^{-1}}$ for $p = 0.17$ and $\approx 38\,\mathrm{Wm^{-1}K^{-1}}$ for $p = 0.66$ at $T = 300\,\mathrm{K}$. These values are much higher than the measured values. Other classical models exist, see e.g. [Tic05] but they yield similar results. Note also that the plotted values have been normalized by $1/(1-p)$, which makes the difference even larger.

size of the system, it is therefore reasonable to define the structure size δ as the length between two adjacent holes. For samples with large structure sizes this can be determined from the cross-sectional SEM images, where the shortest distance between two pores is taken as structure size. This becomes increasingly difficult for smaller structure sizes though, because the image is only a two-dimensional projection of a three-dimensional structure. The visible wall thickness between two pores varies and depends on the orientation of the visible edge with respect to the pore arrangement. However, one can determine the average periodicity of the sample by counting the number of pores within a certain length. Together with the known porosity this can be used to estimate δ. The diameter d of the pores and δ are related for a given periodicity such that d increases with increasing porosity while δ increases; the exact relation depends on the specific geometry. We can determine this relation for three simple cases. First let us assume square pores that are arranged with a tetragonal symmetry as shown in Figure 4.11a). The structure size is given by $\delta = a - d$, where a is the periodicity and d the side length of the pore. Since $d^2 \stackrel{!}{=} pA = pa^2$, where A is the area of the square, it follows for the structure size

$$\delta_{\mathrm{sq}} = a(1 - \sqrt{p})\,. \tag{4.10}$$

If we assume round pores in tetragonal arrangement the relation changes to

$$\delta_{\mathrm{sq,r}} = a\left(1 - \sqrt{\frac{4}{\pi}}\sqrt{p}\right) \approx a(1 - 1.1\sqrt{p})\,. \tag{4.11}$$

For the third case let us assume round pores that are arranged in a hexagonal arrangement as shown in Figure 4.11b). Using $A = 1.5\sqrt{3}a^2$ and $3 \cdot \pi/4d^2 \stackrel{!}{=} pA$ it follows for the structure size

$$\delta_{\mathrm{hex}} = a\left(1 - \sqrt{\frac{2\sqrt{3}}{\pi}}\sqrt{p}\right) \approx a(1 - 1.05\sqrt{p})\,, \tag{4.12}$$

i.e. the result is very similar to a square pore arrangement. The real pSi shows neither perfect hexagonal nor tetragonal ordering but since the results for the three cases are very similar Eq. (4.12) can be used to estimate the structure size of the porous Si samples. Self-organized processes like pSi formation often tend to follow a hexagonal symmetry, therefore Eq. (4.12) is probably the most realistic assumption. Note that for perfectly ordered pores the counted number of visible pores might depend on the orientation of the visible sample edge with respect to the sample unit cell. However, since the ordering is not perfect the pore distribution is approximately isotropic and the visible number of pores is independent of the orientation of the sample edge if averaged over a sufficient long distance.

The porosity of the macroporous Si sample has been determined from a top-view SEM image, see Figure C.1, while the structure size was determined from a

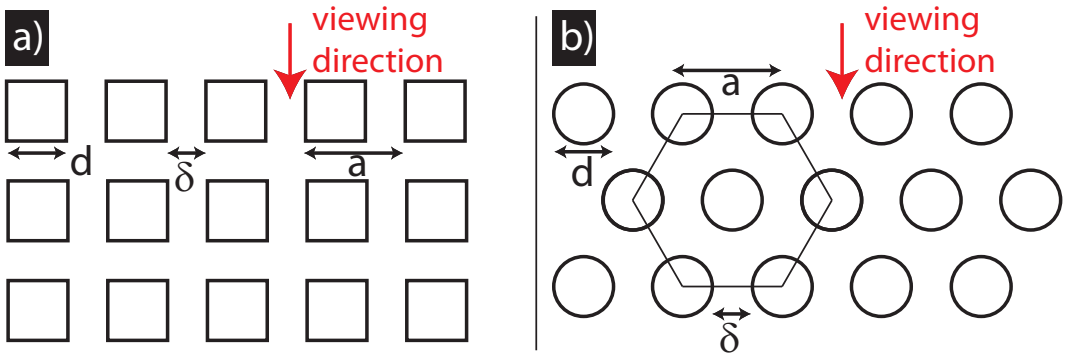

Figure 4.11: Determination of structure size of pSi samples for in idealized sample with tetragonal symmetry in a) and hexagonal symmetry in b). The periodicity can be obtained from the SEM images by counting pores while the structure size δ can be calculated from Eqs. (4.10) and (4.12) using the known porosity p. The results are similar for both arrangements and therefore the precise geometry of the real pSi samples is of minor importance. Note though, that the real samples are not perfectly ordered and therefore the pore distribution is roughly isotropic.

cross-sectional image as shown in Figure 4.9e). Geometrical and electrochemical parameters of the measured samples are summarized in Table 4.3.3

sample no.	wafer ρ	curr. dens. j	por. p	period. a	struc. size δ
1	$15-20\,\mathrm{m\Omega cm}$	$12\,\mathrm{mAcm^{-2}}$	0.43	28 nm	9 nm
2	$15-20\,\mathrm{m\Omega cm}$	$4\,\mathrm{mAcm^{-2}}$	0.33	32 nm	13 nm
3	$15-20\,\mathrm{m\Omega cm}$	$8\,\mathrm{mAcm^{-2}}$	0.40	35 nm	12 nm
4	$15-20\,\mathrm{m\Omega cm}$	$10\,\mathrm{mAcm^{-2}}$	0.66	47 nm	7 nm
5	$20-50\,\mathrm{m\Omega cm}$	$4\,\mathrm{mAcm^{-2}}$	0.17	64 nm	36 nm
6	$20-50\,\mathrm{m\Omega cm}$	$14\,\mathrm{mAcm^{-2}}$	0.6	235 nm	44 nm
7 m. pSi		–	0.42	–	114 nm
8 pSiGe	$35\,\mathrm{m\Omega cm}$	$14\,\mathrm{mAcm^{-2}}$	0.66	110 nm	17 nm

Table 4.1: Geometrical and electrochemical parameters of the six mesoporous Si, the macroporous Si and the porous SiGe sample that are analyzed in this thesis.

For further discussion it is useful to compare the measurement results with literature data for nanostructured Si. Li *et al.* measured the thermal conductivity of Si nanowires grown by the vapor-liquid-solid mechanism for different nanowire diameters [Li03], while Hochbaum *et al.* measured similarly sized nanowires obtained by electroless etching (see Section 2.2) [Hoc08]. Tang *et al.* structured thin Si films with nanosphere lithography/block-copolymers and reactive ion etching and obtained holey Si [Tan10]. This material is quite similar to pSi from a geometry point of view, except that it is better ordered than pSi and that only thin films were be created. Figure 4.12a) directly compares this reference data with the results for some of the measured pSi samples. Though different in absolute values the data sets show the

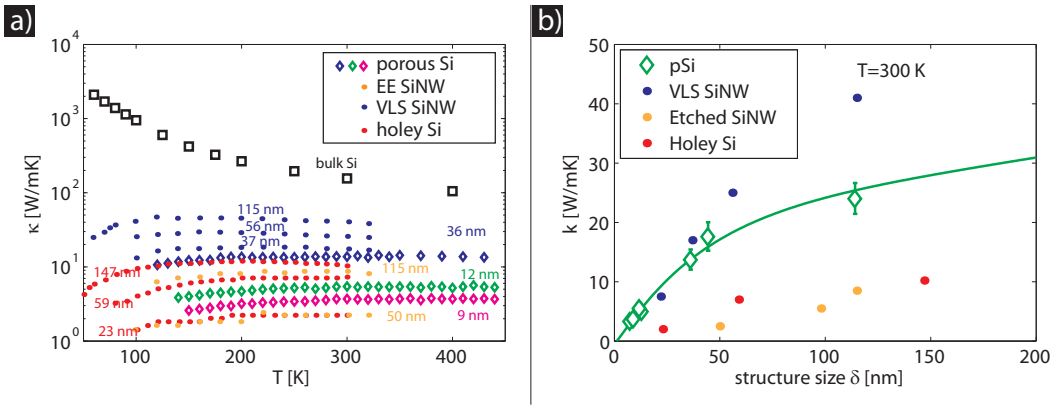

Figure 4.12: Thermal conductivity of pSi in comparison with reference data for Si nanostructures from several sources [Hoc08, Li03, Tan10]. All data sets show a decrease of the thermal conductivity at low temperatures but otherwise a much less pronounced temperature dependence than bulk Si. b) shows the thermal conductivity at $T = 300\,\mathrm{K}$ over structure size. Porous silicon exhibits a lower thermal conductivity than VLS grown SiNW but a higher thermal conductivity than the results reported for electroless etched SiNW.

same trends. Starting from low temperatures the thermal conductivity increases with temperature and shows a very broad peak or settles at a plateau value. For the VLS grown nanowires a shift and a decrease of the Umklapp peak to higher temperatures with decreasing structure size has been observed. In contrast, the curves show no distinct peak for the holey Si and the pSi samples[11].

As discussed previously the Umklapp peak in Si arises because at low temperatures the phonon mean free path $l^{\gamma}_{\mathrm{mfp}}$ is given by the crystal dimensions and κ increases with the specific heat c. With higher temperature phonon-phonon scattering increases and κ decreases when the scattering length for phonon-phonon interaction becomes smaller than the scattering length for phonon-interface interaction, i.e. the crystal size. For the VLS grown nanowires $l^{\gamma}_{\mathrm{mfp}}$ is of the order of the diameter of the nanowires. With increasing temperature phonon-phonon scattering increases again, but the temperature were it becomes comparable to phonon-interface scattering is higher, since the size of the nanowires is smaller than a bulk crystal. In consequence, the smaller the nanowire diameter, the higher the temperature of the Umklapp peak. The reasoning in principle also holds for pSi. However, the Umklapp peak becomes less pronounced for smaller structure sizes as was e.g. observed for holey Si [Tan10] and smears out further for pSi since the structure size is less clear defined than for SiNWs.

The structure sizes of the samples is also indicated in Figure 4.12a). If one compares those, quantitative differences between the data curves become apparent.

[11]The macroporous Si sample may exhibit a thermal conductivity peak at lower T than were experimentally accessible

This is exemplified in Figure 4.12b) where κ at $T = 300\,\mathrm{K}$ is plotted as function of structure size. With decreasing structure size κ decreases, that is consistent for all curves shown, however, the VLS grown nanowires show a much higher κ for a given structure size than the electroless etched nanowires or the holey Si; the results for pSi fall somewhere in between. Comparing VLS and etched SiNWs it has been argued that the reason for the remarkable difference is the different surface [Hoc08]. The etched SiNWs exhibit a rough surface due to the etching process while the grown SiNWs show an atomically smooth surface. A smoother surface enhances specular phonon scattering and thus the phonon mean free path is longer than the wire diameter, as it would approximately be for diffuse scattering [McC05]. Different surfaces might also explain the difference between holey Si/etched SiNWs and porous Si. Electroless etching of the wires and the electrochemical etching of porous Si are very similar processes, though, one would therefore expect similar surface roughness and consequently similar thermal conductivity for a given structure size. The observed differences in thermal conductivity therefore demand further investigations, in particular since a lower thermal conductivity is desired for high ZT thermoelectric materials.

Also shown in Figure 4.12b) is a fit to the measurement data for porous Si. This allows to interpolate and extrapolate – to a certain extend – the measurement data and thus to fabricate pSi with desired thermal properties. Several reports have been published which model the thermal conductivity, typically as function of structure size or porosity or both. Those however, either have unphysical limits [Lia06] or do not match the measurement data [Alv10], presumably due to modeling assumptions that are not well fulfilled for the measured porous Si samples. It is also not possible to fit the data to a simple expression that depends e.g. on the ratio of structure size and average mean free path. This is not too surprising since it has been discussed before that the concept of an average mean free path is too simple and can not describe transport in nanostructures with sufficient accuracy. The experimental data could be verified though with Boltzmann-transport calculations [Cal59, Hol63] or more advanced modeling [Kaz10]. This however, is beyond the scope of this thesis.

In summary systematic investigations of porous Si samples with different porosities and structure sizes were performed. The temperature dependence of κ is comparable to what has been previously observed for SiNWs. It was also shown that the thermal conductivity depends strongly on the structure size of the porous Si samples and that lower structure size corresponds to smaller thermal conductivity. Overall the thermal conductivity is reduced by one to three orders of magnitude due to increased phonon scattering at the surface of the pSi matrix. Comparing the pSi results with literature thermal conductivity data for SiNWs or similar structures one finds that for a given temperature and structure size the pSi results fall in between the data for VLS grown nanowires with a very smooth surface and a high percentage of specular phonon scattering and rough, etched nanowires, where diffusive phonon scattering is dominant.

Regarding the potential of pSi as thermoelectric material it can be concluded that a structure size of well below 10 nm is necessary for a thermal conductivity $\kappa < 2\,\mathrm{Wm^{-1}K^{-1}}$. This in agreement with the experimental findings of Boukai *et al.* [Bou08]. If the power factor could be largely preserved this would correspond to a ZT approaching unity at room temperature. Fabrication of such structures is possible and has been demonstrated (see Figure 4.12a)), the greatest challenge is probably to preserve the power factor. At this scale the structure size approaches the charge carrier mean free path of around 10 nm (see footnote 7 in Chapter 1) which makes it difficult to keep bulk electrical properties. Furthermore, the effect of surface states gets more pronounced with decreasing structure and good passivation becomes more and more crucial [Sch10a].

If decreasing the structure size turns out to be not successful, the other experimentally adjustable parameter appears to be the surface roughness. Following the argument from Hochbaum *et al.* very low thermal conductivities should be obtainable for moderate structure sizes [Hoc08]. This could be achieved e.g. by an appropriate chemical treatment of the pSi surface. However, there is an ongoing debate how the published results can be explained [Hip10] and there is also a discussion among theoreticians, see e.g. [Moo08] but also [Kaz10]. It therefore remains to be seen whether the results by Hochbaum *et al.* can be reproduced consistently and whether the surface modification effect can be exploited systematically.

Instead an alternative approach to achieve low thermal conductivity is presented in the following.

Thermal conductivity of porous SiGe

Thermal conductivity measurements on porous SiGe with a Germanium content of 2.8 atomic percent have been performed. For such a low Ge content SiGe behaves chemically basically like pure Si and can be fabricated analogously to porous Si. An SEM image was presented in Figure 4.9f) and it can be seen that the structure and texture is comparable to pSi.

It has long been recognized that alloying of materials can lead to materials with thermal conductivities lower than either pure components. The reason is increased phonon scattering at the density variations within the alloy. This is also true for SiGe alloys which are an important high temperature thermoelectric material [Sny08, Iko98, Row06]. It has been shown that the nanostructuring in pSi decreases the thermal conductivity of the sample by several orders of magnitude. If the alloying results in an additional reduction of the thermal conductivity, porous SiGe might be a thermoeletric material with properties superior to pSi or Si nanowires. The thermal conductivity of pSiGe is plotted in Figure 4.13a) and it shows the same temperature dependence as pSi. However, comparing the thermal conductivity as function of structure size it can be seen that the thermal conductivity of pSiGe lies below the results for pSi, see Figure 4.13b). Although more systematic investigations would be necessary to complete the picture it can be concluded that the Ge atoms within

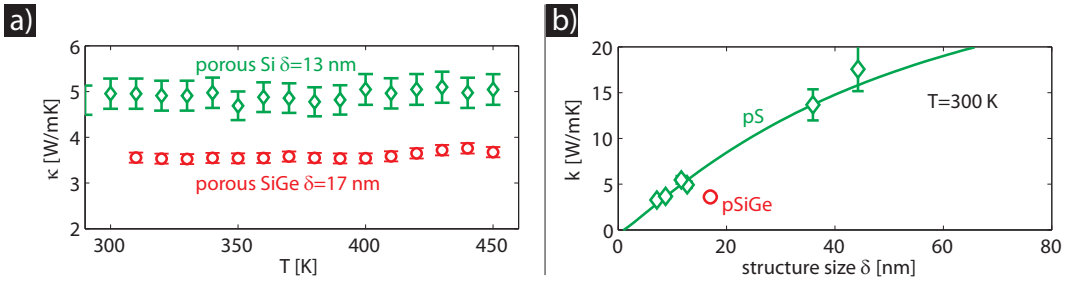

Figure 4.13: Comparison of thermal conductivity of porous Si and porous SiGe with comparable structure size. Though have a slightly higher structure size the thermal conductivity of the pSiGe sample falls below the result of the pSi for all temperatures in a). On the plot κ vs. δ in b) this effect is clearly visible.

the pSiGe cause an additional thermal conductivity reduction. Point scattering centers like the incorporated Ge atoms cause a scattering length $\tau \propto \nu^{-4}$, where ν is the energy of the phonons [Nol01]. Thus predominantly phonons with high energy and small wavelength are scattered by the Ge atoms. This effect is in addition to the scattering of low energy/large wavelengths phonons at the silicon/ambient interface. Since phonons of all energy carry heat, additional scattering of small wavelength phonons cause a further decrease of the thermal conductivity. This might be exploited to fabricate a thermoelectric material with higher ZT than pSi.

4.4 Summary of Chapter 4

Porous Si has been fabricated in an electrochemical cell. In some sense, pSi is the inverse structure of an array of SiNWs and has therefore the potential to combine the silicon specific advantages with the benefits of macroscopic samples (macroscopic measurement techniques, scalable fabrication, simpler contacting). Adjusting the fabrication parameters samples with different porosity and wall thicknesses have been produced. For good electrical conductivity re-doping of the fabricated samples is necessary. This was achieved by liquid-phase doping and both n- and p-type samples with ZT higher than bulk Si have been fabricated. A further increase in efficiency might be expected for pSi with smaller structure size. This has been indicated by systematic thermal conductivity measurements by means of the 3ω method on samples with different porosities and structure sizes. For a thermal conductivity approaching the properties of state-of-the-art materials structure sizes below 10 nm appear to be necessary. Finally it has been shown that porous SiGe exhibits a lower thermal conductivity than pSi of a similar structure size.

Chapter 5

Summary, Open Questions, and Outlook

Summary The purpose of this last part of the thesis is to summarize and discuss the results that were presented in detail in the chapters before. With the aim to investigate the potential of Si as thermoelectric material we have fabricated different forms of nanostructured silicon, developed a new measurement technique, and obtained results for the thermoelectric properties of porous Si.

It has been shown previously that silicon nanowires can have thermoelectric properties comparable to state-of-the-art materials and might therefore be employed in future thermoelectric devices. For real-life modules very large numbers of nanowires are necessary. In Chapter 2 we therefore have presented a process flow for arrays of silicon nanowires potentially applicable in thermoelectric devices. We have exploited a combination of laser interference lithography and metal-assisted etching to fabricate arrays of Si nanowires with a sample size of cm^2, i.e. macroscopic dimension. Laser interference lithography is a powerful prestructuring technique that allows the fabrication of strictly periodic templates with user-defined geometry and arrangement. Metal-assisted etching is a wet-chemical etching process enabling the selective Si dissolution in the vicinity of a noble metal film. Using gold meshes defined by laser interference lithography we have obtained Si nanowires with uniform

diameters ranging from 350 nm down to 65 nm. A uniform and tailorable wire geometry is crucial since the thermoelectric properties of Si are size-dependent. The obtained wires are furthermore single crystalline and have a uniform height and can thus easily be contacted. Characteristics like the single-crystallinity, the large-area, parallel fabrication process, and the uniform, user-defined geometry let the samples appear very promising from a device point of view. We have furthermore shown improvements of the laser interference lithography process itself. The developed immersion laser interference lithography setup has been used to fabricate patterns with a periodicity significantly smaller than what is achievable with the standard setup. A two-mirror setup allows for hexagonal patterning at a single shot and thus for even faster and more convenient pattern fabrication.

Thermoelectric characterization is one of the bottlenecks for progress in thermoelectrics since repeated measurements are necessary for optimized thermoelectric materials. In Chapter 3 we have presented a novel measurement method that enables a complete thermoelectric characterization on a single sample. The method is based on the established van der Pauw method for electrical characterization and combines measurement of the electrical conductivity, the thermal conductivity, the Seebeck coefficient, and the thermoelectric figure of merit. A consequent realization of four-point measurements renders the method insensitive to thermal and electrical contact resistances; it furthermore contains several inherent possibilities to cross-check the obtained experimental data. A thorough analysis of the errors of the measurement technique has revealed heat loss by radiation as the most severe problem, at least at higher temperatures. A simple analytical equation to estimate this error has been derived and several strategies to decrease the radiative heat loss have been explored and successfully experimentally implemented.

With Chapter 4 we have returned to nanostructured silicon. Porous silicon is – like the arrays of silicon nanowires shown in Chapter 2 – nanostructured, single

crystalline silicon. Samples with macroscopic dimensions have been produced in a simple electrochemical process. The average wall thickness of the porous Si samples has been adjusted through the electrochemical parameters which has also allowed controlling the thermoelectric properties of the material. Using the developed thermoelectric van der Pauw method we have shown that porous Si can have a higher figure of merit than its bulk counterpart if properly doped and passivated. This proves the validity of the concept that nanostructuring can be used to enhance the thermoelectric properties of materials. We have shown this for both p- and n-doped material which is a prerequesite for thermoelectric devices which consist of both types of materials. Using the 3ω method systematic investigation of the thermal conductivity as function of average wall thickness have been performed. The results indicate that wall thicknesses below 10 nm are necessary to obtain material that is competitive with state-of-the-art materials like Bi_2Te_3. Using SiGe wafers with a Ge content of around 3 atomic percent we have shown that the fabrication of porous SiGe samples is possible. Initial results on the thermal conductivity of the sample have revealed a lower thermal conductivity than comparable porous Si samples and have demonstrated that the thermal conductivity can be decreased further by a combination of alloy scattering and scattering at the silicon/ambient interfaces.

In total we have presented progress in thermoelectric characterization, nanostructuring, and the use of silicon as thermoelectric material.

Open questions and outlook It is presumably the nature of research to open more questions than answers have been given. We want to discuss here shortly the most important uncovered questions/topics that arose during the course of this thesis; roughly following the thematic outline of the thesis.

Since they are almost in a device-like state, thermoelectric characterization of the arrays of silicon nanowires would be very interesting, in particular since the presented immersion interference lithography setup could be used to obtain wires with even smaller diameters. However, since this kind of measurement is inherently a two-point measurement, a controlled contacting procedure, which yields low contact resistances, is indispensable.

The developed thermoelectric van der Pauw method proved to be a powerful tool in thermoelectric research. Unfortunately, the effect of radiative heat loss limits its applicability range. It has been proven that the applicability range can be increased by good heat-shielding and optimized sample geometry; in the current state the use of the method is nevertheless restricted to temperatures not far beyond room temperature for most thermoelectric materials. Further progress might be achieved by changing from steady-state to transient measurements. Two further concepts for high temperature figure of merit measurements are currently under investigation. One of these concepts relies on a four-point cross-plane figure of merit measurement. Cross-plane measurements have a much smaller heated region than in-plane measurements which reduces the influence of radiative heat loss.

The thermoelectric van der Pauw method can be readily combined with a Hall coefficient measurement by applying a magnetic field perpendicular to the sample plane. The contact arrangement used in the van der Pauw measurements is already a standard geometry for Hall measurements and the obtained results for charge carrier density and mobility would lead to deeper insight in the properties of the material under investigation and a more rapidly converging optimization of the thermoelectric properties. On top of that thermogalvanometric effects like the Nernst-, the Ettingshausen-, and the Righi-Leduc effect could also be measured. This would

provide a multitude of information about transport in the material and improve the physical understanding.

Concerning porous Si we expect higher efficiencies for samples that have a smaller average structure size. This has been unsuccessful so far, presumably due to insufficient surface passivation which becomes more challenging at smaller structure sizes. Further insight is expected from mobility measurements, a Hall measurement station is currently set up. While the measured thermal conductivity of porous SiGe is promising, further electrical and figure of merit measurements are necessary to explore the possibilities of porous SiGe as thermoelectric material.

Silicon has undeniably numerous advantages compared to other (potential) thermoelectric materials, it is furthermore the base of todays semiconductor industry. Therefore chances are good that some kind of nanostructured Si will eventually be used commercially as a thermoelectric material. Providing a fabrication route for arrays of silicon nanowires capable of being integrated into thermoelectric devices, a novel thermoelectric characterization technique, and a study on the thermoelectric properties of porous silicon, this thesis has added a drop of insight to the sea of knowledge.

There has been significant progress in the field of thermoelectrics within the last three years. This holds for the development of new materials, the enhancement of "old" materials as well as for the fundamental understanding; eventually this will lead to a larger and broader impact of thermoelectrics on society. However, although stated frequently in publications, it is not evident how thermoelectrics could be the answer to the energy/climate crisis of the 21st century. For this to be true thermoelectric generators would have to be competitive with other heat engines at energy scales of megawatts or higher. Even believing the most optimistic predictions for future figure of merit values this is highly unlikely. That said, thermoelectrics remains a rapidly developing field with a lot of interesting physics and a diversity of actual and potential applications.

Appendix A

Convection and Thermal Conductivity of Air at Low Pressures

For an ideal gas, the mean free path of the gas particles is given by [Kle06]

$$l_{\mathrm{mfp}} = \frac{1}{\sqrt{2} n \sigma_t}\,, \tag{A.1}$$

where n is the particle density and $\sigma_t = \pi d^2$ the scattering cross-section of the particles with diameter d. Using the ideal gas law $pV = Nk_BT$, where k_B is Boltzmann's constant the mean free path is given as function of pressure by

$$l_{\mathrm{mfp}} = \frac{k_BT}{\sqrt{2}\pi d^2 p}\,, \tag{A.2}$$

Using $d = 155\,\mathrm{pm}$, the van der Waals radius of nitrogen [wik10c], the mean free path is of the order of $10^1\,\mathrm{m}$ at $p = 10^{-5}\,\mathrm{mbar}$ and therefore orders of magnitude larger than the dimensions of the measurement system. Since convection is collective transport based upon particle-particle interaction it can be concluded that heat transport by convection does not take place for the employed measurement conditions.

Let us now consider heat transport by individual gas particles, i.e. conduction by air at low pressures. Using again ideal gas laws the heat transport between two bodies with area A and a temperature difference ΔT is given in the ballistic regime by [Dem02]

$$P = A\frac{n\bar{v}k_Bf}{8}\Delta T\,, \tag{A.3}$$

where n is the particle density, $\bar{v} = \sqrt{8k_BT/(\pi m)}$ the average velocity of the particles and f the number of degrees of freedom. If we define a thermal conductivity for for

this system in analogy to $P = \kappa A \Delta T / d$ we obtain

$$\kappa_{\text{ball}} = \frac{dn\bar{v}k_B f}{8}\,, \tag{A.4}$$

where d is the distance between the two bodies[1] Using again the ideal gas law this can be written as function of gas pressure

$$\kappa_{\text{ball}} = \frac{dp\bar{v}f}{8T}\,, \tag{A.5}$$

Using the values of nitrogen $m = 4.6710^{-26}\,\text{kg}$, $f = 6$ it follows $\kappa_{\text{ball}} \approx 1.2 \cdot 10^{-4}\,\text{Wm}^{-1}\text{K}^{-1}$ for $T = 300\,\text{K}$ and $d = 0.1\,\text{m}$. The "thermal conductivity" of air at low presssures is therefore negligible.

It can be concluded that neither convection nor conduction through the ambient gas are relevant at pressures below $10^{-5}\,\text{mb}$.

[1] It may appear counterintuitive that $\kappa \propto d$, however, since we are in the ballistic regime, the transported heat does not depend directly on d and therefore the apparent κ increases with d.

Appendix B

Further Errors of Thermoelectric van der Pauw Measurements

In the error analysis of the thermoelectric van der Pauw method (Section 3.4) several errors have been omitted. Though apparently less important than the errors discussed in the main text the errors that are analyzed here are consequential for at least two reasons. Firstly some of the errors are only less significant because of experimental measures to decreases them and secondly errors of less importance for this work may cause severe problems under different conditions or with different samples.

Errors that are discussed in the following include the effect of sample geometry (finite sample thickness) and contact arrangement (finite contact size, contact not placed exactly at the edges) (Section B.2), the effect of wire self-heating (B.3), thermal contact resistances (B.4) and electrical contact resistances (on the Harman ZT_H measurement) (B.5). It is furthermore explained why a resistance-temperature calibration is necessary in Section B.6, what the consequences of an incorrect calibration are (B.7), and how the errors of the two-heater van der Pauw method compare to the three heater method (B.8). At first, though, I want to discuss error propagation for the van der Pauw equation and justify discussing errors on a square sample with symmetrical contact arrangement.

B.1 Error propagation for the van der Pauw equation

The quantities obtained from the van der Pauw equation (3.2) are σ and κ, but experimental errors occur for e.g. the measured resistances $R_{21,43} := R_1$ and $R_{31,42} := R_2$. To relate the errors in the measured quantities to the errors in σ and κ error propagation has to be discussed. The van der Pauw equation (3.2) is transcendental, but

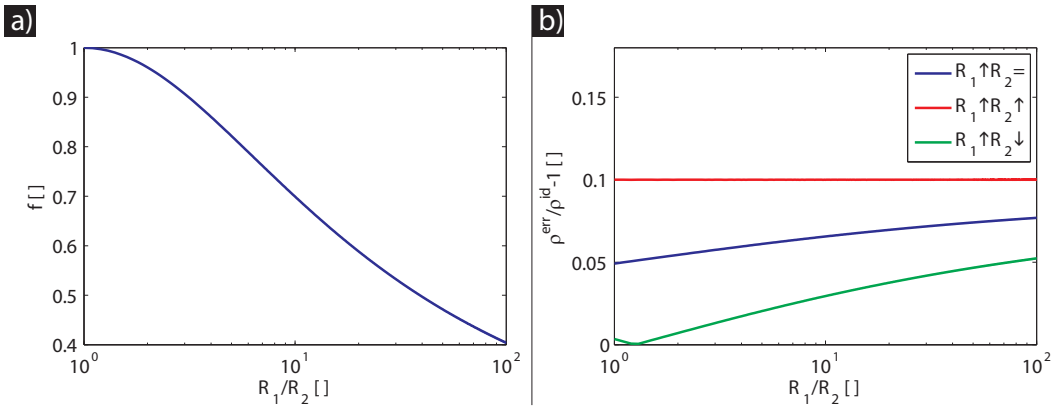

Figure B.1: a): f from Eq. (B.1). b):Relative error in ρ for $R_1 \neq R_2$, if R_1 is 10% too large (blue), R_1 and R_2 are measured 10% too large (red), and if R_1 is measured 10% too large and R_2 10% too small. The error is largest if both R_1 and R_2 are measured too large and is the same as for the special case $R_1 = R_2$

can be rearranged to [vdP58a]

$$\rho = \frac{\pi d}{\ln 2} \frac{R_1 + R_2}{2} f(R_1/R_2)\,, \tag{B.1}$$

where $f(R_1/R_2)$ depends on the ratio of R_1/R_2 only and varies slowly with it. For $R_1 = R_2 \;\rightarrow f = 1$ and

$$\rho = \frac{\pi d}{\ln 2} R_1 \tag{B.2}$$

holds. If uR_1 is the relative error of the measured resistance and ud the relative error of the measured thickness then the uncertainty of the calculated resistivity is

$$\frac{u\rho}{\rho} = \frac{uR_1}{R_1} + \frac{ud}{d}\,. \tag{B.3}$$

For a sample of arbitrary shape and contacts anywhere at the sample edges $R_{21,43} \neq R_{31,42}$. In this case the solution given by Eq. (B.1) and f is defined by [vdP58b]

$$\cosh\left[\frac{R_1/R_2 - 1}{R_1/R_2 + 1 \frac{\ln 2}{f}}\right] = \frac{1}{2} \exp\left[\frac{\ln 2}{f}\right]\,. \tag{B.4}$$

The geometrical function f is plotted in Figure B.1a) and it can be seen that it varies slowly with R_1/R_2.

The special case $R_1 = R_2$ was discussed previously, here we want to analyze how errors in R_1 or R_2 affect ρ for $R_1 \neq R_2$. Or put differently, if R_1 is measured 10% too large, how much is ρ off from the correct value? Figure B.1b) shows the relative error of ρ, which is given by $|1 - \rho^{\mathrm{err}}/\rho^{\mathrm{id}}|$ for various R_1/R_2. ρ^{id} is given by Eq. (B.1) and for ρ^{err} three limiting cases are considered: Firstly, only R_1 is 10% too large but

R_2 has the correct value; secondly, both R_1 and R_2 are 10% too large; thirdly R_1 is 10% too large and R_2 is measured 10% too small. It can be seen that the relative error is largest for the second case and smaller for the other two. However, this is the same relative error as for symmetric van der Pauw equation (B.2) and so Eq. (B.3) is indeed an upper limit for the relative error.

B.2 Systematic errors due to sample and contact geometry

For the van der Pauw equation to be exactly valid (see Eqs. (3.2) and (3.3)) the sample has to be homogeneous, free of holes and the infinitesimal small contacts have to be at the edge of the sample. It is furthermore required that the current flow is purely two-dimensional, i.e. homogeneous over the sample thickness and that the sample is insulated from the environment except for the two points where the current enters and leaves.

Several authors, including van der Pauw himself, have investigated the effect of violations to these initial assumptions [vdP58a, Koo89]. It turns out that the van der Pauw method is quite robust against deviations from the ideal conditions, as discussed in the following. Weiss *et al.* solved the electrostatic problem of a square sample with side length a and finite thickness d [Wei08]. For this geometry, which resembles the geometry of the used Ni and InSb samples, they investigated the effect of contacts with finite size δ, that are placed a distance Δ away from the sample edge. They found that the agreement between measured and actual sample conductivity is better than 2% for $d/a < 0.5$. Finite sized contacts cause deviations of $< 1\%$, as long as $\delta/a < 0.15$ and $\Delta/a < 0.1$.

In order to prove that contact size and placement lead indeed to small systematic errors, electrical van der Pauw measurements were performed on a sample with six contacts, which are referred to as E_1 to E_6, counted clockwise. The contacts were arranged in an arbitrary manner at the sample edge and while being small, did not have the same size. With six contacts 12 independent measurements with two configurations can be taken. The resistances depend on the contact geometry and can therefore differ by one order of magnitude. The resistivities calculated from the two corresponding measurements, however, coincide nicely as presented in Figure B.2a). It was found that the measured resistivities deviate by less than 1.5% from their average value as visualized in Figure B.2b). For comparison the result of the room temperature measurement with a linear four-probe station [Sch06] is also shown, which agrees well with the van der Pauw measurements. It can be concluded that contact size and (dis)placement does have a small effect on the measured conductivity values and that for electrical measurements the error is $\approx$ 1.5%.

The effect of a finite sample thickness was investigated experimentally by Kasl and Hoch [Kas05]. They measured samples with a cylinder geometry and obtained

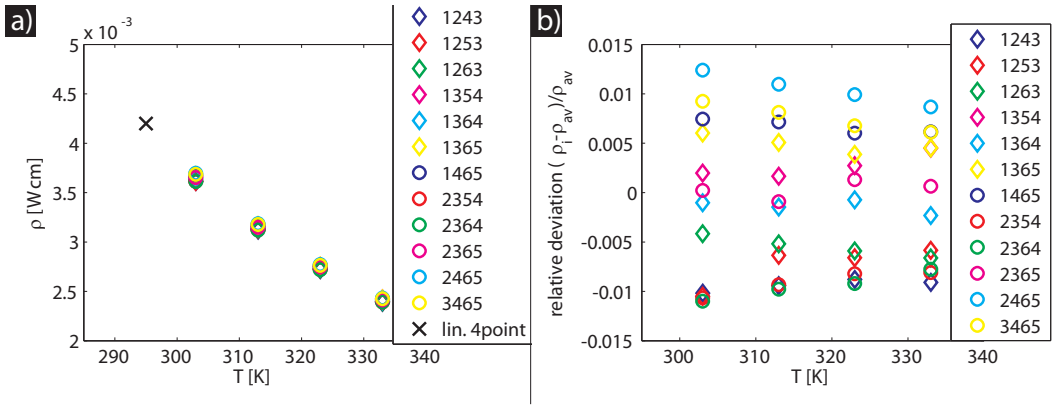

Figure B.2: Electrical van der Pauw measurement of an InSb sample with six contacts. With six contacts 24 resistivity measurements are possible and from the two corresponding resistances 12 resistivities can be calculated. These 12 resistivities calculated with the van der Pauw equation (3.2), agree with each other very well as shown in a). The legend labels the 12 results, where "1243" means $I^+ = E_1, I^- = E_2, U^+ = E_3, U^- = E_4$ and the contacts on the sample are labeled clockwise. The black cross is the result of a linear four-probe measurement and agrees well with the (extrapolation of the) van der Pauw results. b) shows the deviation of each resistivity ρ_i from their mean value ρ_{av} and it can be seen that this deviation is less than 1.5%.

results comparable to the calculations of Weiss *et al.* For the used Ni sample $d/a = 0.025$ and for the InSb sample $d/a = 0.05$, therefore the error due to the finite thickness is in both cases $< 1\%$.

It should also be noted that in other cases, where sample or contact geometry are such that large systematic deviations occur, the obtained experimental values can be multiplied with correction factors [Wei08] to account for sample and contact geometry. Furthermore, incorrections due to the finite sample thickness can be circumvented totally if the contacts are placed at the side faces of the sample. In this geometry the current flow is two-dimensional for all sample thicknesses, provided the contacts are as high as the side faces. In this case the current can enter the sample uniformly, as pointed out by Kasl and Hoch [Kas05].

Apart from the effect of finite sample thickness on the measurement results an error in the thickness measurement also affects the calculated conductivities, see Eq. (B.3). By means of scanning electron microscopy and micrometers the thickness can be determined with an relative error $< 1\%$.

The error due to finite sample thickness and errors in the thickness measurements are the same for the κ measurement as for the σ measurement, i.e. $< 1\%$. The effect of contact size and contact placement can be estimated from [Wei08]: using $\delta/a = 0.12$ and $\Delta/a = 0.06$, the sum of both relative errors amounts to 0.3%. Since it was found experimentally that for σ the error due to contact size and placing

is of the order of 1.5%, this larger, experimental value is used, rather than the smaller theoretical predictions. Therefore, for the employed samples and contacts, the geometrical errors are assumend to be the same for the σ and the κ measurement.

paragraphThe effect of finite sample thickness on the S measurement

The finite sample thickness can cause a systematic error for the Seebeck measuremen. If the heaters are placed at the top of the sample (Figure 3.4) and not at the side surface the temperatures will differ at top and bottom side of the sample, the less the thinner the sample. If the electrical contacts are placed at the bottom side, as was done in our experiments, the Seebeck coefficient will be measured somwhat incorrectly. In order to quantify this, a COMSOL simulation was performed. Using the parameters of the InSb sample, the calculated temperatures at the thermometers H_4 and H_3 where compared to the temperatures at the same lateral positions, but at the bottom side. For the temperatures at the center of H_4 and H_3 the calculation results are $\Delta T_{43}^{\mathrm{top}} = 313.504\,\mathrm{K} - 312.521\,\mathrm{K} = 0.983\,\mathrm{K}$. At the bottom the temperature differences is $\Delta T_{43}^{\mathrm{bot}} = 313.502\,\mathrm{K} - 312.526\,\mathrm{K} = 0.976\,\mathrm{K}$, thus 99.3% of the measured temperature. For the samples measured this systematic error is of minor concern, but will clearly become more important for larger thickness/side length ratio. Note that the error due to finite sample thickness for the Seebeck coefficient measurement is not the same as for the σ and κ measurement, which was discussed in Subsection B.2, although both arise from deviations from purely two-dimensional current flow.

B.3 Self heating of the wires

While long and thin wires are ideal to minimize parasitic heat conduction one also has to be aware of Joule heating of the wires. The wires, where the heating current is driven through, produce Joule heating $P_{\mathrm{J}} = RI^2$. Since a fraction of the Joule heat produced in the wires flows into the heater and the sample this will create a heat flow through the sample. This heat flow is additional to the measured heat flow that is produced in the heater and used in Eq. (3.3). The resulting error will be negligible as long as the resistance of the wires is much smaller than the resistance of the heater $\approx 1000\,\Omega$ but sets an upper limit on how long and thin the wires can be made[1]. For our experiments the resistances of the wires were less than $1\,\Omega$ and therefore did not heat sufficiently to affect the thermal conductivity measurement.

B.4 The influence of thermal contact resistances

Both the analytical and the numerical analysis have so far disregarded the effect of thermal contact resistances that occur between the heater/thermometers and the

[1] One might consider taking a wire material with low thermal but high electrical conductivity, but since electrons are responsible for charge *and* thermal transport in metals both conductivities are coupled, as expressed by the Wiedemann-Franz law, see Eq. (1.11).

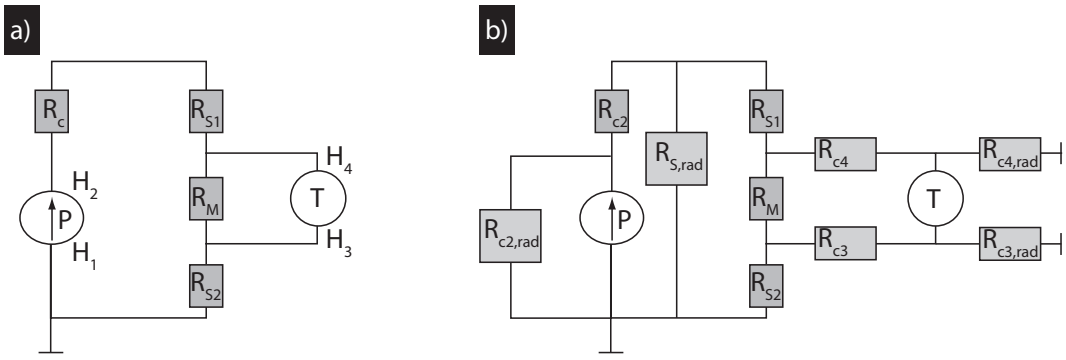

Figure B.3: Circuit diagram for thermal van der Pauw measurement.

sample. It will be shown here, that their effect is indeed negligible. In order to analyze the problem, the thermal van der Pauw measurement has been "translated" into a circuit diagram.

The circuit diagram corresponding to the thermal van der Pauw measurement without radiation losses is shown Figure B.3a), while in Figure B.3b) these are taken into account. Without radiation, one can see a simple series connection of a heat source P, a contact resistance R_c between heat source and sample, and the sample thermal resistance $R_S = R_{S1} + R_M + R_{S2}$. H_1 to H_4 label heat sink, heat source and the two thermometers as in Figure 3.4. The measurement signal is the temperature difference that drops over a fraction R_M of the total sample resistance: $T_M^{\mathrm{id}} = T_4 - T_3 = R_M P_{tot}$. Since it is a series connection the magnitude of R_c does not affect the amount of heat flow through the sample and the measurement signal, i.e. disregarding radiation losses contact resistances do not affect the measurement as expected. The diagram is drawn such that the heat sink (the cold "side" of the heat source) is at the same temperature as the cold side of the sample and the ambient, the "ground". One could consider a thermal contact resistance between sample and heat sink however this resistance can be expected to be small compared to the heater contact resistance. While the heater was glued onto the sample, contact at the heat sink was done by mechanical clamping, with graphite or silver foil for good contacts. This usually results in contact resistances orders of magnitude smaller than gluing [Kho97].

The circuit diagram including radiation losses is shown in Figure B.3b). Radiation losses of the sample itself are treated as a thermal resistance $R_{\mathrm{S,rad}}$ in parallel to the sample resistance. This has been analyzed before, see Eq. (3.39). Not considered beforehand were radiation losses of the heater and of the thermometers. They are considered as heat leakages through the thermal resistance $R_{\mathrm{c2,rad}}$, $R_{\mathrm{c4,rad}}$, and $R_{\mathrm{c3,rad}}$ to ambient temperature (ground).

The amount of radiative heat loss of the heater can be calculated from comparing $R_{\mathrm{c,rad}}$ with the sum of the other thermal resistance in the system, labeled R_{sum}.

Using the rules for electrical parallel and series circuits this can be calculated to

$$R_{\rm sum} = R_{\rm c2,rad} + \frac{R_{\rm S,rad}(R_{S1} + R_M + R_{S2})}{R_{\rm S,rad} + R_{S1} + R_M + R_{S2}} = R_{\rm c2,rad} + \frac{R_{\rm S,rad} R_S}{R_{\rm S,rad} + R_S}\,. \tag{B.5}$$

The fraction of the heat that flows through the contact resistance $P_{\rm Rc2}/P$ is given by

$$\frac{P_{\rm Rc2}}{P} = \frac{R_{\rm c2,rad}}{R_{\rm c2,rad} + R_{\rm sum}}\,, \tag{B.6}$$

and it is clear that this significantly deviates from the ideal value (unity) if $R_{\rm c2,rad} \approx R_{\rm sum}$. If heat loss of the sample itself is considered the heat flow splits again after $R_{\rm c2}$ and a fraction will be lost across $R_{\rm S,rad}$. Only the fraction that enters the sample P_{S1} causes the measured temperature difference and this (normalized) heat flow is given by

$$\frac{P_{S1}}{P} = \frac{R_{\rm c2,rad}}{R_{\rm c2,rad} + R_{\rm sum}} \frac{R_{\rm S,rad}}{R_{\rm S,rad} + R_S}\,, \tag{B.7}$$

Let us now consider the effect of the thermal contact resistances of the thermometers. Without radiation losses, the measured temperature difference is given by $\Delta T^{\rm id} = R_M P_M$. If radiation is considered a parasitic heat flow from the sample through the thermometer will occur. This heat flow is determined by the contact and radiative resistance and given by

$$P_{\rm c4,rad} = \frac{T_4 - T_1}{R_{\rm c4} + R_{\rm c4,rad}}\,; \tag{B.8}$$

$P_{\rm c3,rad}$ is given similarly. This has two effects: first the heat flow through R_M is reduced compared to P_{S1}

$$\frac{P_{RM}}{P} = \frac{P_{S1}}{P} \frac{R_{\rm c4} + R_{\rm c4,rad}}{R_{\rm c4} + R_{\rm c4,rad} + R_M + R_{S2}} \tag{B.9}$$

$$= \frac{R_{\rm c,rad}}{R_{\rm c,rad} + R_{\rm sum}} \frac{R_{\rm S,rad}}{R_{\rm S,rad} + R_S} \frac{R_{\rm c4} + R_{\rm c4,rad}}{R_{\rm c4} + R_{\rm c4,rad} + R_M + R_{S2}}\,, \tag{B.10}$$

and secondly this parasitic heat flow causes a temperature difference at the contact resistance: $\delta T_4 = P_{\rm c4,rad} R_{c4}$. The measured temperature difference is now given by $\Delta T^{\rm real} = R_M P_M - (\delta T_4 - \delta T_3)$. Note that heat loss through the thermometers decreases both measured temperatures, therefore the temperature difference is less affected than the individual temperatures. In fact, if $R_{\rm c4} = R_{\rm c3}$ and $R_{\rm c4,rad} = R_{\rm c3,rad}$, as can be roughly expected, the measured temperature difference depends only on the temperature difference between the thermometers, not on the difference between thermometers and environment

$$\Delta T^{\rm real} = R_M P_M - R_{c4} \frac{T_4 - T_3}{R_{\rm c4} + R_{\rm c4,rad}}\,, \tag{B.11}$$

Finally, the ratio of measured temperature difference and ideal temperature differ-

ence is given by

$$\frac{\Delta T^{\text{real}}}{\Delta T^{\text{id}}} = \frac{R_M P_{RM} - R_{c4}\frac{T_4-T_3}{R_{\text{c4}}+R_{\text{c4,rad}}}}{R_M P} = \frac{P_{RM}}{P} - \frac{R_{c4}}{R_{\text{c4}}+R_{\text{c4,rad}}}\,, \tag{B.12}$$

where Eq. (3.32) was used for the last replacement. With this equation the effect of radiation and thermal contact resistances can be quantified. The sample thermal resistance is given by $R_S = \Delta T/P$, where ΔT is the average temperature increase of the sample due to P. Using Eq. (3.31) and the parameters of the InSb sample R_S is estimated to

$$R_S = \frac{\ln(\sqrt{2}a/\delta)}{\pi\kappa d} \approx 90\,\text{KW}^{-1}\,. \tag{B.13}$$

R_{S2} is roughly half of the total sample resistance, i.e. $50\,\text{KW}^{-1}$ and R_M can be calculated from Eq. (3.32): $R_M \approx 13\,\text{KW}^{-1}$. The resistance of the sample against radiative heat loss $R_{\text{S,rad}}$ can be calculated from Eq. (3.39)

$$R_{\text{S,rad}} = \frac{\Delta T}{P_{\text{loss,rad}}} == \frac{1}{8a^2\epsilon\sigma_B T_0^3 \ln(\sqrt{2}a/\delta)} \approx 1400\,\text{KW}^{-1}\,. \tag{B.14}$$

Similarly, $R_{\text{c,rad}}$ can be computed to $R_{\text{c,rad}} \approx 10^5\,\text{KW}^{-1}$ and is thus much larger than any other resistance. The only remaining unknown are the contact resistances R_c. Those were determined using thermography: the heater were supplied with electrical power and from the observed temperature difference between heater and sample the contact resistance can be estimated. Testing several heaters we found that the thermal contact resistances were $R_c \leq 100\,\text{KW}^{-1}$. Inserting those numbers yields

$$\frac{P_{RM}}{P} = 0.999 \cdot 0.940 \cdot 0.999 \tag{B.15}$$

$$\frac{\Delta T^{re}}{\Delta T^{id}} = 0.938 - 0.001 = 0.937 \approx \frac{R_{\text{S,rad}}}{R_{\text{S,rad}} + R_S} \tag{B.16}$$

It can be seen that the measured temperature difference is affected by radiation losses, as discussed previously. However, the additional effect of the thermal contact resistances between sample and heaters/thermometers leads to relative errors of $\approx 0.1\%$ and is negligible small. Generally, the error due to contact resistances will be $\approx\propto R_c/R_{\text{c,rad}}$. It is no problem to keep this ratio below 1%[2]. In summary the effect of the contact resistances was shown to be negligible and in this sense the measurement is a true four-point measurement. Note though, that the thermal contact resistances are comparable to the sample thermal resistance. If temperature differences were measured in a two-point fashion the results for the thermal

[2]Since the contact area and the emitting area are approximately the same, this can be discussed best in terms of the heat transfer coefficient $h = 1/(RA)$. The heat transfer coefficent is around $6\,\text{Wm}^{-2}\text{K}^{-1}$ for radiation at 300 K, while it can easily exceed $1000\,\text{Wm}^{-2}\text{K}^{-1}$ for mechanical contacts [Kho97, IV08].

conductivity would be grossly wrong.

B.5 Further errors of the HarmanZT_H measurement

Since the Harman ZT_H measurement is based on the formation of a temperature gradient it is affected by heat loss in the same way as the κ measurement, the same holds for the effect of wire self-heating.

Electrical contact resistances and wire heating Let us now investigate the effect of electrical contact resistances and wire resistance on the ZT measurement. Upon current flow a temperature gradient ΔT_P establishes between the two voltage sensing electrical contacts due to Peltier heating and cooling. If there is an electrical contact resistance R_cont at the connection of sample and lead, Joule heat P_J will be produced:$P_\mathrm{J} = R_\mathrm{cont} I^2$.

Likewise, heat is produced in the wires through which the current is driven, due to their intrinsic resistivity. A fraction of this heat will flow into the sample and create a temperature gradient within the sample. This temperature gradient is superimposed on the Peltier gradient and the temperature difference between the two sensing contacts changes by ΔT_J. Since

$$ZT_\mathrm{H,meas} = \frac{U_\mathrm{S,meas}}{U_\Omega} = -S\frac{\Delta T_\mathrm{P} + \Delta T_\mathrm{J}}{U_\Omega} \tag{B.17}$$

this also effects the measured $ZT_\mathrm{H,meas}$. Correct measurements can be taken if the current direction is changed. While the Peltier temperature gradient changes its direction with the applied current, the gradients due to electrical resistances are unaffected. Thus ZT can be obtained correctly by averaging the results for both current directions (superscripted with "+" and "-"):

$$ZT^+_\mathrm{H,meas} = -S\frac{\Delta T_\mathrm{P} + \Delta T_\mathrm{J}}{U^+_\Omega} \tag{B.18}$$

$$ZT^-_\mathrm{H,meas} = -S\frac{-\Delta T_\mathrm{P} + \Delta T_\mathrm{J}}{U^-_\Omega} = -S\frac{+\Delta T_\mathrm{P} - \Delta T_\mathrm{J}}{U^+_\Omega} \tag{B.19}$$

$$\Rightarrow ZT_H = (ZT^+_\mathrm{H,meas} + ZT^-_\mathrm{H,meas})/2\,. \tag{B.20}$$

Both, the effect of electrical resistances on the ZT measurement and also the cancellation upon averaging can be seen from Figure B.4, where measurement data from an InSb sample is presented[3]. In Figure B.4a) the ZT measured for different currents is shown, the average of the values is plotted for comparison as thin black line. It can be seen that $ZT^+_\mathrm{H,meas} < ZT^-_\mathrm{H,meas}$ for all temperatures and that the ZT values measured with 5/10 mA deviate approximately by 5/10% from their mean. It is now necessary to check whether wire or contact resistance can indeed explain

[3]The data shown here has not been corrected for the Seebeck coefficient of the used Ni wires.

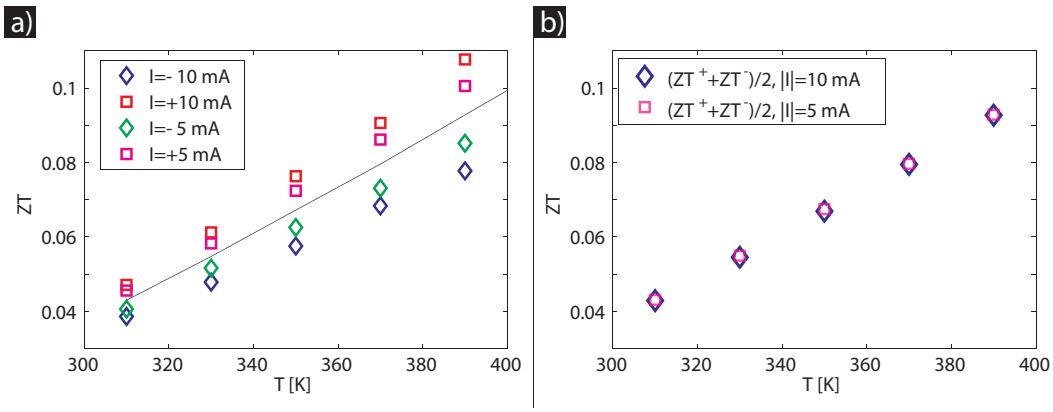

Figure B.4: The effect of Joule heating on the ZT_H measurement. a) Measured ZT_H over temperature for different currents. It can be seen that the measured ZT is always smaller for a positive current than for a negative current. The difference between both values increases with increasing current, the mean of all values is plotted in black. Averaging the measurements of "+" and "-" yields a constant value, independent of current magnitude as shown in b). This illustrates that the effect of electrical contact resistances and wire self-heating can be overcome if both current directions are measured.

the observed values. With $S \approx 3 \cdot 10^{-4}\,\mathrm{VK}^{-1}$ the Peltier heating/cooling is approximately $P_\mathrm{P} = 9 \cdot 10^{-4}\,\mathrm{W}$ for the InSb sample at 300 K and a current of 10 mA. The sum of wire and contact resistance is of the order of 1 Ω and thus the Joule heating amounts to $P_\mathrm{J} = (0.01\,\mathrm{A})^2 1\,\Omega = 1 \cdot 10^{-4}\,\mathrm{W} \approx 0.11 P_\mathrm{P}$. Thus the experimental observed deviations of ZT_H can be explained by the effect of Joule heating due to wire/contact resistances. Since $P_\mathrm{P} \propto I$ but $P_\mathrm{J} \propto I^2$ it is also clear that the deviation of the measured ZT_H from the mean ZT_H increases linearly with current, as can be seen in Figure B.4a). As predicted by Eq. (B.20) the average of $ZT^+_{\mathrm{H,meas}}$ and $ZT^-_{\mathrm{H,meas}}$ is independent of current magnitude and the "correct" ZT_H value.

B.6 Errors of the temperature measurement

The thermoelectric measurements are performed temperature-dependently, where the reference temperature is the temperature of the heat sink. This temperature is measured by a Pt1000 resistance thermometer, see Figure 3.1. The accuracy of the Pt1000 (class B) is specified as $\Delta T = \pm(0.30\,^\circ\mathrm{C} + 0.005T)$ [wik10b], where T is here measured in °C. Thus measuring ca. 150 K around room temperature the resulting uncertainty is of the order of 1 K, which is not sufficient for thermoelectric van der Pauw measurements. However, this large uncertainty is basically an offset between different Pt1000 and stems from differences in the fabrication process. The resistance-temperature coefficient is exact and the reproducibility of Pt1000 readings is very high. Furthermore, only temperature differences have to be know for

the thermoelectric van der Pauw measurements with a high accuracy, not absolute temperatures. One can therefore circumvent the inaccuracy problem by performing a resistance-temperature calibration. To do so, the heat sink temperature was changed and resistance readings of the two sensing Pt1000 were taken, once the temperature of the sample and thus the resistances were stable. The readings were stable within 0.1 Ω and the average of 20 points was taken, i.e. temperature differences were measurable with an accuracy of 0.01 K. The described resistance-temperature calibration was included in each thermoelectric van der Pauw measurement.

In contrast, the absolute temperature is known with smaller accuracy and given by the stated equation for a class B Pt1000, see Eq. 3.4. One should note also that both the S and the κ measurement rely on a temperature gradient within the sample. Since the cold side (heat sink) temperature is kept stable this means that the average temperature of the sample increases slightly upon heat flow. For the Ni sample the difference between heat sink and average sample temperature was $\leq 2\,\mathrm{K}$ and for the InSb sample $\leq 4\,\mathrm{K}$. For materials that posses moderately temperature-dependent properties this is acceptable, for other materials smaller heat flows might be necessary.

B.7 Error due to incorrect resistance-temperature calibration

While a resistance-temperature calibration is necessary for accurate temperature difference measurements it can also be a source of measurement errors. If the thermal contact between sample and heat sink is not good and the temperature of the heat shield is lower than the heat sink temperature, the temperature of the sample can deviate from the heat sink temperature due to thermal exchange with the environment. A calibration under such conditions is shown in Figure B.5. For the small temperature region shown a linear resistance-temperature fit is sufficient (see Eqs. (3.4) and (3.5)) and the parameters for the linear fit of each thermometer are given in the figure. Also shown is the expected resistance temperature curve for a Pt1000. One can clearly see that measured and expected values differ more than can be explained by normal variations between different Pt1000. Furthermore, the differences increase with higher temperatures. This is what one would expect if the heat shield is coupled insufficiently to the heat sink and therefore the temperature difference between heat sink and heat shield increases with rising temperature. In consequence the sensing thermometers are not at heat sink temperature when they are calibrated. This leads to two errors: firstly, for all types of measurements, the reference/heat sink temperature does not correspond to the average sample temperature. For the data shown in Figure B.5a) this means that a measurement with a reference temperature of 370 K would actually be taken at $\approx 355\,\mathrm{K}$. Secondly, the S and κ measurement are affected. Both are determined from measured temperature

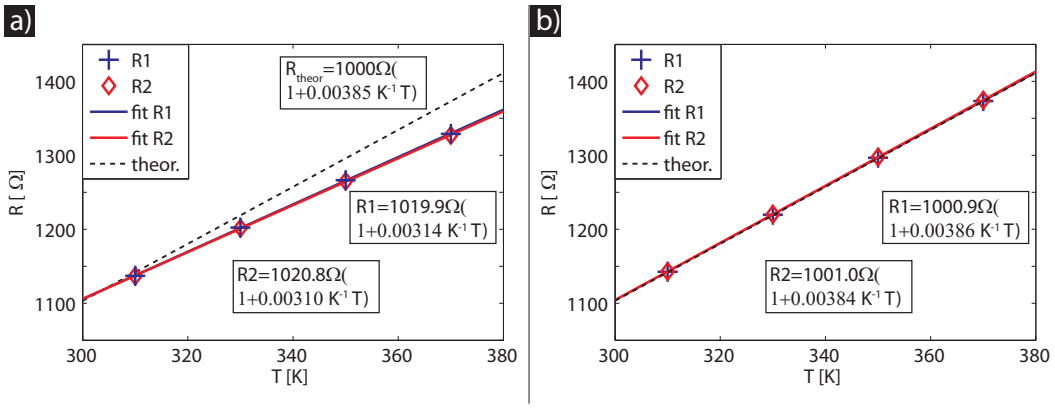

Figure B.5: Correct and incorrect resistance temperature calibration of the two sensing Pt1000 on the same sample. In a) the measured resistances R1 and R2 are lower than expected from a Pt1000 at heat sink temperature. The reason is radiative exchange of the sample with a heat shield at too low temperature, which causes the sample temperature to be below the heat sink temperature as well. For the measurement shown in b) the heat shield temperature was regulated with an independent heater-temperature control loop to match the heat sink temperature. In this case the measured resistances follow closely the expected values.

differences and since

$$R(T) = R_0(1+\alpha T) \;\Rightarrow\; \Delta T \;=\; \alpha(R_1 - R_2) \tag{B.21}$$

$$\kappa \propto \frac{1}{R^{\mathrm{th}}} \propto \frac{1}{\Delta T} \;\propto\; \frac{1}{\alpha} \tag{B.22}$$

$$S \propto \Delta T \;\propto\; \alpha\,, \tag{B.23}$$

κ is measured too large and S too small if the linear resistance coefficient α is calibrated too small.

The described problem can easily be circumvented by a good thermal exchange between heat shield, heat sink and sample and/or by a separate temperature regulation for the heat shield. A calibration for the same sample this time with separate heating of the shield can be seen in Figure B.5b). Here the expected and the measured values lie very close together.

B.8 Errors of the two-heater thermoelectric van der Pauw measurement

Now the systematic errors of the two-heater measurement are to be discussed in comparison with the three-heater measurement. Most prominent of the errors was the effect of heat loss by radiation. Using for error analysis again the simplified form

of the van der Pauw equation for symmetrical contacts (3.13) can be written as

$$\frac{\kappa}{S} = -\frac{\ln 2}{\pi d}\frac{P}{U_S}\,. \tag{B.24}$$

Since $U_S \propto \Delta T$, the κ/S measurement is thus affected by radiation loss. For a given P the established temperature difference and thus the Seebeck voltage will be too small, consequently κ/S will be determined too large. The amount of the error is the same as for the κ and ZT measurement described in Section 3.4 and can be estimated by Eq. (3.39). The Seebeck coefficient is determined from the product of ZT and κ/S using Eq. (3.17) and since the former is measured too small and the latter too large with the same systematic error, S itself is not affected by radiation losses. The thermally conductivity finally, is determined too large due to radiation losses, see Eq. (3.19). This analysis is qualitatively supported by the measurement results shown in Figure 3.10. The measured ZT is smaller than the reference ZT and the difference increses for higher temperatures. The Seebeck coefficient S, on the other hand, shows good agreement with the reference data, while κ is determined clearly too large. The three-heater and two-heater κ should be affected equally by radiation losses and it remains unclear why the two-heater measurements exhibits systematically larger deviations from the reference data than the three-heater data.

Appendix C

Fabrication of Porous Silicon

The section will start with a short outline on general Si (electro-)chemistry. The different types of pS will be introduced and the different mechanism leading to pore formation will be discussed. The effect of sample parameters (doping, orientation) and etching parameters (composition of the etching solution, applied bias) on the resulting pore geometry will be analyzed. In addition, SEM images of the samples used for characterization but not shown in the main text are presented. Porous Si can be categorized according to the pore diameter. Following the IUPAC convention, microporous Si has pore sizes below 2 nm, mesoporous between 2 nm and 50 nm and macroporous Si pore diameter > 50 nm[Iup72]. Measurements were performed mainly on mesoporous Si from n-type wafers.

Electrochemical dissolution of Si Si can be dissolved in a solution containing HF under anodic bias. A typical electrochemical cell is sketched in Figure 4.1a).

Under anodic bias, i.e. with a negative electrical potential at the silicon sample compared to the other electrode, two different electro-chemical reactions are possible to dissolve Si. Applying a current density below a critical current density Si is dissolved directly

$$\mathrm{Si} + 4\mathrm{HF}_2^- + \mathrm{h}^+ \rightarrow \mathrm{SiF}_6^{2-} + 2\mathrm{HF} + \mathrm{H}_2 + \mathrm{e}^- \,, \tag{C.1}$$

while above this threshold current density Si is first oxidized and then dissolved by HF:

$$\begin{aligned} \mathrm{Si} + \mathrm{H_2O} + 4\mathrm{h}^+ &\rightarrow \mathrm{SiO_2} + 4\mathrm{H}^+ && \text{(C.2)} \\ \mathrm{SiO_2} + 2\mathrm{HF}_2^- + 2\mathrm{HF} &\rightarrow \mathrm{SiF}_6^{2-} + 2\mathrm{H_2O}\,. && \text{(C.3)} \end{aligned}$$

In both reaction paths holes (h^+) are consumed. The samples used were fabricated below the critical current density, i.e according to Eq. (C.1). Details and microscopic reaction analysis can be found in the literature [Leh02].

Formation of porous Si The formation of porous Si by etching has been the object of intense research and several models have been developed [Smi88, Joh95, Cul97]. Indeed, even knowing that Si can principally be dissolved electrochemically in HF, the questions remains why a porous structure is formed (and Si is not dissolved completely) and why the obtained structures often show a certain regularity e.g in terms of interpore distance. The fact that parts of the initial silicon wafer are etched away, while others remain, shows that there is a "passivation" mechanism at work which protects some Si parts but others not.

One of these mechanism is of quantum mechanical nature and stems from the fact that the Si bandgap increases if the structure size approaches the exciton bohr radius, which is around 5 nm for Si [Rea92]. The dissolution of Si requires consumption of a hole h^+ as shown in Eqs. (C.1) and(C.2). With decreasing wall size the holes from the bulk need additional energy to enter the confined region since the band gap increases with decreasing size [Leh91]. At given experimental conditions hole injection into the confined area becomes energetically unfavorable below a certain structure size, the Si dissolution stops and the confined area is stable. At the unconfined regions hole consumption is still possible and so these are etched. The quantum confinement passivation mechanism is responsible for pSi with structure sizes of a few nm, the so-called microporous Si [Leh02]. This etching mechanism shows no dependence on crystal orientation nor doping [Leh02]. The quantum confinement effect is also the reason for the experimentally observed blue shift of the absorption and the visible photoluminescence, which led to an extensive research on pSi in the last two decades [Leh91, Cul97, Hoc09]. Often a thin layer of microporous Si covers meso- or macropores.

The second passivation and pore formation mechanism arises from the applied electrical field: n-type Si is under reverse conditions if the positive electrode is at the sample. Therefore a depleted region (also called space charge region) with the width width w_{SCR} forms between the electrolyte and the bulk Si. This depleted region forms an energy barrier for hole consumption but can be overcome by charge carriers by several mechanisms, e.g. tunneling and avalanche breakdown. The curvature of the Si/electrolyte interface is largest at the pore tip. Therefore the electric field is larger at the pore tips than at the pore walls. This implies that the depletion layer can be overcome more easily at the pore tips, while the pore walls are protected. Different types of passivation breakdown lead to different structure sizes and pSi types. Tunneling is the relevant mechanism for the formation of mesoporous Si, while thermionic emission and minority carrier collection (created e.g. by illumination) are responsible for the formation of macroporous Si.

The depleted region is also the reason why macro/meso pSi usually shows a typical structure size: The pores tend to be separated by the twofold width of the depleted layer W_{SCR}. The distance can not be smaller because the region between two pores at this distance is depleted and hole consumption is unlikely. If the distance between two pores was much larger part of the Si in between would still be

active and another pore would be formed. The width of the depleted layer depends in general on the pore geometry, for a planar geometry it can be defined as

$$W_{\mathrm{SCR}} = \sqrt{\frac{2\epsilon\epsilon_0 V}{eN}}\,, \tag{C.4}$$

where $\epsilon \approx 11.9$ [Sze81] is the relative permittivity of Si, ϵ_0 the free space permittivity, e the elementary charge and N the dopant density. The voltage V is the build in potential of the Si/electrolyte contact (around 0.5V) minus the externally applied potential and kT/e [Leh02]. While Eq. (C.4) is only a rule of thumb for real pSi it nevertheless shows that the structure size can be tuned by the doping density of the sample used and by the externally applied voltage.

For the measurement of structure-size dependent thermal conductivity and for optimizing pSi thermoelectric properties samples with various structure sizes have been produced, examples are shown in Figure 4.1, Figure 4.9, and Figure C.1.

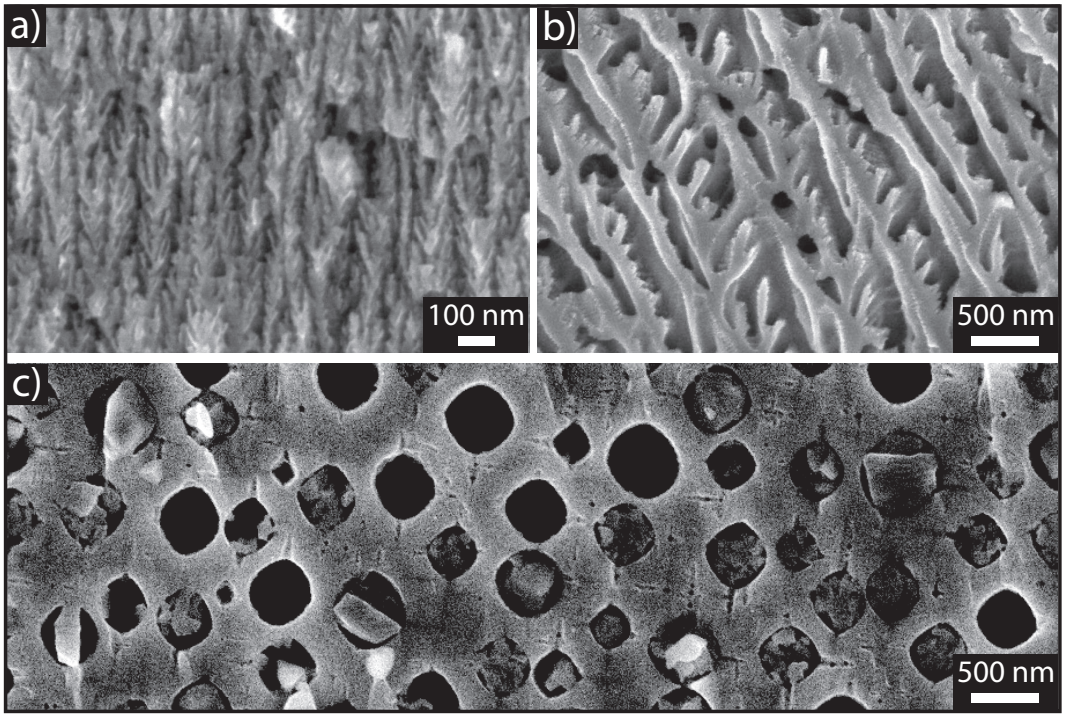

Figure C.1: SEM images of the samples not shown in the main text. a) Sample with porosity of $p = 0.43$. b) Image of the type of samples that was used for the electrical measurements discussed in Section 4.2, $p = 0.6$. d) Top view image of the macroporous Si sample after oxidation and mild etching to remove the microporous layer as well as cutting and polishing. The particles which fill some of the pores are residuals from the polishing process.

Figure 4.1c) and d) are magnified images of different regions of the sample shown

in 4.1b). It can be seen that the sample is approximately homogeneous on a microscopic scale. Sometimes a slight pore increase was observed with increasing film thickness, this is due to a decrease of the HF concentration. HF is consumed during the Si dissolution, and so if the pores become deeper the HF concentration sinks due to diffusion limitations. This can be prevented by a slow etching speed and so for the samples produced in house fabrication usually took several hours.

It was found experimentally that the porosity increases with current density and decreases with HF concentration. Furthermore, pore diameter increases with current density which can be applied to lift the pSi layer off the substrate and obtain a free-standing film[Leh00, Leh02, Sim95]. Free-standing membranes have been used for the electrical characterization discussed in Section 4.2, while films on substrates were used for the thermal conductivity measurements with the 3ω -method, see Section 4.3.

By adjusting fabrication parameters or initial wafer doping densities pSi samples with different structure sizes and porosities have been produced. Compared to SiNW the control about these parameters is less precise for pSi, however, pSi samples are macroscopic and can be characterized by macroscopic techniques which make them an object much easier to study.

Appendix D

Details and Error Analysis of the 3ω Method

This chapter gives further insight into the sample preparation, the instrumentation, and the data analysis that was employed to obtain the thermal conductivity data shown in Chapter 4. The results shown were divided by a correction factor which was of the order of 1.1. This correction factor is first motivated and afterwards details of the calculation are presented.

D.1 Details of the 3ω measurement

Let us discuss the experimental realization of a 3ω measurement first. A metal stripe used as heater and thermometer is a key component for the 3ω method and can be brought onto the sample by lithographic pre-structuring, metal evaporation and subsequent lift-off. In order to insulate the sample electrically from the metal stripe a thin insulation layer needs to be brought onto the sample, this can be done by evaporating, sputtering or spin-coating. The such prepared sample is brought onto a sample holder similar to what is shown in Figure 3.1b); electrical contacts between between 3ω heaters and the sample holder are made by soldering and high temperature silver paste (Polytec PT, Germany), while good thermal contact between sample and holder is ensured by thermally conductive paste (RS components, Germany). The sample is then mounted in the measurement system shown in Figure 3.1a); electrical connections are made to the measurement devices and the analyzing PC. The measurement devices comprises of a frequency generator (A33220 Agilent Technologies Inc., USA) and a signal conditioner. The frequency generator creates a periodic voltage signal at a chosen frequency which is transformed into a periodic alternating current. This current causes the measured voltage signal which contains the temperature amplitude information. In order to retrieve the 3ω signal it is necessary to eliminate the large 1ω component of the voltage signal. For this reason the excitation current is driven through a reference resistor that has the same

resistance as the metal heater but no temperature dependent 3ω component. In the signal conditioner the voltages from the metal heater and the reference resistor are subtracted so that mainly the 3ω signal from the metal line remains which can now be analyzed. This is illustrated in Figure D.1, where a) shows reference and sample signal before the subtraction and b) the difference of reference and sample signal, after the reference resistance was matched to the heater resistance. In b) a 3ω signal is clearly visible, while in a) it is buried in the much larger 1ω signal. The electronic components and the software were obtained from Fraunhofer IPM,

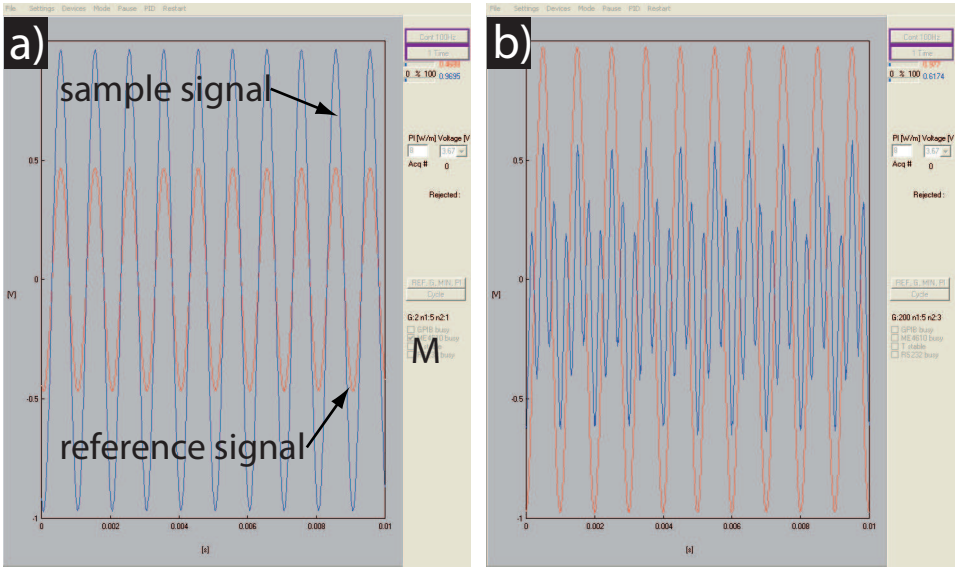

Figure D.1: Screenshot of 3ω measurement a): Initial phase of the resistance matching process. Red shows the reference signal, i.e. the voltage dropping over the internal reference resistor. Blue is the voltage signal from the heater on the sample; here only a signal proportional to the reference signal is visible, the 1ω signal with a frequency of 1000 Hz. During the resistance matching process the reference and the sample signal are subtracted and the remaining voltage is amplified; "M" indicates the current amplification factor. This is repeated iteratively until a clear 3ω signal is obtained as shown in b): final phase of the resistance matching process. The blue line is now the amplified result of reference minus sample voltage. It varies with triple frequency compared to the reference signal and is proportional to the temperature amplitude of the thermal wave in the heater. This 3ω signal is convoluted with a remaining 1ω signal. Note that the amplification factor is 200 in b), which shows that the 3ω signal is orders of magnitude smaller than the 1ω signal and explains the necessity of the resistance-matching algorithm.

Freiburg, Germany.

Let us now examine the measurement and data analysis process. The employed sample is fused silica ("Lithosil" Heraeus GmbH, Germany), wich was delivered as reference sample together with the setup. The thickness of the sample was 0.5 mm,

the heater width $b = 10\,\mu$m and the length of the heater 1 mm. As can be seen from Eqs. (4.6) and (4.8) the linear resistance-temperature coefficient α has to be known in order to obtain the thermal conductivity. Therefore, a resistance-temperature calibration was integral part of each 3ω measurement. Such a calibration is shown in Figure D.2 together with the obtained linear and quadratic resistance-temperature coefficient.

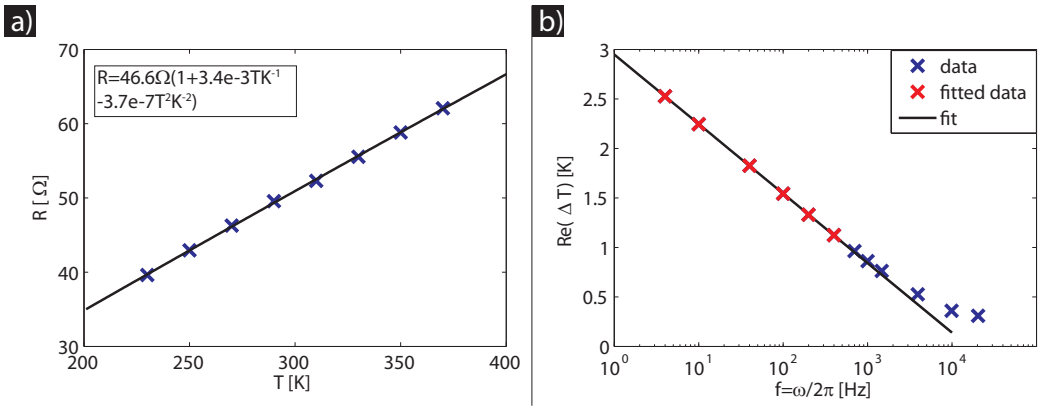

Figure D.2: a:) Resistance-temperature calibration for an evaporated Pt heater with width $2b = 10\,\mu$m and thickness ≈ 100 nm. The calibration is basically linear with a small quadratic component. A good resistance-temperature fit is crucial for the measurement. b): Real part of the temperature amplitude as a function of frequency (logarithmic); sample is fused silica. In the region where the thermal penetration depth is larger than half the heater width but smaller than the sample thickness $\Re(\Delta T) \propto \ln f$ and the thermal conductivity can be obtained from the slope. The frequency region that was used for fitting is indicated as well as the linear fit, which coincides very well with the measured data points. At higher frequencies a deviation from the linear fit can be observed, here the penetration depth becomes smaller/comparable to b and Eq. (4.8) becomes invalid.

The heater was made of platinum and it can be seen that the fit is basically linear with a small quadratic component. Comparing the obtained α with reference data for platinum, see e.g. Eq. (3.4) or Figure 3.5a), the question arises why α is smaller here. The reason is that thermally evaporated or sputtered metal films are usually polycrystalline. Due to increased charge carrier scattering the resistivity of the material increases, while the temperature dependence decreases compared to single-crystalline material [May70, Tel77, Tel79, Völ09].

After calibration the amplitude and the phase of the 3ω signal are measured for several frequencies at each chosen temperature. Temperatures could be chosen in terms of a start and a final temperature as well as a temperature interval. Measurement frequencies were fixed to $f = 1\,\text{Hz}, 4\,\text{Hz}, 10\,\text{Hz}, ..., 10000\,\text{Hz}, 20000\,\text{Hz}$ with the option to define up to ten additional measurement frequencies. As specified by the supplier, only the data for frequencies up to 1500 Hz is heavily re-

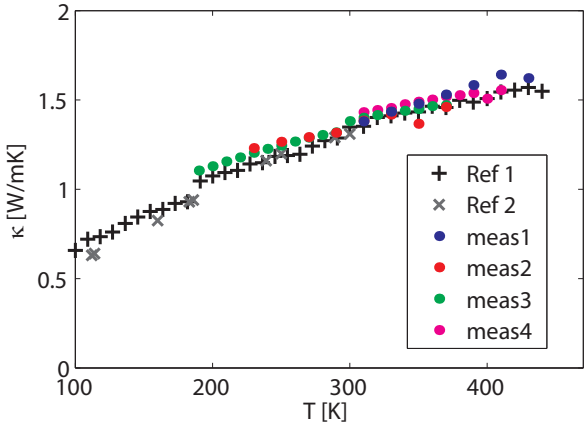

Figure D.3: Thermal conductivity of fused silica. The colored circles are the data from several measurements, while the black pluses are reference data provided from the 3ω setup vendor and the gray crosses are literature data from [Maq96]. The individual measurements are consistent with each other and differ from the reference data by less than 10%.

liable, which is why higher frequency data is sometimes shown but not used for thermal conductivity retrieval. In Figure 4.8b) the real part of the temperature amplitude is shown at a measurement temperature of 370 K over $\ln f \propto \ln \omega$. Up to frequencies of $\approx 1000\,\mathrm{Hz}$ the real part of the temperature amplitude decreases linearly with $\ln f$, for higher frequencies it decreases sublinearly. After Eq. (4.8) the thermal conductivity can be obtained from the slope of the linear regime, i.e. the regime where $b \ll |q^{-1}| \ll d$. Fused silica has the following properties: $\kappa \approx 1.4\,\mathrm{Wm^{-1}K^{-1}}$, $\rho \approx 2200\,\mathrm{kgm^{-3}}$, $c \approx 740\,\mathrm{Jkg^{-1}K^{-1}}$. This allows to calculate $|q^{-1}|$ and it is found that $|q^{-1}(f = 4\,\mathrm{Hz})| \approx 120\,\mu\mathrm{m}$ and $|q^{-1}(f = 400\,\mathrm{Hz})| \approx 12\,\mu\mathrm{m}$; i.e. for $4\,\mathrm{Hz} < f < 400\,\mathrm{Hz}$ the condition for the validity of Eq. (4.8) $b \ll |q^{-1}| \ll d$ is fulfilled. Therefore this frequency regime can be used for fitting and κ is obtained from

$$\kappa = \frac{P}{2\pi l} \frac{\partial \ln f}{\partial \Re(\Delta T)}\,, \tag{D.1}$$

where P, the power supplied to the heater, is predefined in the measurement program. A more thorough discussion on how good the condition $b \ll |q^{-1}| \ll d$ has to be fulfilled is given below.

The final result, the temperature dependent thermal conductivity of fused silica, is shown in Figure D.3. In order to convey a feeling for the accuracy of the 3ω method data from several measurements (colored circles) and reference data is shown. The individual measurements differ by less than 10%, i.e. the individual measurements are consistent. The black '+' (Ref1) is measurement data from the vendor of the equipment who measured on an identical sample. The grey crosses are literature data

from [Maq96][1]. The agreement between measurement data and the two references is better than 10%.

Some final remarks on the 3ω technique in general. First of all, the fitting region was estimated by calculating the thermal penetration depth from Eq. (4.7). The penetration depth itself depends on κ, the very quantity one wants to measure, so this approach may appear inconsistent. In most cases, however, one does have at least a vague expectation on the material properties and can make a guess for κ. Secondly, if the κ obtained from the slope and Eq. (4.9) is inconsistent with the κ that was used to estimate the fitting region one simply redefines the fitting region with the new κ and checks whether the results are consistent now. Thirdly if not chosen too large, the exact choice of the fitting region affects the results for κ only slightly. From Figure 4.8b) it can be seen that including one additional data point would have changed the fit and thus κ very little. Note also, that the fitting region can be different for different measurement temperatures if the sample thermal properties are strongly temperature dependent; this is not the case for used fused silica sample [Cah87, Yue06].

Compared to other thermal conductivity measurement techniques, the 3ω method has several advantages. While radiation losses are a fundamental, significant problem for steady-state measurement techniques these are of minor concern for the 3ω technique; for standard materials high accuracy is expected up to 1000 K [Cah87]. The reason for this is twofold: first the heated region is confined to a very small region of the sample and second the temperature increase per input power (and therefore the radiation loss) decreases with increasing excitation frequency.

In contrast to other transient techniques like Flash- and time-domain-thermoreflectance-method [Par61, Cah04] the 3ω method yields κ, not only the thermal diffusivity $D = \kappa/(\rho c)$. A further important advantage is that it can be used to measure the thermal conductivity of films on a substrate since the thermal wave can be confined into the film. This has been exploited for the thermal conductivity measurements of porous Si. It is furthermore worth noting that if applied as presented, i.e. κ obtained from Eq. (4.9), the method is insensitive to thermal contact resistances. The thermal resistance of a thin insulation layer or a thermal contact resistance would add a frequency independent contribution to the measured temperature amplitude. Since κ is obtained from the slope a constant offset does not affect the result.

The 3ω method can also be used to measure very thin films with a thickness in the order of 100 nm. For these kind of samples the thermal wave can usually not be confined into the film because the necessary frequencies are too high and the metal heaters too wide. Consequently κ can not be obtained from Eq. (4.9). Instead, κ is then obtained from the temperature amplitude difference between a sample with the to-be-measured film and a reference sample without it. Although less robust

[1] Note that the thermal conductivity of fused silica samples may slightly differ from each other due to differences in the production process.

this method has been employed successfully e.g. for superlattice structures grown by molecular beam epitaxy or chemical beam epitaxy [Yan02, Lee08b].

Drawbacks of the 3ω technique are the elaborated sample preparation and the requirement of flat surfaces for the lithography step.

D.2 Error analysis of the 3ω method

As mentioned in Section 4.3 the slope method (Eq. (4.9)) requires a frequency fitting region where $b \ll |q^{-1}(f)| \ll d$ holds; i.e. the thermal penetration depth has to be between film thickness and half the heater width. However, this statement is rather qualitative and it does not say how good the relation have to be fulfilled to get accurate results. That means that it is unclear what ratio between b and q^{-1} as well as d and q^{-1} is necessary so that Eq. (4.9) is accurate within the desired value. Furthermore, if the sample/heater geometries are fixed due to experimental restrictions it may be useful to calculate the error the slope method yields compared to an exact solution of the problem, since this error might be used as an correction factor.

Borca-Tasciuc *et al.* calculated the measured temperature amplitude of a heater with half-width b on a sample with finite thickness d and compared the results with the results from Cahill's simple slope formula Eq. (4.9)[BT01]. They assumed adiabatic boundary conditions on the bottom of the sample and studied the requirements for the slope equation to be correct. If a relative error of $<1\%$ is desired $ab \leq |q^{-1}(f)| \leq d/a$ with $a = 5$ must be fulfilled. On the other hand if $a = 1$ they found that the relative error of the thermal conductivity is $\approx 23\%$, a fact that has been repeatedly ignored in the analysis of experimental data, see e.g. [Ges97]. Their treatment shows that a large ratio of d/b is desirable for 3ω experiments. However, if this is not possible due to experimental restrictions, the deviations due to the sample geometry can be used as a systematic correction factor.

Adiabatic boundary conditions at the bottom of the sample correspond to a perfect thermal insulator. For the investigated pSi samples the situation is rather opposite: the porous layer with low conductivity is on top of a bulk Si substrate which has a very high thermal conductivity; this corresponds approximately to a sample with isothermal boundary at the bottom. Following their treatment the temperature amplitude at the heater for a sample with isothermal boundary conditions can be derived and is given by

$$\begin{aligned} \Delta T &= \frac{-P}{l\pi\kappa_y}\int_0^\infty \frac{-\tanh(Bd)}{B}\frac{\sin^2(b\lambda)}{(b\lambda)^2}\mathrm{d}\lambda \text{ with} \\ B &= (\kappa_{xy}\lambda^2 + \frac{2i\omega}{D})^{1/2}, \end{aligned} \tag{D.2}$$

where κ_y is the cross-plane and κ_x the in-plane thermal conductivity, $\kappa_{xy} = \kappa_x/\kappa_y$

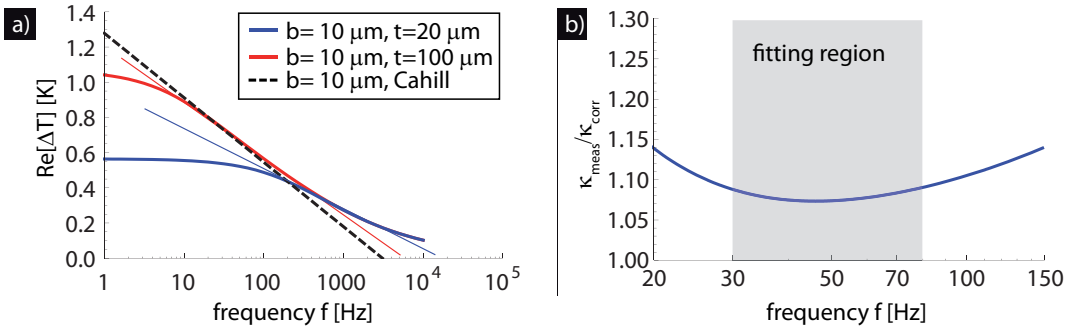

Figure D.4: a): Real part of the temperature amplitude for finite samples with different thicknesses (blue and red) and the limiting case of $d \to \infty$ from Eq. (4.8), whose validity is assumed for the experimental data. It can be seen that the slope of the real samples (indicated as thin lines) is always smaller than the limit and therefore κ is determined too large as shown in b). From the deviation in the fitting region (gray shadowed) a correction factor can be determined and used to correct the experimental data.

the anisotropy, and D the thermal diffusivity of the material. The exact solution of the temperature amplitude is plotted in Figure D.4 for $P/l = 1\,\mathrm{Wm}^{-1}$, $\kappa_x = \kappa_y = 1\,\mathrm{Wm}^{-1}\mathrm{K}^{-1}$, $D \approx 6.110^{-7}\,\mathrm{m}^2\mathrm{s}^{-1}$ but different d and b. For small frequencies the temperature amplitude of the finite sample with isothermal boundary conditions is smaller than the result of Cahill's slope equation which assumes an semi-infinite sample. Below a certain frequency the thermal wave is not confined in the sample anymore and "sees" the sample boundary which exhibits no thermal resistance. At high frequencies the thermal penetration depth is smaller than half of the heater width and Cahill's approximation Eq. (4.8) yields too small results. Over the whole frequency region the slope of the curves from Eq. (D.2) is smaller than from Eq. (4.8). In the analysis of the experimental data the validity of Eq. (4.8) is assumed and κ is determined from Eq. (4.9), i.e. $\kappa = \frac{P}{2\pi l}\frac{\partial \ln f}{\partial \Re(\Delta T)}$. Thus, since the slope of a sample with finite d and b is always smaller than the slope of the ideal case the thermal conductivity determined from the experimental data will always be too large.

From the experimental data κ was determined from a fit of the measurement data in the frequency interval $ab \leq |q^{-1}(f)| \leq d/a$. Obviously the deviation of the measured thermal conductivity κ_{meas} from the real sample thermal conductivity κ_{ideal} decreases with increasing a. a is limited by two things: first by the ratio of half the heater width and sample thickness $a^2 \leq d/b$ and secondly by the necessity to have a sufficient number of data points in the chosen region. For the typical case $b = 10\,\mu$m and $d = 100\,\mu$m a could be chosen around 2.5. For this case $\kappa_{\mathrm{meas}}/\kappa_{\mathrm{ideal}}$ is plotted in Figure D.4b) and the fitting region for a = 2.5 is indicated. It can be seen that κ is measured systematically $\approx 8\%$ too large. However, since the sample geometry is known this ratio can be calculated and thus the experimental data can

be corrected for this systematic deviation. This has been done for the curves shown in Section 4.3.

Furthermore the correction factor also affects the shown relative error. This was chosen to 5% plus half the correction factor. The 5% are a typical value for the reproducibility of experimental data while the latter was chosen for several reasons. First, while bulk Si has a very high thermal conductivity, the assumed isothermal boundary condition is not met perfectly. Second, anisotropic thermal conductivity can alter the correction factor in both directions. Finally, the maximal deviation of the slope has been used as correction factor, but the deviation is not exactly constant within the fitting region, see Figure D.4b).

Note furthermore that the fitting region can also be affected by the available measurement regime. For the samples with high κ the optimal fitting region partially exceeds frequencies of 1500 Hz, which was the instrumentational limit for reliable data acquisition. This is particular severe at low temperatures (κ high, C small) where small values for a had to be chosen. This results in relatively large correction factors and also large relative errors.

References

[Aga10] R. M. B. Agaiby, M. Becker, S. B. Thapa, U. Urmoneit, A. Berger, A. Gawlik, G. Sarau, and S. H. Christiansen. Stress and doping uniformity of laser crystallized amorphous silicon in thin film silicon solar cells. *Journal of Applied Physics*, **107**(5), 2010.

[Alv10] F. X. Alvarez, D. Jou, and A. Sellitto. Pore-size dependence of the thermal conductivity of porous silicon: A phonon hydrodynamic approach. *Applied Physics Letters*, **97**(3), 033103, 2010.

[Asa93] M. Asano, J. Ogata, and Y. Yosinaga. Quantitative-evaluation of contact thermal conductance in a vacuum as a result of simulating the effect of cooling. In *High Heat Flux Engeneering*, volume 1739 of *Proceedings of the Society of Photo-Optical Instrumentation Engineers (SPIE)*, pages 652–656, 1993.

[Aus04] M. D. Austin, H. X. Ge, W. Wu, M. T. Li, Z. N. Yu, D. Wasserman, S. A. Lyon, and S. Y. Chou. Fabrication of 5 nm linewidth and 14 nm pitch features by nanoimprint lithography. *Applied Physics Letters*, **84**(26), 5299–5301, 2004.

[Bae69] N.G. Baecklund. *Thermal Conductivity 8.* Plenum Press, New York, 1969.

[Bas94] J. C. Bass, N. B. Elsner, and F. A. Leavitt. Performance of the 1 kW thermoelectric generator for diesel engines. *AIP Conference Proceedings*, **316**(1), 295–298, 1994.

[Bau97] T. Baum and D. J. Schiffrin. AFM study of surface finish improvement by ultrasound in the anisotropic etching of Si $< 100 >$ in KOH for micromachining applications. *Journal of Micromechanics and Microengineering*, **7**(4), 338–342, 1997.

[Ben97] G. Benedetto, L. Boarino, and R. Spagnolo. Evaluation of thermal conductivity of porous silicon layers by a photoacoustic method. *Applied Physics A: Materials Science & Processing*, **64**, 155–159, 1997.

[Ber03] L. Bertini, C. Stiewe, M. Toprak, D. Williams, S .and Platzek, A. Mrotzek, Y. Zhang, C. Gatti, E. Müller, M. Muhammed, and M. Rowe. Nanostructured Co1-xNixSb3 skutterudites: Synthesis, thermoelectric properties, and theoretical modeling. *Journal of Applied Physics*, **93**(1), 438–447, 2003.

[Ber09] K. Bertram, M. Stordeur, F. Heyroth, and H. S. Leipner. Dynamic in situ observations of electrical and structural changes in thin thermoelectric (Bi0.15Sb0.85)(2)Te-3 films. *Journal Of Applied Physics*, **106**(6), 2009.

[Bin86] L. Binkele. Significance of discrete lorentz function levels at high temperatures resulting from new metallic conductivity measurements. *High Temperatures - High Pressures*, **18**, 599–607, 1986.

[Bis00] O. Bisi, S. Ossicini, and L. Pavesi. Porous silicon: a quantum sponge structure for silicon based optoelectronics. *Surface Science Reports*, **38**(1-3), 1–126, 2000.

[Blo06] T. M. Bloomstein, M. F. Marchant, S. Deneault, D. E. Hardy, and M. Rothschild. 22-nm immersion interference lithography. *Optics Express*, **14**(14), 6434–6443, 2006.

[Bof05] O. Boffoué, A. Jacquot, A. Dauscher, B. Lenoir, and M. Stölzer. Experimental setup for the measurement of the electrical resistivity and thermopower of thin films and bulk materials. *Review of Scientific Instruments*, **76**(5), 053907, 2005.

[Bou04] A. Bourov, Y. Fan, F. C. Cropanese, N. V. Lafferty, L. V. Zavyalova, H. Kang, and B. W. Smith. Immersion microlithography at 193 nm with a talbot prism interferometer. volume 5377, pages 1573–1578. SPIE, 2004.

[Bou08] A. I. Boukai, Y. Bunimovich, J. Tahir-Kheli, J.-K. Yu, W. A. Goddard III, and J. R. Heath. Silicon nanowires as efficient thermoelectric materials. *Nature*, **451**, 168–171, 2008.

[Bow59] R. Bowers, R. W. Ure Jr., J. E. Bauerle, and A. J. Cornish. InAs and InSb as Thermoelectric Materials. *Journal of Applied Physics*, **30**(6), 930–934, 1959.

[Bow61] A. E. Bowley, H.J. Goldsmid, L. Cowles, and G. J. Williams. Measurement of Figure of Merit of a Thermoelectric Material. *Journal of Scientific Instruments*, **38**(11), 433–&, 1961.

[BP09] BP. Statistical Review of World Energy 2009, 2009.

[Bra06] D. Bratton, D. Yang, J. Y. Dai, and C. K. Ober. Recent progress in high resolution lithography. *Polymers For Advanced Technologies*, **17**(2), 94–103, 2006.

[Bru95] M. Bruel. Silicon-on-Insulator Material Technology. *Electronic Letters*, **31**(14), 1201–1202, 1995.

[Bru05] S. R. J. Brueck. Optical and Interferometric Lithography -Nanotechnology Enablers. *P. IEEE*, **93**(10), 1704–1721, 2005.

[BT01] T. Borca-Tasciuc, A. R. Kumar, and G. Chen. Data reduction in 3 omega method for thin-film thermal conductivity determination. *Review of Scientific Instruments*, **72**(4), 2139–2147, 2001.

[Bul68] W.M. Bullis, F.H. Brewer, C.D. Kolstad, and L.J. Swartzendruber. Temperature coefficient of resistivity of silicon and germanium near room temperature. *Solid-State Electronics*, **11**(7), 639 – 646, 1968.

[Bul93] C. Bulucea. Recalculation of Irvin Resistivity Curves for Diffused Layers in Silicon Using Updated Bulk Resistivity Data. *Solid-State Electronics*, **36**(4), 489–493, 1993.

[Bur01] A. T. Burkov, A. Heinrich, P. P. Konstantinov, T. Nakama, and K. Yagasaki. Experimental set-up for thermopower and resistivity measurements at 100-1300 k. *Meas. Sci. Technol.*, **12**, 264–272, 2001.

[Bus61] G. Busch and E. Steigmeier. Waermeleitfaehigkeit, elektrische Leitfaehigkeit, Hall-Effekt und Thermospannung von InSb. *Helv. Phys. Acta*, **34**, 1, 1961.

[Bux09] S. K. Bux, R. G. Blair, P. K. Gogna, H. Lee, G. Chen, M. S. Dresselhaus, R. B. Kaner, and J.-P.Fleurial. Nanostructured Bulk Silicon as an Effective Thermoelectric Material. *Advanced Functional Materials*, **19**, 2445–2452, 2009.

[Cah87] D.G. Cahill and R.O. Pohl. Thermal conductivity of amourphous solids above the plateau. *Physical Review B*, **35**(8), 4067–4073, 1987.

[Cah89] D. G. Cahill, H. E. Fischer, T. Klitsner, E. T. Swartz, and R. O. Pohl. Thermal conductivity of thin films: Measurements and understanding. *Journal of Vacuum Science & Technology A: Vacuum, Surfaces, and Films*, **7**, 1259–1266, 1989.

[Cah90] D. G. Cahill. Thermal conductivity measurement from 30 to 750 K: the 3 omega method. *Review of Scientific Instruments*, **61**(2), 802–808, 1990.

[Cah04] D. G. Cahill. Analysis of heat flow in layered structures for time-domain thermoreflectance. *Review of Scientific Instruments*, **75**(12), 5119–5122, 2004.

[Cal59] Joseph Callaway. Model for Lattice Thermal Conductivity at Low Temperatures. *Physical Reviews*, **113**(4), 1046–1051, 1959.

[Cam95] S. A. Campbell, K. Cooper, L. Dixon, R. Earwaker, S. N. Port, and D. J. Schiffrin. Inhibition of Pyramid Formation In the Etching of Si P[100] In Aqueous Potassium Hydroxide-isopropanol. *Journal of Micromechanics and Microengineering*, **5**(3), 209–218, 1995.

[Cha09] S.-W. Chang, V. P. Chuang, S. T. Boles, C. A. Ross, and C. V. Thompson. Densely Packed Arrays of Ultra-High-Aspect-Ratio Silicon Nanowires Fabricated using Block-Copolymer Lithography and Metal-Assisted Etching. *Advanced Functional Materials*, **19**, 2495–2500, 2009.

[Che01] D. G. Chen. Anti-reflection (AR) coatings made by sol-gel processes: A review. *Solar Energy Materials And Solar Cells*, **68**(3-4), 313–336, 2001.

[Che02] C. G. Chen, R.K. Heilmann, C. J., P. T. Konkola, G. S. Pati, and M. L. Schattenburg. Beam alignment for scanning beam interference lithography. *J. Vac. Sci. Technol. B*, **20**(6), 3071–3074, 2002.

[Che05] N. Chen, F. Gascoin, G. J. Snyder, E. Müller, G. Karpinski, and C. Stiewe. Macroscopic thermoelectric inhomogeneities in (AgSbTe[sub 2])[sub x](PbTe)[sub 1 - x]. *Applied Physics Letters*, **87**(17), 171903, 2005.

[Cho95] S. Y. Chou, P. R. Krauss, and P. J. Renstrom. Imprint of sub-25 nm vias and trenches in polymers. *Applied Physics Letters*, **67**(21), 3114–3116, 1995.

[Cho96] S. Y. Chou, P. R. Krauss, and P. J. Renstrom. Nanoimprint lithography. *Journal of Vacuum Science & Technology B*, **14**(6), 4129–4133, 1996. 40th International Conference on Electron, Ion, and Photon Beam Technology and Nanofabrication, Atlanta, GA, May 28-31, 1996.

[Cho08] W. K. Choi, T. H. Liew, M. K. Dawood, Henry I. Smith, C. V. Thompson, and M. H. Hong. Synthesis of Silicon Nanowires and Nanofin Arrays Using Interference Lithography and Catalytic Etching. *Nano Letters*, **8**(11),

3799–3802, 2008.

[COM11] http://www.comsol.com/, 2011.

[Cor10] O.M. Corbino. Thermische Oszillationen wechselstromdurchflossener Lampen mit duennem Faden und daraus sich ergebende Gleichrichterwirkung infolge der Anwesenheit geradzahliger Oberschwingungen. *Phys. Z.*, **11**, 413–417, 1910.

[Cor11] O.M. Corbino. Periodische Widerstandsaenderungen feiner Metallfaeden, die durch Wechselstroeme zum Gluehen gebracht werden, sowie Ableitung ihrer thermischen Eigenschaften bei hoher Temperatur. *Phys. Z.*, **12**, 292–295, 1911.

[Cul97] A.G. Cullis, L.T. Canham, and P.D.J Calcott. The structural and luminescence properties of porous silicon. *Journal of Applied Physics*, **82**(3), 909–965, 1997.

[Cus58] N. Cusack and P. Kendall. The Absolute Scale of Thermoelectric Power at High Temperature. *Proceedings of the Physical Society*, **72**(5), 898, 1958.

[dB09] J. de Boor, N. Geyer, U. Gösele, and V. Schmidt. Three-beam interference lithography: upgrading a Lloyd's interferometer for single-exposure hexagonal patterning. *Optics Letters*, **34**(12), 1783–1785, 2009.

[dB10a] J. de Boor, N. Geyer, J. V. Wittemann, U. Gösele, and V. Schmidt. Sub-100 nm silicon nanowires by laser interference lithography and metal-assisted etching. *Nanotechnology*, **21**(9), 095302 (5pp), 2010.

[dB10b] J. de Boor, D. S. Kim, and V. Schmidt. Sub-50 nm patterning by immersion interference lithography using a Littrow prism as a Lloyd's interferometer. *Optics Letters*, **35**(20), 3450–3452, 2010.

[dB10c] J. de Boor and V. Schmidt. Complete Characterization of Thermoelectric Materials by a Combined van der Pauw Approach. *Advanced Materials*, **22**(38), 4303–4307, 2010.

[Deb12] P. Debye. Zur Theorie der spezifischen Wärmen. *Annalen der Physik*, **344**(14), 789–839, 1912.

[Dem02] W. Demtröder. *Experimentalphysik 1.* Springer, 2002.

[Dre07] M. S. Dresselhaus, G. Chen, M. Y. Tang, R. Yang, H. Lee, D. Wang, Z. Ren, J.-P. Fleuria, and P. Gogna. New Directions for Low-Dimensional Thermoelectric Materials. *Advanced Materials*, **19**, 1043–1053, 2007.

[EG05] M.S. El-Genk and H.H. Saber. Performance analysis of cascaded thermoelectric converters for advanced radioisotope power systems. *Energy Conversion and Management*, **46**(7-8), 1083–1105, 2005.

[Emi10] http://www.engineeringtoolbox.com /emissivity-coefficients-d_447.html, 2010.

[Euc11] A. Eucken. Über die Temperaturabhängigkeit der Wärmeleitfähigkeit fester Nichtmetalle. *Annalen der Physik*, **339**(2), 185– 221, 1911.

[Fel00] J. L. Feldman, D. J. Singh, I. I. Mazin, D. Mandrus, and B. C. Sales. Lattice dynamics and reduced thermal conductivity of filled skutterudites. *Physical*

Review B, **61**(14), R9209–R9212, 2000.

[Fra53] R. Franz and G. Wiedemann. Über die Wärme-Leitungsfähigkeit der Metalle. *Annalen der Physik*, **165**, 497–531, 1853.

[Fra10] W. D. Franke, editor. *Kompendium Erneuerbare Energien*. F.A.Z. Institut fuer Management-, Markt-, und Medieninformationen GmbH, 2010.

[Ful68] W. Fulkerson, J.P. Moore, R. K. Williams, R.S. Graves, and D.L. McElroy. Thermal conductivity, Electrical Resistivity, and Seebeck Coefficient of Silicon from 100 to 1300K. *Physical Review*, **167**(3), 762–785, 1968.

[Gas05] F. Gascoin, S. Ottensmann, D. Stark, S.M. Haile, and G.J. Snyder. Zintl phases as thermoelectric materials: Tuned transport properties of the compounds CaxYb1-xZn2Sb2. *Advanced Functional Materials*, **15**(11), 1860–1864, 2005.

[Geb55] T.H. Geballe and G.W. Hull. Seebeck Effect in Silicon. *Physical Review*, **98**, 940–947, 1955.

[Ges97] G. Gesele, J. Lindsmeier, V. Drach, J. Fricke, and R. Arens-Fischer. Temperature-dependent thermal conductivity of porous silicon. *J. Phys. D: Appl. Phys.*, **30**, 2911–2916, 1997.

[Gey09] N. Geyer, Z. Huang, B. Fuhrmann, S. Grimm, M. Reiche, T.-K. Nguyen-Duc, J. de Boor, H. S. Leipner, P. Werner, and U. Gösele. Sub-20 nm Si/Ge Superlattice Nanowires by Metal-Assisted Etching. *Nano Letters*, **9**, 3106–3110, 2009.

[Gla64] C. J. Glassbrenner and Glen A. Slack. Thermal Conductivity of Silicon and Germanium from 3°K to the Melting Point. *Phys. Rev.*, **134**(4A), A1058–A1069, 1964.

[Gol54] H. J. Goldsmid and R. W. Douglas. The use of semiconductors in thermoelectric refrigeration. *British Journal of Applied Physics*, **5**(11), 386, 1954.

[Haf02] S. Hafizovic and O. Paul. Temperature-dependent thermal conductivities of CMOS layers by micromachined thermal van der Pauw test structures. *Sensors and Actuators A: Physical*, **97-98**, 246 – 252, 2002.

[Hal73] G.M. Hale and M.R. Querry. Optical constants of water in the 200-nm to 200-μm wavelength region. *Applied Optics*, **12**(3), 555–593, 1973.

[Han09] H. Han, R. Ji, Y. J. Park, S. K. Lee, G. Le Rhun, M. Alexe, K. Nielsch, D. Hesse, U. Gösele, and S. Baik. Wafer-scale arrays of epitaxial ferroelectric nanodiscs and nanorings. *Nanotechnology*, **20**(1), 015301 (6pp), 2009.

[Hao09] Q. Hao, G. Chen, and M.-S. Jeng. Frequency-dependent monte carlo simulations of phonon transport in two-dimensional porous silicon with aligned pores. *Journal of Applied Physics*, **106**(11), 114321, 2009.

[Har58] T.C. Harman. Special Techniques for Measurement of Thermoelectric Properties. *Journal of Applied Physics*, **29**(9), 1373–1374, 1958.

[Har59] T.C. Harman, J. H. Cahn, and M.J. Logan. Measurement of thermal conductivity by utilization of the Peltier effect. *Journal of Applied Physics*,

30(9), 1351–1359, 1959.

[Har02] T. C. Harman, P. J. Taylor, M. P. Walsh, and B. E. LaForge. Quantum Dot Superlattice Thermoelectric Materials and Devices. *Science*, **297**(5590), 2229–2232, 2002.

[Har05] T.C. Harman, M.P. Walsh, B.E. Laforge, and G.W. Turner. Nanostructured thermoelectric materials. *Journal of Electronic Materials*, **34**(5), L19–L22, 2005.

[Har06] T. C. Harman, B. E. LaForge C. D. Hoyt R. E. Reeder, M. P. Walsh, and G. W. Turner. High electrical power density from pbte-based quantum-dot superlattice unicouple thermoelectric devices. *Applied Physics Letters*, **88**, 243504–1–3, 2006.

[Hic93a] L. D. Hicks and M. S. Dresselhaus. Effect of quantum-well structures on the thermoelectric figure of merit. *Physical Review B*, **47**(19), 12727–12731, 1993.

[Hic93b] L. D. Hicks and M. S. Dresselhaus. Thermoelectric figure of merit of a one-dimensional conductor. *Physical Review B*, **47**(24), 16631–16634, 1993.

[Hic96] L.D. Hicks, T.C. Harman, X. Sun, and M.S. Dresselhaus. Experimental study of the effect of quantum-well structures on the thermoelectric figure of merit. *Physical Review B*, **53**(16), 10493–10496, 1996.

[Hip10] K. Hippalgaonkar, B. Huang, R. Chen, K. Sawyer, and A. Ercius, P.and Majumdar. Fabrication of Microdevices with Integrated Nanowires for Investigating Low-Dimensional Phonon Transport. *Nano Letters*, **10**(11), 4341–4348, 2010.

[Hoc08] A. I. Hochbaum, R. Chen, R. D. Delgado, W. Liang, E. C. Garnett, M. Najarian, A. Majumdar, and P. Yang. Enhanced thermoelectric performance of rough silicon nanowires. *Nature*, **451**, 163–167, 2008.

[Hoc09] A. I. Hochbaum, D. Gargas, Y. J. Hwang, and P. Yang. Single Crystalline Mesoporous Silicon Nanowires. *Nano Letters*, 2009.

[Hol63] M. G. Holland. Analysis of Lattice Thermal Conductivity. *Phys. Rev.*, **132**(6), 2461–2471, 1963.

[Hua07] Z. Huang, H. Fang, and Zhu J. Fabrication of Silicon Nanowire Arrays with Controlled Diameter, Length, and Density. *Advanced Materials*, **19**, 744–748, 2007.

[Hua08] Z. Huang, X. Zhang, M. Reiche, L. Liu, W. Lee, T. Shimizu, S. Senz, and U. Gösele. Extended Arrays of Vertically Aligned Sub-10 nm Diameter [100] Si Nanowires by Metal-Assisted Chemical Etching. *Nano Letters*, 2008.

[Hua09] Z. P. Huang, T. Shimizu, S. Senz, Z. Zhang, X. X. Zhang, W. Lee, N. Geyer, and U. Gosele. Ordered Arrays of Vertically Aligned [110] Silicon Nanowires by Suppressing the Crystallographically Preferred Etching Directions. *Nano Letters*, **9**(7), 2519–2525, 2009.

[Hua11] Z. Huang, N. Geyer, P. Werner, J. de Boor, and Ulrich Gösele. Metal-assisted chemical etching of silicon: A review. *Advanced Materials*, **23**(2),

1521–4095, 2011.

[Iko98] K. Ikoma, M. Munekiyo, K. Furuya, M. Kobayashi, T. Izumi, and K. Shinohara. Thermoelectric module and generator for gasoline engine vehicles. In *XVII International Conference on Thermoelectrics, Proceedings ICT 98*, pages 464–467, 345 E 47TH ST, New York, NY 10017 USA, 1998. 17th International Conference on Thermoelectrics (ICT98), Nagoya, Japan, May 24-28, 1998.

[Iof10] `http://www.ioffe.ru/SVA/NSM/Semicond/Si/thermal.html`, 2010.

[Iof11] `http://www.ioffe.ru/SVA/NSM/Semicond/Si/electric.html`, 2011.

[Iup72] Iupac. Manual of symbols and terminology for physicochemical quantities and units appendix ii. *Pure Appl. Chem.*, **31**(4), 577–638, 1972.

[IV08] J. H. Lienhard IV and J. H. Lienhard V. *A Heat Transfer Textbook*. Phlogiston Press, Cambridge, Massachusetts, USA, 2008.

[Iwa05] H. Iwasaki and H. Hori. Thermoelectric property measurements by the improved harman method. *Thermoelectrics, 2005. ICT 2005. 24th International Conference on*, pages 513–516, 2005.

[Jac99] J. D. Jackson. *Classical Electrodynamics*. John Wiley & Sons, Inc., 3 edition, 1999.

[Ji08] R. Ji. *Templated Fabrication of Periodic Nanostructures Based on Laser Interference Lithography*. PhD thesis, MPI Halle,

[Joh95] G. C. John and V. A. Singh. Diffusion-induced nucleation model for the formation of porous silicon. *Physical Review B*, **52**(15), 11125–11131, 1995.

[Ju99] Y. Ju. Phonon scattering in silicon films with thickness of order 100 nm. *Applied Physics Letters*, **74**(20), 3005–3007, 1999.

[Kap06] S. G. Kaplan and J. H. Burnett. Optical properties of fluids for 248 and 193 nm immersion photolithography. *Appl. Opt.*, **45**(8), 1721–1724, 2006.

[Kas05] C. Kasl and M.J.R. Hoch. Effects of sample thickness on the van der Pauw technique for resistivity measurements. *Review of Scientific Instruments*, **76**(3), 2005.

[Kaw89] H. Kawata, J. M. Carter, A. Yen, and H. I. Smith. Optical projection lithography using lenses with numerical apertures greater than unity. *Microelectronic Engineering*, **9**(1-4), 31 – 36, 1989.

[Kaz10] M. Kazan, G. Guisbiers, S. Pereira, M. R. Correia, P. Masri, A. Bruyant, S. Volz, and P. Royer. Thermal conductivity of silicon bulk and nanowires: Effects of isotopic composition, phonon confinement, and surface roughness. *Journal of Applied Physics*, **107**(8), 083503, 2010.

[Kho97] A.M. Khounsary, D. Chojnowski, L. Assoufid, and W.M. Worek. Thermal contact resistance across a copper-silicon interface. In Khounsary, AM and Macrander, AT, editor, *High Heat Flux and Synchrotron Radiation Beamlines*, volume 3151 of *Proceedings of the Society of Photo-Optical Instrumentation Engineers (SPIE)*, pages 45–51, 1997.

[Kim07] D. S. Kim, R. Ji, H. J. Fan, F. Bertram, R. Scholz, A. Dadgar, K. Nielsch,

A. Krost, J. Christen, U. Gösele, and M Zacharias. Laser-interference lithography tailored for highly symmetrically arranged ZnO nanowire arrays. *Small*, **3**(1), 76–80, 2007.

[Kle06] K. Kleinermanns, editor. *Bergmann Schaefer, Lehrbuch der Experimentalphysik. Band 5: Gase, Nanosysteme, Fluessigkeiten*, volume 5. Walter de Gruyter, 2. edition, 2006.

[Kob08] W. Kobayashi, W. Tamura, and I. Terasaki. Thermal Conductivity of Thermoelectric Rhodium Oxides Measured by a Modified Harman Method. *Journal of the Physical Society of Japan*, **77**(7), 074606, 2008.

[Köh99] M. Köhler. *Etching in Microsystem Technology.* Wiley-VCH, 1999.

[Koo89] D.W. Koon. Effect of Contact Size and Placement, and of Resistive Inhomogeneities on van der Pauw Measurements. *Review of Scientific Instruments*, **60**(2), 271–274, 1989.

[Lai05] N. D. Lai, W. P. Liang, J. H. Lin, C. C. Hsu, and C. H. Lin. Fabrication of two- and three-dimensional periodic structures by multi-exposure of two-beam interference technique. *Optics Express*, **13**(23), 9605–9611, 2005.

[Lam97] M.A. Lambert and L.S. Fletcher. Review of models for thermal contact conductance of metals. *Journal of Thermophysics and Heat Transfer*, **11**(2), 129–140, 1997.

[Lan96] W. Lang. Silicon microstructuring technology. *Materials Science & Engineering R-Reports*, **17**(1), 1–55, 1996.

[Lee06] W. Lee, R. Ji, C. A. Ross, U. Gösele, and K. Nielsch. Wafer-Scale Ni Imprint Stamps for Porous Alumina Membranes Based on Interference Lithography. *Small*, **2**, 978–982, 2006.

[Lee08a] J. Lee, G. A. Galli, and J. C. Grossman. Nanoporous Si as an Efficient Thermoelectric Material. *Nano Letters*, **8**(11), 3750–3754, 2008.

[Lee08b] M. L. Lee and R. Venkatasubramanian. Effect of nanodot areal density and period on thermal conductivity in SiGe/Si nanodot superlattices. *Applied Physics Letters*, **92**(5), 053112, 2008.

[Leh91] V. Lehmann and Gösele, U. Porous Silicon Formation - A Quantum Wire Effect. *Applied Physics Letters*, **58**(8), 856–858, 1991.

[Leh00] V. Lehmann, R. Stengl, and A. Luitgart. On the morphology and the electrochemical formation mechanism of mesoporous silicon. *Materials Science&Engineering B*, **69**, 11–22, 2000.

[Leh02] V. Lehmann. *Electrochemistry of Silicon.* Wiley-VCH, Weinheim, Germany, 2002.

[Lev98] G. Leveque and M. Nouaoura. Temperature measurements by optical pyrometry during the epitaxial growth of semiconductors. *European Physical Journal-Applied Physics*, **4**(2), 227–233, 1998.

[Li98] F. Y. Li, L. Zhang, and R. M. Metzger. On the growth of highly ordered pores in anodized aluminum oxide. *Chemistry Of Materials*, **10**(9), 2470–2480, 1998.

[Li00] X. Li and P. W. Bohn. Metal-assisted chemical etching in HF/H2O2 produces porous silicon. *Applied Physics Letters*, **77**(16), 2572–2574, 2000.

[Li03] D. Li, Y. Wu, P. Kim, L. Shi, P. Yang, and A. Majumdar. Thermal conductivity of individual silicon nanowires. *Applied Physics Letters*, **83**(14), 2934–2936, 2003.

[Lia06] L. H. Liang and B. Li. Size-dependent thermal conductivity of nanoscale semiconducting systems. *Physical Review B*, **73**, 15330, 2006.

[Liu04] W. Liu and M. Asheghi. Phonon–boundary scattering in ultrathin single-crystal silicon layers. *Applied Physics Letters*, **84**(19), 3819–3821, 2004.

[Lu07] C. Lu, X. K. Hu, S. S. Dimov, and R. H. Lipson. Controlling large-scale film morphology by phase manipulation in interference lithography. *Applied Optics*, **46**(29), 7202–7206, 2007.

[Mac92] L. Mach. Über einen Interferenzrefraktor. *Zeitschrift für Instrumentenkunde*, **12**, 89–93, 1892.

[Mai66] C. Mai and J. Looney. Thermal Growth and Chemical Etching of Silicon Dioxide Films. *Semiconductor products and solid state technology*, **9**(1), 19–24, 1966.

[Mal65] I. H. Malitson. Interspecimen comparison of the refractive index of fused silica. *J. Opt. Soc. Am.*, **55**(10), 1205–1208, 1965.

[Maq96] M. Maqsood, M. Arshad, M. Zafarullah, and A. Maqsood. Low-temperature thermal conductivity measurement apparatus: design assembly, calibration and measurement on (y123, bi2223) superconductors. *Superconductor Science and Technology*, **9**(4), 321, 1996.

[Mar03] J.I. Martín, J. Nogués, Kai Liu, J.L. Vicente, and Ivan K. Schuller. Ordered magnetic nanostructures: fabrication and properties. *Journal of Magnetism and Magnetic Materials*, **256**(1-3), 449–501, 2003.

[Mas88] W.P. Maszara, G. Goetz, A. Caviglia, and J.B. McKitterick. Bonding of Silicon-Wafers for Silicon-on-Insulator. *Journal of Applied Physics*, **64**(10, Part 1), 4943–4950, 1988.

[Mat02] K. Matsubara. Development of a high efficient thermoelectric stack for a waste exhaust heat recovery of vehicles. In *xxi International Conference On Thermoelectrics, Proceedings ICT '02*, pages 418–423. IEEE, 2002. 21st International Conference on Thermoelectrics (ICT 02), LONG BEACH, CA, AUG 25-29, 2002.

[MAT11] `http://www.mathworks.de`, 2011.

[May70] A. F. Mayadas and M. Shatzkes. Electrical-resistivity model for polycrystalline films: the case of arbitrary reflection at external surfaces. *Physical Review B*, **1**(4), 1382–1389, 1970.

[McC05] A. D. McConnell and K. E. Goodson. Thermal conduction in silicon micro- and nanostructures. *Annual Review of Heat Transfer*, **14**, 129–168, 2005.

[Min04] N. Mingo. Thermoelectric figure of merit and maximum power factor in iii–v semiconductor nanowires. *Applied Physics Letters*, **84**(14), 2652–2654,

2004.

[mob10] http://britneyspears.ac/physics/mobility/mobility.htm, 2010.

[Moo96] I. K. Moon, Y. H. Jeonga, and S. I. Kwun. The 3 omega technique for measuring dynamic specific heat and thermal conductivity of a liquid or solid. *Review of Scientific Instruments*, **67**, 29–35, 1996.

[Moo06] J. Moon, J. Ford, and S. Yang. Fabricating three-dimensional polymeric photonic structures by multi-beam interference lithography. *Polym. Adv. Technol.*, **17**(2), 83–93, 2006.

[Moo07] S. Y. Moon and J. M. Kim. Chemistry of photolithographic imaging materials based on the chemical amplification concept. *Journal Of Photochemistry And Photobiology C-Photochemistry Reviews*, **8**(4), 157–173, 2007.

[Moo08] A. L. Moore, S. K. Saha, R. S. Prasher, and L. Shi. Phonon backscattering and thermal conductivity suppression in sawtooth nanowires. *Applied Physics Letters*, **93**(8), 083112, 2008.

[Mül03] E. Müller, C. Drasar, J. Schilz, and W. A. Kaysser. Functionally graded materials for sensor and energy applications. *Materials Science and Engineering A-Structural Materials Properties Microstructure and Processing*, **362**(1-2), 17–39, 2003.

[Nic82] E. H. Nicollian and J. R. Brews. *MOS (Metal Oxide Semiconductor) Physics and Technology*. John Wiley & Sons, 1982.

[Nie01] K Nielsch, RB Wehrspohn, J Barthel, J Kirschner, U Gosele, SF Fischer, and H Kronmuller. Hexagonally ordered 100 nm period nickel nanowire arrays. *Applied Physics Letters*, **79**(9), 1360–1362, 2001.

[Nol01] G. S. Nolas, J. Sharp, and H. J. Goldsmid. *Thermoelectrics*. Springer, 2001.

[Okh72] A. S. Okhotin, A. S. Pushkarskii, and V. V. Gorbachev. *Thermophysical Properties of Semiconductors*. "Atom" Publ. House, 1972.

[Osz88] M. Oszwalldowski and M. Zimpel. Temperature dependence of intrinsic carrier concentration and density of states effective mass of heavy holes in insb. *Journal of Physics and Chemistry of Solids*, **49**(10), 1179 – 1185, 1988.

[Par61] W.J. Parker, R.J. Jenkins, C.P. Butler, and G.L. Abbott. Flash method of determining thermal diffusivity, heat capacity and thermal conductivity. *Journal of Applied Physics*, **32**(9), 1679–1685, 1961.

[Pau99] O. Paul, L. Plattner, and H. Baltes. A Thermal van der Pauw Test Structure. *P. IEEE*, **12**, 56–61, 1999.

[Pbw11] http://en.wikipedia.org/wiki/Lead, Januar 2011.

[Pei29] R. Peierls. Zur kinetischen Theorie der Wärmeleitung in Kristallen. *Annalen der Physik*, **395**(8), 1055–1101, 1929.

[Pen06] K. Peng, J. Hu, Y. Yan, Y. Wu, H. Fang, Y. Xu, S.T. Lee, and J. Zhu. Fabrication of single-crystalline silicon nanowires by scratching a silicon surface with catalytic metal particles. *Advanced Functional Materials*, **16**, 387–394, 2006.

[Per09] A. I. Persson, Y. K. Koh, D. G. Cahill, L. Samuelson, and H. Linke. Thermal conductance of inas nanowire composites. *Nano Letters*, 2009.

[Pou06] P. F. P. Poudeu, J. D'Angelo, H. Kong, A. Downey, J. L. Short, T. P. Pcionek, R.and Hogan, C. Uher, and M. G. Kanatzidis. Nanostructures versus Solid Solutions: Low Lattice Thermal Conductivity and Enhanced Thermoelectric Figure of Merit in Pb9.6Sb0.2Te10-xSex Bulk Materials. *Journal of the American Chemical Society*, **128**(44), 14347–14355, 2006.

[Pow65] R.W. Powell, R.P. Tye, and M.J. Hickman. The thermal conductivity of nickel. *International Journal of Heat and Mass Transfer*, **8**, 679–688, 1965.

[Ram08] V. Ramanan, E. Nelson, A. Brzezinski, P. V. Braun, and P. Wiltzius. Three dimensional silicon-air photonic crystals with controlled defects using interference lithography. *Applied Physics Letters*, **92**(17), 2008.

[Ran09] J. Randrianalisoa and D. Baillis. Combined analytical and phonon-tracking approaches to model thermal conductivity of etched and annealed nanoporous silicon. *Advanced Engineering Materials*, **11**, 852–861, 2009.

[Rea92] A.J. Read, R.J. Needs, K.J. Nash, L.T. Canham, P.D.J. Calcott, and A. Qteish. 1st-Principles Calculations of the Electronic-Properties of Silicon Quantum Wires. *Physical Review Letters*, **69**(8), 1232–1235, 1992.

[Ros61] F.D. Rosi, E.F. Hockings, and N.E. Lindenblad. Semiconducting Materials for Thermoelectric Power Generation. *RCA Review*, **22**(1), 82–121, 1961.

[Row95] D. M. Rowe and Gao Min. Alpha-in sigma plot as a thermoelectric material performance indicator. *Journal of Materials Science Letters*, **14**, 617–619, 1995.

[Row06] D. M. Rowe, editor. *Thermoelectrics Handbook*. Taylor & Francis, 2006.

[Sal09] A. Salazar, A. Mendioroz, and R. Fuente. The strong influence of heat losses on the accurate measurement of thermal diffusivity using lock-in thermography. *Applied Physics Letters*, **95**(12), 121905, 2009.

[Sch06] Dieter K. Schroder. *Semiconductor Material and Device Characterization*, volume 3. John Wiley & Sons, Inc., 2006.

[Sch10a] V. Schmidt, J. V. Wittemann, and U. Gösele. Growth, thermodynamics, and electrical properties of silicon nanowires. *Chemical Reviews*, **110**, 361–388, 2010.

[Sch10b] J. A. Schuller, E. S. Barnard, W. Cai, Y. C. Jun, J. S. White, and M. L. Brongersma. Plasmonics for extreme light concentration and manipulation. *Nature Materials*, **9**(4), 193, 2010.

[See23] T.J. Seebeck. Magnetische Polarisation der Metalle und Erze durch Temperatur-Differenz. *Abh. K. Akad. Wiss., Berlin*, **265**, 1823.

[Seh62] R. Sehr and L. R. Testardi. The optical properties of p-type Bi2Te3—Sb2Te3 alloys between 2-15 microns. *Journal of Physics and Chemistry of Solids*, **23**(9), 1219 – 1224, 1962.

[Sei90] H. Seidel, L. Csepregi, A . Heuberger, and H. Baumgartel. Anisotropic Etching of Crystalline Silicon in Alkaline Solutions 1. Orientation Depen-

dence and Behavior of Passivation Layers. *Journal of The Electrochemical Society*, **137**(11), 3612–3626, 1990.

[Sim95] A.J. Simons, T.I. Cox, M.J. Uren, and P.D.J. Calcott. The Electrical-Properties of Porous Silicon Produced from n(+) Silicon Substrates. *Thin Solid Films*, **255**(1-2), 12–15, 1995. Symposium F - Porous Silicon and Related Materials, at the 1994 Spring Conference of the European-Materials-Research-Society, Strasbourg, France, May 24-27, 1994.

[Sin09] R. Singh and A. Shakouri. Thermostat for high temperature and transient characterization of thin film thermoelectric materials. *Review of Scientific Instruments*, **80**(2), 025101, 2009.

[Siv10] V. A. Sivakov, K. Hoeflich, M. Becker, A. Berger, T. Stelzner, K.-E. Elers, V. Pore, M. Ritala, and S. H. Christiansen. Silver Coated Platinum Core-Shell Nanostructures on Etched Si Nanowires: Atomic Layer Deposition (ALD) Processing and Application in SERS. *CHEMPHYSCHEM*, **11**(9), 1995–2000, 2010.

[Smi88] R.L. Smith, S.F. Chuang, and S.D. Collins. A Theoretical-Model of the Formation Morphologies of Porous Silicon. *Journal of Electronic Materials*, **17**(6), 533–541, 1988.

[Smi04] B. Smith. 25nm immersion lithography at a 193nm wavelength. *Proceedings of SPIE–the international society for optical engineering*, **5754**, 141–147, 2004.

[Sny08] G. S. Snyder and E. S. Toberer. Complex thermoelectric materials. *Nature Materials*, **7**(2), 105–114, 2008.

[Sol99] H. H. Solak, D. He, W. Li, and F. Cerrina. Nanolithography using extreme ultraviolet lithography interferometry: 19 nm lines and spaces. *J. Vac. Sci. Technol. B*, **17**, 3052, 1999.

[Son04] D. Song and G. Chen. Thermal conductivity of periodic microporous silicon films. *Applied Physics Letters*, **84**(5), 687–689, 2004.

[Sze81] S. M. Sze. *Physics of Semiconductor devices*. John Wiley & Sons, 2. edition, 1981.

[Tab81] M. Tabe, K. Arai, and H. Nakamura. Effect of Growth Temperature on Si MBE Film. *Japanese Journal of Applied Physics*, **20**(4), 703–708, 1981.

[Tan10] J. Tang, H.-T. Wang, D. H. Lee, M. Fardy, Z. Huo, T. P. Russell, and P. Yang. Holey Silicon as an Efficient Thermoelectric Material. *Nano Letters*, **10**(10), 4279–4283, 2010.

[Tel77] C. R. Tellier and A. J. Tosser. Analytical approximate equations for the resistivity and its temperature coefficient in thin polycrystalline metallic films. *Applied Physics A: Materials Science & Processing*, **14**, 221, 1977.

[Tel79] C. R. Tellier, C. R. Pichard, and A. J. Tosser. Approximate expressions for the product of the resistivity and its TCR in very thin polycrystalline films. *Journal of Physics F: Metal Physics*, **9**(12), 2377–2380, 1979.

[Tic05] G. Tichá, W. Pabst, and D. Smith. Predictive model for the thermal con-

ductivity of porous materials with matrix-inclusion type microstructure. *Journal of Materials Science*, **40**, 5045–5047, 2005.

[Tri08] T. M. Tritt, H. Boettner, and L. Chen. Thermoelectrics: Direct solar thermal energy conversion. *MRS BULLETIN*, **33**(4), 366–368, 2008.

[Tur58] D.R. Turner. Electropolishing Silicon in Hydrofluoric Acid Solutions. *Journal of the Electrochemical Society*, **105**(7), 402–408, 1958.

[Uhl56] A. Uhlir. Electrolytic Shaping of Germanium and Silicon. *BELL System Technical Journal*, **35**(2), 333–347, 1956.

[vdP58a] L. J. van der Pauw. A method of measuring specific resistivity and hall effect of discs of arbitrary shape. *Philips Research Reports*, **13**, 1–9, 1958.

[vdP58b] L.J. van der Pauw. A method of measuring the resistivity and hall coefficient on Lamellae of arbitrary shape. *Philips Technical Review*, **20**(8), 220–224, 1958.

[Ven01] R. Venkatasubramanian, E. Siivola, T. Colpitts, and B. O'Quinn. Thin-film thermoelectric devices with high room-temperature figures of merit. *Nature*, **413**(6856), 597–602, 2001.

[Vin09] C. B. Vining. An inconvenient truth about thermoelectrics. *Nature Materials*, **8**, 83–85, 2009.

[Völ90] F. Völklein. Thermal-Conductivity and Diffusivity of a Thin-Film SiO2-Si3N4 Sandwich System. *Thin Solid Films*, **188**(1), 27–33, 1990.

[Völ09] F. Völklein, H. Reith, T. W. Cornelius, M. Rauber, and R. Neumann. The experimental investigation of thermal conductivity and the Wiedemann-Franz law for single metallic nanowires. *Nanotechnology*, **20**(32), 2009.

[Völ10] F. Völklein, H. Reith, M. C. Schmitt, M. Huth, M. Rauber, and R. Neumann. Microchips for the Investigation of Thermal and Electrical Properties of Individual Nanowires. *Journal of Electronic Materials*, **39**(9), 1950–1956, 2010. 28th International Conference on Thermoelectrics/7th European Conference on Thermoelectrics, Freiburg, Germany, JUL 26-30, 2009.

[Wal04] M. E. Walsh. *On the design of lithographic interferometers and their application.* PhD thesis, MIT, 2004.

[Wan09] H. Wang and M. Sen. Analysis of the 3-omega method for thermal conductivity measurement. *International Journal of Heat and Mass Transfer*, **52**(7-8), 2102 – 2109, 2009.

[Web91] L. Weber and E. Gmelin. Transport properties of silicon. *Applied Physics A*, **53**, 136–140, 1991.

[Wei08] J. D. Weiss, R. J. Kaplar, and K. E. Kambour. A derivation of the van der Pauw formula from electrostatics. *Solid-State Electronics*, **52**(1), 91–98, 2008.

[wik10a] `http://en.wikipedia.org/wiki/2009_United_Nations_Climate_Change_Conference`, 2010.

[wik10b] `http://de.wikipedia.org/wiki/Pt1000`, August 2010.

[wik10c] `http://en.wikipedia.org/wiki/Nitrogen`, 2010.

[Win92] H. F. Winters and J. W. Coburn. Surface science aspects of etching reactions. *Surface Science Reports*, **14**(4-6), 161–269, 1992.

[Wit89] J. Wittbrodt and W. Erhardt. An Inexpensive and Versatile Computer-Controlled PCR Machine Using a Peltier Element as Thermoelectric Heat-Pump. *Trends in Genetics*, **5**(7), 202–203, 1989.

[Wol06] A. Wolf and R. Brendel. Thermal conductivity of sintered porous silicon films. *Thin Solid Films*, **513**(1-2), 385–390, 2006.

[Woo08] S. Wood and A. T. Harris. Porous burners for lean-burn applications. *Progress in Energy and Combustion Science*, **34**(5), 667–684, 2008.

[Yam99] A. Yamamoto, H. Takazawa, and T. Ohta. Thermoelectric transport properties of porous silicon nanostructure. In *18th international Conference on Thermoelectrics*, 1999.

[Yan02] B. Yang, W. L. Liu, J. L. Liu, K. L. Wang, and G. Chen. Measurements of anisotropic thermoelectric properties in superlattices. *Applied Physics Letters*, **81**(19), 3588–3590, 2002.

[Yan08] S. H. Yang, T. J. Zhu, T. Sun, S. N. Zhang, X. B. Zhao, and J. He. Nanostructures in high-performance (GeTe)(x)(AgSbTe2)(100-x) thermoelectric materials. *Nanotechnology*, **19**(24), 2008.

[Yer99] V.Y. Yerokhov and I.I. Melnyk. Porous silicon in solar cell structures: a review of achievements and modern directions of further use. *Renewable & Sustainable Energy Reviews*, **3**(4), 291–322, 1999.

[Yue06] D.-T. Yue, Z.-C. Tan, Y.-Y. Di, X.-R. Lv, and L.-X. Sun. Specific Heat Capacity and Thermal Conductivity of Foam Glass (Type 150P) at Temperatures from 80 to 400 K. *International Journal of Thermophysics*, **27**, 270–281, 2006. 10.1007/s10765-006-0026-5.

[Zeh91] L. Zehnder. Ein neuer Interferenzrefraktor. *Zeitschrift für Instrumentenkunde*, **11**, 275–285, 1891.

[Zha09] Z. Zhang, T. Shimizu, S. Senz, and U. Gösele. Ordered High-Density Si [100] Nanowire Arrays Epitaxially Grown by Bottom Imprint Method. *Advanced Materials*, **21**(27), 2824+, 2009.

[Zha10] Y. Zhang, C. L. Hapenciuc, E. E. Castillo, T. Borca-Tasciuc, R. J. Mehta, C. Karthik, and G. Ramanath. A microprobe technique for simultaneously measuring thermal conductivity and seebeck coefficient of thin films. *Applied Physics Letters*, **96**(6), 062107, 2010.

[Zhe08] Jin-cheng Zheng. Recent advances on thermoelectric materials. *Frontiers of Physics in China*, **3**(3), 269–279, 2008.

[Zho05] Z. Zhou and C. Uher. Apparatus for seebeck coefficient and electrical resistivity measurements of bulk thermoelectric materials at high temperature. *Review of Scientific Instruments*, **76**(2), 023901, 2005.

[Zid06] J. M. O. Zide, D. Vashaee, Z. X. Bian, G. Zeng, J. E. Bowers, A. Shakouri, and A. C. Gossard. Demonstration of electron filtering to increase the Seebeck coefficient in $In_{0.53}Ga_{0.47}/AsIn_{0.53}Ga_{0.28}Al_{0.19}As$ superlattices.

Physical Review B, **74**(20), 205335, 2006.

[Zwe10] K. Zweibel. The Impact of Tellurium Supply on Cadmium Telluride Photovoltaics. *Science*, **328**(5979), 699–701, 2010.

Acknowledgements

Without the help, support, and encouragement of a whole bunch of people this thesis wouldn't be as it is, probably it wouldn't be at all.

I want to express my deep gratitude to my supervisor Volker Schmidt for the chance to ask questions whenever I like, for quick and helpful replies, but most of all for the multitude of brilliant ideas that he develops and shares so easily. Without his support and ideas this thesis would probably be half as good and not even half as interesting as I think it is now. I tried to learn as much as possible from you but but will miss your insight sooner or later.

I am also deeply indebted to my wife who had to share and stand my daily failures and successes. *Ich bin Dir zutiefst dankbar für dein Verständniss, wenn ich am Montag um sechs aufgestanden bin, um mich für die übernächste Woche am SEM einzuschreiben oder am Wochenende nochmal 'ne Messung gestartet habe. Außerdem haben wir ja festgestellt, daß ich besser arbeiten kann, wenn Du oder Ihr bei mir seid, also bist Du auch noch Schuld daran, daß ich alles rechtzeitig über die Bühne gebracht habe.*

I would like to have thanked Prof. Gösele for giving me the opportunity to do a PhD at the MPI of Microstructure Physics. He was a great scientist, but also a nice guy and a motivating leader.

Dr. Leipner I want to thank for taking over the job as doctoral advisor, refereeing the thesis and fruitful discussions.

In some sense, it's the fault of Jörg v. Wittemann that I did/do my PhD at the MPI in Halle. If he hadn't told me about the great opportunities here, who knows where I'd have ended up. On top of that he was a mostly friendly and always helpful roommate and fellow sufferer. I'll miss discussions about nanowires, politics and Megan Fox!

Dr. Dong Sik Kim proved to be indispensable for the progress of my work. I would like to thank him for fabricating thousands of porous Si samples and for helpful discussions on etching, laser interference lithography as well as nanodots and nanochannels.

I'd like to thank Alexander Vogel for the cheerful week in Boston and for bravely reading and correcting several versions of this thesis. On top of that I'd like to acknowledge the very fruitful and uncomplicated collaboration. If it only was always like that with collaborations...

Further thanks go to Hilmar Straube for proof-reading and deep insights on thermal transport and microscopic pictures of the Peltier effect. *Darüber hinaus für Zeichensatzhaarspalterei und interessante und sinnlose Diskussionen über hypothetische Elektronen in abstrakten Materialien; sinnlos im Wesentlichen deshalb, weil ich mich all zu gerne auf das physikalische Problem vor meiner Nase und nicht das große Ganze stürze.*

Also, I'd like to thank Nadine Geyer, for turning a potential conflict into a friendly cooperation. Her insight and help on metal-assisted etching is gratefully acknowledged.

An introduction to Raman spectroscopy was provided by Michael Becker and I'd like to thank him for this.

The help of Dirk Hagen with setting up the measurement system and for helpful measurement technique discussions is gratefully acknowledged; Raik Urbansky I'd like to thank for the help with the KOH samples.

I am also grateful to Dr. Jacquot and Dr. Böttner from the Fraunhofer Institute for Physical Measurement Technology in Freiburg for introduction to the 3ω method and general support.

Dr. A. Cojocaru from the University of Kiel and Dr. Ao. are acknowledged for providing porous Si samples.

A fat "thanks" also goes to the whole MPI, in particular to the mechanics workshop, the electronic workshop, Dr. Alexe for discussions on measurements, Dr. Reiche and Mr. Ilbrig for the lithography, Mrs. Hopfe for the TEM preparation, Dr. Erfurth for the e-beam lithography, Mrs. Sklarek for the sputtering, Mrs. Doss for her help with the interference lithography, and Mrs. Ducke for digging out various papers.

Der vorletzte Dank richtet sich an die Familie und noch nicht genannte Freunde für Ablenkung und Unterstützung in allen Lebenslagen.

Finally, I'd like to acknowledge the rest of the TAB crew, in particular Klaus, JayBee, Sam, Daniel, and Florian, for support in spirits.

Publikationsliste

1. J. P. Bothma, J. de Boor, U. Divakar, P. E. Schwenn, P. Meredith Device-Quality Electrically Conducting Melanin Thin Films *Advanced Materials*, **20**(18), 3539–3542, 2008.

2. J. de Boor, N. Geyer, U. Gösele, and V. Schmidt. Three-beam interference lithography: upgrading a Lloyd's interferometer for single-exposure hexagonal patterning. *Optics Letters*, **34**(12), 1783–1785, 2009.

3. N. Geyer, Z. Huang, B. Fuhrmann, S. Grimm, M. Reiche, T.-K. Nguyen-Duc, J. de Boor, H. S. Leipner, P. Werner, and U. Gösele. Sub-20 nm Si/Ge Superlattice Nanowires by Metal-Assisted Etching. *Nano Letters*, **9**, 3106–3110, 2009.

4. J. de Boor, N. Geyer, J. V. Wittemann, U. Gösele, and V. Schmidt. Sub-100 nm silicon nanowires by laser interference lithography and metal-assisted etching. *Nanotechnology*, **21**(9), 095302 (5pp), 2010.

5. J. de Boor, D. S. Kim, and V. Schmidt. Sub-50 nm patterning by immersion interference lithography using a Littrow prism as a Lloyd's interferometer. *Optics Letters*, **35**(20), 3450–3452, 2010.

6. J.V. Wittemann, A. Kipke, E. Pippel, S. Senz, A.T. Vogel, J. de Boor, D.S. Kim, T. Hyeon, and V. Schmidt. Citrate-stabilized palladium nanoparticles as catalysts for sub-20 nm epitaxial silicon nanowires. *Applied Physics Letters*, **97**(2), 023105 (3 pp.), 12 July 2010.

7. J. de Boor and V. Schmidt. Complete Characterization of Thermoelectric Materials by a Combined van der Pauw Approach. *Advanced Materials*, **22**(38), 4303–4307, 2010.

8. A. T. Vogel, J. de Boor, M. Becker, J. V. Wittemann, S. L. Mensah, P. Werner, and V. Schmidt. Ag-assisted CBE growth of ordered InSb nanowire arrays. *Nanotechnology*, **22**(1), JAN 7 2011.

9. Z. Huang, N. Geyer, P. Werner, J. de Boor, and Ulrich Gösele. Metal-assisted chemical etching of silicon: A review. *Advanced Materials*, **23**(2), 1521–4095, 2011.

10. A. T. Vogel, J. de Boor, J. V. Wittemann, S. L. Mensah, P. Werner, and V. Schmidt. Fabrication of high quality InSb nanowire arrays by chemical beam epitaxy. *submitted*

Proceedings

1. A. Cojocaru, J. Carstensen, J. de Boor, D. S. Kim, V. Schmidt, and H. Föll Production and Investigation of Porous Si-Ge Structures for Thermoelectric Applications. In *218th ECS Meeting*,Las Vegas, USA, *in press*.

2. J. de Boor and V. Schmidt. Complete Characterization of Thermoelectric Materials by a Combined van der Pauw Approach and the Effect of Radiation Losses. In *MRS 2010 Fall Meeting*,Boston, USA, *in press*.

Other

- US Patent (provisional) 61/397,614: "Method for Thermoelectric Characterization"

- Graduate Student Talk Award at MRS 2010 Fall Meeting, Symposium LL: Thermoelectric Materials for Solid-State Power Generation and Refrigeration

Lebenslauf

Name:	Johannes de Boor
Geburtsdatum:	25. 06. 1981
Geburtsort:	Waren (Müritz)
Geschlecht:	männlich
Akademischer Grad:	Diplom-Physiker, Master of Philosophy
Familienstand:	verheiratet, 1 Kind

Werdegang

03/08 –	Promotion am Max-Planck-Institut für Mikrostrukturphysik
02/07 – 12/07	MPhil an der University of Queensland, Brisbane, Australien; Thema: “Charge Transport in Eumelanin”
11/06 – 01/07	Wissenschaftlicher Mitarbeiter an der Universität Rostock
10/01 – 09/06	Physik Diplom an der Universität Rostock; Thema: “Excitonic Screening in Semiconductors”
01/04 – 04/06	Erasmusstudent an der University of Glasgow, Schottland
09/00 – 07/01	Wehrersatzdienst
1990 – 2000	Abitur am Richard-Wossidlo-Gymnasium in Waren
1988 – 1990	Grundschule in Waren

Eidesstattliche Erklärung

Hiermit erkläre ich, dass ich meine Dissertation selbständig und ohne fremde Hilfe verfasst und keine anderen als die von mir angegebenen Quellen und Hilfsmittel zur Erstellung meiner Dissertation verwendet habe. Den benutzten Werken wörtlich oder inhaltlich entnommene Stellen sind als solche gekennzeichnet.

Johannes de Boor Halle (Saale), Januar 2011